Institut für Physik und Astronomie
Arbeitsgruppe *Astrophysik I*, Prof. Dr. Wolf-Rainer Hamann

Radiatively driven winds of hot stars: Coupling hydrodynamics with detailed non-LTE radiative transfer

Dissertation

zur Erlangung des akademischen Grades
"doctor rerum naturalium"
(Dr. rer. nat.)
in der Wissenschaftsdisziplin
Astrophysik

eingereicht an der
Mathematisch-Naturwissenschaftlichen Fakultät
der

Universität Potsdam

von
Andreas Alexander Christoph Sander
ansander@astro.physik.uni-potsdam.de

Potsdam, den 31. August 2015

This document was created using the LaTeX document processing system including BibTeX and KOMA-Script. LaTeX has originally been developed by Leslie Lamport, based on TeX typesetting system created by Donald Knuth.
All figures have been generated with WRplot developed by Wolf-Rainer Hamann.

Contents

Appendix contents

Chapter 1

Introduction

Hot, massive stars play an important role across cosmic times. From the very first, presumably extremely massive stars in the early Universe till the present day, massive stars have decisive influence on the evolution of galaxies. They ionize their environment by their strong UV radiation, they enrich the interstellar medium (ISM) with metals due to the processed material in their strong stellar winds, and they transfer momentum by their stellar wind on their environment, shaping structures around them. Their energetic influence integrated over their lifetime is comparable to the amount of energy released during their final supernova explosion, thereby providing important constraints to other astrophysical fields.

One, if not the most striking feature of hot, massive stars are their winds. Although the Wolf-Rayet phenomenon was known since the discoveries by Wolf & Rayet (1867) and already speculated as a result of a strong continuous matter outflow due to radiation pressure by Beals (1929), it was not until the beginning of the ultraviolet (UV) astronomy era (Morton, 1967a,b) that mass-loss was identified as common attribute of all hot and massive stars. Since then it is clear that stellar mass-loss is a fundamental ingredient in the life of hot stars and the chemical evolution of galaxies.

For hot stars, Snow & Morton (1976) concluded from UV observations with the Copernicus satellite that significant mass outflow is present in all hot stars above a certain luminosity ($\log L/L_\odot \gtrsim 4.3$). The idea of line driving, i.e. the momentum transfer due to absorption of radiation in spectral lines, can be traced back to Saha (1919) who wrote down his ideas shortly after the discovery of the quantum nature of light, trying to explain the tails of comets. After Milne (1924a,b, 1925) and Johnson (1925) developed the basics for line-driven wind theory by considering line absorption as an important way for atoms to overcome gravity, Milne (1926) realized that outward moving atoms can be significantly accelerated by radiation pressure due to the Doppler effect shifting the resonance frequency, thereby exposing the matter to unattenuated radiation.

Only a few years later, Kosirev (1934) suggested that some supergiants, including Wolf-Rayet stars, might have extended photospheres to explain the unusual color-temperatures obtained for these objects. Kosirev (1934) also calculated a mass-loss rate of $\dot{M} \approx 10^{-5}\,\mathrm{M}_\odot/\mathrm{yr}$, assuming a wind velocity of 1000 km/s for Wolf-Rayet stars, thereby matching the parameter range that is obtained today with the help of much more elaborated stellar atmosphere models.

Before the discoveries in the UV spectra, stellar wind theory mostly focused on the solar wind (see, e.g., the review from Parker, 1965), but already shortly afterwards major progress was made in the field of hot star winds. Lucy & Solomon (1970) showed that radiative absorption in UV resonance lines of certain ions can be sufficient to overcome gravity, thereby causing a

continuous mass outflow, i.e. a stellar wind. While Lucy & Solomon (1970) considered only a handful of lines and explicitly evaluated the line acceleration integral numerically, analytical approximations for the radiative force on many lines were performed (Castor, 1974) which lead – in combination with oscillator strength calculations – to the seminal work of Castor, Abbott, & Klein (1975), afterwards known as the CAK-theory. Empirical methods to obtain mass-loss rates for OB stars from the radio (Wright & Barlow, 1975) or infrared (Barlow & Cohen, 1977) regime yielded values comparable with the CAK predictions, thereby backing the idea of radiation-driven winds, even though it later turned out that some of the underlying assumptions in the CAK theory did not hold in the general case. Nevertheless, the basic ideas and approaches from CAK for the radiative force remained as their description was extended by various correction factors (see, e.g., Friend & Abbott, 1986; Pauldrach et al., 1986; Kudritzki et al., 1989), but never completely replaced.

Already shortly after the formulation of the CAK theory, concepts for instabilities or density perturbations occurring in line-driven winds were developed (see, e.g., Nelson & Hearn, 1978; MacGregor et al., 1979; Martens, 1979; Abbott, 1980). Lucy & White (1980) invoked that such instabilities might explain the discovery of X-rays in O stars (Harnden et al., 1979; Seward et al., 1979). The Auger effect caused by X-rays in hot star winds had also been proposed by Cassinelli & Olson (1979) to explain the superionization seen in the UV spectra of some hot stars. Further indications for instabilities came from several discoveries pointing towards variations on shorter time scales, such as non-thermal radio emission (Abbott et al., 1981), narrow shifted absorption features in the UV P Cygni line profiles (Lamers et al., 1982, nowadays referred to as "discrete absorption components", DACs), and enhanced thermal infrared emission correlated with Hα variations (Abbott et al., 1984). It became clear that, even though the bulk of the spectral appearance seemed to be constant over longer time scales, additional processes happen on shorter time scales. This deviates from the picture of a smooth and spherical wind with a monotonic velocity law, which would otherwise be sufficient (see, e.g., the discussion in Lucy, 1982). After various formal linear stability analyses (e.g. MacGregor et al., 1979; Lucy, 1984; Owocki & Rybicki, 1984), also time-dependent numerical calculations (e.g. Owocki et al., 1988; Feldmeier, 1995) were performed, eventually relaxing more and more approximations (e.g. Owocki & Puls, 1996, 1999) and partially extending to multi-dimensional approaches (e.g. Dessart & Owocki, 2003, 2005). Even though the substantial improvements were made in the models, one of the basic conclusions from Owocki (1992) is still valid nowadays, namely that only tiny fractions of the material are accelerated to very high velocities while the bulk of the matter is only affected by the result that instabilities are causing the breaking up of a smooth wind into clumps. This means that, if wind inhomogeneities are considered appropriately, the long-term spectral appearance of hot stars can be understood by assuming a stationary wind. Meanwhile, the theoretical indications for inhomogeneities, also referred to as "clumping", have been backed up by a variety of evidences from observations (see, e.g., Hillier, 1991; Eversberg et al., 1998; Bouret et al., 2003; Kramer et al., 2003). A detailed overview about clumping in hot star winds and their consequences, including several discussions, can be found in Hamann et al. (2008).

In order to estimate the stellar and wind parameters of massive stars from their observed spectra, model atmospheres are necessary. Based on them, synthetic spectra needed to be calculated then compared to the observations in order to deduce the stellar and wind parameters. Modeling such atmospheres requires very complex calculations. The outer layers are not even close to local thermodynamical equilibrium (LTE), thus the population numbers must be calculated from the statistical equations. For a sufficient treatment, large model atoms with

hundreds of levels in total have to be considered. Furthermore, the radiative transfer becomes complicated in an expanding environment, requiring approximations. As a consequence, the calculation is typically replaced by the analytical mCAK-description or performed via either a Monte Carlo (MC) simulation, or a brute-force evaluation of the acceleration integral using a comoving frame (CMF). On top of these two major tasks, i.e. solving the statistical equations and the radiative transfer, several further challenges exist, such as iron-line blanketing or the need for a consistent calculation of the temperature stratification in an expanding, non-LTE environment.

Given the intricacy of the situation, modern model atmospheres rely on numerical calculations. Only in the last few decades computers have become so powerful, that they can accurately simulate an expanding stellar atmosphere and provide synthetic spectra which sufficiently reproduce observations. Although the calculation of helium spectra goes back to Auer & Mihalas (1972), it was not until the end of the 1980s that the pioneering works on the various aspects (e.g. Kurucz, 1979; Hamann, 1980, 1981, 1985; Hillier, 1987; Pauldrach, 1987; Hamann & Schmutz, 1987; Pauldrach & Herrero, 1988) were combined into so-called *unified model atmospheres* (Gabler et al., 1989), where not only the statistical equations and the radiative transfer were handled consistently, but also the separate treatment between the sub- and supersonic layers was removed. From these early approaches, a handful of codes have emerged which are able to model stars with expanding atmospheres, including PHOENIX (Hauschildt, 1992; Baron et al., 2003), WMBASIC (Pauldrach et al., 1994, 2001), FASTWIND (Santolaya-Rey et al., 1997; Puls et al., 2005), CMFGEN (Hillier, 1990; Hillier & Miller, 1998), and the Potsdam Wolf-Rayet (PoWR, Gräfener et al., 2002; Hamann & Gräfener, 2003) stellar atmosphere code which will be used in this work.

In addition to the atmosphere codes mentioned above, which use a CMF approach or mCAK to obtain the line acceleration, there is also the way to calculate the line acceleration via MC simulations for the radiative transfer. This concept goes back to Abbott & Lucy (1985) and was later extended by de Koter et al. (1993, 1997) and Vink et al. (1999). The MC approach allows an inclusion of multiple line scattering, which is not covered by CAK, while being generally faster than the CMF calculations. The spectral reproduction with models using MC radiative transfer significantly supported the idea that radiative driving is sufficient even for objects like O stars with dense winds or Wolf-Rayet stars where mCAK fails (Abbott & Lucy, 1985; de Koter et al., 1993, 1997). Using a grid of MC models, Vink et al. (2000, 2001) have been able to obtain mass-loss rate predictions for OB stars and later also for WR stars (Vink & de Koter, 2005). However, such models use a prescribed velocity law and thus obtain hydrodynamical consistency only on a global scale.

Given the importance of mass loss and the problems of the mCAK theory to describe dense winds, the need for stellar atmosphere models that include a locally consistent treatment of the hydrodynamics is evident. Such models would allow it to obtain a detailed, hydrodynamically consistent wind stratification, thereby yielding mass-loss rates and velocity fields that do not depend on CAK-like approximations. For such an elaborated treatment, a code with a CMF radiative transfer such as PoWR is the best choice, even though the calculations are computationally expensive. Originally developed for Wolf-Rayet (WR) stars, the PoWR code iteratively solves the radiative transfer in the comoving frame together with the statistical equations and the conservation of energy, thereby implicitly accounting for aspects like line-overlapping or multiple scattering. The code therefore provides an excellent basis for a variety of studies, such as testing whether the much denser winds of Wolf-Rayet stars can also be radiatively driven or if additional physics might have to be considered to understand these

objects. So far, the PoWR code has mostly been used to reproduce observed spectra and obtain the stellar and wind parameters of the corresponding stars. For this purpose it is sufficient to prescribe the wind velocity field and the stellar mass-loss rates. In order to study the driving of hot star winds, however, the wind stratification must be directly coupled to the radiative transfer calculations. This means that the hydrodynamic equation must be included consistently into an already extensive code. Pioneering work in this field with codes using a CMF radiative transfer has been done by Pauldrach et al. (1986, 1994, 2001) for WMBASIC. For the PoWR code, a first attempt was made by Gräfener & Hamann (2005, 2008), obtaining models a WC star and hydrogen-rich WN stars. However, their approach has certain limitations in term of applicability as will be discussed later in this work.

Since stellar winds are presumably line-driven, it is extremely important to include as much contributing line transitions as possible. This implies that a stellar atmosphere model has to account for a large number of atomic levels. Due to the non-LTE situation, the statistical equations have to be solved for each of these levels, thereby introducing a certain conflict between opacity completeness and numerical stability. Hence, code improvements had to be made to overcome this and also some other problems that could otherwise harm the calculation of accurate hydrodynamically consistent models. Upgrading the PoWR code from a spectral analysis instrument to a multifunctional stellar atmosphere laboratory was therefore a vital step towards the results presented in this work.

The basics of the PoWR code and some important performed extensions are described in Chapter 2. The underlying concepts of including the hydrodynamics as well as the differences to the method of Gräfener & Hamann (2005) will be outlined in detail in Chapter 3. Prototypical results for hydrodynamically consistent models of different spectral classes are presented in Chapter 4, together with demonstrating the benefits and caveats of this new type of atmosphere models. The more general implications and theoretical questions arising from this work are discussed in Chapter 5 before drawing the conclusions in Chapter 6. Technical concepts for the implementations are given in the appendix.

Chapter 2

The PoWR expanding stellar atmosphere code

2.1 The concept of model atmospheres

In the last three decades, complex stellar atmosphere models have become a standard tool to analyze and understand hot stars. The idea behind this concept is to model the outer layers of a star, where the emergent spectrum is formed. Basically, stellar atmosphere models should provide the the population numbers, the temperature structure, and the radiation field. With these being calculated consistently, the emergent spectrum of a model can be synthesized and used for comparison with observations. The physics used in the models should be as detailed as needed to obtain realistic spectra on the one hand, but also simple enough to allow calculations in a reasonable time on the other hand.

In the outer layers of a hot star, the concept of a local thermodynamically equilibrium (LTE) is not appropriate. The consequence is that complex calculations need to be performed, such as the solution of a large number of statistical equations to obtain the population numbers. This (and other calculations) can only be done numerically, and therefore the development of model atmospheres is coupled to the progression of computers. In the past two decades standard computers have become so powerful that they can run the current generation of one-dimensional stellar atmosphere codes in a reasonable time. Still, the most complex codes, such as the one described in this work, have to remain at a one-dimensional description as more-dimensional approaches on this level of complexity are still beyond current computation limits.

For hot stars with non-negligible winds, the atmospheric expansion needs to be taken into account for the radiative transfer which is needed to obtain the radiation field and the radiative acceleration. The numerical handling of this requires either a calculation in a comoving frame (see Sect. 2.8) or a major simplification such as the Sobolev approach (see Sect. 3.6).

Furthermore, comparisons between model spectra and observations have shown that the additional effects such as clumping (see, e.g. Hamann & Koesterke, 1998) and iron-line blanketing need to be taken into account by the atmosphere models. In total, the following objectives should be achieved by a code calculating a stellar atmosphere:

- Solution of the statistical equations in non-LTE
- Solution of the radiative transfer in the comoving frame

- Energy conservation (yields the temperature structure)
- A proper accounting for the influence of iron group elements
- Accounting for inhomogeneities ("clumping") in the atmosphere
- Consistency between the wind stratifications and the radiation field

Apart from the last point, which is actually the main focus of this work, the current generation of stellar atmosphere codes is performing quite well in reaching these objectives. However, there are certain simplifications - apart from the restriction to 1D - that could need an improvement. Several of them will be addressed in the following sections with performed improvements described in detail. Nevertheless, the biggest task is actually concealed in the last bullet point, namely a consistent description between the results of the radiative transfer calculation and the wind stratification. This is addressed in detail in Chapter 3.

2.2 Basic assumptions

Apart from small scale variabilities happening on the order of the dynamic time scale, observations reveal that the spectra of most hot and massive stars do not change significantly over time. The Potsdam Wolf-Rayet (PoWR) stellar atmosphere code therefore assumes a stationary, homogeneous and spherically symmetric outflow. From these basic assumptions, one obtains the equation of continuity

$$\dot{M} := \frac{\mathrm{d}M}{\mathrm{d}t} = 4\pi\ r^2\ \rho(r)\ v(r) = \text{const.} \tag{2.1}$$

A major consequence of Eq. (2.1) is that for a given radius r, the density $\rho(r)$ is directly coupled to the wind velocity $v(r)$. This has fundamental implications for the implementation of the hydrodynamic equation but also introduces certain limitations. Both will be discussed later on in this work.

In total, a PoWR model atmosphere is described by a set of fundamental physical parameters. These are:

- Two out of the three values connected by Stefan-Boltzmann's law, namely:
  - the stellar radius R_*, defined at a specified Rosseland continuum optical depth $\tau_{\max}$ (default: $\tau_{\max} = 20$)
  - the effective temperature T_* related to R_*
  - the luminosity $L_* = 4\pi R_*^2 \sigma_{\mathrm{SB}} T_*^4$
- the clump* density contrast $D(r)$
- the mass-loss rate $\dot{M}$ or implying value (see below)
- the terminal wind velocity v_∞ and the wind velocity law

*$D(r)$ only refers to optically thin clumps ("microclumping") with a void interclump medium. In the calculation of the formal integral, PoWR can also account for optically thick clumps in an approximative way, see Oskinova et al. (2007) for details. A very rough approximation for optically thick clumps during the main model iteration is discussed in Sect. 5.4.

- the stellar mass M_*, either given directly as an input value (M_* or $\log g$) or calculated from the luminosity L_*[†]
- the chemical composition X_i of all elements that should be considered, usually in form of mass fractions

Instead of directly specifying the mass-loss rate $\dot{M}$, one can also specify a line emission measure in the form of either the *transformed radius*

$$R_\mathrm{t} := R_* \left[\frac{v_\infty}{2500\,\mathrm{km/s}} \Big/ \frac{\dot{M}\sqrt{D}}{10^{-4}\,\mathrm{M_\odot/yr}} \right]^{\frac{2}{3}} \tag{2.2}$$

(Schmutz et al., 1989; Hamann & Koesterke, 1998, for the current form) or the *wind strength parameter*

$$Q := \frac{\dot{M}\sqrt{D}}{(R_* v_\infty)^{3/2}} \tag{2.3}$$

(Puls et al., 1996, 2008, for the current form) which then imply a certain value of $\dot{M}$ as all the other parameters in their definitions need to be specified anyhow. Using R_t or $\log Q$ can be helpful when calculating model grids or searching for models with a similar emission line strength in their normalized spectra.

In hydrodynamically consistent models, $\dot{M}$ and $v(r)$ are adjusted in order to ensure that hydrodynamic equation is fulfilled throughout the atmosphere. However, as they define the density stratification, starting values are still required as an input for the calculations.

On top of these fundamental physical parameters, several numerical parameters can also be customized by the user. Ideally, their particular value does not influence the physical results obtained in a model calculation. However, certain physical parameter regimes can lead to different numerical situations and thus some numerical treatments that might work well in one regime might not be sufficient in others. Adjusting numerical parameters is therefore done in order to adjust the numerics in such a way, that the intended stellar atmosphere models can be sufficiently calculated.

2.3 The prescribed wind velocity law

In the standard branch of the PoWR code, the velocity field $v(r)$ is not calculated self-consistently, but instead prescribed. Based on the results of the CAK theory (Castor et al., 1975, see also Sect. 3.6), $v(r)$ in a stellar wind is typically described by a so-called *beta law*, i.e.

$$v(r) = v_\infty \left(1 - \frac{R_*}{r}\right)^\beta . \tag{2.4}$$

A slightly more advanced description of the velocity field is the so-called *two-beta law* which is simply the sum of two weighted beta laws:

$$v(r) = v_\infty \left[(1-q) \left(1 - \frac{R_*}{r}\right)^{\beta_1} + q \left(1 - \frac{R_*}{r}\right)^{\beta_2} \right] \tag{2.5}$$

[†]Depending on the stellar type, the mass-luminosity-relations from Langer (1989) or Gräfener et al. (2011) are used if the stellar mass is not given otherwise.

The values of β_1 and β_2 must be prescribed as well as the weight q. (For $q = 0$ the two-beta law reduces to the beta law (2.4) with $\beta = \beta_1$.)

Note that both laws imply $v = 0$ at $r = R_*$, which is a problem in the models as it would lead to an infinitely high density due to the equation of continuity (2.1). To avoid this singularity, the velocity law in the deeper, quasi-static layers is either approximated by a barometric law or consistently obtained by integrating the hydrostatic equation. (This method is discussed in more detail in Sect. 3.4.) In order to ensure a smooth connection, the beta law (2.4) is written in a slightly modified way in the PoWR code, namely

$$v(r) = p_1 \left(1 - \frac{R_*}{r + p_2}\right)^{\beta}. \tag{2.6}$$

The two parameters p_1 and p_2 depend on v_∞ and the inner boundary of the beta law regime R_{con} plus the velocity $v_{\mathrm{con}} = v(R_{\mathrm{con}})$. The connection point is usually obtained from the condition that v and $\frac{\mathrm{d}v}{\mathrm{d}r}$ must be continuous. However, as other codes tend to use a distinct transition point, such as a certain fraction of the sound speed (see, e.g. Table 1 in Sander et al., 2015), it is alternatively possible to fix the connection point to such a fraction. The formulae for calculating the p-parameters is given in Sect. A.2 of the appendix.

2.4 The PoWR scheme

The calculation of a model atmosphere comprises a large and complex set of routines, way too many to list them all in particular in this work. The basic scheme, however, can be outlined as follows:

1. Model Start: Setup of radius and frequency grid, first velocity stratification, start approximation for n_i and J_ν
2. Main iteration
   a) Solution of the radiative transfer in the co-moving frame
   b) Temperature corrections,
   c) solution of the statistical equations,
   d) (optional) velocity stratification update
3. Formal integration: Calculation of the emergent spectrum in the observer's frame

A more technical outline of the scheme with references to individual programs can be found in Sect. A.1. The concepts of the major tasks of the main iteration, namely the solution of the statistical equation, the temperature corrections, the solution of the radiative transfer in the co-moving frame and the (optional) update of the velocity stratification, will be outlined in the following sections with a focus on updates that have been performed in the framework of this thesis.

2.5 Solution of the statistical equations

2.5.1 General concept

One, if not the main task of the `STEAL` program is the calculation of the population numbers. Due to the non-LTE situation, this has to be done by solving the system of statistical equations

with accelerated lambda iteration (ALI, see e.g. Hamann, 1985, 1986). The system for the losses and gains of all N atomic levels considered in a stellar atmosphere model can be written as

$$\forall j = 1..N: \quad \sum_{i \neq j}^{N} n_i P_{ij} = \sum_{i \neq j}^{N} n_j P_{ji}. \tag{2.7}$$

The rate coefficient matrix $\mathbf{P}$ contains all the transitions rate coefficients, including radiative and collisional transitions. The entry P_{ij} describes the transition rate coefficient from level i to level j. Thus the left-hand side of Eq. (2.7) summarizes the gains for level j from all other levels while the right-hand side contains the sum of all losses for the same level. Adding the number conservation

$$\sum_{i=1}^{N} n_i = 1 \tag{2.8}$$

and the charge conservation

$$\sum_{i=1}^{N} n_i Z_i = n_\mathrm{e}, \tag{2.9}$$

with Z_i describing the charge of the corresponding ion, to the system, one can write Eq. (2.7) in the form

$$\vec{n} \cdot \mathbf{P} - \vec{b} = \vec{0}. \tag{2.10}$$

The vector $\vec{b}$ contains mainly zeros apart from a few entries that account for the number conservation. Due to the ALI procedure, the rate coefficient matrix itself depends on the populations numbers, i.e. $\mathbf{P} = \mathbf{P}(\vec{n})$. The population numbers n_i which fulfill Eq. (2.10) are thus the zeros of a multidimensional system of equations. To find them, a Newton-Raphson approach can be applied. This iterative approach finds the new populations numbers $\vec{n}^{(k+1)}$ for a given set $\vec{n}^{(k)}$ by calculating

$$\vec{n}^{(k+1)} = \vec{n}^{(k)} - \left(\vec{n}^{(k)} \cdot \mathbf{P} - \vec{b}\right) \cdot \boldsymbol{\mathcal{M}}^{-\mathbf{1}}. \tag{2.11}$$

The matrix $\mathcal{M}$ is the derivative of $\vec{n} \cdot \mathbf{P}$ with respect to the population numbers, i.e.

$$\mathcal{M}_{ij} = \frac{\partial}{\partial n_i} \left(\sum_{m=1}^{N} n_m P_{mj} \right) \tag{2.12}$$

2.5.2 Matrix inversion splitting

The inversion of the matrix $\mathcal{M}$ is required for the Newton-Raphson approach (see Eq. 2.11), but one of the most time-consuming steps. Furthermore, numerical errors tend to grow with the rank of the matrix. As the statistical equations need to be solved consistently for all elements and all their levels, the matrix $\mathcal{M}$ grows extensively when more and more elements and levels are being used in a model atmosphere. However, the recent usage of PoWR models for O and B stars and also the needs of this work, i.e. the importance to include all levels with a relevant contribution to the radiative acceleration, require models with several hundreds of levels.

In order to reduce both calculation time and error margin, one can make use of the special inner structure of the matrix $\mathcal{M}$. Due to transitions occurring only between levels of the same

element, the transition matrix $\mathbf{P}$ has – apart from the charge conservation line – a block-diagonal form with the number of blocks NA being equal to the number of elements used in a model. This propagates into the derivative matrix $\mathcal{M}$. For a block-diagonal matrix, the inverse of the whole matrix can be obtained by simply inversion the blocks, i.e.

$$\mathcal{M} = \begin{bmatrix} A_1 & & & \\ & A_2 & & \\ & & \ddots & \\ & & & A_{\mathrm{NA}} \end{bmatrix} \quad \Rightarrow \quad \mathcal{M}^{-1} = \begin{bmatrix} A_1^{-1} & & & \\ & A_2^{-1} & & \\ & & \ddots & \\ & & & A_{\mathrm{NA}}^{-1} \end{bmatrix} \tag{2.13}$$

Although the inversion has to be done for each block now, this is much more convenient. The rank of each block is much lower and thus numerical inversion is quicker and more precise.

In order to apply this "inversion splitting", the charge conservation, which is needed to calculate the proper electron densities, has to be solved separately afterwards now. This equation would not stick to the block format and instead cover a complete row of the matrix, thus spoiling the block structure. However, in various test calculations the readjustment of the electron density after the solution of the statistical equations did not turn out to have any noticeable effects, neither on the atmospheric stratification, nor on the obtained spectra.

In fact, very few non-diagonal elements appear in $\mathcal{M}$ due to the ALI procedure which avoids the convergence problems of a normal lambda iteration in optically thick situations by a prediction of the new population numbers. Technically this translates to a modification of the radiation field used to calculate the rate matrix $\mathbf{P}$. Apart from the charge conservation, $\mathbf{P}$ still keeps a block-diagonal structure, but its derivative matrix $\mathcal{M}$ does not. These non-block entries in $\mathcal{M}$ have to be neglected in the splitting-approach, introducing a small difference in the result calculated for $\mathcal{M}^{-1}$ compared to the complete inversion without using the block approach. An error in the derivative is not a problem for a Newton-Raphson approach as long as the overall convergence is still reached. Several test calculations have been performed to check this matter, comparing models calculated with and without splitting approach. Those which run fine even without using the splitting approach, usually due to their lower number of levels, did converge in a similar behavior than and did not show noticeable differences in their emergent spectra or their stratifications. Instead models which had numerical problems without the split run fine when using the split approach. While this provides the basis for calculating models with much more elements and levels than before, there still seem to be upper limits, but much higher ones than before.

2.6 The temperature stratification

The consistent determination of the electron temperature $T(r)$ throughout an expanding non-LTE stellar atmosphere has been a complicated task in the past. The temperature and its corrections are depending on the radiation field and the population numbers, which are already coupled themselves. Some stellar atmosphere models therefore either use a completely fixed temperature stratification or simplified the task by additional assumptions, such as using LTE and/or a gray atmosphere. It was not until 1990s that such restrictions have been removed in the code that we now refer to as PoWR.

Nowadays these limitations are no longer necessary, but the precise determination of $T(r)$ is still an important task and can be crucial for the successful convergence of a particular

atmosphere model. In the field of hot and massive stars, two major concepts are used in state-of-the-art stellar atmosphere codes. The first one is referred to as the "radiative equilibrium" method after it's basic assumption, while the second one is called "thermal balance" and stems from the energy balance of the electrons.

2.6.1 Temperature corrections via radiative equilibrium

Using the radiative equilibrium for developing a temperature correction goes back to the suggestions of Unsöld (1951) (see also Böhm, 1954) and Lucy (1964). Its first application was done by Auer & Mihalas (1968, 1969) and since then this method has become the "standard" approach for obtaining the temperature stratification in a stellar atmosphere. The radiative equilibrium is usually written in the following two forms which already implicitly include the energy equation:

$$4\pi \int_0^\infty \kappa_\nu \left(S_\nu - J_\nu\right) \mathrm{d}\nu = 0 \tag{2.14}$$

$$4\pi \int_0^\infty H_\nu \mathrm{d}\nu = \sigma_{\mathrm{SB}} T_{\mathrm{eff}}^4 \tag{2.15}$$

Usually the first form (2.14) is meant when the term "radiative equilibrium" is used while the second one (2.15) is referred to as "flux conversation" as H_ν is the so-called Eddington flux and T_{eff} is constant. In fact, both forms reflect the energy conservation. Frequency integration of the zeroth moment of the transport equation leads to the second equation for H_ν when using the first one, so it is implicitly included anyhow. The first one is therefore sometimes called the "differential form" while the second one is referred to as the "integral form" of radiative equilibrium. Note that the Eqs. (2.14) and (2.15) refer to a static, plane-parallel atmosphere and needs to be adjusted for the application in the PoWR code. This generalization to spherically expanding non-gray atmospheres of method from Unsöld (1951, 1955) and Lucy (1964) is described in detail in Hamann & Gräfener (2003). It eventually leads to the following expression for the temperature correction:

$$\begin{aligned}\Delta T(r) = \frac{\pi}{4\sigma_{\mathrm{SB}}} \frac{1}{T^3(r) r^2 \kappa_S(r)} \Bigg\{ & - \int_0^\infty \left(\eta_\nu - \kappa_\nu J_\nu\right) \mathrm{d}\nu \\ & + \frac{\kappa_J(r)}{(qf)_J(r)} \int_{r'=r}^{R_{\max}} (q\kappa)_H(r') \left[\tilde{H}_0(r') - \tilde{H}(r')\right] \mathrm{d}r' \\ & + \kappa_J(r) \frac{(qf)_J(R_{\max})}{(qf)_J(r)} \frac{\tilde{H}_0(R_{\max}) - \tilde{H}(R_{\max})}{h_J(R_{\max})} \Bigg\}\end{aligned} \tag{2.16}$$

The first line of Eq. (2.16) after the bracket reflects the radiative equilibrium Eq. (2.14) while the second and the third stem from an integral over the generalized version of Eq. (2.15) with the second line referring to the integral and the third one to a constant that can be fixed by the boundary values at $R_{\max}$[‡].

[‡]All three terms can be multiplied with a weighting factor in the PoWR code in order to force specific corrections being preferred or even switched off.

In a thin atmosphere the Eq. (2.14) can cause numerical problems. The situation is dominated by resonance lines where κ_ν is basically zero and S_ν and J_ν are large but should cancel each other as they do not contribute the free electrons and therefore should not affect the temperature. In fact, it can happen that small numerical errors are multiplied with a large value and therefore do not cancel each other, but lead to unphysical corrections.

2.6.2 Temperature corrections via thermal balance

A nice way to avoid the previously mentioned problems is to consider the thermal balance of the electrons, where bound-bound line transitions do not enter, instead of the radiative equilibrium. Although this temperature correction method was not used for hot star atmospheres until the 1990s, it goes back to the ideas of Hummer & Seaton (1963) and Hummer (1963) who applied it for planetary nebulae. Before the implementation in PoWR, it was only used for temperature corrections in the Munich codes FASTWIND and WMBASIC while most other hot star atmosphere codes, such as CMFGEN, but also plane-parallel codes (e.g. TLUSTY) use the radiative equilibrium method (Puls, 2008).

Since a proper temperature structure is crucial for a successful application of the hydrodynamic routines described later in this work, the "thermal balance" method was included in PoWR as a part of this thesis. While the method is described in detail by Kubát et al. (1999) and Kubát (2001), their notation is considerably different in certain details. Therefore the main equations will be given here in the notation that follows the particular implementation in PoWR. When comparing these equations with Kubát et al. (1999), it should be noted that PoWR does not use the so-called occupation probabilities w_i, i.e. we set $w_i \equiv 1$ in their equations.

The thermal balance of electrons is written as the difference between heating (Q^{H}) and cooling (Q^{C}) terms:

$$\Delta Q := Q^{\mathrm{H}} - Q^{\mathrm{C}} \tag{2.17}$$

$$:= Q^{\mathrm{H}}_{\mathrm{ff}} + Q^{\mathrm{H}}_{\mathrm{bf}} + Q^{\mathrm{H}}_{\mathrm{c}} - Q^{\mathrm{C}}_{\mathrm{ff}} - Q^{\mathrm{C}}_{\mathrm{bf}} - Q^{\mathrm{C}}_{\mathrm{c}} \tag{2.18}$$

Both, heating and cooling terms, consist of three contributions, namely free-free and bound-free transitions as well as collisions. In an ideal situation with a perfect balance we should have $\Delta Q = 0$. In reality the situation will of course differ, but it is exactly this aim that is used to obtain a correction term for the current temperature stratification.

The straight-forward way to obtain a temperature correction is to implement a Newton-Raphson scheme, i.e. calculating the temperature derivative of ΔQ and calculate the new temperature via

$$T_{\mathrm{new}} = T_{\mathrm{old}} - \frac{\Delta Q(T)}{\frac{\partial}{\partial T}(\Delta Q)}. \tag{2.19}$$

An example of the corrections for the thermal balance method compared to those from radiative equilibrium is shown in Fig. 2.1. For such a cool model, the correction from the thermal balance method in the outer part is much smoother than those obtained by radiative equilibrium. In the innermost part, flux consistency is usually more reliable and the thermal balance corrections are switched off.

In the following paragraphs the calculation of Q_{ff}, Q_{bf}, and Q_{c} as well as their temperature derivatives are described. The choice of the Newton-Raphson method especially requires a calculation of the derivatives. For the population numbers N_j and the radiation field J_ν no

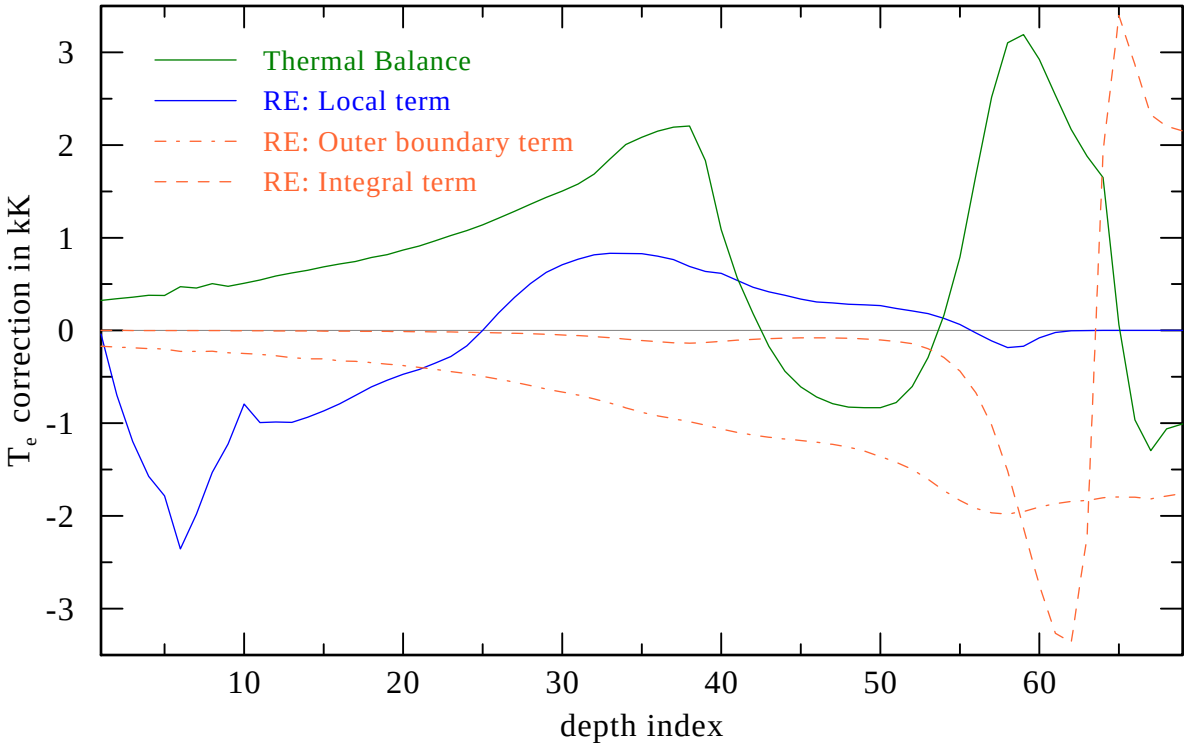

Figure 2.1 – Electron temperature correction example for a non-converged B-star model with $T_* = 26\,\mathrm{kK}$: The corrections suggested by the thermal balance method (green curve) is compared to the three correction components from Eq. 2.16 based on radiative equilibrium (RE, blue and orange curves). The two orange curves together resemble the flux consistency terms.

analytical derivatives exist and no proper numerical derivative can be calculated within an effort that would be legitimate for the purpose of providing a temperature correction in each iteration. Therefore N_j and J_ν are treated as if they would not depend on the temperature in the following calculations. This approximation is probably not as bad as it sounds as the "thermal balance" method focuses especially on the outer parts of the stellar atmosphere where the temperature dependencies of both, N_j and J_ν, should be weak. Furthermore, the derivatives only determine the convergence radius in the Newton-Raphson method, not the actual value of the solution.

Free-Free transitions

In free-free transitions all energy is transferred between the radiation field and the electrons. The heating terms describe the electron energy gains, thus $Q_{\mathrm{ff}}^{\mathrm{H}}$ consists of the energy gained by absorption, i.e.

$$Q_{\mathrm{ff}}^{\mathrm{H}} = 4\pi n_{\mathrm{e}} \sum_j N_j \int_0^\infty \alpha_{\mathrm{ff},j}(\nu,T) J_\nu \mathrm{d}\nu \tag{2.20}$$

with n_{e} being the electron density, and $\alpha_{\mathrm{ff},j}$ the free-free cross section. The radiation field J_ν is the radiation field on a coarse frequency grid, i.e. `XJC` in the PoWR code. For the cooling

term $Q_{\rm ff}^{\rm C}$ we now have to sum up the emission processes, i.e.

$$Q_{\rm ff}^{\rm C} = 4\pi n_{\rm e} \sum_j N_j \int_0^\infty \alpha_{{\rm ff},j}(\nu,T) \left(J_\nu + \frac{2h\nu^3}{c^2} \right) e^{-\frac{h\nu}{kT}} {\rm d}\nu. \tag{2.21}$$

Note that both, $Q_{\rm ff}^{\rm H}$ and $Q_{\rm ff}^{\rm C}$, vanish for non-charged stages ($Z = 0$) due to the cross-section $\alpha_{\rm ff}$ being proportional to Z^2:

$$\alpha_{{\rm ff},j}(\nu,T) = \frac{4e_0^6 Z^2}{3ch} \sqrt{\frac{2\pi}{3km_{\rm e}}} \frac{g_{\rm ff}(\nu,T)}{\nu^3\sqrt{T}} \tag{2.22}$$

$$= 1.37 \cdot 10^{-23} {\rm cm}^5 Z^2 \left(\frac{T}{\rm K} \right)^{-\frac{1}{2}} \left(\frac{\lambda}{\rm cm} \right)^3 g_{\rm ff}(\nu,T) \tag{2.23}$$

Now the temperature derivative of both terms is needed. Neglecting the temperature dependencies of the population number and radiation field, only the $\alpha_{\rm ff}$ coefficient remains in the heating term. Its derivative can be calculated straight forward:

$$\frac{\partial}{\partial T} \alpha_{{\rm ff},j}(\nu,T) = -\frac{1}{2T} \alpha_{{\rm ff},j}(\nu,T) + \frac{4e_0^6 Z^2}{3ch} \sqrt{\frac{2\pi}{3km_{\rm e}}} \frac{\partial g_{\rm ff}(\nu,T)}{\partial T} \frac{1}{\nu^3\sqrt{T}} \tag{2.24}$$

For the Gaunt factor $g_{\rm ff}$ there is no analytic formula, but only tables depending on frequency ν and temperature T. However, this allows us to calculate $g_{\rm ff}(T)$ as well as $g_{\rm ff}(T+\delta t)$ in order to approximate the derivative of $g_{\rm ff}$ by a difference quotient. With all these terms given, the derivatives for the free-free heating and cooling terms can be obtained:

$$\frac{\partial}{\partial T} Q_{\rm ff}^{\rm H} = 4\pi n_{\rm e} \sum_j N_j \int_0^\infty \frac{\partial \alpha_{{\rm ff},j}}{\partial T} J_\nu {\rm d}\nu \tag{2.25}$$

$$\frac{\partial}{\partial T} Q_{\rm ff}^{\rm C} = 4\pi n_{\rm e} \sum_j N_j \int_0^\infty \left(\frac{\partial \alpha_{{\rm ff},j}}{\partial T} + \frac{h\nu}{kT^2} \alpha_{{\rm ff},j} \right) \cdot \left(J_\nu + \frac{2h\nu^3}{c^2} \right) e^{-\frac{h\nu}{kT}} {\rm d}\nu \tag{2.26}$$

The longer expression for the derivative of the cooling term (2.26) follows from the exponential factor in Eq. (2.21).

Bound-free transitions

The thermal balance of electrons is not affected by bound-bound transitions – in contrast to the radiative equilibrium – but by bound-free (BF) transitions where an electron is released or captured. Here ionizations lead to free electrons and therefore contribute excess kinetic energy to the heating. The resulting gain is

$$Q_{\rm bf}^{\rm H} = 4\pi \sum_{\rm Kon=(l,u)} N_l \int_{\nu_{lu}}^\infty \sigma_{lu}(\nu) J_\nu \left(1 - \frac{\nu_{lu}}{\nu} \right) {\rm d}\nu, \tag{2.27}$$

with l denoting the lower (bound) level,u the upper level and ν_{lu} the ionization edge frequency. The term $\left(1 - \frac{\nu_{lu}}{\nu}\right)$ accounts for the subtraction of the energy fraction that is transferred to

the atoms, ensuring that only the energy transferred into electrons is covered here. In a similar way as for the free-free case, the corresponding term for cooling by recombination is

$$Q_{\mathrm{bf}}^{\mathrm{C}} = 4\pi \sum_{\mathrm{Kon=(l,u)}} N_u \frac{N_l^*}{N_u^*} \int_{\nu_{lu}}^{\infty} \sigma_{lu}(\nu) \left(J_\nu + \frac{2h\nu^3}{c^2} \right) e^{-\frac{h\nu}{kT}} \left(1 - \frac{\nu_{lu}}{\nu} \right) \mathrm{d}\nu. \tag{2.28}$$

Population numbers marked with an asterisk, e.g. N_l^*, refer to the LTE-population number of the corresponding level. Neglecting the temperature dependence of the non-LTE populations numbers N and the radiation field J_ν, the temperature derivative of the heating term is zero. For the cooling term, there is an implicit Saha-Boltzmann factor in N_l^*/N_u^* and an explicit exponential factor that has to be taken into account:

$$\frac{\partial}{\partial T} Q_{\mathrm{bf}}^{\mathrm{H}} = 0 \tag{2.29}$$

$$\frac{\partial}{\partial T} Q_{\mathrm{bf}}^{\mathrm{C}} = -\left(\frac{3}{2T} + \frac{h\nu_{lu}}{kT^2} \right) Q_{\mathrm{bf}}^{\mathrm{C}} + 4\pi \frac{h}{kT^2} \sum_{\mathrm{Kon=(l,u)}} N_u \frac{N_l^*}{N_u^*} \int_{\nu_{lu}}^{\infty} \sigma_{lu}(\nu) \left(J_\nu + \frac{2h\nu^3}{c^2} \right) e^{-\frac{h\nu}{kT}} \left(1 - \frac{\nu_{lu}}{\nu} \right) \nu \, \mathrm{d}\nu \tag{2.30}$$

Collisions

Energy can also be transferred between atoms and electrons without involving the radiation field, namely by collisions. The heating component here consists of collisional recombinations and de-excitations

$$Q_{\mathrm{c}}^{\mathrm{H}} = n_{\mathrm{e}} \sum_{l,u} N_u \frac{N_l^*}{N_u^*} \, \Omega_{lu}(T) \, h\nu_{lu}, \tag{2.31}$$

while the cooling terms consists of ionization and excitation via collisions

$$Q_{\mathrm{c}}^{\mathrm{C}} = n_{\mathrm{e}} \sum_{l,u} N_l \, \Omega_{lu}(T) \, h\nu_{lu}. \tag{2.32}$$

Ω_{lu} is the so-called *collision strength*, its product with the electron density gives the collisional rates $C_{lu} = n_{\mathrm{e}}\Omega_{lu}$ which enter the rate coefficient matrix for the statistical equations. With the help of the LTE populations numbers, one can use the relation $N_l^* \, \Omega_{lu} = N_u^* \, \Omega_{ul}$. Note that the ratio between the LTE population numbers can be expressed by the (Saha-)Boltzmann equation and therefore introduces a temperature dependence. The temperature dependency of Ω_{lu} itself is not trivial as different formulae are used for each element.

In the PoWR code, the double sum over all upper and lower levels is replaced by more convenient loops. As collisions come in two different flavors, namely from line transitions (collisional excitation and deexcitation) and bound-free transitions (collisional ionization and recombination), the collisional rates are calculated differently. For the line transitions, Ω_{lu} is calculated internally, while it is Ω_{ul} for the bound-free transitions, so this has to be taken into account for the derivatives later on. This is the only part where line transitions affect the thermal balance. Additional care has to be taken for iron superlevels as it can happen that there are no radiative transitions between two levels which means that such transitions are

not covered in a standard loop using the radiative transition list (`IND index`). As there can still be transitions via collisions, these contributions have to be added afterwards. However, their derivatives are not different in type and hence all equations are the same as for the other line transitions. We thus rewrite equations (2.31) and (2.32) for the line transitions in the following way:

$$Q^{\mathrm{H}}_{\mathrm{c,IND}} = n_{\mathrm{e}} \sum_{l,u} N_u \frac{N^*_l}{N^*_u}\ \Omega_{lu}(T)\ h\nu_{lu} \tag{2.33}$$

$$= n_{\mathrm{e}} \sum_{l,u} N_u \Omega_{ul}(T)\ h\nu_{lu} \tag{2.34}$$

$$= \sum_{l,u} N_u C_{ul}(T)\ h\nu_{lu} \tag{2.35}$$

$$Q^{\mathrm{C}}_{\mathrm{c,IND}} = \sum_{l,u} N_l \frac{N^*_u}{N^*_l}\ C_{ul}(T)\ h\nu_{lu} \tag{2.36}$$

This form reflects that for line transitions C_{ul} is calculated as $C_{ul} = n_{\mathrm{e}}\Omega_{ul}$ internally while C_{lu} is obtained by multiplication with the LTE population number ratio using the relation $C_{lu} = n_{\mathrm{e}}\ \frac{N^*_l}{N^*_u}\ \Omega_{ul}$. The temperature derivatives of the $Q_{\mathrm{c,IND}}$-terms can then be obtained by using an analytic derivative for the Boltzmann factor originating from the LTE population number ratio while the derivative of C_{ul} can be calculated numerically. Once again neglecting any temperature dependency of the non-LTE population number, the temperature derivatives are

$$\frac{\partial}{\partial T} Q^{\mathrm{H}}_{\mathrm{c,IND}} = \sum_{l,u} N_u \frac{\partial C_{ul}}{\partial T}\ h\nu_{lu} \tag{2.37}$$

$$\frac{\partial}{\partial T} Q^{\mathrm{C}}_{\mathrm{c,IND}} = \sum_{l,u} N_l \frac{N^*_u}{N^*_l} \left(\frac{\partial C_{ul}}{\partial T} + \frac{h\nu_{lu}}{kT^2} C_{ul} \right) h\nu_{lu}. \tag{2.38}$$

The collisional rates for the ionizations are calculated just the other way round. Here, $C_{lu} = n_{\mathrm{e}}\Omega_{lu}$ is calculated directly via Eq. (6.39) in Jefferies (1968) while C_{ul} is obtained via scaling with the corresponding Saha-Boltzmann factor. Hence, the equations are now written

$$Q^{\mathrm{H}}_{\mathrm{c,KON}} = \sum_{l,u} N_u \frac{N^*_l}{N^*_u}\ C_{lu}(T)\ h\nu_{lu} \tag{2.39}$$

$$Q^{\mathrm{C}}_{\mathrm{c,KON}} = \sum_{l,u} N_l\ C_{lu}(T)\ h\nu_{lu} \tag{2.40}$$

The corresponding temperature derivatives are:

$$\frac{\partial}{\partial T} Q^{\mathrm{H}}_{\mathrm{c,KON}} = \sum_{l,u} N_u \frac{N^*_l}{N^*_u} \left[\frac{\partial C_{lu}}{\partial T} - \left(\frac{3}{2T} + \frac{h\nu_{lu}}{kT^2} \right) C_{lu} \right] h\nu_{lu} \tag{2.41}$$

$$\frac{\partial}{\partial T} Q^{\mathrm{C}}_{\mathrm{c,KON}} = \sum_{l,u} N_l \frac{\partial C_{lu}}{\partial T}\ h\nu_{lu} \tag{2.42}$$

Note that there is a Saha-Boltzmann factor for the bound-free transitions instead of the pure Boltzmann factor as it was for the line transitions. Furthermore it might seem strange at first

that ionizations enter in the heating term for bound-free transitions, while they appear in the cooling term for collisions, but one has to keep in mind that the latter ionizations are caused by another electron, so there is a net loss of electron energy in contrast to the bound-free transitions, where the ionization energy is provided by the radiation field.

2.6.3 Connection between radiative equilibrium and thermal balance

The two equations, radiative equilibrium and thermal balance, are in fact mathematically equivalent. The previously defined Q^{H} and Q^{C} reflect the energy gains and losses for the free electrons. These values could also be obtained by the sum of the the radiative energy and the product of the ionization energies and the changes in the population numbers. Hence we can write

$$\frac{\mathrm{d}Q}{\mathrm{d}t} = \underbrace{4\pi \int_0^\infty \kappa_\nu \left(S_\nu - J_\nu\right) \mathrm{d}\nu}_{=0 \text{ in radiative equilibrium}} + \underbrace{\sum_i h\nu_i \frac{\mathrm{d}N_i}{\mathrm{d}t}}_{=0 \text{ in statistical equilibrium}} \tag{2.43}$$

(see also Hillier & Miller, 1998). The second term on the right hand side vanishes in statistical equilibrium, as the population numbers N_i do not change then. What remains is the first term which exactly vanishes in radiative equilibrium. Therefore in a situation with statistical and radiative equilibrium, the left hand side should be zero, but this is what we already have described as thermal balance. This illustrates that in statistical equilibrium, both correction methods should in theory lead to the same temperature structure. Numerically this is usually not the case, as both methods have different strengths and weaknesses which were previously mentioned. The proper method therefore has to be chosen depending on the specific model situation. The effective temperature or the departure from LTE in a certain part of the atmosphere can have a huge effect on how successful one or the other method exactly is.

2.7 Conservation of optical depth

An important scale for a stellar atmosphere is the optical depth τ, i.e. the inward integrated opacity. In a non-gray stellar atmosphere, the opacity κ is frequency-dependent and so would be the simple definition of the optical depth. In order to have a frequency-independent scale one has to find a proper average over the frequency. The "flux-weighted mean" definition of the so-called Rosseland (mean) opacity

$$\kappa_{\mathrm{Ross}}(r) := \frac{\int_0^\infty \frac{\partial B_\nu}{\partial T} \mathrm{d}\nu}{\int_0^\infty \frac{1}{\kappa(\nu,r)} \frac{\partial B_\nu}{\partial T} \mathrm{d}\nu} \tag{2.44}$$

with the resulting Rosseland optical depth

$$\tau_{\mathrm{Ross}}(r) := \int_{R_{\max}}^{r} \kappa_{\mathrm{Ross}}(r') \mathrm{d}r'. \tag{2.45}$$

best describes flux conservation and is therefore the right choice here. Depending on which opacities $\kappa_{\rm Ross}$ are used in the integral, the $\tau_{\rm Ross}$-scale can have different absolute values. In order to be precise and known which values should be compared with what, there are two definitions in PoWR, namely

- a Rosseland optical depth $\tau_{\rm Ross}$ including all line and continuum opacities,
- a Rosseland optical depth $\tau_{\rm Ross,cont}$ including all continuum opacities only.

To sufficiently cover the photosphere in a stellar atmosphere model, the optical depth at the inner boundary has to be large enough. In PoWR we use $\tau_{\rm Ross,cont}$ for this purpose and define $\tau_{\rm max} = \tau_{\rm Ross,cont}(R_*)$. This value has to be specified at the start of a model and implicitly defines an inner boundary value for the resulting velocity and density stratification. However, at the start of a model the optical depth can only be approximated as the converged values for population numbers and the radiative acceleration are not yet known. Therefore the final value of τ at R_* in the converged model can differ from the start approximation. As long as $\tau_{\rm max}$ is much larger than the region where the spectrum is formed, this is not really a problem for deducing the stellar parameters, but values such as T_* and R_* are not good reference values when comparing models as they might not refer to the same radius in each model[§]. Updating the inner velocity field, such that $\tau_{\rm max}$ is guaranteed at R_* removes this problem. Furthermore, at large optical depths, the electron temperature T is coupled to τ. Conserving τ at the inner boundary therefore also avoids temperature corrections which would be caused by a changing optical depth at the inner boundary.

The Rosseland continuum optical depth is now ensured by a new feature referred to as the "$\tau_{\rm max}$-iteration". As soon as the current Rosseland continuum optical depth $\tau_{\rm Ross,cont}(R_*)$ differs from the specified $\tau_{\rm max}$ by more than ε_τ, the inner part of the velocity field is adjusted to re-ensure that $\tau_{\rm Ross,cont}(R_*)$ matches $\tau_{\rm max}$. The detailed implementation of this concept in the PoWR code is outlined in Sect. A.3 of the appendix.

2.8 Radiative transfer in the comoving frame

To properly account of the expanding atmosphere situation, the (spherical) radiative transfer equation can be solved in a comoving frame (CMF). Using the CMF has the enormous advantage that the opacities κ_ν, emissivities η_ν, and the profile functions $\phi(\nu)$ remain isotropic. Furthermore the calculation of the radiation field can be restricted to frequency ranges covering the local scattering zones, thus saving a lot of computing time. A limitation of this method is its restriction to monotonic velocity fields, which will be a significant constraint when obtaining velocity fields from the hydrodynamic equation.

2.8.1 The general concept

As the observed velocities are still significantly below the speed of the light, the non-relativistic limit is sufficient and the CMF frequencies $\nu_{\rm cmf}$ can be expressed by

$$\nu_{\rm cmf} = \nu \left(1 + \mu \frac{v(r)}{c}\right). \tag{2.46}$$

[§]For observational purposes, values like $T(\tau = \frac{2}{3})$ can be used, which can always be calculated from a converged model. However, $\tau = \frac{2}{3}$ is often not located in the quasi-hydrostatic layers, which is a caveat when comparing atmosphere models with structure models

Introducing a dimensionless frequency

$$x := \frac{v_{\mathrm{dop}}}{c} \ln\left(\frac{\nu}{\nu_{\mathrm{ref}}}\right) \tag{2.47}$$

with a reference frequency ν_{ref} and the Doppler velocity v_{dop} describing the line broadening considered in the CMF radiative transfer calculation. With this definition the radiative transfer equation can be written in the form

$$\mu \frac{\partial I_\nu}{\partial r} + \frac{1-\mu^2}{r} \frac{\partial I_\nu}{\partial \mu} - P(r,\mu) \frac{\partial I_\nu}{\partial x} = \eta_\nu - \kappa_\nu I_\nu \tag{2.48}$$

with

$$P(r,\mu) := \mu^2 \frac{1}{v_{\mathrm{dop}}} \frac{\mathrm{d}v}{\mathrm{d}r} + \left(1-\mu^2\right) \frac{1}{v_{\mathrm{dop}}} \frac{v(r)}{r} \tag{2.49}$$

All line and continuum opacities and emissivities are added up to enter the transfer equation. The actual calculation of the radiation field is performed in two main steps: In a first step, angle-dependent intensities I_ν^+ and I_ν^- are calculated via the so-called "ray-by-ray" integration using short characteristics. This method is described in detail in Koesterke et al. (2002). It includes the calculation of the moments

$$[J_\nu; H_\nu; K_\nu; N_\nu] := \frac{1}{2} \int_{-1}^{1} I_\nu \left[1; \mu; \mu^2; \mu^3\right] \mathrm{d}\mu \tag{2.50}$$

using the calculated intensities, such that

$$[J_{\nu,\mathrm{ray}}; K_{\nu,\mathrm{ray}}] := \frac{1}{2} \int_{0}^{1} \left(I_\nu^+(\mu) + I_\nu^-(-\mu)\right) \left[1; \mu^2\right] \mathrm{d}\mu \tag{2.51}$$

$$[H_{\nu,\mathrm{ray}}; N_{\nu,\mathrm{ray}}] := \frac{1}{2} \int_{0}^{1} \left(I_\nu^+(\mu) - I_\nu^-(-\mu)\right) \left[\mu; \mu^3\right] \mathrm{d}\mu. \tag{2.52}$$

Moments calculated via the "ray-by-ray" method are only used to obtain the Eddington factors

$$f_\nu = \frac{K_{\nu,\mathrm{ray}}}{J_{\nu,\mathrm{ray}}} \text{ and } g_\nu = \frac{N_{\nu,\mathrm{ray}}}{H_{\nu,\mathrm{ray}} + \epsilon J_{\nu,\mathrm{ray}}}. \tag{2.53}$$

The moments (2.50) are then calculated again by solving the moment equations where all higher moments K_ν and N_ν can be expressed by products of a lower one and an Eddington factor. The solution of the zeroth moment equation is performed by a second-order Feautrier method described in Mihalas (1978), where for each frequency point an equation system of the form

$$\begin{bmatrix} B_1 & C_1 & & & & \\ A_2 & B_2 & C_2 & & & \\ & A_3 & B_3 & C_3 & & \\ & & & \ddots & & \\ & & & A_{\text{ND-1}} & B_{\text{ND-1}} & C_{\text{ND-1}} \\ & & & & A_{\text{ND}} & B_{\text{ND}} \end{bmatrix} \bullet \begin{bmatrix} J_{\nu,1} \\ J_{\nu,2} \\ J_{\nu,3} \\ \vdots \\ J_{\nu,\text{ND-1}} \\ J_{\nu,\text{ND}} \end{bmatrix} = \begin{bmatrix} W_1 \\ W_2 \\ W_3 \\ \vdots \\ W_{\text{ND-1}} \\ W_{\text{ND}} \end{bmatrix} \tag{2.54}$$

is solved by numerically inversion of the tridiagonal matrix in Eq. (2.54), to obtain the angle-integrated intensity J_ν at all ND depth points. The coefficients A_l, B_l, C_l and W_l are complex terms arising from the discretization of the zeroth moment equation

$$\frac{\partial \tilde{H}_\nu}{\partial r} - \left(\frac{\mathrm{d}V}{\mathrm{d}r} - \frac{V}{r}\right) \frac{\partial}{\partial x}\left(f_\nu J_\nu\right) - \frac{V}{r}\frac{\partial \tilde{J}_\nu}{\partial x} = \tilde{\eta}_\nu^{\mathrm{true}} - \kappa_\nu^{\mathrm{true}} \tilde{J}_\nu \tag{2.55}$$

with $V(r) = v(r)/v_{\mathrm{dop}}$. The quantities marked with a tilde are multiplied with r^2, e.g. $\tilde{J}_\nu = r^2 J_\nu$. Due to the frequency derivatives in Eq. (2.55), the equation system (2.54) is coupled in both, space and frequency. Fortunately, the frequency coupling of the system can be written in such a way that all required quantities only depend on the current and the last frequency. (This is also the case in the "ray-by-ray" method.) With this approach it is possible to calculate the whole radiation field via a frequency loop running from the blue to the red end where the upper calculation is performed at each frequency point (if needed). Immediately after solving the system (2.54), H_ν is calculated afterwards from the first moment equation. The arrangement furthermore allows that also the total frequency integration can be performed in the same overall frequency loop.

As the Eddington factors tend to stay constant as long as the overall changes are relatively small, they do not need to be calculated during every iteration. Instead computing time can be saved by storing the obtained Eddington factors and performing only the solution of the moment equations, i.e. skipping the ray-by-ray solution. The PoWR implementation is outlined in Sect. A.4 of the appendix.

2.8.2 Boundary conditions

For the inner and outer boundary, additional calculations need to be done. For the intensity $I_\nu^+(\mu)$ at the inner boundary, the diffusion approximation is used, i.e.

$$I_\nu^+(\mu) = B_\nu(T_{\mathrm{ND}}) + \frac{\mu}{\kappa_{\nu,\mathrm{ND}}} \left.\frac{\partial B_\nu}{\partial r}\right|_{r=R_*} . \tag{2.56}$$

The resulting flux at the inner boundary $H_{\nu,\mathrm{ND}}$ is not necessarily identical to the ideal diffusion flux

$$H_{\nu,\mathrm{diff}} = -\frac{1}{3\kappa_\nu}\frac{\partial B_\nu}{\partial r} \tag{2.57}$$

that is obtained by integrating Eq. (2.56) as the incoming radiation I^- is not known from scratch. Only if I^- would also have the form (2.56), one would simply obtain $H_{\nu,\mathrm{ND}} = H_{\nu,\mathrm{diff}}$. Therefore using $H_{\nu,\mathrm{diff}}$ as input for the moment equations induces an error at the inner boundary. For hot star atmospheres this error is usually small and the spectrum is usually not affected at all. However, this error can cause problems when solving the hydrodynamic equations and updating the innermost region throughout the iteration. A more precise treatment can be obtained by introducing a special quantity

$$H_{\nu,\mathrm{spec}} := \frac{1}{2}\int_0^1 \left(I_\nu^+ + I_\nu^-\right)\mu \mathrm{d}\mu \tag{2.58}$$

Note that $H_{\nu,\mathrm{spec}}$ has a an intensity-like integral core, but a flux-like weight and thus a very special definition. However, this quantity can be easily calculated during the ray-by-ray method

and is always positive to the sum of the two intensities, allowing the definition of a special Eddington factor

$$h_{\nu,\mathrm{in}} := \frac{H_{\nu,\mathrm{spec}}}{J_{\nu,\mathrm{ray},1}}. \tag{2.59}$$

Similar to the other Eddington factors, $h_{\nu,\mathrm{in}}$ can now be used to remove remove I_ν^- from the moment equations at the inner boundary. The sum of $H_{\nu,\mathrm{spec}}$ and the ordinary flux definition (2.52) yields

$$H_{\nu,\mathrm{ND}} + H_{\nu,\mathrm{spec}} = \int_0^1 I_\nu^+ \mu \mathrm{d}\mu \tag{2.60}$$

$$H_{\nu,\mathrm{ND}} + h_{\nu,\mathrm{in}} J_{\nu,\mathrm{ND}} = \frac{1}{2} B_\nu - \frac{1}{3\kappa_\nu} \frac{\partial B_\nu}{\partial r} \tag{2.61}$$

$$\Rightarrow H_{\nu,\mathrm{ND}} = H_{\nu,\mathrm{diff}} + \frac{1}{2} B_\nu - h_{\nu,\mathrm{in}} J_{\nu,\mathrm{ND}} \tag{2.62}$$

The final Eq. (2.62) demonstrates that that flux at the inner boundary is basically still the diffusion term $H_{\nu,\mathrm{diff}}$, but with two additional terms correcting for deviations of $J_{\nu,\mathrm{ND}}$ from the Planck function. In the ideal case of $J_{\nu,\mathrm{ND}} = B_\nu$, one obtains $h_{\nu,\mathrm{in}} = 0.5$ and the correction terms vanish.

The outer boundary is much more easy if one assumes $I_\nu^- = 0$. In this case $H_{\nu,\mathrm{spec}}$ is identical to the true flux $H_{\nu,1}$ and the special Eddington factor can simply be calculated by

$$h_{\nu,\mathrm{out}} = \frac{H_{\nu,\mathrm{ray},1}}{J_{\nu,\mathrm{ray},1}}. \tag{2.63}$$

In the moment equations, the boundary term can then be represented by the simple form

$$H_{\nu,1} = h_{\nu,\mathrm{out}} J_{\nu,1}. \tag{2.64}$$

2.9 Superlevel approach for iron group elements

Iron and other iron group elements are treated in form of one *generic* element, internally labeled as G. This is due to the fact these elements have thousands of levels and millions of lines which cannot be treated explicitly in a stellar atmosphere code. Nevertheless the elements are extremely important as their huge number of lines have a significant blanketing effect and thus significantly change the situation in a stellar atmosphere. For PoWR models this has been demonstrated in Gräfener et al. (2002). Furthermore, the huge number of lines provides a major opacity source, even though the combined abundance of these elements is only on the order of $X_\mathrm{G} \approx 0.1\%$, even for solar metallicity. The significant opacity in turns means that iron group elements provide a major contribution to the wind driving. This can even be quantified for calculated PoWR models and some results be shown and discussed in Chapter 4.

This section introduces the basic concepts of the superlevel approach and shows the basics of their their implementation in the PoWR code. For ionization stages below G X, it contains all elements with atomic numbers from 21 to 28, i.e. scandium, titanium, vanadium, chromium, manganese, iron, cobalt, and nickel. The required atomic data is taken from the Kurucz database. For higher ions, where no Kurucz data is available, only iron is used, taking all the

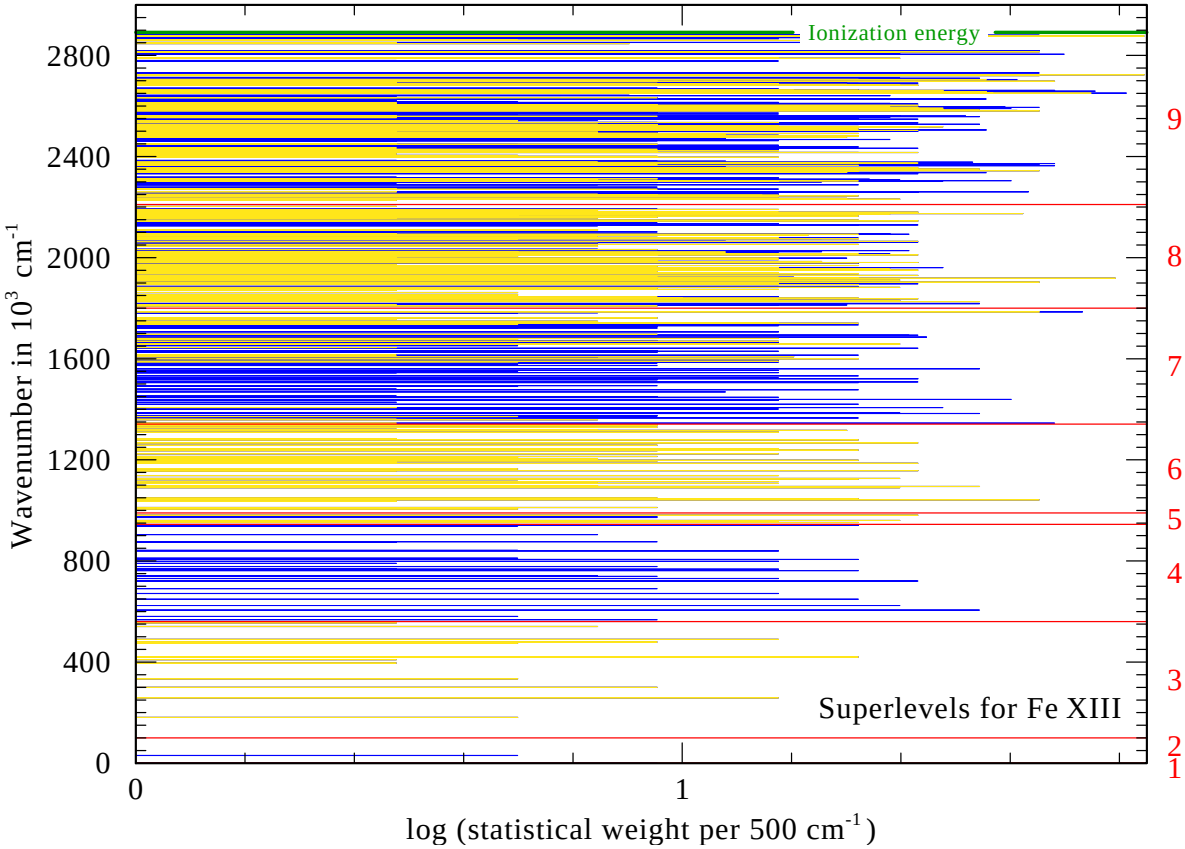

Figure 2.2 – Superlevel assignment for Fe XIII: The sum of the statistical weights of all considered levels is shown in bins of 500 kayser. The yellow lines refer to the contributions of levels with an even parity while the blue color denotes those with odd parity. The red horizontal lines indicate the sorting in a certain superlevel and the green line marks the ionization energy of the ion. The corresponding superlevel indices are given by the red numbers on the right.

required data from TOPbase, the Opacity Project database (Cunto & Mendoza, 1992). The relative abundances of the elements are listed in Gräfener et al. (2002).

In order to summarize levels, which will now be called sublevels here, into superlevels, energy bands have to be defined for each ionization stage. An example for such a superlevel grouping can be seen in Fig. All sublevels that inside each energy band are assumed to have an occupation probability based on an LTE-description using a characteristic temperature $T_{\rm exc}$ for this ion. This temperature is called the *excitation temperature* and has to be given[¶]. This allows the define the following quantities, where capital indices always refer to superlevels, while lowercase indices refer to the sublevels which are added up to a superlevel:

[¶]In practice, a significant values for the $T_{\rm exc}$ of a particular ion can be determined iteratively by calculating a stellar atmosphere model and check at which electron temperature this ion is the leading ion.

$$E_L = \frac{\sum_{i,l} E_l \, a_i \, g_l \exp\left(-\frac{E_l}{kT_{\rm exc}}\right)}{\sum_{i,l} a_i \, g_l \exp\left(-\frac{E_l}{kT_{\rm exc}}\right)} \tag{2.65}$$

$$g_{i,l} = a_i \, g_l \exp\left(\frac{E_L - E_l}{kT_{\rm exc}}\right) \tag{2.66}$$

$$G_L := \sum_{i,l} g_{i,l} = \sum_{i,l} a_i \, g_l \exp\left(\frac{E_L - E_l}{kT_{\rm exc}}\right) \tag{2.67}$$

The term E_L then denotes the energy of a superlevel, while E_l refers to the sublevel energy. G_L is the weight of the superlevel. It is actually the sum of the generalized sublevel weights g_i,l, which in turn contains the actual weight g_l of the sublevel and the occupation probability. Note that even though PoWR does not use occupation probabilities for normal levels, these factors cannot be neglected for superlevels. Only in the limit of $T_{\rm exc} \to \infty$ this factor vanishes and the total weight turns into a simple addition of individual weights. The factor a_i describes the relative abundance of a real element in the generic element.

The population number of a sublevel $n_{i,l}$ can be obtained from the corresponding superlevel population number n_L via

$$n_{i,l} = n_L \frac{g_{i,l}}{G_L}. \tag{2.68}$$

To obtain the transition rates as well as the emissivity and opacity for the superlevels, the particular values have to be summed. In a first step, the individual cross-sections σ_{lu} are added up to the superlevel cross-sections σ_{LU} such that the product of the superlevel weight and the superlevel cross-section matches the sum of the weighted individual cross-sections, i.e.

$$\sigma_{LU} := \frac{1}{G_L} \sum_{i,l,u} g_{i,l} \sigma_{lu}. \tag{2.69}$$

An example for the complex, wavelength-dependent structure of the resulting superlevel cross sections can be seen in Fig. 2.3. Due to the exponential terms in the definition of the superlevel weight (2.67), the equation $\sigma_{lu} g_l = \sigma_{ul} g_u$ is not automatically fulfilled for the superlevels:

$$\sigma_{UL} = \frac{1}{G_U} \sum_{i,l,u} g_{i,u} \sigma_{ul} \tag{2.70}$$

$$= \frac{1}{G_U} \sum_{i,l,u} a_i g_u \exp\left(\frac{E_U - E_u}{kT_{\rm exc}}\right) \sigma_{ul} \tag{2.71}$$

$$= \frac{G_L}{G_U} \frac{1}{G_L} \sum_{i,l,u} a_i \frac{g_l}{g_u} g_l \frac{\exp\left(\frac{E_U - E_u}{kT_{\rm exc}}\right)}{\exp\left(\frac{E_L - E_l}{kT_{\rm exc}}\right)} \exp\left(\frac{E_L - E_l}{kT_{\rm exc}}\right) \sigma_{ul} \tag{2.72}$$

$$= \frac{G_L}{G_U} \frac{1}{G_L} \sum_{i,l,u} a_i g_l \frac{\exp\left(\frac{E_U - E_L}{kT_{\rm exc}}\right)}{\exp\left(\frac{E_u - E_l}{kT_{\rm exc}}\right)} \exp\left(\frac{E_L - E_l}{kT_{\rm exc}}\right) \sigma_{lu} \tag{2.73}$$

$$= \frac{G_L}{G_U} \frac{1}{G_L} \sum_{i,l,u} g_{i,l} \exp\left[\frac{h}{kT_{\rm exc}} (\nu_{UL} - \nu_{ul})\right] \sigma_{lu} \tag{2.74}$$

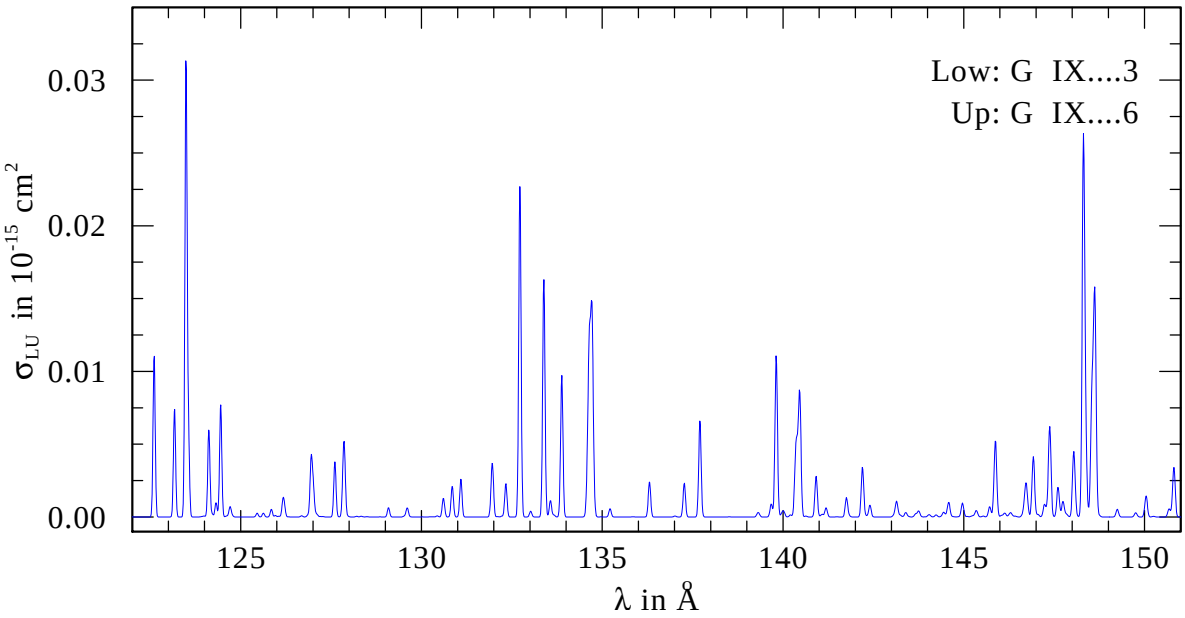

Figure 2.3 – An excerpt of the superlevel cross section σ_{LU} for a transition of the G IX state of the generic element representing the iron group elements.

It is precisely the exponential term with the brackets that prevents a straight-forward transformation from σ_{LU} to σ_{UL}. The exponential term vanishes only in the limit of an infinite excitation temperature $T_{\rm exc}$ or if $\nu_{ul} = \nu_{UL}$. The latter is approximately true if the superlevels are small enough. However, a look at Fig. 2.2 illustrates, that for the important ionization stages, this is not possible without losing the advantage of superlevel, i.e. a significant reduction of the total number of levels. Thus, the fact that σ_{UL} cannot be calculated from σ_{LU} as simple as for normal levels has significant consequences and requires a special treatment for the radiative rates, opacities and emissivities in the PoWR code.

In the current blanketing approach in PoWR, which is described in Gräfener et al. (2002), only σ_{LU} is precalculated and stored in the iron data file, while σ_{UL} has to be calculated. Based on the fact that only active transitions are considered in the comoving frame, i.e. those where the current integration frequency ν is in a certain range around ν_{UL}, the Eq. (2.74) is further approximated by replacing ν_{ul} with ν. This allows to get the exponential term out of the sum. Furthermore the excitation temperature $T_{\rm exc}$ is replaced by the current electron temperature $T_{\rm e}$, so the expression used in the code is:

$$\sigma_{UL} = \frac{G_L}{G_U}\frac{1}{G_L}\exp\left[\frac{h}{kT_{\rm e}}\left(\nu_{UL}-\nu\right)\right]\sum_{i,l,u} g_{i,l}\sigma_{lu} \tag{2.75}$$

$$= \frac{G_L}{G_U}\exp\left[\frac{h}{kT_{\rm e}}\left(\nu_{UL}-\nu\right)\right]\sigma_{LU} \tag{2.76}$$

This approach has proven to be quite successful in normal models which usually use ions only up to G X. In this regime, the difference between $T_{\rm e}$ and $T_{\rm exc}$ is usually not large in the regions where a line is active. The usage of $T_{\rm e}$ is also motivated in order to regain the LTE limit at the inner boundary. However, this approach seems to have problems when using the higher ions, especially if combined with stellar temperatures above $\approx 175\,\mathrm{kK}$. Already below this

limit the high ions produce insufficiently high transitions rates, but this could be neglected by implementing a more sophisticated "switch-off" for levels which are not significantly populated. For higher temperatures however, the temperature correction method is also affected and the coupling of the electron temperature T_e with η, κ, and the rates seems to produce situations where the corrections might produce a non-converging or even diverging situation. This is one of the reasons why WO models are hard to calculate, which will later become important when discussing a hydrodynamically consistent WO model in Sect. 4.2.

Regardless of how accurate the terms of σ_{UL} are produced, the way of calculating the superlevel rates as well as the line opacities and emissivities are always the same. The line opacities of the superlevels can than be calculated by simply adding up their sublevel line opacities:

$$\kappa_{lu} = n_l\sigma_{lu}\left(1 - \frac{n_u}{n_l}\frac{g_l}{g_u}\right) = n_l\sigma_{lu} - n_u\sigma_{ul} \tag{2.77}$$

$$\kappa_{LU} := \sum_{l,u}\kappa_{lu} = \sum_{i,l,u} n_{i,l}\sigma_{lu}\left(1 - \frac{n_{i,u}}{n_{i,l}}\frac{g_l}{g_u}\right) \tag{2.78}$$

$$= \frac{n_L}{G_L}\sum_{i,l,u} g_{i,l}\sigma_{lu}\left(1 - \frac{n_U}{n_L}\frac{g_{i,u}}{G_U}\frac{G_L}{g_{i,l}}\frac{g_l}{g_u}\right) \tag{2.79}$$

$$= \frac{n_L}{G_L}\sum_{i,l,u} g_{i,l}\sigma_{lu} - \frac{n_U}{G_U}\sum_{i,l,u} g_{i,u}\sigma_{lu}\frac{g_l}{g_u} \tag{2.80}$$

$$= \frac{n_L}{G_L}\sum_{i,l,u} g_{i,l}\sigma_{lu} - \frac{n_U}{G_U}\sum_{i,l,u} g_{i,u}\sigma_{ul} \tag{2.81}$$

$$= n_L\sigma_{LU} - n_U\sigma_{UL} \tag{2.82}$$

In a similar way the superlevel line emissivities can be calculated:

$$\eta_{lu} = \frac{2h\nu_{lu}^3}{c^2} n_u \frac{g_l}{g_u}\sigma_{lu} \tag{2.83}$$

$$\eta_{LU} = \sum_{l,u}\eta_{lu} = \sum_{i,l,u}\frac{2h\nu_{lu}^3}{c^2} n_{i,u}\frac{g_l}{g_u}\sigma_{lu} \tag{2.84}$$

$$= \frac{2h}{c^2}\frac{n_U}{G_U}\sum_{i,l,u}\nu_{lu}^3 g_{i,u}\frac{g_l}{g_u}\sigma_{lu} \tag{2.85}$$

The last expression can be reduced further, if one assumes that $\nu_{lu} \approx \nu_{LU}$ and hence

$$\eta_{LU} \approx \frac{2h\nu_{LU}^3}{c^2}\frac{n_U}{G_U}\sum_{i,l,u} g_{i,u}\sigma_{ul} \tag{2.86}$$

$$= \frac{2h\nu_{LU}^3}{c^2} n_U\sigma_{UL} \tag{2.87}$$

The to total radiative transition rate is the sum of all subrates. Using this requirement and inserting Eq. (2.68) leads to

$$n_L R_{LU} = \sum_{i,l,u} n_{i,l}R_{lu} = n_L\sum_{i,l,u}\frac{g_{i,l}}{G_L}R_{lu} \tag{2.88}$$

which immediately provides the formula how to add up the rate coefficients of the sublevels:

$$R_{lu} = 4\pi \int_0^\infty \frac{\sigma_{lu}}{h\nu} J_\nu \mathrm{d}\nu \tag{2.89}$$

$$R_{LU} = \sum_{i,l,u} \frac{g_{i,l}}{G_L} R_{lu} \tag{2.90}$$

$$= 4\pi \sum_{i,l,u} \frac{g_{i,l}}{G_L} \int_0^\infty \frac{\sigma_{lu}}{h\nu} J_\nu \mathrm{d}\nu \tag{2.91}$$

$$= 4\pi \int_0^\infty \frac{J_\nu}{h\nu} \sum_{i,l,u} \frac{g_{i,l}}{G_L} \sigma_{lu} \mathrm{d}\nu \tag{2.92}$$

$$= 4\pi \int_0^\infty \frac{J_\nu}{h\nu} \sigma_{LU} \mathrm{d}\nu \tag{2.93}$$

The same scheme can be used for slightly more complex R_{UL}:

$$R_{ul} = 4\pi \frac{g_l}{g_u} \int_0^\infty \frac{\sigma_{lu}}{h\nu} \left[\frac{2h\nu^3}{c^2} + J_\nu \right] \mathrm{d}\nu \tag{2.94}$$

$$R_{UL} = \sum_{i,l,u} \frac{g_{i,u}}{G_U} R_{ul} \tag{2.95}$$

$$= 4\pi \sum_{i,l,u} \frac{g_{i,u}}{G_U} \frac{g_l}{g_u} \int_0^\infty \frac{\sigma_{lu}}{h\nu} \left[\frac{2h\nu^3}{c^2} + J_\nu \right] \mathrm{d}\nu \tag{2.96}$$

$$= 4\pi \int_0^\infty \frac{1}{h\nu} \left[\frac{2h\nu^3}{c^2} + J_\nu \right] \sum_{i,l,u} \frac{g_{i,u}}{G_U} \sigma_{ul} \mathrm{d}\nu \tag{2.97}$$

$$= 4\pi \int_0^\infty \frac{1}{h\nu} \left[\frac{2h\nu^3}{c^2} + J_\nu \right] \sigma_{UL} \mathrm{d}\nu \tag{2.98}$$

The Eqs. (2.93) and (2.98) show that the radiative transition rates for the superlevels have the same form as those for normal levels, except that the cross-sections σ_{ul} and σ_{lu} are replaced by their superlevel counterparts σ_{UL} and σ_{LU}, which means no additional assumptions or approximations have to be made beside those entering the calculation of the superlevel cross sections. However, for the normal rates the $(h\nu)^{-1}$-term is often approximated to $(h\nu_{ul})^{-1}$ and thus can be put in front of the frequency integral. This is also the case in the PoWR code, where the "normal" radiative rates are calculated using the coarse frequency grid. For the rates of the generic element however, the $(h\nu)^{-1}$ is kept and the rates are calculated on the fine frequency grid, in parallel with the CMF radiative transfer.

For a start approximation which has to be available before the first radiative transfer calculation, the rates of the generic element are also calculated in the approximated form as it is done for the other rates. This is also done during the solution of the statistical equations, where the have to be recalculated based on updated population numbers. Here the more

accurate rates from the CMF calculations are used, but afterwards updated by adding the differences between the approximated rates. By using only the differences of the rates and not their absolute value, the error should be kept small.

Chapter 3

The concepts for hydrodynamically consistent models

Stellar atmosphere models such as PoWR or CMFGEN use a prescribed velocity field as outlined in Sect. 2.3. Solving the statistical equations in non-LTE consistent with the co-moving frame radiative transfer already requires extensive numerical calculations. Fixing the velocity and thus the density stratification by using a β-law and an approximation for the hydrostatic part were therefore a natural choice, especially as resulting spectra are in good agreement with observations for Wolf-Rayet stars.

However, this approach has certain limits in the usage of these models. The approximative treatment of the hydrostatic layers is not sufficient as soon as the spectrum is at least partly formed in those layers. Parameters deduced from the emergent spectrum of such a model will have significant uncertainty, especially in $\log g$. The proper treatment of the hydrostatic layers requires a calculation that takes the actual radiative acceleration in those layers into account (see Sect. 3.4 for details). This in turn requires the CMF radiative transfer results and thus the velocity field needs to be updated throughout the model iterations. The consistent solution of the hydrostatic part thereby extends the applicability of PoWR models significantly, not only to WR stars with absorption lines, but also to the large field of O and B stars.

Nevertheless the consistent treatment of the quasi-hydrostatic layers is just an intermediate step. Even though such models greatly increase the applicability of the PoWR models for deducing stellar parameters, they are still not sufficient to use them as virtual laboratories for studying the wind physics. To fully couple the wind stratification with the results from the radiative transfer, the entire velocity field has be obtained by solving the hydrodynamic equation. A converged model with a velocity field obtained in this way would provide a self-consistent description throughout the stellar atmosphere, thereby allowing to test current theories and predictions about wind driving and potentially even provide important hints about what happens in the layers below the photosphere. If the winds of hot stars could be sufficiently explained by radiative driving, the models would reach predictive power and could provide wind parameters for other astrophysical fields, e.g. for stellar feedback and evolutionary calculations.

In the following sections of this chapter, the concepts for a consistent treatment of the wind stratification and the radiative transfer results as well as their implementation in the PoWR code will be outlined. After introducing the basics and the simpler quasi-hydrostatic case, the CAK concept and the first approach by Gräfener & Hamann (2005, 2008) will be described. Afterwards, the new method developed during this work will be introduced and the differences

to the previous approach will be outlined. Applications and limitations are discussed in the subsequent chapter 4. In contrast to the earlier approach by Gräfener & Hamann (2005), the solution of the hydrodynamic equation has been fully implemented in the PoWR code and the corresponding calculation do no longer require multiple model calculations. More information on the technical implementation can be found in the appendix.

3.1 The hydrodynamic equation for stationary wind models

Due to the simplifying assumption of spherical symmetry, the hydrodynamic equations can be reduced to the one-dimensional form of Euler's equation

$$\frac{\mathrm{d}v}{\mathrm{d}t} + \frac{1}{\rho}\frac{\mathrm{d}P}{\mathrm{d}r} = a_{\mathrm{out}} \tag{3.1}$$

and the equation of continuity (2.1). The first term in (3.1) is actually the Lagrangian derivative, which translates to

$$\frac{\mathrm{d}}{\mathrm{d}t} = \frac{\partial}{\partial t} + v\frac{\mathrm{d}}{\mathrm{d}r}. \tag{3.2}$$

With the assumption of stationarity, the partial derivative with respect to time can be dropped. Equation (3.1) therefore becomes

$$v\frac{\mathrm{d}v}{\mathrm{d}r} + \frac{1}{\rho}\frac{\mathrm{d}P}{\mathrm{d}r} = a_{\mathrm{out}} \tag{3.3}$$

In case of a star, the outer force, or to be more precise, acceleration a_{out} is consisting of gravitational and radiative acceleration

$$a_{\mathrm{out}} = a_{\mathrm{rad}} + a_{\mathrm{grav}}. \tag{3.4}$$

The gravity term $a_{\mathrm{grav}} = -GMr^{-2} = -g$ is directed inwards, while radiation and gas pressure try to push material outwards. Inserting the outer accelerations in Eq. (3.3) and resorting the equation, putting outward accelerations on the right and inward accelerations on the left side, yields

$$v\frac{\mathrm{d}v}{\mathrm{d}r} + g = a_{\mathrm{rad}} - \frac{1}{\rho}\frac{\mathrm{d}P}{\mathrm{d}r} \tag{3.5}$$

$$a_{\mathrm{mech}} + g = a_{\mathrm{rad}} + a_{\mathrm{press}}. \tag{3.6}$$

In Eq. (3.6), the definitions $a_{\mathrm{press}} := -\frac{1}{\rho}\frac{\mathrm{d}P}{\mathrm{d}r}$ for the gas pressure and $a_{\mathrm{mech}} = v\frac{\mathrm{d}v}{\mathrm{d}r}$ for the inertia term were used. The next step is to replace the mechanical pressure P with the help of an equation of state. In a stellar atmosphere it is sufficient to describe the gas via the ideal gas law

$$P = \rho\frac{\mathcal{R}T}{\mu} \tag{3.7}$$

with $\mathcal{R} = k_{\mathrm{B}}m_{\mathrm{H}}^{-1}$ being the gas constant and μ the mean particle mass (including electrons) in the gas. This equation can be simplified to $P = \rho a^2$ by introducing the (isothermal) sound speed

$$a := \sqrt{\frac{\mathcal{R}T}{\mu}}. \tag{3.8}$$

This velocity is depth-dependent, mainly due to the non-constant temperature stratification $T(r)$, but also $\mu(r)$ can change throughout a stellar atmosphere. It is often referred to as the isothermal sound speed in order to distinguish it from the adiabatic sound speed, which is defined as

$$a_{\mathrm{ad}} := \sqrt{\gamma \frac{\mathcal{R}T}{\mu}} \tag{3.9}$$

and thus is larger than a by a factor of $\sqrt{\gamma}$, i.e. the square root of the adiabatic index.

The definition (3.8) should not be confused with the definition of the *thermal speed*

$$v_{\mathrm{th}} := \sqrt{2 \frac{k_{\mathrm{B}} T}{m_{\mathrm{ion}}}} \tag{3.10}$$

which is specifically for each ion*. The mean thermal velocity uses $m_{\mathrm{ion}} = \mu m_{\mathrm{H}}$ and hence is

$$\bar{v}_{\mathrm{th}} := \sqrt{2 \frac{\mathcal{R}T}{\mu}} = \sqrt{2}a. \tag{3.11}$$

The sound speed a enters the hydrodynamic equation, while the thermal speed v_{th} is important for thermal line broadening.

In addition to the gas pressure, turbulent pressure contributes to the total mechanical pressure P. With a turbulence velocity v_{turb}, P can be expressed in the form

$$P = \rho \left(a^2 + v_{\mathrm{turb}}^2\right). \tag{3.12}$$

In the literature (e.g. Hubeny et al., 1991), the turbulence pressure is also written as $P_{\mathrm{turb}} = \frac{1}{2}\rho v_{\mathrm{mic}}^2$ with v_{mic} describing the microturbulence. These expressions are equivalent and the connection between the two velocities is $v_{\mathrm{mic}} = \sqrt{2} \cdot v_{\mathrm{turb}}$ In the PoWR code, the velocity v_{turb} is currently a free, depth-independent input parameter reflecting a possible microturbulence. Spectral analyses with several codes (see, e.g. Massey et al., 2013) have demonstrated that microturbulent velocities of the order of 10 to 20 km/s help to reproduce the observed spectral lines in certain parameter regimes for O and B stars. It is an ongoing debate whether such velocities represent a real turbulent motion in the photosphere, as originally suggested for hot stars by Struve & Elvey (1934) and prominently reintroduced by Hubeny et al. (1991), or if they are rather a "fudge factor" for other, not considered physics in the models.

As the PoWR code currently allows only constant values for v_{turb}, no additional derivatives occur for $v_{\mathrm{turb}} > 0$ and the inclusion of turbulence acts just as a shift of the sound speed in the equations. In order to keep the formulae simple, $v_{\mathrm{turb}} = 0$ will be applied throughout the following equations, unless otherwise notified. The full form of the equations can be recovered by replacing a^2 with $a^2 + v_{\mathrm{turb}}^2$.

With the given equation of state for P, the pressure term can now be rewritten:

$$\begin{aligned} a_{\mathrm{press}} &:= -\frac{1}{\rho}\frac{\mathrm{d}P}{\mathrm{d}r} && (3.13)\\ &= -\frac{1}{\rho}\frac{\mathrm{d}}{\mathrm{d}r}\left(\rho a^2\right) && (3.14)\\ &= -\frac{1}{\rho}a^2\frac{\mathrm{d}\rho}{\mathrm{d}r} - \frac{\mathrm{d}a^2}{\mathrm{d}r} && (3.15) \end{aligned}$$

*In practice, the individual electron masses are often neglected and the same thermal speed is instead used for all ions of the same element.

The density derivative in the first term can be replaced further by using the equation of continuity (2.1):

$$-\frac{1}{\rho}a^2\frac{\mathrm{d}\rho}{\mathrm{d}r} = -\frac{4\pi r^2 v}{\dot{M}}a^2\frac{\dot{M}}{4\pi}\frac{\mathrm{d}}{\mathrm{d}r}\left(\frac{1}{r^2 v}\right) \tag{3.16}$$

$$= r^2 a^2 v\left(\frac{1}{r^2 v^2}\frac{\mathrm{d}v}{\mathrm{d}r}+\frac{2}{r^3 v}\right) \tag{3.17}$$

$$= v\frac{a^2}{v^2}\frac{\mathrm{d}v}{\mathrm{d}r}+\frac{2a^2}{r} \tag{3.18}$$

The full pressure term is therefore:

$$a_{\mathrm{press}} = v\frac{a^2}{v^2}\frac{\mathrm{d}v}{\mathrm{d}r}+\frac{2a^2}{r}-\frac{\mathrm{d}a^2}{\mathrm{d}r} \tag{3.19}$$

Plugging this into Euler's equation (3.1) and sorting the terms such that the two terms with the velocity gradient are on the left side, one obtains the form (3.21) which is typically given in the literature about stellar atmospheres:

$$v\frac{\mathrm{d}v}{\mathrm{d}r}-v\frac{a^2}{v^2}\frac{\mathrm{d}v}{\mathrm{d}r}-\frac{2a^2}{r}+\frac{\mathrm{d}a^2}{\mathrm{d}r} = a_{\mathrm{rad}}-g \tag{3.20}$$

$$v\left(1-\frac{a^2}{v^2}\right)\frac{\mathrm{d}v}{\mathrm{d}r} = a_{\mathrm{rad}}-g+\frac{2a^2}{r}-\frac{\mathrm{d}a^2}{\mathrm{d}r} \tag{3.21}$$

With the definition of Γ_{rad} as the ratio between radiative acceleration and gravity

$$\Gamma_{\mathrm{rad}}(r) := \frac{a_{\mathrm{rad}}(r)}{g(r)} \tag{3.22}$$

this equation can be written as

$$v\left(1-\frac{a^2}{v^2}\right)\frac{\mathrm{d}v}{\mathrm{d}r} = g\left(\Gamma_{\mathrm{rad}}-1\right)+\frac{2a^2}{r}-\frac{\mathrm{d}a^2}{\mathrm{d}r}. \tag{3.23}$$

3.2 Global energy budget and work ratio

The acceleration balance for stellar atmosphere models is described by Eq. (3.6). Multiplying this equation with the mass-loss rate $\dot{M}$ and integrating from the inner boundary R_* to infinity, one obtains an equation that now balances the work which is performed by the gas pressure and the radiation field (right-hand side) with what is called the "mechanical wind luminosity" L_{Wind}:

$$\dot{M}\int_{R_*}^{\infty}\left(a_{\mathrm{mech}}+g\right)\mathrm{d}r = \dot{M}\int_{R_*}^{\infty}\left(a_{\mathrm{rad}}+a_{\mathrm{press}}\right)\mathrm{d}r \tag{3.24}$$

$$\dot{M}\int_{R_*}^{\infty}\left(v\frac{\mathrm{d}v}{\mathrm{d}r}+\frac{GM_*}{r^2}\right)\mathrm{d}r = \dot{M}\int_{R_*}^{\infty}\left(a_{\mathrm{rad}}-\frac{1}{\rho}\frac{\mathrm{d}P}{\mathrm{d}r}\right)\mathrm{d}r \tag{3.25}$$

$$\dot{M}\left[\frac{1}{2}\underbrace{\left(v_\infty^2-v_{\mathrm{min}}^2\right)}_{\approx v_\infty^2}+\frac{GM_*}{R_*}\right] = \dot{M}\int_{R_*}^{\infty}\left(a_{\mathrm{rad}}-\frac{1}{\rho}\frac{\mathrm{d}P}{\mathrm{d}r}\right)\mathrm{d}r \tag{3.26}$$

$$L_{\mathrm{Wind}} = W_{\mathrm{Wind}} \tag{3.27}$$

As the evaluation of the integral on the left hand side shows, L_{Wind} can be calculated directly from the wind parameters. This "mechanical wind luminosity" describes also the difference between the luminosity L_* at R_* and the observed luminosity L_∞, i.e.

$$L_\infty = L_* - L_{\mathrm{Wind}}. \tag{3.28}$$

For a wind that is purely driven by radiation and gas pressure, Eq. (3.27) must be fulfilled. However, since the wind parameters in a typical PoWR model are prescribed, this is not necessarily the case. In fact, models that are calculated in order to reproduce observations usually have $L_{\mathrm{Wind}} > W_{\mathrm{Wind}}$, i.e. they do not provide the energy needed to drive the wind that they describe. In order to quantify this difference in a simple way, one can define the *work ratio*

$$Q := \frac{W_{\mathrm{Wind}}}{L_{\mathrm{Wind}}}. \tag{3.29}$$

Due to Eq. (3.27), a hydrodynamically consistent model must have $Q = 1$. Typical WR models, such, as those used in in Sander et al. (2012) or Hainich et al. (2014), usually have values between 0.2 and 0.5. This shortfall is attributed to the incompleteness of the opacities which are included in the model. Calculating models with $Q \approx 1$ is an important step in order to have a good start for the hydrodynamically consistent models which will be discussed in the next chapter. However, it is important to keep in mind that $Q = 1$ only ensures that the energy budget is consistent on a global scale. As it stems from an integrated form of the hydrodynamic equation, it does not give any information about a hydrodynamically consistent stratification.

3.3 Wind momentum efficiency

Aside from the Q-value defined above, another basic quantity can be calculated from basic stellar and wind parameters only, requiring no knowledge about the particular atmosphere stratification. The rate of momentum carried away in the wind can be written for $r \gg R_*$ as

$$p_{\mathrm{Wind}} := \dot{M} v_\infty \tag{3.30}$$

while the radiative momentum rate is given by

$$p_{\mathrm{rad}} := \frac{L_*}{c}. \tag{3.31}$$

The ratio of these two momentum rates defines the so-called *wind momentum efficiency*

$$\eta := \frac{p_{\mathrm{Wind}}}{p_{\mathrm{rad}}} = \frac{\dot{M} v_\infty c}{L_*}, \tag{3.32}$$

sometimes also labeled η_{mom} in the literature in order to distinguish it from other efficiency parameters such as η_{kin} and η_{pot} which are obtained from the ratio of the wind luminosity L_{wind} and the radiative luminosity L_*:

$$\frac{L_{\mathrm{Wind}}}{L_*} \approx \frac{\dot{M} v_\infty^2}{2 L_*} + \frac{\dot{M} G M_*}{R_* L_*} \equiv \eta_{\mathrm{kin}} + \eta_{\mathrm{pot}} \tag{3.33}$$

Unless indicated otherwise, the notation $\eta \equiv \eta_{\mathrm{mom}}$ will be used throughout this work. It should be noted that $\eta_{\mathrm{mom}} \gg \eta_{\mathrm{kin}}$ and $\eta_{\mathrm{mom}} \gg \eta_{\mathrm{pot}}$ for both, WR and OB stars, indicating

that the momentum transfer from photons to the gas is much more important than energy transfer for driving the winds of these stars. However, the particular values for η differ greatly between OB and WR stars. For most WR stars, η is larger than unity while OB stars have values below or at most on the order of unity. This has further implications which are discussed in Sect. 3.6.

3.4 The solution of the hydrostatic equation

Before discussing the full hydrodynamic equation and its solution, it is very instructive to take a look at the limit where the inertia term $a_{\rm mech}$ vanishes. In this case, the hydrodynamic equation (3.3) simplifies to the hydrostatic equation

$$\frac{1}{\rho}\frac{\mathrm{d}P}{\mathrm{d}r} = a_{\rm out}. \tag{3.34}$$

Including the proper terms for outer forces (3.4), yields the well known form of the equation

$$\frac{\mathrm{d}P}{\mathrm{d}r} = -\rho(r)\left(g(r) - a_{\rm rad}(r)\right) \tag{3.35}$$

$$= -\rho(r) g(r)\left[1 - \Gamma_{\rm rad}(r)\right]. \tag{3.36}$$

In a hydrostatic situation there is by definition no outflow and thus no velocity appears in this equation. However, the hydrostatic equation is still a very useful approximation for the subsonic layers, as below the sonic point ($a = v$) the inertia term quickly drops and becomes negligible further inwards, leading to a quasi-hydrostatic situation. Nevertheless, in this regime the equation of continuity (2.1) must still be satisfied. Thus all the calculations that lead to Eq. (3.23) can be done for the quasi-hydrostatic case as well, leading to:

$$\frac{a^2}{v}\frac{\mathrm{d}v}{\mathrm{d}r} = g(r)\left(1 - \Gamma_{\rm rad}(r)\right) - \frac{2a^2}{r} + \frac{\mathrm{d}a^2}{\mathrm{d}r} \tag{3.37}$$

$$\frac{\mathrm{d}v}{\mathrm{d}r} = \frac{v}{a^2}\left[g(r)\left(1 - \Gamma_{\rm rad}(r)\right) - \frac{2a^2}{r} + \frac{\mathrm{d}a^2}{\mathrm{d}r}\right] \tag{3.38}$$

Note that Eq. (3.37) corresponds to (3.23) without the inertia term. Nevertheless this small difference removes the non-linearity, making Eq. (3.38) a simple linear differential equation. With a given velocity value, e.g. the inner boundary value $v_{\rm min}$, this equation can be solved by direct integration. However, it is numerically advantageous to do first a certain transformation based on the assumption that the "true" solution is not so far away from a barometric formula. We therefore revert the manipulations (3.13)-(3.15) and write:

$$\frac{a^2}{v}\frac{\mathrm{d}v}{\mathrm{d}r} = g(r)\cdot\left[1 - \Gamma_{\rm rad}(r)\right] - \frac{2a^2}{r} + \frac{\mathrm{d}a^2}{\mathrm{d}r} \tag{3.39}$$

$$-\frac{1}{\rho}\frac{\mathrm{d}P}{\mathrm{d}r} = g(r)\cdot\left[1 - \Gamma_{\rm rad}(r)\right] \tag{3.40}$$

$$\frac{\mathrm{d}P}{\mathrm{d}r} = -\rho\, g(r)\cdot\left[1 - \Gamma_{\rm rad}(r)\right] \equiv -\rho\, g_{\rm eff}(r) \tag{3.41}$$

$$\frac{\mathrm{d}P}{\mathrm{d}r} = -\frac{P(r)}{a^2} g_{\rm eff}(r) = -\frac{P(r)}{H(r)} \tag{3.42}$$

In contrast to the barometric formula with a constant scale height $H_0 = a^2(T_*)/g_{\rm eff}$, a depth-dependent $H(r) = a^2(r)/g_{\rm eff}(r)$ is used here. H_0 and $H(r)$ can then be used for the quasi-barometric ansatz

$$P(r) = P_0 \exp\left(-\frac{r - R_*}{H_0} + b(r)\right) \tag{3.43}$$

with an arbitrary function $b(r)$ and the yet to be determined normalization constant P_0. Plugging the derivative of Eq. (3.43)

$$\frac{{\rm d}P}{{\rm d}r} = P_0 \exp\left(-\frac{r - R_*}{H_0} + b(r)\right) \cdot \left(-\frac{1}{H_0} + \frac{{\rm d}b}{{\rm d}r}\right) \tag{3.44}$$

$$= -\frac{P}{H_0} + P\frac{{\rm d}b}{{\rm d}r} \tag{3.45}$$

into (3.42) yields:

$$-\frac{P}{H(r)} = -\frac{P}{H_0} + P\frac{{\rm d}b}{{\rm d}r} \tag{3.46}$$

$$\frac{{\rm d}b}{{\rm d}r} = \frac{1}{H_0} - \frac{1}{H(r)} \tag{3.47}$$

With the boundary value $b(R_*) = 0$, Eq. (3.47) is then numerically integrated instead of (3.37). Afterwards, the velocity field can be obtained via

$$v(r) \propto \frac{1}{\rho r^2} = \frac{a^2}{P(r) r^2} \tag{3.48}$$

$$v(r) \propto \frac{a^2}{r^2} \exp\left(\frac{r - R_*}{H_0} - b(r)\right) \tag{3.49}$$

$$\tag{3.50}$$

The required normalization constant is provided by the inner boundary value $v_{\rm min}$, thus leading to the final form of the hydrostatic solution for the velocity field:

$$v(r) = v_{\rm min} \frac{a^2(r)}{a^2(R_*)} \frac{R_*^2}{r^2} \exp\left(\frac{r - R_*}{H_0} - b(r)\right) \tag{3.51}$$

The complexity of $a_{\rm rad}$ is hidden in $b(r)$ here, which contains $H(r)$ and therefore $g_{\rm eff}$. For a self-consistent solution, the full $\Gamma_{\rm rad}$, i.e. the full radiative acceleration, needs to be applied here. The choice of the right Γ is crucial for the inner density stratification of a stellar atmosphere model. Tests with the POWR code have shown significant differences in the obtained spectra for O and B stars if $\Gamma_{\rm e}$, accounting only for Thomson scattering, is used here instead of $\Gamma_{\rm rad}$ (see Sander et al., 2015). Additional information on the numerical implementation of the hydrostatic solution can be found in Sect. A.5 of the appendix.

3.5 The effective gravity

It is helpful to introduce the so-called *effective gravity* $g_{\rm eff}$ to simplify the notation of the hydrostatic equation. While this term can also have different meanings in the literature, it

will be used here for the gravity that has been reduced by the radiative acceleration $a_{\rm rad}$ throughout this work. As already implicitly written in Eq. (3.41), $g_{\rm eff}$ is therefore defined as

$$g_{\rm eff}(r) := g(r)\,[1 - \Gamma_{\rm rad}(r)]\,. \tag{3.52}$$

Note that the full radiative acceleration enters here. Using only a certain fraction instead of the full acceleration significantly affects the resulting stratification and might lead to wrong estimations of the stellar mass. This is discussed in detail in Sander et al. (2015).

The $g_{\rm eff}(r)$ in Eq. (3.52) is depth-dependent due to $g(r)$ and $\Gamma_{\rm rad}(r)$. However, sometimes there is a certain need for a "reference value" which can be used for comparisons, especially for $\Gamma_{\rm rad}(r)$. One could take the value at the inner boundary R_*, but as this point does not affect the spectrum any more, this value is not really representative. The next candidate would therefore be the radius corresponding to $\tau_{\rm Ross} \approx 2/3$ in the photosphere where the emergent spectrum is mainly formed. However, this point might already be located in the wind for certain stellar atmosphere models. Instead of using a fixed point it is therefore helpful to define a weighted mean of $\Gamma_{\rm rad}$ via

$$\overline{\Gamma}_{\rm rad} := \int_{\tau_{\rm max}}^{\tau_{\rm sonic}} \Gamma_{\rm rad}(\tau_{\rm Ross})\; e^{-\tau_{\rm Ross}}\; {\rm d}\tau_{\rm Ross}. \tag{3.53}$$

The upper limit $\tau_{\rm sonic}$ of the integral in Eq. (3.53) denotes the optical depth of the sonic point. To ensure a meaningful representation of the optically thick regime, values below 0.1 are not allowed, even in the rare cases where the actual sonic point would be in such a regime, so the upper limit of the integral in Eq. (3.53) is in fact the maximum of 0.1 and $\tau_{\rm sonic}$. The calculated value of $\overline{\Gamma}_{\rm rad}$ is used to relate $\log g_{\rm eff}$ and $\log g$ via

$$\log g_{\rm eff} = \log g + \log\left(1 - \overline{\Gamma}_{\rm rad}\right). \tag{3.54}$$

This relation can then be used for any proper reference radius where g is calculated. Typically these are R_* or $R(\tau_{\rm Ross} = \frac{2}{3})$.

3.6 The CAK solution

Already for the hydrostatic situation, but even more for the full hydrodynamic Eq. (3.21), it is crucial to know the radiative acceleration

$$a_{\rm rad}(r) = \frac{1}{\rho(r)} \frac{4\pi}{c} \int_0^\infty \kappa_\nu(\nu,r) H_\nu(\nu,r) {\rm d}\nu. \tag{3.55}$$

Its calculation for an expanding atmosphere requires either major simplifications (which will be discussed in this section) or a time-consuming calculation in the co-moving frame as it is done in the PoWR code. As the latter is computationally expensive even with today's hardware, the historical breakthroughs in the field were achieved by simplifying the calculations. The fundamental simplifications typically applied are compiled in the powerful formalism from Castor, Abbott, & Klein (1975, hereafter CAK) that replaced the evaluation of the integral in Eq. (3.55) by a parameterized analytical expression. The basic steps of their concept will be discussed in this section.

The radiative acceleration $a_{\rm rad}$ can be separated into the continuum and line contribution. Typically the continuum contribution is defined such that it also includes the Thomson scattering. Whenever these should be separated, the rest will be referred to as the *true continuum*. Hence one can write:

$$a_{\rm rad} = a_{\rm lines} + a_{\rm cont} = a_{\rm lines} + a_{\rm thom} + a_{\rm true\ cont} \tag{3.56}$$

Using the Thomson opacity κ_e, the electron scattering term can be written as

$$a_{\rm thom} = \frac{\kappa_e \mathfrak{F}}{\rho c} = q_{\rm ion} \frac{\sigma_e \mathfrak{F}}{m_{\rm H} c}. \tag{3.57}$$

$\mathfrak{F} = 4\pi H$ denotes the astrophysical flux, $q_{\rm ion}$ the ionization parameter, i.e. the number of free electrons per unit mass, and σ_e is the frequency-independent Thomson cross-section. Instead of specifying the absolute value of $a_{\rm thom}$, it is usually more interesting to define the fraction with respect to gravity. This ratio is commonly known as the *Eddington Gamma*

$$\Gamma_{\rm e} = \frac{a_{\rm thom}}{g} = \frac{\sigma_e}{4\pi c m_{\rm H} G} q_{\rm ion} \frac{L}{M_*}. \tag{3.58}$$

However, one has to be careful with the term "Eddington Gamma", as it is also applied to $\Gamma_{\rm rad}$, i.e. when the full radiative acceleration is used for calculating the ratio. To avoid any confusion, Γ_e and $\Gamma_{\rm rad}$ will always be denoted explicitly throughout this work.

With the previously discussed splitting of the radiative acceleration and the help of the Thomson Eddington Gamma $\Gamma_{\rm e}$ (3.58) we can rewrite equation (3.21) as

$$v \left(1 - \frac{a^2}{v^2}\right) \frac{{\rm d}v}{{\rm d}r} = -g\,(1 - \Gamma_{\rm e}) + \frac{2a^2}{r} - \frac{{\rm d}a^2}{{\rm d}r} + a_{\rm true\ cont} + a_{\rm lines}\ . \tag{3.59}$$

In the CAK approach by Castor et al. (1975) the true continuum term is neglected ($a_{\rm true\ cont} \approx 0$) which is actually only a valid approximation for the wind part, but not for the photosphere. The line acceleration is formally written as a multiple $\mathcal{M}$ of the Thomson term, thus introducing the so-called *force multiplier*

$$\mathcal{M} := \frac{a_{\rm lines}}{a_{\rm thom}} = \frac{a_{\rm lines}}{\Gamma_{\rm e} g} = \frac{\Gamma_{\rm lines}}{\Gamma_{\rm e}}\ . \tag{3.60}$$

Confusingly, the term $a_{\rm lines}$ is sometimes called $a_{\rm rad}$ in the literature, as the true continuum is neglected anyhow and the electron scattering is expressed via $\Gamma_{\rm e}$. To avoid any misunderstandings, this work will stick with $a_{\rm lines}$ for consistency. Correspondingly the previously defined $\Gamma_{\rm rad}$ is connected to $\Gamma_{\rm lines}$ via

$$\Gamma_{\rm rad} = \Gamma_{\rm lines} + \Gamma_{\rm true\ cont} + \Gamma_{\rm e}. \tag{3.61}$$

The force multiplier $\mathcal{M}$ represents the effect of all lines and is parameterized by Castor et al. (1975) in the form

$$\mathcal{M}(t) = k\, t^{-\alpha} \tag{3.62}$$

with k and α as being depth-independent. This was actually a fit to numerical calculations of the force multiplier $\mathcal{M}$ versus an optical-depth like, but line-strength independent quantity

$$t := \frac{\kappa_{\rm e}}{\kappa_{\rm L}} \tau_{\rm L} \tag{3.63}$$

with τ_L and κ_L being the optical depth and opacity resulting purely from lines. The first attempts from Castor et al. (1975) were based on C III multiplets and led to values of $k \approx \frac{1}{30}$ and $\alpha \approx 0.7$.

A central aspect of the CAK theory is the calculation of t (or τ_L) which is different in the static and the expanding part of the atmosphere. In the static part, the optical depth is defined in the conventional way ($\mathrm{d}\tau_\mathrm{L} = \kappa_\mathrm{L}\mathrm{d}r$), while in the expanding situation the optical depth is only affected by a fraction of the absorbers, namely those which are in a column where the velocity changes by the amount of the thermal velocity v_th. In this case the opacity of a line $\kappa(\nu)$ can be expressed by

$$\kappa(\nu) = \kappa_\mathrm{L}\delta\left(\frac{\nu_\mathrm{cmf} - \nu_0}{\Delta\nu}\right), \tag{3.64}$$

i.e. the profile function becomes a delta function with ν_cmf as defined in Eq. (2.46) and $\Delta\nu = \frac{\nu_0}{c}v_\mathrm{th}$ assuming pure thermal broadening. Calculating the radial ($\nu = 1$) optical depth then yields

$$\tau_\mathrm{L} = \int_{R_*}^{\infty} \kappa(\nu(r))\ \mathrm{d}r \tag{3.65}$$

$$= \kappa_\mathrm{L} \int_{v(R_*)}^{\infty} \delta\left(\frac{\nu_\mathrm{cmf} - \nu_0}{\Delta\nu}\right)\left|\frac{\mathrm{d}r}{\mathrm{d}v}\right|\mathrm{d}v \tag{3.66}$$

$$\approx \kappa_\mathrm{L} v_\mathrm{th}\left|\frac{\mathrm{d}r}{\mathrm{d}v}\right| \int_0^{\infty} \delta\left(\frac{\nu_\mathrm{cmf} - \nu_0}{\Delta\nu}\right)\mathrm{d}\nu_\mathrm{cmf} \tag{3.67}$$

$$= \kappa_\mathrm{L}\frac{v_\mathrm{th}}{\left|\frac{\mathrm{d}v}{\mathrm{d}r}\right|} \tag{3.68}$$

The relation $\mathrm{d}\nu_\mathrm{cmf} = \frac{\nu_0}{c}\mathrm{d}v = \frac{\Delta\nu}{v_\mathrm{th}}\mathrm{d}v$ helps to get from velocity to frequency space in Eq. (3.67). The final result is called the *Sobolev approximation* and was originally invented by Sobolev (1957). The calculations above for τ_L can be carried out in detail for all values of μ and have been published in Castor (1970, 1974). Combining the resulting Eq. (3.68) for the expanding case with the definition of t (Eq. 3.63) leads to the parameterization given in Castor et al. (1975):

$$t = \begin{cases} \int_r^{\infty} \kappa_\mathrm{e}\mathrm{d}r & \text{if static} \\ \kappa_\mathrm{e}\frac{v_\mathrm{th}}{\left|\frac{\mathrm{d}v}{\mathrm{d}r}\right|} & \text{if expanding} \end{cases} \tag{3.69}$$

Roughly speaking, the static situation should usually occur for $\tau > 1$, while the expanding situation is expected for $\tau \leq 1$. In fact, Castor et al. (1975) did not use the optical depth criterion to distinguish between the two cases[†], but simply calculate both terms and take whichever leads to a lower value for t^{-1}. The resulting fit formula (3.62) uses the expanding case to describe t. In order to completely separate the radius and velocity dependence, the

[†]The simplification based on considering only the two cases $\tau_\mathrm{L} \ll 1$ and $\tau_\mathrm{L} \gg 1$ is introduced by Abbott (1980), where the original CAK equations are taken in a reduced form for a perturbation analysis.

opacity κ_e is replaced by the product of density and mass absorption coefficient $\varkappa_\mathrm{e}$, so that the equation of continuity can be used:

$$t = \kappa_\mathrm{e} \frac{v_\mathrm{th}}{\frac{\mathrm{d}v}{\mathrm{d}r}} \tag{3.70}$$

$$= \varkappa_\mathrm{e} \rho \frac{v_\mathrm{th}}{\frac{\mathrm{d}v}{\mathrm{d}r}} \tag{3.71}$$

$$= \frac{\dot{M} \varkappa_\mathrm{e} v_\mathrm{th}}{4\pi} \left(r^2 v \frac{\mathrm{d}v}{\mathrm{d}r} \right)^{-1} \tag{3.72}$$

The absolute of the gradient can be dropped if the situation is restricted to strictly monotonic velocity fields, so that $\frac{\mathrm{d}v}{\mathrm{d}r} > 0$ is automatically ensured. As this is already needed for the radiative transfer formalism used in the PoWR code, this restriction was given anyhow.

Using (3.62) and new obtained form of t, we can now obtain the CAK equation of motion:

$$v \left(1 - \frac{a^2}{v^2} \right) \frac{\mathrm{d}v}{\mathrm{d}r} = -\frac{GM_*}{r^2} (1 - \Gamma_\mathrm{e}) + \frac{2a^2}{r} - \frac{\mathrm{d}a^2}{\mathrm{d}r} + k\Gamma_\mathrm{e} \frac{GM_*}{r^2} \left(\frac{\dot{M} \varkappa_\mathrm{e} v_\mathrm{th}}{4\pi} \right)^{-\alpha} \left(r^2 v \frac{\mathrm{d}v}{\mathrm{d}r} \right)^{\alpha} \tag{3.73}$$

Using the $\bar{Q}$-notation introduced by Gayley (1995), one can alternatively replace

$$k = \frac{1}{1-\alpha} \left(\frac{v_\mathrm{th}}{c} \right)^{\alpha} \bar{Q}^{1-\alpha} \tag{3.74}$$

and write the CAK equation of motion in the form

$$v \left(1 - \frac{a^2}{v^2} \right) \frac{\mathrm{d}v}{\mathrm{d}r} = -\frac{GM_*}{r^2} (1 - \Gamma_\mathrm{e}) + \frac{2a^2}{r} - \frac{\mathrm{d}a^2}{\mathrm{d}r} + \frac{\bar{Q}^{1-\alpha}}{1-\alpha} \Gamma_\mathrm{e} \frac{GM_*}{r^2} \left(\frac{\dot{M} \varkappa_\mathrm{e} c}{4\pi} \right)^{-\alpha} \left(r^2 v \frac{\mathrm{d}v}{\mathrm{d}r} \right)^{\alpha}, \tag{3.75}$$

which removes the somewhat arbitrary occurrence of v_th. Furthermore, Gayley (1995) identifies $\bar{Q}$ as a dimensionless line-strength parameter that is roughly constant with values on the order of ≈ 2000, but scales with metallicity.

In the original work by Castor et al. (1975), the star itself, i.e. the static layers, is treated as a point source and only the wind is considered to be extended. This approximation is good far away from the star, but becomes poorer the closer it gets to the (quasi-)static layers. Therefore, a correction factor (D_f) to $\mathcal{M}(t)$ already suggested in the CAK paper was introduced later on (Friend & Abbott, 1986; Pauldrach et al., 1986) that accounts for an extended stellar disk, commonly referred to as *finite disk* (FD) correction. Additionally, more elaborated line-strength calculations (e.g. Kudritzki et al., 1989; Gayley, 1995) helped to gain proper descriptions of O-star winds using the (modified) CAK theory (mCAK). Thus, after the extensions of Abbott (1982) and Pauldrach et al. (1986) the equation (3.62) was modified to

$$\mathcal{M}(t) = k\, t^{-\alpha} \hat{n}^{\delta} D_f, \tag{3.76}$$

with D_f correcting for the finite disk and the term in parenthesis accounting for the non-constant ionization stage in the wind. The photoionization rate depends on the electron density n_e and the flux of the star which dilutes by the factor

$$W(r) := \frac{1}{2} \left[1 - \sqrt{1 - \left(\frac{R_*}{r} \right)^2} \right]. \tag{3.77}$$

For an easier notation, these two are combined in the definition

$$\hat{n} := \frac{n_\mathrm{e}}{10^{11}\,\mathrm{cm}^{-3}} \frac{1}{W(r)} \tag{3.78}$$

(see, e.g., Kudritzki, 2002). The exponent δ stems from a simple power-law approach, trying to approximate the calculations from Abbott (1982). For hot stars of solar metallicity, δ is in the range of 0.0 to 0.2 (Kudritzki, 2002). After the already introduced quantities α and k, this makes δ the third force multiplier parameter which becomes important as soon as ionization changes are not negligible. The difference between α and δ, which often appears in resulting relations from mCAK models, e.g. for $\dot{M}$, is typically abbreviated as $\alpha' := \alpha - \delta$. The mCAK α-parameter will be discussed in more detail in Sect. 3.9, where it is compared to α-parameter defined in the approach from Gräfener & Hamann (2005).

3.6.1 The supersonic (zero sound speed) approximation

The Eq. (3.73) can be solved analytically if the pressure terms ($a \to 0$) are neglected, which is usually a sufficient approximation for the supersonic part of the atmosphere. Introducing the constant $C = k\Gamma_\mathrm{e} GM_* \left(\frac{\dot{M}\varkappa_\mathrm{e} v_\mathrm{th}}{4\pi}\right)^{-\alpha}$ to summarize the quantities in the last term which are not radial dependent, Castor et al. (1975) obtained by multiplying (3.73) with r^2:

$$r^2 v \frac{\mathrm{d}v}{\mathrm{d}r} = -GM_* \left(1 - \Gamma_\mathrm{e}\right) + C \left(r^2 v \frac{\mathrm{d}v}{\mathrm{d}r}\right)^{\alpha} \tag{3.79}$$

This differential equation can be transformed into an algebraic equation by certain substitutions. Forcing the resulting algebraic equation to have exactly one solution, Castor et al. (1975) obtain the equation

$$r^2 v \frac{\mathrm{d}v}{\mathrm{d}r} = \frac{\alpha}{1-\alpha} GM_* \left(1 - \Gamma_\mathrm{e}\right) = \text{const.} \tag{3.80}$$

which leads to a β-type velocity law with $\beta = \frac{1}{2}$:

$$v(r) = v_\infty \left(1 - \frac{R_*}{r}\right)^{\frac{1}{2}} \qquad \Rightarrow \qquad r^2 v \frac{\mathrm{d}v}{\mathrm{d}r} = \frac{1}{2} v_\infty^2 R_* \tag{3.81}$$

Combining this result with the previous Eq. (3.80) leads to a relation between the terminal and the escape velocity:

$$v_\infty = \sqrt{\frac{\alpha}{1-\alpha}} v_\mathrm{esc} \qquad \text{with} \qquad v_\mathrm{esc} := \sqrt{\frac{2GM_* \left(1 - \Gamma_\mathrm{e}\right)}{R_*}} \tag{3.82}$$

3.6.2 The CAK solution with non-vanishing sound speed

The solution for the complete CAK equation of motion including the pressure terms and the finite disk correction

$$v \left(1 - \frac{a^2}{v^2}\right) \frac{\mathrm{d}v}{\mathrm{d}r} = -\frac{GM_*}{r^2} \left(1 - \Gamma_\mathrm{e}\right) + \frac{2a^2}{r} - \frac{\mathrm{d}a^2}{\mathrm{d}r} + \frac{C}{r^2} \left(r^2 v \frac{\mathrm{d}v}{\mathrm{d}r}\right)^{\alpha}, \tag{3.83}$$

with the previously introduced C summarizing the various constants from Eq. (3.73), can only be obtained numerically. Good analytical approximations have been made by Kudritzki et al. (1989). The decisive ingredient in Eq. (3.83) is the last term on the right-hand side which is proportional to the velocity gradient to the power α. The left-hand side of Eq. (3.83) becomes zero at $v = a$, i.e. the *sonic point*. In the case of $C \equiv 0$, this point would also be the critical point, because if the right-hand side does not vanish the velocity gradient would go to infinity. With $C \neq 0$ there is also a critical point, but this point is not identical (but further out, though often close to) the sonic point.

A thing that is so far "hidden" in the CAK formalism is its restriction to stars which are below the so-called single scattering limit. This is a result of how the formalism treats the absorption of the radiative momentum. The power law approach for the force multiplier $\mathcal{M}$ (see Eq. 3.62) assumes that the momentum is absorbed by independent lines. This means that overlapping effects from thick lines are ignored (e.g. Owocki, 2004).

The star's radiative momentum L/c is reduced by roughly a factor v_∞/c for each "typical" thick line if overlapping effects are not taken into account. This approximation stems from a simple textbook calculation (see, e.g., Lamers & Cassinelli, 1999), namely that the absorbed luminosity for a line with the frequency ν_0 in the wind is

$$L_{\mathrm{abs}} = \int_{\nu_0}^{\nu_0(1+v_\infty/c)} L_\nu \, \mathrm{d}\nu \tag{3.84}$$

$$\approx L_\nu(\nu_0)\Delta_\nu(\nu_0) \tag{3.85}$$

$$= \nu_0 L_\nu(\nu_0)\frac{v_\infty}{c}. \tag{3.86}$$

Due to the expanding situation, photons in a whole range of frequencies are absorbed. Close to the star where $v(r) \approx 0$, photons of the rest frequency ν_0 can be absorbed, while in the outermost layers where $v(r) \to v_\infty$, the absorption frequency changes to $\nu_0 \cdot (1 + v_\infty/c)$. Assuming that L_ν is roughly constant over $\Delta\nu(\nu_0)$, the integral in Eq. (3.84) can be approximated by a rectangle, leading to Eq. (3.86). For a line in the UV, i.e. the flux maximum of hot stars, Eq. (3.86) can be further simplified by $\nu_0 L_\nu(\nu_0) \approx f \cdot L$ with $f = \mathcal{O}(1)$. This leads to

$$L_{\mathrm{abs}} \approx fL\frac{v_\infty}{c} \approx L\frac{v_\infty}{c}, \tag{3.87}$$

i.e. the star's luminosity is reduced by approximately v_∞/c if ν_0 is an optically thick line in the range of the flux maximum and thus was called "typical" above. The same holds for the radiative momentum L/c. The total wind momentum $\dot{M}v_\infty$ is now the fraction η of the radiative momentum

$$\dot{M}v_\infty = \eta\frac{L}{c}. \tag{3.88}$$

Therefore the fraction η must be equal to the "effective" number of lines N_{eff} times their absorbed momentum:

$$\eta = N_{\mathrm{eff}}\frac{v_\infty}{c} \tag{3.89}$$

Without line overlap, at maximum the whole radiative momentum can be consumed and therefore N_{eff} is limited to values lower than c/v_∞, i.e. η must be lower than unity. This is called the *single scattering limit* because it is derived on the assumption that each photon contributes to the radiative acceleration only once. This assumption is inherit to the CAK theory

where each line interacts with the unscattered radiation field of the stellar photosphere. Friend & Castor (1983) already pointed out that the inclusion of multi-line effects can significantly change the result and would be crucial for reproducing Wolf-Rayet winds. The influence for O-stars was investigated by Abbott & Lucy (1985) and Puls (1987). Puls (1987) concluded that for O-stars like ζ Pup the multi-line effects could be approximated by lowering the value for k and thus avoiding costly adjustments to the calculations. Abbott & Lucy (1985) developed a Monte-Carlo approach to test the multi-line effects. This provide the basis for the later work of Vink et al. (2000) and their predictions of mass-loss rates for O and B stars. Vink et al. (2000) used a similar Monte-Carlo approach to account for multiple scattering in their calculations of the radiative acceleration. The same technique was later also used to model Galactic Wolf-Rayet stars (Vink & de Koter, 2005), using WC8 star WR 135 and the WN8 star WR 40 as prototypes, revealing that the main difference for the higher mass-loss rates compared to O-stars of the the same luminosity is the significantly lower mass of WR stars, but underpredicting the absolute empirically obtained $\dot{M}$-value for the WC star.

3.7 Solutions without Sobolev approximation

One of the basic ideas of the CAK theory is the simplified description of the optical depth in the expanding atmosphere as written in Eq. (3.72), more commonly formulated as

$$\tau_S = \rho\varkappa\frac{v_{\rm th}}{{\rm d}v/{\rm d}r} = \rho\varkappa l_{\rm sob} \tag{3.90}$$

The corresponding length scale $l_{\rm sob}$ is called the *Sobolev length*. Using Eq. (3.90) instead of a full calculation of the optical depth which would require a non-local spatial integration is a powerful simplification allowing the previously described semi-analytical CAK formalism. It also reduces computing times in stellar atmosphere models significantly, thus allowing codes such as FASTWIND (Puls et al., 2005) or WMBASIC (Pauldrach et al., 2001) to obtain a converged solution in an hour or even less.

However, the Sobolev approximation assumes that all absorption and scattering occurs in a narrow layer of $l_{\rm sob}$. This approximation relies on the assumption that $v_{\rm th} \ll v$. This is true in the outer wind, but not in the region around the sonic point (see Eq. 3.11). Thus, if the critical point is close to the sonic point, $v(r)$ might still be on the order of $v_{\rm th}$. In this case, the scattering layer is not small any more and the Sobolev approximation would not be sufficient.

For Wolf-Rayet stars, also multiple scattering must be considered as previously mentioned. Instead of using the Sobolev approximation for the radiative transfer to get rid of the non-local spatial integration in the expanding atmosphere, one can instead follow the approach of Mihalas et al. (1975, 1976) and do the radiative transfer calculation in the comoving frame. This allows the computation of the radiation field, as well as the (Rosseland) optical depth and the radiative acceleration without limiting the absorption and scattering range. Nevertheless it is computationally more expensive and therefore stellar atmosphere codes with this approach, such as POWR (Gräfener et al., 2002; Hamann & Gräfener, 2003) or CMFGEN (Hillier & Miller, 1998) run longer and usually need at least a few hours to obtain a converged solution for a stellar atmosphere.

If the radiative acceleration $a_{\rm rad}$ is computed directly via the evaluation of Eq. (3.55), one could in principle plug the result directly into Eq. (3.21). However, to obtain a velocity

stratification via

$$\frac{\mathrm{d}v}{\mathrm{d}r} = \frac{1}{v\left(1-\frac{a^2}{v^2}\right)}\left[a_{\mathrm{rad}}(r) - g(r) + \frac{2a^2}{r} - \frac{\mathrm{d}a^2}{\mathrm{d}r}\right] \tag{3.91}$$

with a given starting value v_0 would fail at the sonic point $v = a$ where this equation has a critical point. In order to have a removable singularity, the term in brackets has to vanish at the sonic point. This requires $\Gamma_{\mathrm{rad}} < 1$ for a finite velocity gradient at the sonic point in the case of monotonic temperature stratification[‡]. Unlike the CAK equation of motion, Eq. (3.91) does not explicitly dependent on $\dot{M}$ and thus neither the equation itself nor the conditions for a removable singularity provide any constraints on the value of the mass-loss rate.

3.8 The generalized CAK approach

In order to avoid the limitations of the CAK theory on the one hand but still have the advantage of an explicit description for the $\frac{\mathrm{d}v}{\mathrm{d}r}$-dependence of a_{rad}, Gräfener & Hamann (2005) developed a kind of "generalized" CAK approach with depth-dependent parameters. They introduce a column density

$$\mathrm{d}s = \rho\ \mathrm{d}r, \tag{3.92}$$

which is used for simplifying, both the equations and the notation itself. In Gräfener & Hamann (2005) s is termed τ and referred to as *optical depth*. To avoid any confusion, the terms s and $\mathrm{d}s$ will be used throughout this work while τ and $\mathrm{d}\tau$ will refer to the usual definition of the optical depth $\mathrm{d}\tau = \varkappa\,\rho\,\mathrm{d}r = \kappa\,\mathrm{d}r$ which includes the opacity κ.

In the PoWR code, the total radiative acceleration a_{rad} as well as the acceleration due to the radiation intercepted by electrons and continuum opacities a_{cont} are calculated during the CMF radiative transfer. The remaining line acceleration is the difference,

$$a_{\mathrm{lines}} = a_{\mathrm{rad}} - a_{\mathrm{cont}}. \tag{3.93}$$

In order to parameterize a_{lines}, Gräfener & Hamann (2005) now follow the basic CAK approach and write:

$$a_{\mathrm{lines}} = \frac{GM}{r^2}\Gamma_{\mathrm{e}}\mathcal{M}\left(\frac{1}{\rho}\frac{\mathrm{d}v}{\mathrm{d}r}\right) = \frac{C}{r^2}\left(\frac{1}{\rho}\frac{\mathrm{d}v}{\mathrm{d}r}\right)^{\alpha} = \frac{C}{r^2}\left(\frac{\mathrm{d}v}{\mathrm{d}s}\right)^{\alpha} \tag{3.94}$$

All quantities which are not depth-dependent (including $\Gamma_{\mathrm{e}} \approx$ const.) are combined in the proportional constant C here. The parameter α introduced in the original work from Castor et al. (1975) is not depth-dependent, but this restriction has to be removed in order to keep the simple notation from Eq. (3.94) and avoid any of the previously discussed CAK extensions. Unfortunately, using a depth-dependent $\alpha(r)$ increases the complexity of the problem. A linearization of Eq. (3.94) is necessary to obtain an analytic expression for the velocity gradient. Linearizing is done by performing a first order Taylor expansion of (3.94)

[‡]In fact, the temperature stratification does not have to be completely monotonic, but $\frac{\mathrm{d}T}{\mathrm{d}r} < 0$ at the sonic point automatically forces $\Gamma_{\mathrm{rad}} < 1$ there.

around a fixed velocity v_0 with respect to the gradient $\frac{\mathrm{d}v}{\mathrm{d}s}$:

$$a_{\mathrm{lines}} = \frac{C}{r^2}\left(\frac{\mathrm{d}v}{\mathrm{d}s}\right)^{\alpha} \tag{3.95}$$

$$\approx \frac{C}{r^2}\left(\frac{\mathrm{d}v_0}{\mathrm{d}s}\right)^{\alpha} + \alpha\frac{C}{r^2}\left(\frac{\mathrm{d}v_0}{\mathrm{d}s}\right)^{\alpha-1}\left[\frac{\mathrm{d}v}{\mathrm{d}s} - \frac{\mathrm{d}v_0}{\mathrm{d}s}\right] \tag{3.96}$$

$$= (1-\alpha)\frac{C}{r^2}\left(\frac{\mathrm{d}v_0}{\mathrm{d}s}\right)^{\alpha} + \alpha\frac{C}{r^2}\left(\frac{\mathrm{d}v_0}{\mathrm{d}s}\right)^{\alpha-1}\frac{\mathrm{d}v}{\mathrm{d}s} \tag{3.97}$$

Following the basic idea of the (m)CAK theory incl. Puls et al. (2000), the two terms can now be attributed to optical thin ($\propto r^{-2}$) and optical thick lines ($\propto r^{-2}\frac{\mathrm{d}v}{\mathrm{d}s}$). The total line acceleration is written as

$$a_{\mathrm{lines}} = a_{\mathrm{thin}} + a_{\mathrm{thick}}. \tag{3.98}$$

Adding the continuum part, one obtains the total radiative acceleration:

$$a_{\mathrm{rad}} = a_{\mathrm{cont}} + a_{\mathrm{thin}} + a_{\mathrm{thick}}. \tag{3.99}$$

As the thin lines and the continuum contributions both do not dependent on the velocity gradient in this approach, they can be treated in the same way and summarized into one term. The radiative acceleration can thus be written as

$$a_{\mathrm{rad}} = \frac{GM\Gamma(s)}{r^2} + \frac{k(s)}{r^2}\frac{\mathrm{d}v}{\mathrm{d}s}, \tag{3.100}$$

with Γ and k combining all of the coefficients. Due to the depth-dependence of α (and a_{cont}) both, Γ and k, will be depth-dependent quantities, too. Assuming that the interpretation

$$\alpha = \frac{a_{\mathrm{thick}}}{a_{\mathrm{lines}}} \tag{3.101}$$

(Puls et al., 2000) also holds for $\alpha(r)$ from Gräfener & Hamann (2005), one obtains

$$k(s) = \alpha r^2 \frac{a_{\mathrm{lines}}}{\frac{\mathrm{d}v}{\mathrm{d}s}}. \tag{3.102}$$

By comparing (3.99) to (3.100), one gets also an expression for Γ:

$$\Gamma(s) = \frac{r^2}{GM}\left(a_{\mathrm{cont}} + a_{\mathrm{thin}}\right) \tag{3.103}$$

It is possible to replace a_{thin} with the terms actually calculated, namely a_{rad}, a_{cont}, and α, hence Γ is actually obtained in Gräfener & Hamann (2005) via

$$\Gamma = \frac{r^2}{GM}\left[a_{\mathrm{cont}} + (1-\alpha)a_{\mathrm{lines}}\right] \tag{3.104}$$

$$= \frac{r^2}{GM}\left[a_{\mathrm{cont}} + (1-\alpha)\cdot(a_{\mathrm{rad}} - a_{\mathrm{cont}})\right] \tag{3.105}$$

$$= g^{-1}\left[(1-\alpha)\ a_{\mathrm{rad}} + \alpha\ a_{\mathrm{cont}}\right]. \tag{3.106}$$

This Γ, i.e. without subscript, is not identical to any of the ones with subscript, but can be connected to the earlier introduced Γ_e and $\Gamma_{\rm rad}$. The continuum acceleration $a_{\rm cont}$ contains the Thomson term plus the true continuum term. One can therefore define

$$\Gamma_{\rm cont} := \frac{a_{\rm cont}}{g} \tag{3.107}$$

$$= \frac{a_{\rm thom}}{g} + \frac{a_{\rm true\ cont}}{g} \tag{3.108}$$

$$= \Gamma_{\rm e} + \Gamma_{\rm true\ cont} \tag{3.109}$$

and derive

$$\Gamma = (1-\alpha)\,\Gamma_{\rm rad} + \alpha\,\Gamma_{\rm cont}. \tag{3.110}$$

In the special case of $\alpha(r) \equiv 0$, the definitions of Γ and k simplify to

$$\Gamma = \Gamma_{\rm rad} \qquad \text{and} \qquad k \equiv 0. \tag{3.111}$$

This means that for $\alpha \equiv 0$, the k-term in Eq. (3.100) vanishes and $a_{\rm rad} = g\Gamma_{\rm rad}$, i.e. the original, non-parameterized form of the hydrodynamic equation (3.23) is restored.

3.9 The alpha parameter in the linearized approach

In the previous Sect. 3.8, Γ and k have been introduced. Both terms are depending on α, which is a so-called *force multiplier parameter* in (m)CAK. In the linearized approach of Gräfener & Hamann (2005), $\alpha(r)$ is in fact not explicitly a parameter of the force multiplier $\mathcal{M}$ any more, but instead a parameter of the force multiplier parameters Γ and k. This can be seen when calculating the new force multiplier with $a_{\rm rad}$ now written as in Eq. (3.100):

$$\mathcal{M} := \frac{a_{\rm lines}}{\Gamma_{\rm e} g} \tag{3.112}$$

$$= \frac{1}{\Gamma_{\rm e} g}\left[a_{\rm rad} - a_{\rm cont}\right] \tag{3.113}$$

$$= \frac{1}{\Gamma_{\rm e} g}\left[g\Gamma(r) + \frac{k(r)}{r^2}\frac{1}{\rho}\frac{{\rm d}v}{{\rm d}r} - a_{\rm cont}\right] \tag{3.114}$$

$$= \frac{\Gamma(r)}{\Gamma_{\rm e}} - \frac{\Gamma_{\rm cont}}{\Gamma_{\rm e}} + \frac{k(r)}{GM\Gamma_{\rm e}}\frac{1}{\rho}\frac{{\rm d}v}{{\rm d}r} \tag{3.115}$$

In the wind part, the true continuum contribution is negligible, so $\Gamma_{\rm cont} \approx \Gamma_{\rm e}$ removes one parameter from the force multiplier equation (3.115). This simplification does not hold in the hydrostatic domain, but instead in the quasi-hydrostatic part $\alpha(r)$ is approaching zero, so due to $k \propto \alpha$ the third term vanishes there.

With Eq. (3.115) given for the force multiplier, it is actually not exact to call $\alpha(r)$ a force multiplier parameter, even though the explicit force multiplier parameters Γ and k contain a strong implicit α-dependency. In a way one can therefore call $\alpha(r)$ an *implicit force multiplier parameter* but for simplicity it will mostly be just referred to as *alpha parameter* throughout the rest of this work.

Calculating the alpha parameter

As briefly mentioned in Sect. 3.6, the classical CAK-α is calculated from line strength distribution functions (e.g. Gayley, 1995; Puls et al., 2000). In this approach, described in Puls et al. (2000), line forces for a large number of lines are calculated (in Sobolev approximation) and a so-called "line strength" is defined which is related to the Sobolev optical depth τ_{S}. Afterwards all line forces are added to yield the total radiative acceleration. Lines with $\tau_{\mathrm{S}} < 1$ (thin) are weighted with τ_{S} as "interaction probability" while the ones with $\tau_{\mathrm{S}} \geq 1$ (thick lines) are weighted with a factor of 1. Next, Puls et al. (2000) assume that the number of lines in a frequency and line strength interval follows a power law with a slope of $\alpha - 2$ ($0 < \alpha < 1$) and replace the summation by integrals. With this approach they obtain

$$a_{\mathrm{lines}} \propto \frac{1}{1-\alpha} t^{-\alpha} + \frac{1}{\alpha} t^{-\alpha}. \tag{3.116}$$

As the first term originates from the thick lines and the second one from the thin lines, Eq. (3.116) is the source of interpreting α as the fraction of thick lines:

$$a_{\mathrm{thick}} \propto \frac{1}{1-\alpha} t^{-\alpha} \quad \text{and} \quad a_{\mathrm{thin}} \propto \frac{1}{\alpha} t^{-\alpha} \tag{3.117}$$

$$\frac{a_{\mathrm{thin}}}{a_{\mathrm{thick}}} = \frac{1-\alpha}{\alpha} \tag{3.118}$$

$$\frac{a_{\mathrm{lines}} - a_{\mathrm{thick}}}{a_{\mathrm{thick}}} = \frac{a_{\mathrm{lines}}}{a_{\mathrm{thick}}} - 1 = \frac{1}{\alpha} - 1 \tag{3.119}$$

$$\frac{a_{\mathrm{thick}}}{a_{\mathrm{lines}}} = \alpha \tag{3.120}$$

It has to be stressed that this result is based on the assumption that there is a line force distribution following a power law[§] with the slope $\alpha - 2$ and implicitly contains the Sobolev approximation. If one, however, defines a quantity $\hat{\alpha}$ by writing

$$a_{\mathrm{lines}} \propto X^{\hat{\alpha}}, \tag{3.121}$$

with another arbitrary quantity X, there is no underlying assumption of $\hat{\alpha}$ and thus it is called an *effective* alpha parameter. It can be calculated by

$$\hat{\alpha} = \frac{\mathrm{d}(\log a_{\mathrm{lines}})}{\mathrm{d}(\log X)}. \tag{3.122}$$

In a CAK analogue approach, one would place the velocity gradient divided by the density as X, yielding an expression similar to (3.94):

$$a_{\mathrm{lines}} \propto \left(\frac{1}{\rho} \frac{\mathrm{d}v}{\mathrm{d}r} \right)^{\hat{\alpha}} \tag{3.123}$$

Nevertheless the previous Eq. (3.121) is simply a postulate which has yet to be checked for validity. Puls et al. (2000) have shown that with the Sobolev approximation one can obtain

$$\hat{\alpha} \approx \frac{a_{\mathrm{thick}}}{a_{\mathrm{lines}}}, \tag{3.124}$$

[§]This assumption is not arbitrary, but motivated from fits to calculated distribution functions. See Puls et al. (2000) for details.

when neglecting second order terms after differentiation.

To calculate numerical α-values, one can use Eq. (3.94) and investigate how $a_{\rm lines}$ reacts on a change of the velocity gradient. This is done by calculating the radiative transfer which yields $a_{\rm rad}$ and $a_{\rm cont}$, twice, first with a modified value for velocity $v(r)$ and its gradient $\frac{{\rm d}v}{{\rm d}r}$, then with the normal ones. In the original approach from Gräfener & Hamann (2005), the modification was 10%, yielding for the modified values marked with a tilde

$$\tilde{v} = 0.9 \cdot v \text{ and } \frac{{\rm d}\tilde{v}}{{\rm d}s} = 0.9 \cdot \frac{{\rm d}v}{{\rm d}s}. \tag{3.125}$$

Afterwards the ratio

$$\delta = \frac{\tilde{a}_{\rm lines}}{a_{\rm lines}} \tag{3.126}$$

is calculated for each depth point i. In order to eliminate possible side effects of the velocity modification on the total level of the radiative acceleration, they are normalized to the total flux $H_{\rm tot}$. The numerical calculation of δ_i therefore is

$$\delta_i = \frac{H_{{\rm tot},i}}{\tilde{H}_{{\rm tot},i}} \frac{\tilde{a}_{\rm rad} - \tilde{a}_{\rm cont}}{a_{\rm rad} - a_{\rm cont}}. \tag{3.127}$$

As α is an exponent in (3.94), the logarithm has to be taken to find

$$\alpha_i = \frac{\log \delta_i}{\log 0.9} \tag{3.128}$$

The modification factor $\lambda = 0{,}9$ from Gräfener & Hamann (2005) is more or less arbitrary. Indeed, one can obtain a generalized of Eq. (3.128) for any λ. Starting with the ratio of the modified and unmodified line acceleration

$$\delta = \frac{\tilde{a}_{\rm lines}}{a_{\rm lines}} = \frac{\frac{C}{r^2}}{\frac{C}{r^2}} \left(\frac{\frac{{\rm d}\tilde{v}}{{\rm d}s}}{\frac{{\rm d}v}{{\rm d}s}} \right)^{\alpha}, \tag{3.129}$$

one can use the fact that only the velocity fields and their gradients differ while the unknown coefficient $C(r)$ is the same in both cases and thus cancels together with r^2. Moreover, it is known that the modification is just done via multiplication with a constant factor λ, i.e.

$$\tilde{v} = \lambda v \text{ and } \frac{{\rm d}\tilde{v}}{{\rm d}s} = \lambda \frac{{\rm d}v}{{\rm d}s}. \tag{3.130}$$

This allows to replace the modified values by the original ones which then also cancel. The only remaining factor is λ and thus one obtains the generalized form of (3.128):

$$\delta = \lambda^{\alpha} \qquad \Leftrightarrow \qquad \alpha = \log_{\lambda} \delta = \frac{\log \delta}{\log \lambda} \tag{3.131}$$

With the obtained $\alpha(r)$ and the two accelerations $a_{\rm rad}$ and $a_{\rm cont}$ given by the radiative transfer, k and Γ can then be calculated:

$$k(r) = \alpha r^2 \frac{a_{\rm rad} - a_{\rm cont}}{\frac{{\rm d}v}{{\rm d}s}} \tag{3.132}$$

$$\Gamma(r) = \frac{r^2}{GM} \left[a_{\rm cont} + (1-\alpha) \left(a_{\rm rad} - a_{\rm cont} \right) \right]. \tag{3.133}$$

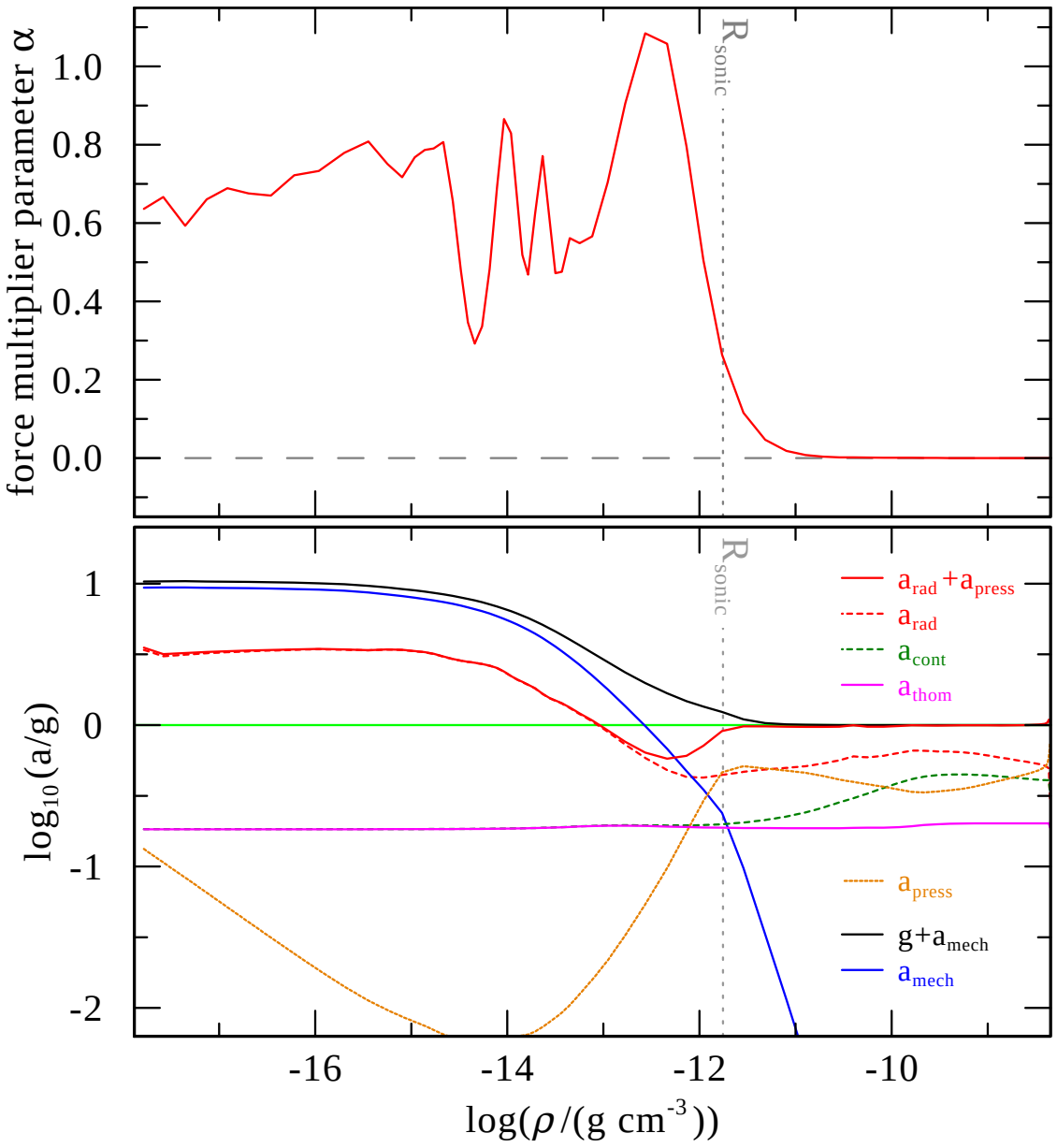

Figure 3.1 – Calculated $\alpha(r)$-values for an OB star model ($T_* = 32\,\mathrm{kK}$, $\dot{M} = 10^{-8}\,M_\odot/\mathrm{yr}$) with a consistent stratification in the quasi-hydrostatic part (upper panel). For comparison, the contributions to the acceleration in the model are shown in the lower panel.

An example of the $\alpha(r)$-values calculated for typical OB-star model with a velocity modification factor of $\lambda = 0.9$ can be seen in Fig. 3.1. Although in the wind part $\alpha(r)$ reaches CAK-like values of $0.6 \ldots 0.8$, there is a significant depth-dependent scatter which is not reflected in the radiative acceleration of the model. In the first increase after the sonic point, $\alpha(r)$ reaches even values above unity.

3.10 Solution of the hydrodynamic equation in the generalized CAK approach

Plugging the description of the radiative force in the generalized CAK approach (3.100) from Sect. 3.8 in the hydrodynamic equation (3.21) using the definition (3.92) becomes

$$\rho v \left(1 - \frac{a^2}{v^2}\right) \frac{\mathrm{d}v}{\mathrm{d}s} = \frac{GM\Gamma(r)}{r^2} + \frac{k(r)}{r^2}\frac{\mathrm{d}v}{\mathrm{d}s} - \frac{GM}{r^2} + 2\frac{a^2}{r} - \rho\frac{\mathrm{d}a^2}{\mathrm{d}s} \tag{3.134}$$

The explicit appearance of the density can be replaced using the equation of continuity in the form

$$\rho v = \frac{\dot{M}}{4\pi r^2}. \tag{3.135}$$

After bringing the k-term to the left side and an additional multiplication with r^2, one obtains the form that is used in Gräfener & Hamann (2005):

$$\frac{\mathrm{d}v}{\mathrm{d}s}\left[\left(1 - \frac{a^2}{v^2}\right)\frac{\dot{M}}{4\pi} - k(r)\right] = -GM\left[1 - \Gamma(r)\right] + 2a^2 r - \frac{\dot{M}}{4\pi v}\frac{\mathrm{d}a^2}{\mathrm{d}s}. \tag{3.136}$$

The Eq. (3.136) now contains only known quantities. An overview of the quantities and where they are calculated in the PoWR code is given in Sect. A.6.1 of the appendix.

In principle, integration of (3.136) now yields the velocity field $v(s)$. To actually get the required $v(r)$, a second equation has to be solved in parallel, namely the change of r with respect to s which are connected by the continuity equation:

$$\frac{\mathrm{d}r}{\mathrm{d}s} = \frac{1}{\rho} = \frac{4\pi v r^2}{\dot{M}} \tag{3.137}$$

The two differential Eqs. (3.136) and (3.137) form a system and can be numerically integrated at the same time[¶]. The calculation of $\frac{dr}{\mathrm{d}s}$ is trivial for a given set of values, but the calculation of $\frac{\mathrm{d}v}{\mathrm{d}s}$ is not trivial around the critical point as it cannot be done directly via (3.136). For an easier illustration of the situation around the critical point, it is useful to rewrite (3.136) in the form

$$\frac{\mathrm{d}v}{\mathrm{d}s}\mathcal{G} = -\mathcal{F}. \tag{3.138}$$

At the critical point ($\mathcal{G} \to 0$) the gradient $\frac{\mathrm{d}v}{\mathrm{d}s}$ will approach infinity, unless $\mathcal{F} \to 0$ at the critical point as well. It becomes immediately clear that instead of the direct calculation via

$$\frac{\mathrm{d}v}{\mathrm{d}s} = -\frac{\mathcal{F}}{\mathcal{G}}, \tag{3.139}$$

[¶]For details of the numerical implementation, see Sect. A.6.2 of the appendix.

l'Hospital's rule has to be applied for calculating the derivative around the critical point:

$$\frac{\mathrm{d}v}{\mathrm{d}s} = -\frac{\frac{\mathrm{d}\mathcal{F}}{\mathrm{d}s}}{\frac{\mathrm{d}\mathcal{G}}{\mathrm{d}s}} \tag{3.140}$$

$\mathcal{G}$ is explicitly depending on v, yielding a quadratic equation in $\frac{\mathrm{d}v}{\mathrm{d}s}$:

$$-2\frac{\dot{M}}{4\pi}\frac{a^2}{v^3}\left(\frac{\mathrm{d}v}{\mathrm{d}s}\right)^2 + \left[2\frac{\dot{M}}{4\pi}\frac{1}{v^2}\frac{\mathrm{d}a^2}{\mathrm{d}s} + \frac{\mathrm{d}k}{\mathrm{d}s}\right]\frac{\mathrm{d}v}{\mathrm{d}s} + GM\frac{\mathrm{d}\Gamma}{\mathrm{d}s} + 2\left[r\frac{\mathrm{d}a^2}{\mathrm{d}s} + a^2\frac{\mathrm{d}r}{\mathrm{d}s}\right] + \frac{\dot{M}}{4\pi}\frac{1}{v}\frac{\mathrm{d}^2}{\mathrm{d}s^2}\left(a^2\right) = 0 \tag{3.141}$$

This is an equation of the form

$$A\left(\frac{\mathrm{d}v}{\mathrm{d}s}\right)^2 + B\frac{\mathrm{d}v}{\mathrm{d}s} + C = 0. \tag{3.142}$$

with the following two solutions:

$$\frac{\mathrm{d}v}{\mathrm{d}s}_{1,2} = -\frac{B}{2A} \pm \sqrt{\left(\frac{B}{2A}\right)^2 - \frac{C}{A}} \tag{3.143}$$

$$= -\frac{1}{2A}\left(B \mp \sqrt{B^2 - 4AC}\right) \tag{3.144}$$

In order to have physical (real) solution, the radicand must not be negative. If the root does not vanish, two solutions exist with only one of them leading to a lower velocity with decreasing radius. This is the appropriate solution for a monotonic wind. Furthermore, a strictly monotonic velocity field is also required by the comoving frame radiative transfer scheme as outlined in Sect. 2.8.

3.10.1 The $\mathcal{F}$-$\mathcal{G}$-analysis plot

The definitions introduced in Eq. (3.138) are very handy to simplify equations. Using the expressions for the generalized CAK approach introduced in Sect. 3.8, $\mathcal{F}$ and $\mathcal{G}$ have the following form:

$$\mathcal{F} := GM\left[1 - \Gamma(r)\right] - 2a^2 r + \frac{\dot{M}}{4\pi v}\frac{\mathrm{d}a^2}{\mathrm{d}s} \tag{3.145}$$

$$\mathcal{G} := \left(1 - \frac{a^2}{v^2}\right)\frac{\dot{M}}{4\pi} - k(r) \tag{3.146}$$

These terms will also be used during later sections. Therefore it is useful to write them also without using the column density s defined in Eq. (3.92). Hence, Eq. (3.145) can be written as

$$\mathcal{F} = GM\left[1 - \Gamma(r)\right] - 2a^2 r + r^2\frac{\mathrm{d}a^2}{\mathrm{d}r} \tag{3.147}$$

while Eq. (3.146) does not change. Note that Eq. (3.147) demonstrates that $\mathcal{F}$ does not explicitly depend on either the velocity field $v(r)$, nor the mass-loss rate $\dot{M}$, while $\mathcal{G}$ explicitly depends on both of them.

Although $\mathcal{F}$ and $\mathcal{G}$ are excellent definitions in order to write the hydrodynamic equation in a simple way, they are not really good to illustrate a current stratification, due to their different units and value range. For this purpose it is much more convenient to define dimensionless quantities, namely:

$$\tilde{\mathcal{F}} := \frac{\mathcal{F}}{GM} = 1 - \Gamma(r) - 2\frac{a^2 r}{GM} + \frac{r^2}{GM}\frac{\mathrm{d}a^2}{\mathrm{d}r} \tag{3.148}$$

$$\tilde{\mathcal{G}} := \frac{4\pi\mathcal{G}}{\dot{M}} = 1 - \frac{a^2}{v^2} - \frac{4\pi k(r)}{\dot{M}} \tag{3.149}$$

These definitions are in fact only scalings of $\mathcal{F}$ and $\mathcal{G}$ and therefore do not change the geometry of the solution. Plotting $\tilde{\mathcal{F}}$ and $\tilde{\mathcal{G}}$ therefore provides an excellent graphical diagnostic for analyzing a given atmosphere model. Already from the curves one can see whether a given stellar atmosphere model is a sufficient start approach for calculating a hydrodynamically-consistent, but also monotonic velocity field.

For $\alpha \equiv 0$ and thus $k(r) \equiv 0$, one obtains $\Gamma(r) = \Gamma_{\mathrm{rad}}(r)$ and the equations transform into the general case without any particular parameterization of the radiative acceleration. Nevertheless the hydrodynamic equation can still be written in the form of Eq. (3.139) or, without using the column density s:

$$\frac{\mathrm{d}v}{\mathrm{d}r} = -\rho\frac{\mathcal{F}}{\mathcal{G}} \tag{3.150}$$

with

$$\mathcal{F} = GM\left[1 - \Gamma_{\mathrm{rad}}(r)\right] - 2a^2 r + r^2\frac{\mathrm{d}a^2}{\mathrm{d}r} \tag{3.151}$$

$$\mathcal{G} = \left(1 - \frac{a^2}{v^2}\right)\frac{\dot{M}}{4\pi}. \tag{3.152}$$

The additional ρ-term appears on the right-hand side of Eq. (3.150) when the equation is written for $\frac{\mathrm{d}v}{\mathrm{d}r}$ instead of $\frac{dv}{\mathrm{d}s}$. Due to the equation of continuity (2.1), ρ implicitly contains the mass-loss rate itself, which also enters the denominator $\mathcal{G}$. Using Eq. (2.1), one can further rewrite the hydrodynamic equation in a form that uses the "normalized" quantities:

$$\frac{\mathrm{d}v}{\mathrm{d}r} = -\frac{g}{v}\frac{\tilde{\mathcal{F}}}{\tilde{\mathcal{G}}} \tag{3.153}$$

In this form, the hydrodynamic equation does not have any explicit dependency on the mass-loss rate $\dot{M}$, which will be an important point when discussing solutions without using the generalized CAK approach.

Two examples for $\mathcal{F}$-$\mathcal{G}$-analysis plots are shown in Fig. 3.2. The upper panel shows a B-star model with $Q \approx 1$, using a prescribed velocity law. While the hydrostatic layers have been treated consistently, the total model is not self-consistent. In non-consistent atmosphere models, $\mathcal{F}$ and $\mathcal{G}$ (and thus also $\tilde{\mathcal{F}}$ and $\tilde{\mathcal{G}}$) will usually not vanish at the same radius, although this can rarely happen just by chance. As long as this is not the case, the mass-loss rate and/or the velocity field has to be adjusted. In the calculation approach without using a force multiplier parameter (i.e. $\alpha \equiv 0$) the position of $\mathcal{G} = 0$ marks the sonic point of the current model while $\mathcal{F} = 0$ marks the location of $\Gamma_{\mathrm{rad}} \approx 1$ as the two gas pressure terms are usually (and also in the case shown in Fig. 3.2) very small compared to $1 - \Gamma_{\mathrm{rad}}$. Another example, this time for a model where the approach from Gräfener & Hamann (2005) with force multiplier

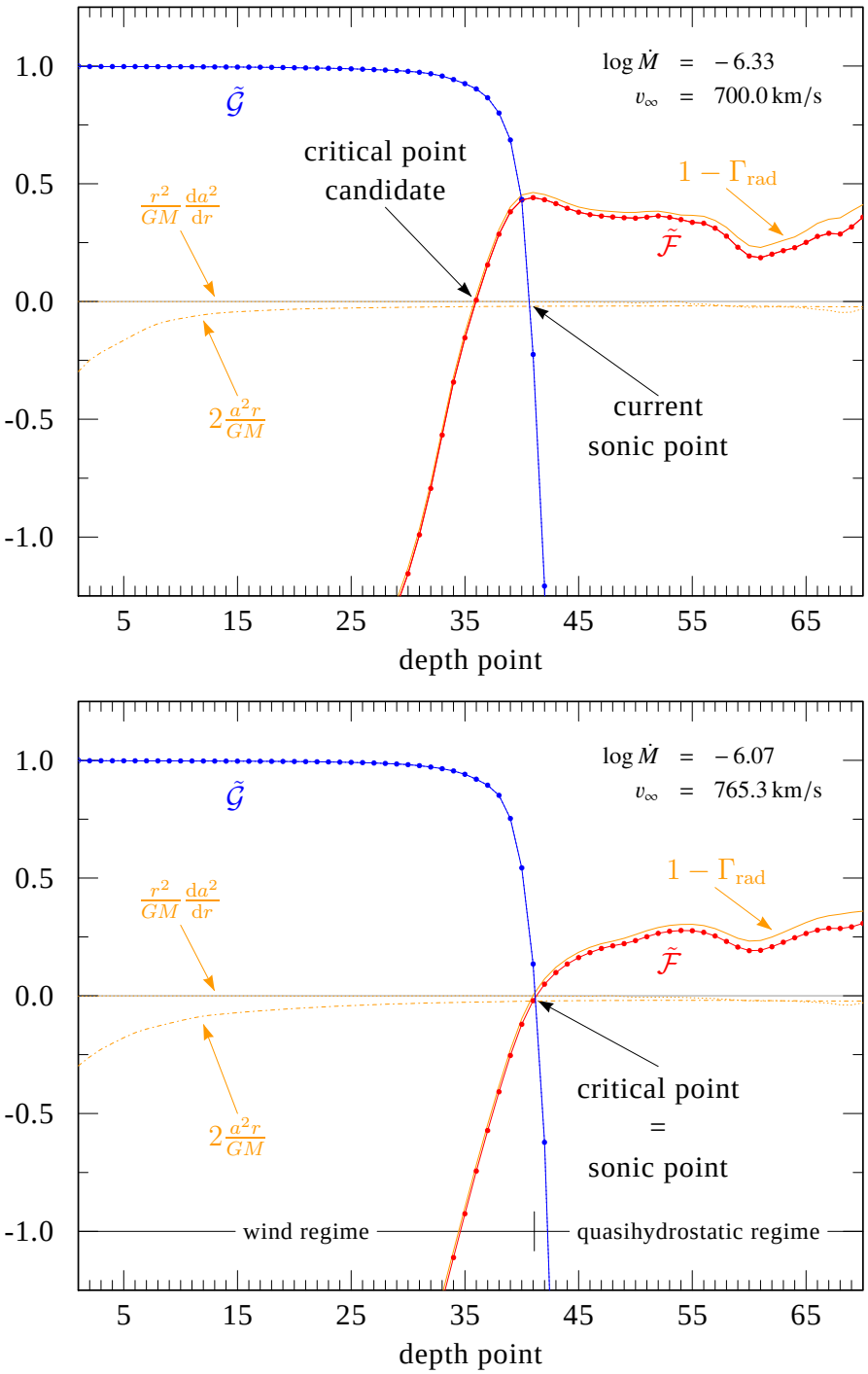

Figure 3.2 – $\mathcal{F}$-$\mathcal{G}$-analysis plots for a model ($T_* = 26\,\mathrm{kK}$) with prescribed wind velocity law (upper panel) and a hydrodynamically-consistent velocity law (lower panel). In both panels, the dimensionless quantities $\tilde{\mathcal{F}}$ (red curve) and $\tilde{\mathcal{G}}$ (blue curve) are shown and have been computed without a force multiplier parameter. For non-consistent models, the locations $r(\mathcal{F} = 0)$ and $r(\mathcal{G} = 0)$ in general do not match. The three contributions of $\tilde{\mathcal{F}}$ are also indicated by yellow curves using different line styles.

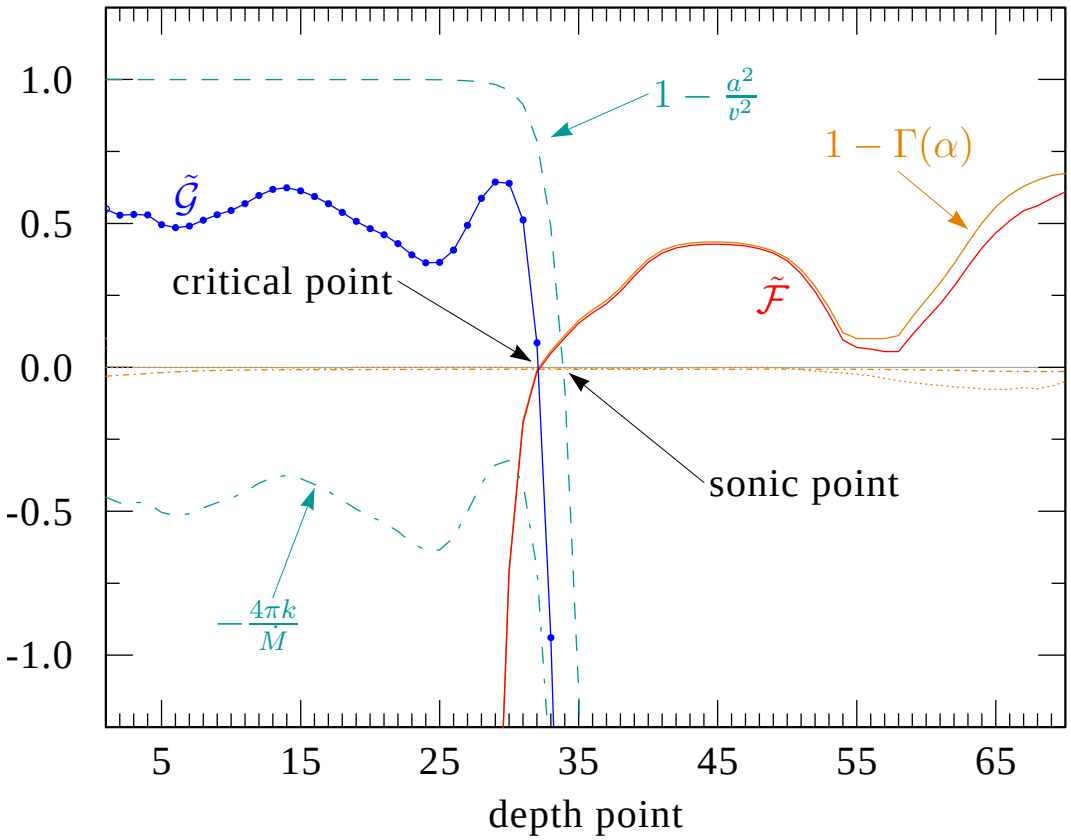

Figure 3.3 – $\mathcal{F}$-$\mathcal{G}$-analysis plot for a hydrodynamically-consistent model ($T_* = 30\,\mathrm{kK}$) where the dimensionless quantities $\tilde{\mathcal{F}}$ (red curve) and $\tilde{\mathcal{G}}$ (blue curve) have been computed using the a_{rad}-description from Gräfener & Hamann (2005) with force multiplier parameters. The colors and line styles are identical to Fig. 3.2 with the additional cyan curves marking the two contributions to $\tilde{\mathcal{G}}$. In the approach of Gräfener & Hamann (2005), $\tilde{\mathcal{F}}$ does not contain the optically thick lines. Instead they enter $\tilde{\mathcal{G}}$ via the k-term.

parameters is used, can be seen in Fig. 3.3. Due to the additional k-term which enters $\mathcal{G}$, the scattering of $\alpha(r)$ demonstrated in the upper panel of Fig. 3.1 propagates into $\tilde{\mathcal{G}}$.

Generally one can say that higher mass-loss rates move the position of $\mathcal{F} = 0$ inwards, while lower values of $\dot{M}$ move the position outwards. However, the complex non-linear reactions in the radiative transfer on the combined changes of $\dot{M}$ and the velocity field after a hydrodynamic update do not allow a more precise trend prediction. In the rare cases when a model with a prescribed velocity law already leads to $\mathcal{F}$ and $\mathcal{G}$ vanishing at the same radius, the mass-loss rate $\dot{M}$ and the velocity at the sonic point do not have to be adjusted, but the overall function $v(r)$ might still have to. To visually check if $v(r)$ is consistent or not, the $\mathcal{F}$-$\mathcal{G}$-analysis plot alone is not sufficient. Instead the acceleration plot (see, e.g., lower panel of Fig. 3.1) is needed. The acceleration plot, however, does not provide a good diagnostic for the solution topology of the current problem. Thus, the $\mathcal{F}$-$\mathcal{G}$-analysis plot and the acceleration plot can be seen as complementary diagnosis tools.

3.10.2 Calculation of the mass-loss rate and the critical point

In the generalized CAK approach the critical point in Eq. (3.136) is not identical to the sonic point, due to the $k(r)$-term in $\mathcal{G}$. This provides an explicit handle to obtain a consistent mass-loss rate. In the original numerical implementation by Gräfener & Hamann (2005), the Eqs. (3.139) and (3.137) were integrated in parallel starting at the outer boundary ($r = R_{\max}, s = 0$). In order to find the critical point, $\mathcal{F}$ and $\mathcal{G}$ were calculated and checked. In the outer regime where the radiative force exceeds gravity we have $\mathcal{F} < 0$. If we are beyond the critical point, there is also $\mathcal{G} > 0$, thus yielding a positive velocity gradient.

As soon as either $\mathcal{F}$ or $\mathcal{G}$ passes through zero, the regime where the critical point has to be searched is entered. For a consistent solution, the locations of $\mathcal{F} = 0$ and $\mathcal{G} = 0$ must be exactly the same. However, this is not automatically fulfilled when calculating a stellar atmosphere model, so during the inward integration one of them will pass through zero first. In order to achieve that both pass through zero at the same location, at least one of the terms has to be adjusted. This is much easier for $\mathcal{G}$, as one can force $\mathcal{G}$ to be zero at a certain location r_{c} or, to be more precise, $r(s_{\mathrm{c}})$, via adjusting the mass-loss rate $\dot{M}$:

$$\mathcal{G} = \left(1 - \frac{a_{\mathrm{c}}^2}{v_{\mathrm{c}}^2}\right) \frac{\dot{M}}{4\pi} - k \stackrel{!}{=} 0 \tag{3.154}$$

$$\Rightarrow \dot{M} = 4\pi k_{\mathrm{c}} \left(1 - \frac{a_{\mathrm{c}}^2}{v_{\mathrm{c}}^2}\right)^{-1} \tag{3.155}$$

The corresponding values at the critical point candidate are denoted $v_{\mathrm{c}} = v(s_{\mathrm{c}})$, k_c, a_c and so on. For a given location with $\mathcal{F} = 0$, it is therefore easy to calculate the corresponding mass-loss rate in order to obtain also $\mathcal{G} = 0$. However, Eq. (3.155) includes the velocity itself and thus depends on the result of the inward integration. This result changes of course when adjusting $\dot{M}$. Therefore, the whole process needs to be iterated. The outward integration is started again with the new mass-loss rate until $\mathcal{F} = \mathcal{G} = 0$ is fulfilled at the same point without any further need for adjusting $\dot{M}$.

The structure of Eq. (3.155) reveals that $k \neq 0$ is required to always have a solution without demanding $v_{\mathrm{c}} = a_{\mathrm{c}}$, i.e. the critical point to be the sonic point. Due to Eq. (3.132), this implies that both α and a_{lines} may not vanish at the critical point. Assuming $\alpha > 0$ and thus $k > 0$, one obtains $v_{\mathrm{c}} > a_{\mathrm{c}}$, i.e. the critical point is located beyond the sonic point, further out in the wind. If the critical point would be identical to the sonic point ($k_{\mathrm{c}} = 0$, $v_{\mathrm{c}} = a_{\mathrm{c}}$), $\mathcal{G}$ vanishes for any value of $\dot{M}$ and no adjustment criterion is available from $\mathcal{G}$.

The whole direct $\dot{M}$ adjustment process from Gräfener & Hamann (2005) works only if $\mathcal{F} = 0$ occurs further outside than $\mathcal{G} = 0$. Otherwise the velocity gradient would be negative, i.e. the resulting velocity field is not monotonic. This in turn would harm the adjustment calculation via Eq. (3.155) and spoil the further iteration process. In such a case, Gräfener & Hamann (2005) simply increase the mass-loss rate by 10% if $\mathcal{G} = 0$ occurs further out than $\mathcal{F} = 0$ for the first time. During later iterations, results from the previous mass-loss rate adjustments are used to provide limits for a slightly more precise adjustment step in this situation.

3.10.3 The terminal velocity and the inner boundary

After the critical point has been found and the mass-loss rate has been fixed, the integration is continued inwards in the approach from Gräfener & Hamann (2005). As they do not integrate directly over r, but instead over s, it is not guaranteed that the innermost value $R_{\rm in} = r(s_{\rm max})$ is identical to R_*. In fact, both cases, $R_{\rm in} > R_*$ as well as $R_{\rm in} < R_*$ can occur. In order to get rid of this discrepancy, the terminal velocity v_∞, which is the starting value of the whole iteration process, is adjusted and the whole iteration process from the outermost point is starting again, including the search for the critical point. This v_∞-adjustment is motivated by the well-known scaling of v_∞ with $v_{\rm esc}$ in the CAK theory. Dividing the required escape speed $v_{\rm esc}(R_*)$ by the value obtained from the current iteration $v_{\rm esc}(R_{\rm in})$, one obtains the following correction factor:

$$\frac{v_{\rm esc}(R_*)}{v_{\rm esc}(R_{\rm in})} = \frac{\sqrt{\frac{2GM}{R_*}}}{\sqrt{\frac{2GM}{R_{\rm in}}}} = \sqrt{\frac{R_{\rm in}}{R_*}} \tag{3.156}$$

In the code implementation, Gräfener & Hamann (2005) use the root of this term, which damps the reaction:

$$f_{v_\infty} = \sqrt[4]{\frac{R_{\rm in}}{R_*}} \tag{3.157}$$

This means that if R_* is not reached by the integration process ($R_{\rm in} > R_*$), the terminal velocity is increased. If the integration instead goes beyond R_*, the terminal velocity is lowered. To avoid major changes between two iterations, f_{v_∞} is limited to a range between 0.9 and 1.1. Note that the change of the (terminal) velocity has a direct impact on the radius integration, due to

$$\frac{{\rm d}r}{{\rm d}s} = \frac{1}{\rho} = 4\pi r^2 v\dot{M}. \tag{3.158}$$

While $\dot{M}$ is adjusted directly by a constraint coming from the hydrodynamic equation, it seems that v_∞ is basically motivated by a boundary effect. In fact the condition $r(s_{\rm max}) = R_*$ is a form of mass and energy conservation as it ensures that the integrated density stratification does not change.

When $R_{\rm in}$ is so close to R_* that the resulting terminal velocity changes are negligible, Gräfener & Hamann (2005) consider the hydro iteration to be converged. The velocity field for all outer points that might not have been considered for the integration regime, are now filled by a monotonic extrapolation of the velocity field using a very small gradient (10 m/s).

3.10.4 Method limitations and restriction of α

Using the approach from Gräfener & Hamann (2005) with force multiplier parameter α can lead to various situations where no monotonic velocity field can be obtained. These situations are not identical to those where the actual physics require a non-monotonic velocity field. The situations discussed in this section instead address those cases, where an approach without using α would work (see Sect. 3.11 for more details) but using the calculation results of α will prevent the calculation of a velocity field.

A typical example of such a situation is illustrated in the lower panel of Fig. 3.4. Although also affected by $\alpha(r)$, the $\tilde{\mathcal{F}}$-term is more or less "well-shaped" as it passes zero only once. In

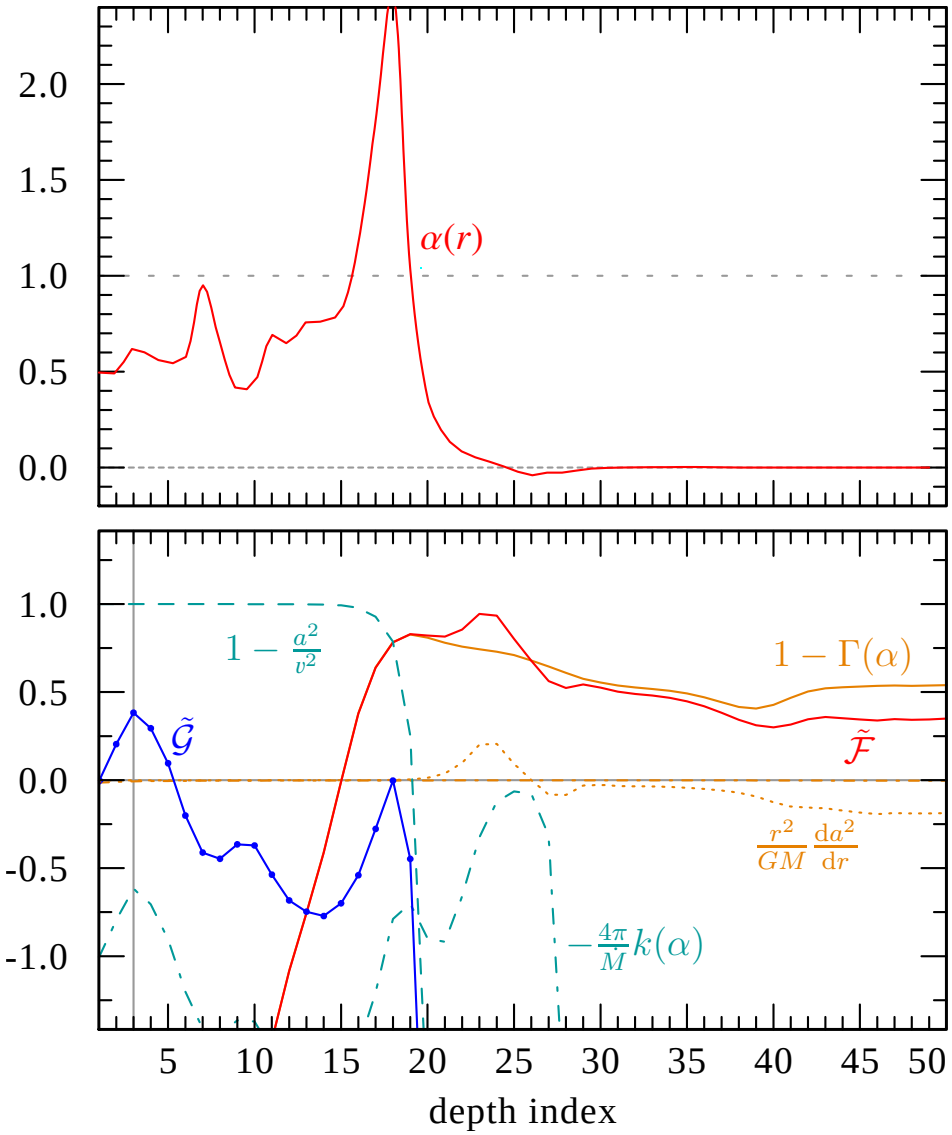

Figure 3.4 – Upper panel: The force multiplier parameter $\alpha(r)$ has been calculated for non-consistent O-star model. In the outer part, $\alpha(r)$ clearly exceeds unity. Before the steep rise, $\alpha(r)$ is negative in a certain depth range.
Lower panel: The dimensionless quantities $\tilde{\mathcal{F}}$ (red curve) and $\tilde{\mathcal{G}}$ (blue curve) including their contributions have been computed for a model with a similar $\alpha(r)$-behavior than illustrated above. Via the k-term, the large variety in $\alpha(r)$ propagates into the $\tilde{\mathcal{G}}$-term which shows negative values even in the supersonic regime. With this behavior of $\tilde{\mathcal{G}}$, no monotonic velocity field can be obtained. Note also that $\tilde{\mathcal{F}}$ exceeds $1-\Gamma$ in the region where the temperature is not monotonic (positive $\frac{\mathrm{d}a^2}{\mathrm{d}r}$ gradient).

contrast, the $\tilde{\mathcal{G}}$-term has a local maximum above (or here very close to) zero, but drops again below in the outer parts, thus making a monotonic solution impossible as $\tilde{\mathcal{F}}$ and $\tilde{\mathcal{G}}$ now have the same sign which in turn leads to a negative velocity gradient. The point in the far outer wind where $\tilde{\mathcal{G}}$ increases significantly above zero is also clearly not a proper candidate for the critical point as it would lead to an extremely low mass-loss rate.

When looking at the structure of

$$\tilde{\mathcal{G}} = \left(1 - \frac{a^2}{v^2}\right) - \frac{4\pi\, k}{\dot{M}}, \tag{3.159}$$

it immediately becomes clear that the k-term is responsible for this troublesome behavior since the first term in parenthesis is monotonic as long as there is a monotonic velocity field is and a monotonic behavior in the sound speed above the sonic point. The latter is guaranteed for a monotonic temperature stratification which can be enforced and the former is also ensured, namely by adjustments during or after the hydro integration and by using a β-law for the starting model. In order to better analyze the situation, the k-term (3.132) is slightly rewritten as

$$k = \alpha r^2 \rho \frac{a_{\rm rad} - a_{\rm cont}}{\frac{{\rm d}v}{{\rm d}r}} \tag{3.160}$$

$$= \frac{\dot{M}}{4\pi} \frac{\alpha}{v} \frac{a_{\rm rad} - a_{\rm cont}}{\frac{{\rm d}v}{{\rm d}r}} \tag{3.161}$$

$$\frac{4\pi\, k}{\dot{M}} = \alpha \frac{a_{\rm rad} - a_{\rm cont}}{a_{\rm mech}} \tag{3.162}$$

In the wind domain, the term in parenthesis in Eq. (3.159) is close to unity due to $v \gg a$, so to ensure $\tilde{\mathcal{G}} > 0$, one basically needs to restrict the k-term such that

$$\frac{4\pi k}{\dot{M}} < 1. \tag{3.163}$$

Applying this restriction to the right-hand side of (3.162) leads directly to a maximum α-value for a given set of accelerations:

$$1 > \alpha \frac{a_{\rm rad} - a_{\rm cont}}{a_{\rm mech}} \tag{3.164}$$

$$\alpha < \frac{a_{\rm mech}}{a_{\rm rad} - a_{\rm cont}} \tag{3.165}$$

One might argue that $a_{\rm mech}$ will be changed during the hydro iteration, but it has to be taken into account that an iterative approach is used here. Thus, the $a_{\rm mech}$ of the velocity field used before the start of a hydro step directly enters the α values and this means that a "bad" start approach can spoil the whole hydro iteration.

The restriction of α allows to find monotonic solutions, but the need for such restrictions already raises the question whether α is a useful quantity. The upper panel of Fig. 3.4 demonstrates that the calculated values of α can exceed the expected range between 0 and 1 significantly. This result strongly questions if the α defined by Gräfener & Hamann (2005) can really be interpreted as the fraction of thick lines. If this is not the case, α will still reflect the reaction of the radiative acceleration to the velocity gradient, but the linearization of the line acceleration term in Sect. 3.8 might not be appropriate.

In short, the approach of Gräfener & Hamann (2005) seems to work only for a small selection of atmosphere models. When trying to extend the method to other parameter ranges, especially those of O and B stars, several problems occur. The most obstacles that prevent the particular calculation of a velocity field can be lifted by introducing restrictions, scalings and dampings of α, but their motivation is purely technical and hard to justify in a physical sense. The fact that the unmodified α-values tend to exceed the expected range raises the need for a different method that does not rely on the interpretation of α as the fraction of thick lines. Such a method, which does not require a force multiplier parameter at all, will be discussed in the following sections and used for all models discussed in the results Chapter 4.

3.11 Solution without force multiplier parameters

In the previously described solution of the hydrodynamic equation of motion, the parameter α was used to split the radiative acceleration into two parts. One of them, the "thin" part, is described similar to how the electron scattering contribution is described in the CAK theory, namely with an Eddington Gamma Γ. The essential idea of the former method is, however, to describe the "thick" part not in the same way, but instead in a linearized CAK-like approach:

$$a_{\text{thick}} = \frac{k(r)}{r^2 \rho} \frac{\mathrm{d}v}{\mathrm{d}r} \tag{3.166}$$

This is motivated by the CAK idea that the radiative pressure intercepted by optically thick lines depends on the velocity gradient. The linearization is needed to obtain an analytic solution for the velocity gradient via

$$\frac{\mathrm{d}v}{\mathrm{d}r} = -\rho \frac{\mathcal{F}}{\mathcal{G}} = -\rho \frac{GM\left[1-\Gamma(r)\right] - 2a^2 r + r^2 \frac{\mathrm{d}a^2}{\mathrm{d}r}}{\left(1-\frac{a^2}{v^2}\right)\frac{\dot{M}}{4\pi} - k(r)}. \tag{3.167}$$

Due to the k-term, the denominator $\mathcal{G}$ does not vanish at the sonic point. Thus, in the case of $\mathcal{F} = 0$ and $\mathcal{G} = 0$, one can obtain the mass-loss rate $\dot{M}$ directly from the condition $\mathcal{G} = 0$ as described in Sect. 3.10.2. However, this requires the calculation of $\alpha(r)$ and a proper split into the two parts. As previously discussed, the calculated range of $\alpha(r)$ is, especially for O stars, not limited to the range [0,1] as it should be in the sense of its interpretation as the fraction of "thick" lines. Furthermore, the reactions of the line acceleration on the velocity gradient changes are not necessarily smooth in the supersonic part, but can show patterns and oscillation-like features. While the calculated values of $\alpha(r)$ might be correct in the sense that they reflect real physics and potentially hint towards instabilities which occur in time-dependent hydrodynamical simulations, the behavior of $\alpha(r)$ spoils the efforts to find a static solution for the wind.

Due to these caveats, it is interesting to consider methods which do not need a CAK-type α parameter. To do this, the previously established formalism does not need to be heavily modified. Instead, all specially defined quantities, i.e. Γ and k, "vanish" if one considers the special case of $\alpha(r) \equiv 0$ (cf. Eqs. 3.111) and yields

$$\mathcal{F} = GM\left[1-\Gamma_{\text{rad}}(r)\right] - 2a^2 r + r^2 \frac{\mathrm{d}a^2}{\mathrm{d}r} \tag{3.168}$$

$$\text{and} \quad \mathcal{G} = \left(1-\frac{a^2}{v^2}\right)\frac{\dot{M}}{4\pi}. \tag{3.169}$$

The Γ in $\mathcal{F}$ is now identical to the full $\Gamma_{\rm rad}$ and $\mathcal{G}$ vanishes at the sonic point ($v = a$). Given the CAK-interpretation of α as the fraction of thick lines, this would be called a "thin wind situation", but in fact the equations above are valid for any wind as they still take the full radiative acceleration $a_{\rm rad}$ into account. They just do not make any assumptions on the description of $a_{\rm rad}$. As a consequence, any effects of $\Gamma_{\rm rad}$ on the velocity gradient are now solely covered in $\mathcal{F}$, but due to the iterative approach, this is still fully consistent. Therefore the equations (3.168) and (3.169) are just a different, mathematically even simpler approach than (3.145) and (3.146).

In the method invoking an α-dependent k-term, the denominator $\mathcal{G}$ could cause troubles due to non-monotonic behavior. Now, as long as the temperature structure is monotonic itself, $\mathcal{G}$ has a monotonic slope and will not cause any trouble when integrating the hydro equation. However, the price for all this is the loss of the predictive power of $\mathcal{G}$ for the mass-loss rate $\dot{M}$. The critical point is now identical to the sonic point and $\mathcal{G}$ vanishes at $v = a$, regardless of the absolute value of $\dot{M}$.

In the α-approach, the mass-loss rate $\dot{M}$ is adjusted such that $\mathcal{G}$ vanishes at the same point where $\mathcal{F} = 0$. Now one cannot adjust the position of $\mathcal{G} = 0$ via $\dot{M}$, but only via changing the velocity to $v = a$ at $r_{\rm c} := r|_{\mathcal{F}=0}$, i.e. the candidate radius for the critical point. Setting $v(r_{\rm c}) = a(r_{\rm c})$ then acts as the starting value for integrating from $r_{\rm c}$ inwards and outwards to obtain $v(r)$, thereby replacing the pure inward integration from Gräfener & Hamann (2005). However, this method does not give any estimate on how to change the mass-loss rate. Does this mean that there is no restriction of $\dot{M}$ and solutions could be found for any mass-loss rate? Or is the non-dependency of the critical point on $\dot{M}$ just an artifact of this approach, where complex dependencies are hidden in $\Gamma_{\rm rad}(r)$ and/or $a(r)$?

This issue will be discussed further in Sect. 5.1. If one assumes for a moment that $\dot{M}$ needs to have a specific value for a given set of stellar parameters, one needs to think of other methods to constrain $\dot{M}$. Three possible methods, which have all been implemented in the PoWR code as part of this work, will be outlined below, followed by a brief discussion of their advantages and disadvantages.

3.11.1 Method 1: Response calculation

In order to get a handle on the mass-loss rate and being able to adjust $r|_{\mathcal{F}=0}$, one can try to estimate the reaction of $\mathcal{F}$ on changes of $\dot{M}$. As long as the radius with $\mathcal{F} = 0$ differs from the current sonic point $r_{\rm S}$ (where $\mathcal{G} = 0$) which is – for a fixed temperature stratification – not depending on the mass-loss rate, one would have to adjust $\mathcal{F}$ in such a way that it vanishes exactly at the sonic point. The second and third term in (3.168) do not react on changes of $\dot{M}$, but the first one does. Luckily, the second and third term are usually much smaller than the first one, so focusing on the changes of $\Gamma_{\rm rad} = a_{\rm rad}/g$ is promising. This leads back to the calculation of the radiative acceleration $a_{\rm rad}$ in the radiative transfer program, which is obtained from frequency integration (in the co-moving frame) of the product of opacity κ_ν

and Eddington flux H_ν:

$$a_{\rm rad} = \frac{1}{\rho}\frac{4\pi}{c}\int_0^\infty \kappa_\nu H_\nu \mathrm{d}\nu \tag{3.170}$$

$$= \frac{r^2 v}{\dot{M}}\frac{16\pi^2}{c}\int_0^\infty \kappa_\nu H_\nu \mathrm{d}\nu \tag{3.171}$$

From (3.171) one could immediately conclude that $a_{\rm rad}$ should roughly scale with the inverse of the mass-loss rate. In detail however, the integral term also changes. This effect is not negligible on the level of accuracy needed to obtain a consistent hydro solution, especially as Eq. (3.170) could also be written with the mass absorption coefficient $\varkappa$ using $\kappa = \varkappa\rho$, leading to the form

$$a_{\rm rad} = \frac{1}{\rho}\frac{4\pi}{c}\int_0^\infty \rho\varkappa_\nu H_\nu \mathrm{d}\nu \tag{3.172}$$

$$= \frac{4\pi}{c}\int_0^\infty \varkappa_\nu H_\nu \mathrm{d}\nu \tag{3.173}$$

which has no explicit dependence on $\dot{M}$ at all.

The effect therefore has to be studied numerically. Similar to the calculation of the α-values, the radiative transfer program is now run twice, once with $\dot{M}$ and another time with a certain change in the mass-loss rate $\lambda\dot{M}$. From (3.171) one would expect to obtain a constant factor λ for the ratio of $a_{\rm rad}(\dot{M})$ and $a_{\rm rad}(\lambda\dot{M})$ if the integral itself would not change at all. On the other hand, if the opacity κ scales with ρ and thus with $\dot{M}$ as expected for optically thin lines, the effect should cancel out and the radiative acceleration would not change at all, assuming that the integral using the mass absorption coefficient in Eq. (3.173) stays constant. As the calculations show, the actual result is in-between those two extremes. To study the effect in more detail it is helpful to define a *response factor*

$$\mathfrak{r}(r) := \frac{a_{\rm rad}(\dot{M})}{\lambda\, a_{\rm rad}(\lambda\dot{M})} \tag{3.174}$$

where the ratio of the accelerations with unmodified and modified $\dot{M}$ is divided by the modification factor λ. Now this factor $\mathfrak{r}$ describes the "non-trivial" change of the radiative acceleration $a_{\rm rad}$ due to changes of $\dot{M}$ while the product $\mathfrak{r}^{-1}\lambda^{-1}$ reflects the relative change of the acceleration with modified $\dot{M}$ compared to the unmodified. With the definition (3.174) one can describe the reaction of $\mathcal{F}$ on a modified mass-loss rate as:

$$\mathcal{F}(\lambda\dot{M}) = GM\left[1 - \Gamma_{\rm rad}(\lambda\dot{M},r)\right] - 2a^2 r + r^2\frac{\mathrm{d}a^2}{\mathrm{d}r} \tag{3.175}$$

$$= GM\left[1 - \frac{\Gamma_{\rm rad}(\dot{M},r)}{\lambda\cdot\mathfrak{r}(r)}\right] - 2a^2 r + r^2\frac{\mathrm{d}a^2}{\mathrm{d}r} \tag{3.176}$$

Of course λ shall now be adjusted such that $\mathcal{F}$ vanishes at the sonic point r_S. The corresponding calculation is straightforward:

$$0 \stackrel{!}{=} GM \left[1 - \frac{\Gamma_\mathrm{rad}(r_\mathrm{s})}{\lambda \cdot \mathfrak{t}(r_\mathrm{s})}\right] - 2a^2 r_\mathrm{s} + r_\mathrm{s}^2 \left.\frac{\mathrm{d}a^2}{\mathrm{d}r}\right|_{r=r_\mathrm{s}} \tag{3.177}$$

$$\frac{\Gamma_\mathrm{rad}(r_\mathrm{s})}{\lambda \cdot \mathfrak{t}(r_\mathrm{s})} = 1 - \frac{1}{GM}\left(2a^2 r_\mathrm{s} - r_\mathrm{s}^2 \left.\frac{\mathrm{d}a^2}{\mathrm{d}r}\right|_{r=r_\mathrm{s}}\right) \tag{3.178}$$

$$\lambda = \frac{\Gamma_\mathrm{rad}(r_\mathrm{s})}{\mathfrak{t}(r_\mathrm{s})}\left[1 - \frac{1}{GM}\left(2a^2 r_\mathrm{s} - r_\mathrm{s}^2 \left.\frac{\mathrm{d}a^2}{\mathrm{d}r}\right|_{r=r_\mathrm{s}}\right)\right]^{-1} \tag{3.179}$$

Unfortunately test calculations reveal that the term (3.174) is still not independent of λ, as illustrated in the lower panel of Fig. 3.5. This is a problem as the response factor has to be calculated in advance during the CMF radiative transfer and at this point the mass-loss rate modification factor λ obtained in the hydro routine is not known. Comparing the results for different values of λ one can identify a certain trend in the changes of $\mathfrak{t}$ with λ as it seems that the overall slope does only marginally change. It turns out that one can find a scaling relation between the response factors obtained with different values of λ:

$$\mathfrak{t}(r,\lambda) = 1 - [1 - \mathfrak{t}_\mathrm{calc}(r)]\,\frac{\lambda - 1}{\lambda_\mathrm{calc} - 1} \tag{3.180}$$

Here, λ_calc is the value for which the response factor $\mathfrak{t}_\mathrm{calc}$ has be calculated in the radiative transfer program while λ denotes the value required in the hydro iteration. Using this relation, the response factors obtained with different values of λ can be scaled, so that they are in rough agreement, as illustrated in the upper panel of Fig. 3.6

Although the calculation of the response factor $\mathfrak{t}$ intuitively might show similarities to depth-dependent α-parameter (cf. Sect. 3.9) since both require the radiative transfer to be performed twice, they actually trace different things. The α-parameter is based on a modification of the velocity and its gradient and is only calculated from the resulting changes of the line acceleration. The $\mathfrak{t}$ instead reflects reactions of a global density change due to a slightly different mass-loss rate $\dot{M}$. The resulting stratification of $\alpha(r)$ and $\mathfrak{t}(r)$ are therefore quite different, as illustrated in Fig. 3.7.

As the value of the response factor $\mathfrak{t}$ depends on λ, one cannot really use (3.179) to calculate the starting value of λ for the hydro iteration. Instead we need to take (3.180) into account and solve the following equation, which is quadratic in λ:

$$\lambda \cdot \mathfrak{t}(r_\mathrm{s},\lambda) = X_\Gamma := \Gamma_\mathrm{rad}\left[1 - \frac{1}{GM}\left(2a^2 r_\mathrm{s} - r_\mathrm{s}^2 \left.\frac{\mathrm{d}a^2}{\mathrm{d}r}\right|_{r=r_\mathrm{s}}\right)\right]^{-1} \tag{3.181}$$

$$\lambda - \left[\lambda^2 - \lambda\right]\frac{1 - \mathfrak{t}_\mathrm{calc}(r_\mathrm{s})}{\lambda_\mathrm{calc} - 1} = X_\Gamma \tag{3.182}$$

$$0 = \lambda^2 - \left(\frac{\lambda_\mathrm{calc} - 1}{1 - \mathfrak{t}_\mathrm{calc}(r_\mathrm{s})} + 1\right)\lambda + \frac{\lambda_\mathrm{calc} - 1}{1 - \mathfrak{t}_\mathrm{calc}(r_\mathrm{s})} X_\Gamma \tag{3.183}$$

The two solutions are:

$$\lambda_{1,2} = \frac{1}{2}\left(\frac{\lambda_\mathrm{calc} - 1}{1 - \mathfrak{t}_\mathrm{calc}(r_\mathrm{s})} + 1\right) \pm \sqrt{\frac{1}{4}\left(\frac{\lambda_\mathrm{calc} - 1}{1 - \mathfrak{t}_\mathrm{calc}(r_\mathrm{s})} + 1\right)^2 - \frac{\lambda_\mathrm{calc} - 1}{1 - \mathfrak{t}_\mathrm{calc}(r_\mathrm{s})} X_\Gamma} \tag{3.184}$$

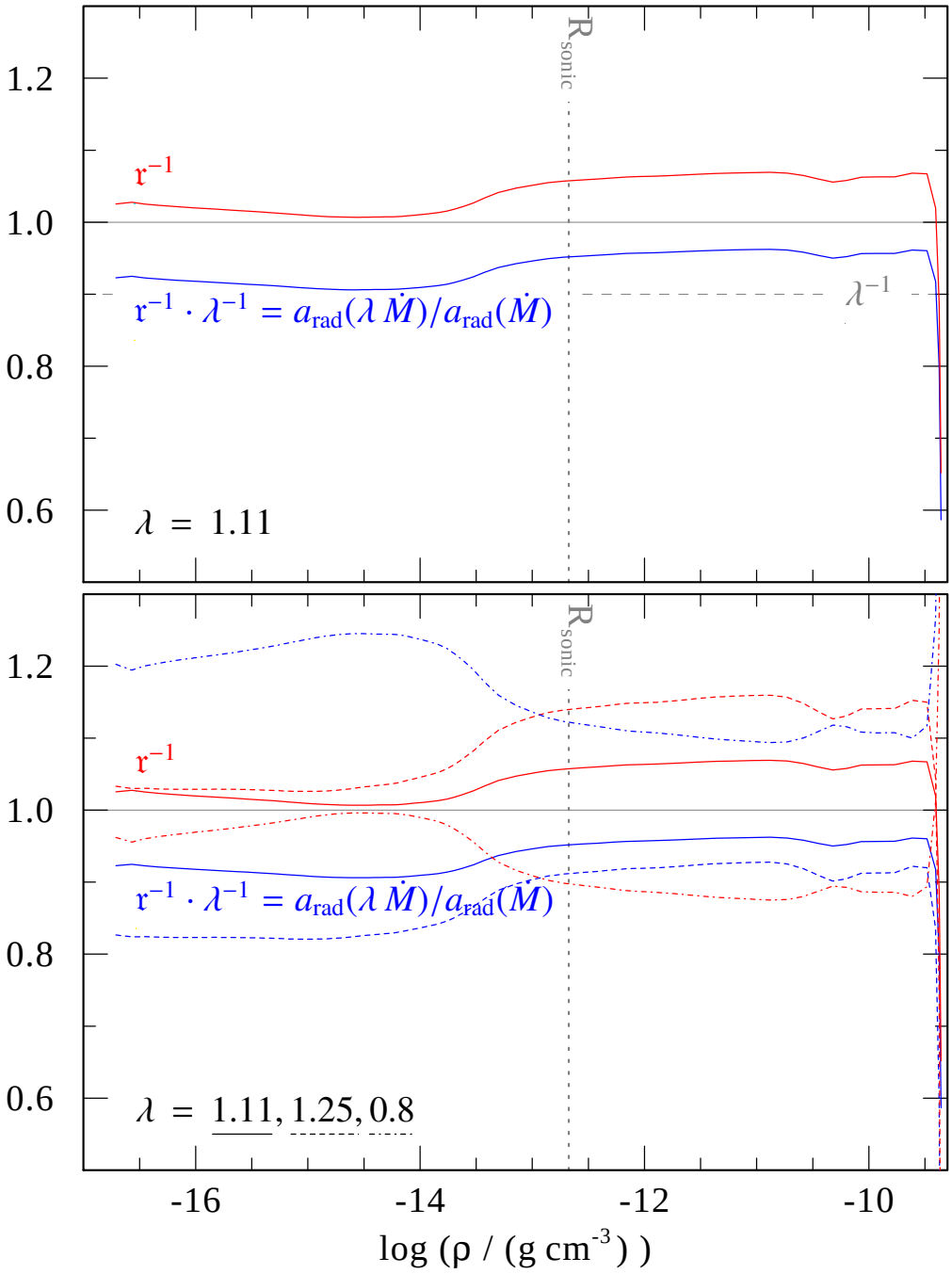

Figure 3.5 – Response of the radiative acceleration $a_{\rm rad}$ to a change of the mass-loss rate $\dot{M}$: In the upper panel, the inverse of the response factor $\mathfrak{r}$ is shown in red while the direct ratio of the modified and the unmodified radiative acceleration is shown in blue. In the lower panel, the same results are plotted using different values for the $\dot{M}$-modification factor λ. The steep drop at the innermost point is artitificial and due to the numerical calculation method of $\mathfrak{r}$.

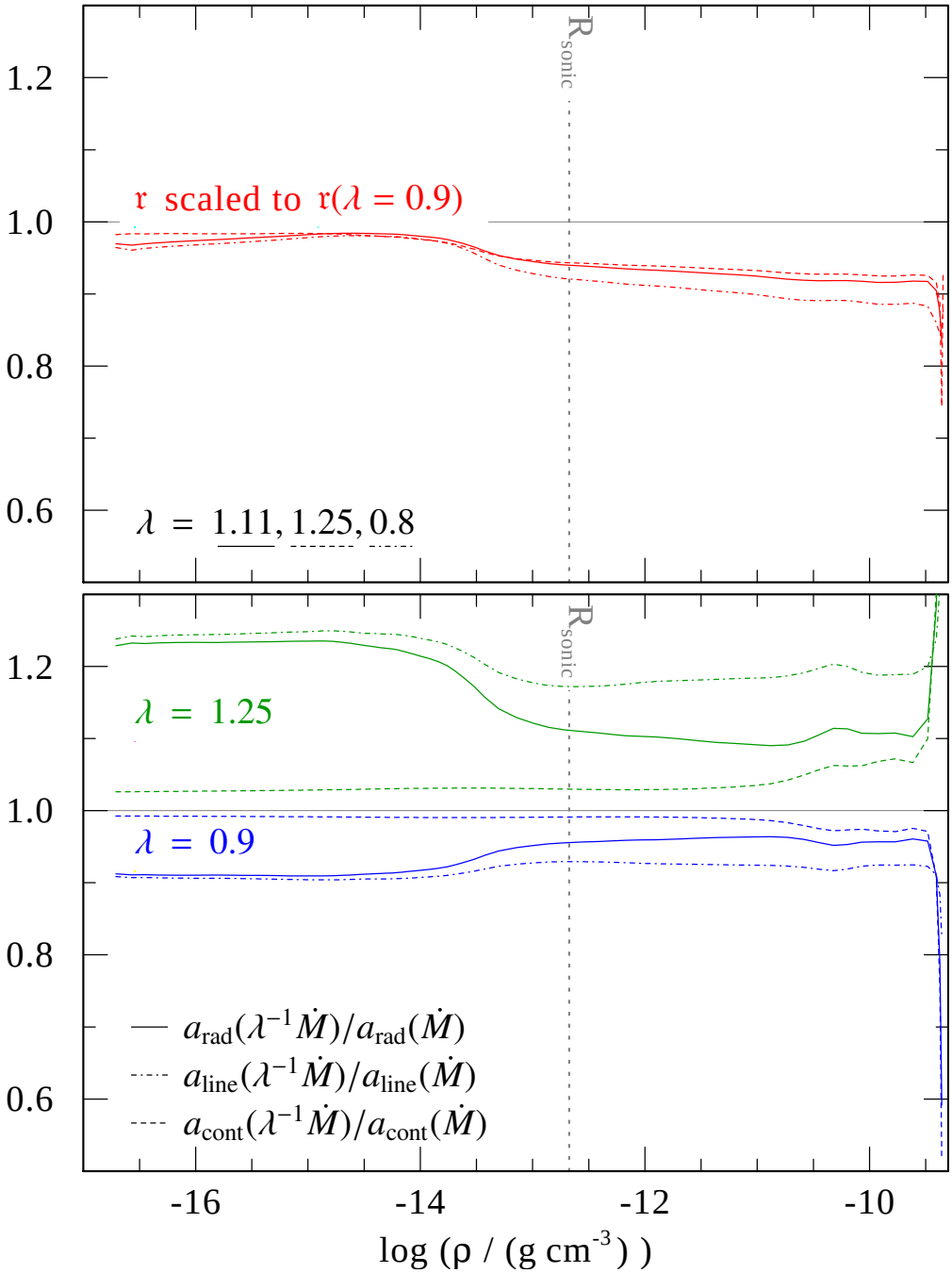

Figure 3.6 – Upper panel: Response factor $\mathfrak{r}$, scaled to $\lambda = 0.9$ using the relation (3.180). Although the values do not match exactly, the slope and the range of obtained values are sufficient enough to allow the use of a precalculated response factor.
Lower panel: The total response of the radiative acceleration for two different modification factors is compared to their contributions from the line and continuum acceleration. The plot reveals that apart from the innermost layers the continuum acceleration only marginally reacts on the density change due to the mass-loss rate adjustment while the line acceleration shows a significant reaction, especially in the wind part where the reaction approaches the inverse of the modification factor.

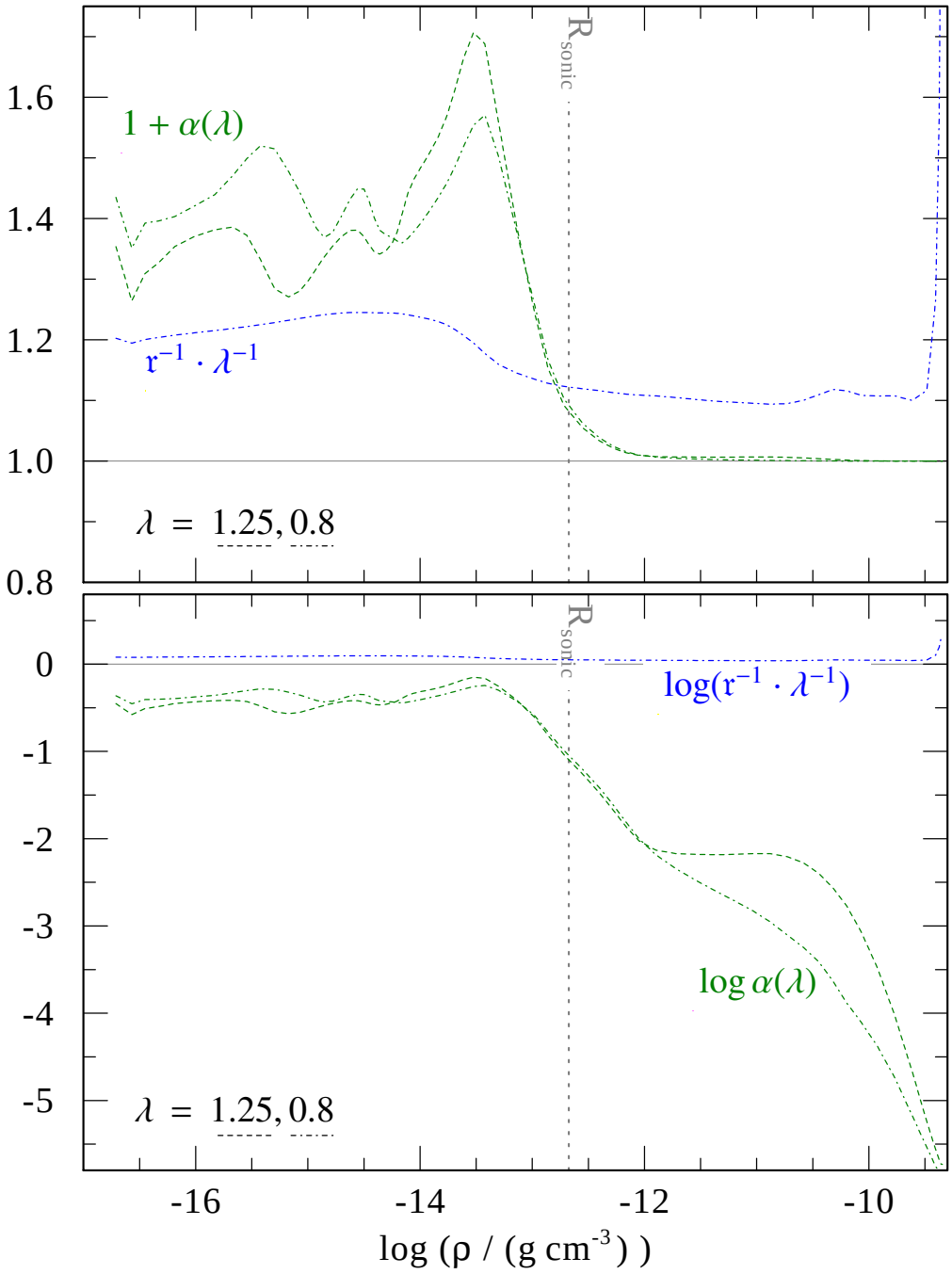

Figure 3.7 – Upper panel: The slope of the density modification (equal to $\mathfrak{r}^{-1}\lambda^{-1}$) is compared to the slope of the α-parameter defined in Sect. 3.8 for two different modification factors. The α-parameter, which reflects only velocity field changes in the line acceleration, shows much more substructure in the wind than the response factor, which in contrast reflects density changes in the total radiative acceleration.
Lower panel: The same quantities are shown on a logarithmic scale, highlighting the very different behavior in the inner part of both quantities.

From these two solutions, only one leads to a change in $\dot{M}$ pointing in the same direction as the simple approach in Eq. (3.179), where the λ-dependence on $\mathfrak{r}$ is neglected. This solution is the appropriate one to obtain the modified

$$\Gamma_{\rm rad}(\lambda\dot{M},r) = \frac{\Gamma_{\rm rad}(\dot{M},r)}{\lambda \cdot \mathfrak{r}(r,\lambda)} \tag{3.185}$$

which then allows to calculate the adjusted $\mathcal{F}(r)$.

This response calculation allows the choice of other values as candidates for the sonic point apart from $r(\mathcal{F}=0)$ by changing the mass-loss rate. It is even possible to use the present sonic point $r(\mathcal{G}=0)$ and adjust $\dot{M}$ in a way that this point is met. However, the response factor $\mathfrak{r}$ has to be calculated with a modified density during the radiative transfer, basically doubling the computing time. Given these high costs, especially for OB star models where lower values of $v_{\rm dop}$ are required, the result is not outstanding as the response scaling is good, but by far not excellent and usually significant damping is required during early hydro iterations where the model is still far from hydrodynamically consistency.

In summary the method has high costs combined with mediocre results, raising the question if there are simpler methods to adjust the mass-loss rate. Such methods are presented in the following sections.

3.11.2 Method 2: Work ratio adjustment

Instead of considering the precise, depth-dependent reaction of $a_{\rm rad}$ on changes of $\dot{M}$ and $v(r)$, one could think of a simpler adjustment of $\dot{M}$ based on radius-integrated values, i.e. considering the work ratio Q defined in Sect. 3.2. It is usually well justified to assume that the velocity at the inner boundary $v_{\rm min}$ is orders of magnitude smaller than the terminal velocity v_∞. With $v_{\rm min}^2 \ll v_\infty^2$, Eq. (3.26) simplifies to

$$\frac{1}{2}v_\infty^2 + \frac{GM}{R_*} = \int_{R_*}^{\infty} a_{\rm rad}(r)\,{\rm d}r - \int_{R_*}^{\infty} \frac{1}{\rho}\frac{{\rm d}P}{{\rm d}r}{\rm d}r. \tag{3.186}$$

All of these terms, including the second integral on the right-hand side over the gas pressure terms, can be immediately calculated after the integration of the hydrodynamic equation, even if $\dot{M}$ has been modified, except for the reaction of the first integral on the right. The previous discussion of the response factor $\mathfrak{r}(r)$ showed that this reaction is not constant at all radii, thus requiring a CMF test calculation to obtain $\mathfrak{r}(r)$ each time before solving the hydrodynamic equation. This is a large effort for eventually just updating the depth-independent value of $\dot{M}$. As further iterations after one hydro step are needed anyhow, a simpler method indicating the trend of $\dot{M}$ should do the work as well. This simpler way is using the radius-integrated quantities in the form of Eq. (3.186), rather than bothering with depth-dependent quantities.

In order to estimate the reaction of $a_{\rm rad}$ on changes of $\dot{M}$ and $v(r)$, the test-calculations for $\mathfrak{r}$ turn out to be useful, but now focusing on the radius-integrated results. In the outer regime, i.e. in the wind, the calculations revealed that if $\dot{M}$ is modified by a factor μ, the radiative line acceleration changes approximately by a factor μ^{-1} while the change to the continuum acceleration is small (see also the lower panel in Fig. 3.6). The wind part dominates the

integral, and hence one can write

$$\int_{R_*}^{\infty} a_{\rm rad}(\mu\dot{M})\,{\rm d}r \approx \frac{1}{\mu}\int_{R_*}^{\infty} a_{\rm line}(\dot{M})\,{\rm d}r + \int_{R_*}^{\infty} a_{\rm cont}(\dot{M})\,{\rm d}r. \tag{3.187}$$

This result is actually not trivial as one would expect that in a first order approximation $a_{\rm rad}$ would not react to changes of $\dot{M}$ at all, especially in an optically thin regime. The numerical test calculations have revealed that this is only the case for the continuum contribution while the reaction of the line acceleration mathematically corresponds to an optical thick situation where the opacity is no longer depending on the density. Note that CAK would predict

$$a_{\rm line}(\mu\dot{M}) = a_{\rm line}(\dot{M}) \cdot \mu^{-\alpha_{\rm CAK}} \tag{3.188}$$

with $\alpha_{\rm CAK} \approx 0.6$, i.e. the test calculations show a much steeper reaction, at least for the radius-integrated line acceleration. For Wolf-Rayet stars where CAK is not appropriate this result is not surprising, but it is also seen in the model for a B-star with $T_* = 26\,{\rm kK}$ where one would expect a good agreement with CAK. The response calculations shown in the Figs. 3.5 to 3.7, which have been performed with a hydrodynamically consistent B-star model, instead point to a steeper relation and therefore show already deviations from the original, unmodified CAK prediction.

Using the results from the test calculation, the modification of the mass-loss rate by a factor μ changes Eq. (3.186) to

$$\frac{1}{2}v_\infty^2 + \frac{GM}{R_*} = \frac{1}{\mu}\int_{R_*}^{\infty} a_{\rm line}(r)\,{\rm d}r + \int_{R_*}^{\infty} a_{\rm cont}(r)\,{\rm d}r - \int_{R_*}^{\infty} \frac{1}{\rho}\frac{{\rm d}P}{{\rm d}r}{\rm d}r. \tag{3.189}$$

On the other hand this means, that if there is a velocity field $v(r)$ obtained by solving the hydrodynamic equation, Eq. (3.189) can be used to obtain the mass-loss rate adjustment factor μ that is required to ensure that the solution will also fulfill $Q = 1$, i.e. the energy balance[‖]. Re-arranging the equation leads to

$$\mu = \frac{\int_{R_*}^{\infty} a_{\rm line}(r)\,{\rm d}r}{\frac{1}{2}v_\infty^2 + \frac{GM}{R_*} + \int_{R_*}^{\infty} \frac{1}{\rho}\frac{{\rm d}P}{{\rm d}r}{\rm d}r - \int_{R_*}^{\infty} a_{\rm cont}(r)\,{\rm d}r}, \tag{3.190}$$

providing an easy recipe to calculate the adjustment factor for $\dot{M}$. In fact, Eq. (3.190) works best, if the velocity v_∞ changes only marginally as the reaction of $v(r)$ has not been considered so far. Test calculation show that applying a modification factor to the velocity field leads to the inverse reaction compared than changing $\dot{M}$, following basically from $\rho \propto v/\dot{M}$. In fact, the reaction is even a bit stronger as changing the velocity in a comoving-frame calculation affects more terms than just the density. Nevertheless, in an iterative approach it is sufficient to assume

$$\int_{R_*}^{\infty} a_{\rm rad}(\lambda v)\,{\rm d}r \approx \lambda\int_{R_*}^{\infty} a_{\rm line}(v)\,{\rm d}r + \int_{R_*}^{\infty} a_{\rm cont}(v)\,{\rm d}r. \tag{3.191}$$

[‖] As Eq. (3.186) stems from the integration of the hydrodynamic equation, it might seem strange that $Q = 1$ is no longer guaranteed, but this is a consequence of waiving any adjustments of $a_{\rm rad}$ during the $v(r)$-calculation, even when changing $\dot{M}$.

and adjust the mass-loss rate via

$$\dot{M}_{\rm new} = \mu \cdot \lambda \cdot \dot{M}_{\rm old}. \tag{3.192}$$

In the code implementation this is iterated until the current work ratio

$$Q_{\rm cur} := \frac{\frac{\dot{M}_{\rm start}}{\dot{M}_{\rm new}} \int\limits_{R_*}^{\infty} a_{\rm line}(r)\,{\rm d}r + \int\limits_{R_*}^{\infty} a_{\rm cont}(r)\,{\rm d}r - \int\limits_{R_*}^{\infty} \frac{1}{\rho}\frac{{\rm d}P}{{\rm d}r}{\rm d}r}{\frac{1}{2}v_\infty^2 + \frac{GM}{R_*}} \tag{3.193}$$

is equal to unity with an accuracy better than one percent.

3.11.3 Method 3: Conservation of optical depth

Another approach to obtain a correction for the mass-loss rate $\dot{M}$ that appears to be completely different at first is to use the conservation of the optical depth. This method (and its success) can be understood as a generalization of the s-conservation in Gräfener & Hamann (2005). By enforcing $r(s_{\rm max}) = R_*$ the total value of

$$s_{\rm max} = \int\limits_{R_{\rm max}}^{R_*} \rho(r)\ {\rm d}r \tag{3.194}$$

was conserved. In their paper, $s_{\rm max}$ was labeled τ_* as they referred to it as "optical depth". Instead of s, which does not include the mass absorption coefficient $\varkappa$, now the true maximum (Rosseland continuum) optical depth

$$\tau_{\rm max} = \int\limits_{R_{\rm max}}^{R_*} \varkappa(r)\rho(r)\ {\rm d}r \tag{3.195}$$

is conserved. In order to demonstrate that this quantity could actually give an estimate on how to adjust $\dot{M}$, it is useful to write it down it its precise form. The intended value of $\tau_{\rm max}$ is actually given at the start of an atmosphere model. As discussed in detail in Sect. 2.7, this value should reflect the Rosseland continuum optical depth at the inner boundary R_*. To check whether this value is really reached there, the current value at the innermost depth point has to be calculated via

$$\tau_* := \tau_{\rm Ross,cont}(R_*) = \int\limits_{R_{\rm max}}^{R_*} \kappa_{\rm Ross,cont}(r)\,{\rm d}r \tag{3.196}$$

$$= \int\limits_{R_{\rm max}}^{R_*} \rho(r)\ \varkappa_{\rm Ross,cont}(r)\,{\rm d}r \tag{3.197}$$

$$= \frac{\dot{M}}{4\pi} \int\limits_{R_{\rm max}}^{R_*} \frac{\varkappa_{\rm Ross,cont}(r)}{r^2\ v(r)}{\rm d}r. \tag{3.198}$$

It is important to remember the relatively weak response of $a_{\rm cont}$ on changes of $\dot{M}$ from the previous section. From this information one can conclude that the mass absorption coefficient $\varkappa(r)$ should approximately stay the same when the mass-loss rate is changed and thus the whole integral in Eq. (3.198) should not change significantly if the change to the velocity field $v(r)$ is small. As a first approximation we can therefore conclude that the value τ_* is roughly proportional to $\dot{M}$. In fact these are way too much rough approximations to obtain a good handle on the value of $\dot{M}$, but it turns out that at least the trend is correct, i.e. τ_* gets larger with increasing $\dot{M}$. Test calculations have shown that the trend predicted by the conservation of $\tau_{\rm max}$ is very similar to the results obtained by conserving $s_{\rm max}$.

As $\tau_{\rm max}$ should be conserved in all PoWR models, the implementation of this method therefore does not use any scaling relations, but calculates the current value of $\tau_\star$ by evaluating the integral including the calculation of the continuum opacities, similar to what is discussed in Sect. 2.7. For $\tau_* < \tau_{\rm max}$, the mass-loss rate is increased, otherwise it is decreased. Afterwards the whole integration of the hydrodynamic equation is performed again, until $|\tau_* - \tau_{\rm max}| < \varepsilon_\tau$ with a pre-specified accuracy ε_τ. In order to avoid oscillations, the changes to $\dot{M}$ are reduced each time the trend changes.

Even though the calculation of τ_* is precise, the conservation of the optical depth does not give a very good prediction for the "true" $\dot{M}$, corresponding to a hydrodynamic solution. This has to do with the fact that the estimate for $\dot{M}$ does not stem from the hydrodynamic equation itself or its integrated form, but instead is based on a kind of boundary condition. Using it without any damping can therefore lead to overshootings on the order of magnitudes in either direction and should be avoided completely. However, the $\tau_{\rm max}$-adjustment has proven to work very decently when combined with $\Gamma_{\rm rad}$-input damping for the integration of the hydrostatic equation. Indeed, using a similar $\Gamma_{\rm rad}$-input damping, including a start value for $\Gamma_{\rm rad}$ inferred from the current velocity field in the very first hydro step, leads to promising results and successfully converging hydro models. The strong input damping and the internal adjustment of the velocity field to ensure $\tau_{\rm max}$ furthermore removes the need for an output damping of the calculated velocity field and the otherwise necessary post-hydro $\tau_{\rm max}$-adjustment of $v(r)$. (Details for the latter methods are described in Sect. A.8 of the appendix.)

The idea behind this concept is in fact not very new. An inward and outward integration from the critical point with a conservation of optical depth has been used by Pauldrach et al. (1986) in order to compare CMF calculations with a modified CAK approach. However, Pauldrach et al. (1986) used a fixed value of the Thomson optical depth $\tau_{\rm thom} := \int \kappa_{\rm e} {\rm d}r$ instead of the Rosseland continuum optical depth used in this work. Furthermore, Pauldrach et al. (1986) used several simplifications, e.g. for the line strengths, the radiative acceleration, and the approximation of the continuum in order to keep his approach identical to his mCAK calculations. The concept idea of using the conservation of the optical depth to constrain $\dot{M}$ was later also picked up by Vink et al. (1999) for their Monte Carlo calculations.

Instead of conserving $\tau_{\rm max}$ or $s_{\rm max}$, one could also think of conserving the total mass of the stellar atmosphere

$$M_{\rm atm} = 4\pi \int_{R_*}^{R_{\rm max}} \rho(r) r^2 {\rm d}r = \dot{M} \int_{R_*}^{R_{\rm max}} \frac{1}{v(r)} {\rm d}r. \tag{3.199}$$

This approach yields a similar trend than the $s_{\rm max}$-conservation, but puts more weight on the outer wind layers due to the additional r^2-factor in the integral. The resulting predictions for $\dot{M}$ can therefore be a bit smaller, but in general the method shows the same weaknesses as

the normal $\tau_{\max}$-conservation, i.e. it predicts changes of many orders of magnitude if the new critical point found in the hydro calculations is far away from the current one.

3.11.4 Selection of the proper method

Given the three different methods described above, there is of course the question which method is the best one to choose? Even after the various calculations which have been performed with the various methods, there is no general answer to this question. Although the calculation times could be significantly reduced compared to the approach of Gräfener & Hamann (2005), who needed about a month to get a converged, hydrodynamically-consistent model, the models still need much longer calculation times if compared to a model with a prescribed wind velocity field. The change of the velocity field is another correction added on top of the corrections for the population numbers and the temperature. All of these three are coupled to the results of the radiative transfer calculations, thus forming an extremely tricky situation.

As none of the three methods provides a really precise prediction of the mass-loss rate $\dot{M}$, the explicit calculation of the response factor is not favorable. From the two other methods, the "work ratio adjustment" (Q-method) and the "conservation of optical depth" (τ-method), the Q-method turned out to be the safer choice, while the τ-method is more effective, if the changes to $\dot{M}$ are small enough. In the Q-method, the adjustments to $\dot{M}$ are usually moderate if starting from a model with $Q \approx 1$, but the conservation of $\tau_{\max}$ is not ensured by default and therefore the velocity field has to be shifted afterwards (see appendix Sect. A.8.2 for details). In the τ-method, this is automatically fulfilled without any further adjustment of the velocity field obtained from the hydrodynamic equation. Therefore, the region around the critical point is usually consistent after very few iterations when using this method. In the Q-method the necessary shifting instead causes differences between the "raw" hydrodynamical solution for $v(r_{\mathrm{c}})$ and the value actually used. As the region around the critical point is crucial, this causes some perturbation leading to larger corrections in the following calculations for the radiative transfer and the solution of the statistical equations.

The τ-method, however, can react with drastic changes of $\dot{M}$, if the location of the critical point changes. This has already been noted by Pauldrach et al. (1986) who used a more or less similar approach, but conserving the Thomson optical depth instead of the Rosseland continuum optical depth. Test calculations with conservation $\tau_{\max,\mathrm{Thom}}$ have shown that the large reactions do not depend on the choice of the τ-scale, but seem to be inherent to the method.

Given these advantages and disadvantages, the Q-method has become "standard" choice for calculating hydrodynamically consistent models. However, if the starting model does not only have $Q \approx 1$, but also the acceleration plot shows that the model is not far from depth-dependent consistency, the τ-method can be tested and will be the better choice if not leading to large changes of $\dot{M}$.

The detailed implementations, including the necessary dampings are discussed in detail in the Sects. A.7 to A.9 of the appendix.

Chapter 4

Hydrodynamic models: Applications and limitations

4.1 Selecting proper starting models

Although PoWR models can be calculated without requiring an old model as a start approach, the calculation of a selfconsistent velocity law demands that the full radiative acceleration is known. This is only possible after a radiative transfer calculation in the comoving frame (CMF). For the CMF calculations the density and velocity stratification must be known and thus a starting approximation for $v(r)$ is required in any case. Although the hydro calculations described in the previous chapter can in principle be performed on any start approximation, it is not guaranteed that there will be a monotonic hydrodynamic solution for any situation.

It is therfore helpful to start from an old model, which is not hydrodynamically consistent, but where the radiative acceleration is known. If the option to calculate in the inner part of $v(r)$ via integrating the hydrostatic equation using the $\Gamma_{\rm rad}$ from the CMF calculations (see Sect. 3.4) had been used in the old model, most of the subsonic part might already be consistent. In any case, the work ratio Q (cf. Sect. 3.2) of a former model provides an easy criterion to select "good" candidate models for starting the calculation of a hydrodynamically-consistent model.

Models with $Q \approx 1$ are already balanced in terms of their global energy budget, i.e. the integrated sum of radiation and gas pressure are sufficient to drive approximately the predicted wind with the parameters v_∞ and $\dot{M}$. As one can see on the left-hand side of Eq. (3.26), the denominator of Q depends only on R_*, M_* and the boundary values v_∞ and $v_{\rm min}$. Due to $v_\infty \gg v_{\rm min}$ the latter one is also not important. Thus, the actual slope of the velocity field or the density stratification is not important and the denominator of Q should stay constant as long as the value of v_∞ remains the same.

How the nominator of Q, which contains the radiation and gas pressure terms, is affected when changing the form of $v(r)$, cannot be predicted intuitively. In order to understand the reaction of the gas pressure term, it is useful to write it in the form of Eq. (3.19), i.e. containing the explicit velocity field. The second and third term of Eq. (3.19) depend only on $a(r)$ and thus the temperature (and, if used, the turbulent velocity) but not the wind velocity. Thus the only term that should be affected if we assume that the temperature structure remains

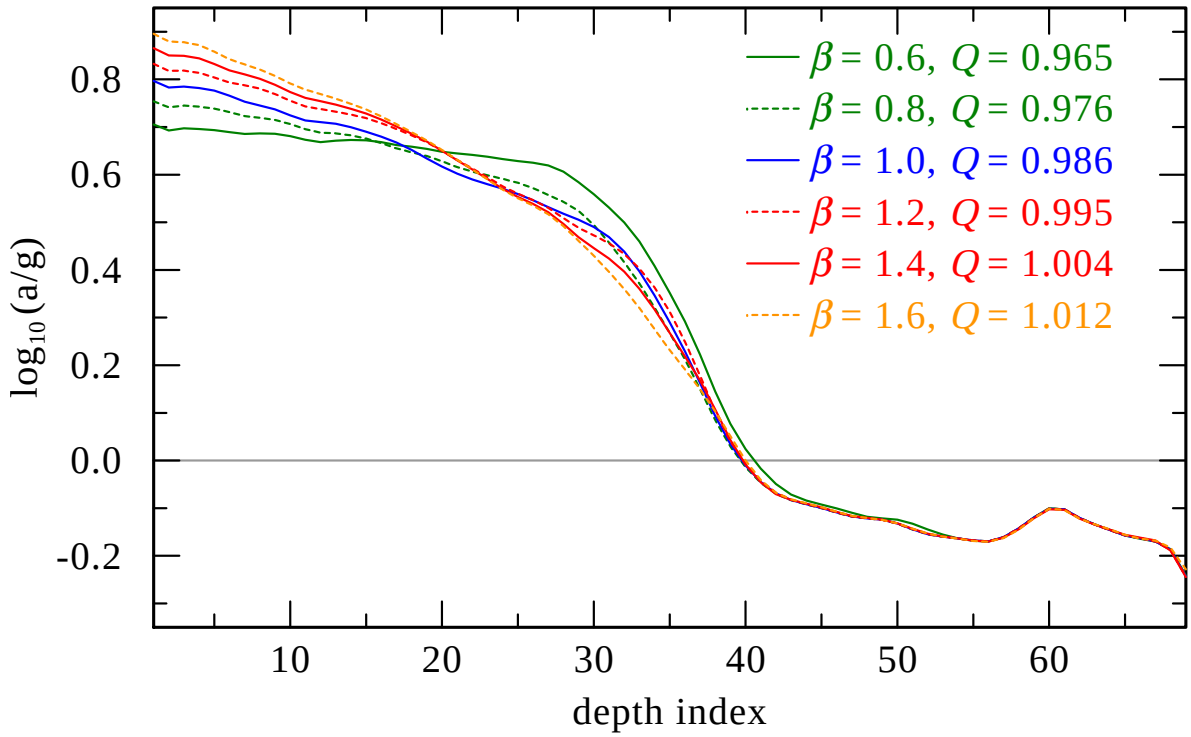

Figure 4.1 – Radiative acceleration und resulting work ratio Q for models with different β-laws. Except of the different β values used in the wind part, the model parameters are identical. The effects on the radiative acceleration are therfore mostly in the wind region (covered by the lower depth indices), although differences (as for $\beta = 0.6$) can also arise from the different connection points between the wind and the quasi-static layers.

more or less the same is the first one. Integration of the radius yields

$$\int_{R_*}^{\infty} \frac{a^2(r)}{v(r)} \frac{\mathrm{d}v}{\mathrm{d}r} \mathrm{d}r \approx a_\mathrm{s}^2 \int_{R_*}^{\infty} \frac{1}{v(r)} \frac{\mathrm{d}v}{\mathrm{d}r} \mathrm{d}r = a_\mathrm{s}^2 \int_{R_*}^{\infty} \frac{\mathrm{d}}{\mathrm{d}r} (\ln v)\, \mathrm{d}r = a_\mathrm{s}^2 \ln\left(\frac{v_\infty}{v_\mathrm{min}}\right). \tag{4.1}$$

This calculation assumes that the sonic speed can be roughly approximated by its value at the sonic point, i.e. $a(r) \approx a_\mathrm{s} := a(R_\mathrm{s})$, which is sufficient in this context, as this calculation is only done to illustrate the basic effects. Looking at Eq. (4.1) reveals that only the ratio of the terminal velocity and the innermost velocity is really important, hence changes of the slope of $v(r)$ are hardly affecting the integrated acceleration due to gas pressure as long as v_min and the terminal velocity do not change drastically.

For the radiative acceleration there is no pure analytical expression as the evaluation of the integral in Eq. (3.55) requires detailed calculation of the opacities and thus has to be done numerically. In order to study how large the effect of different slopes are on the overall work ratio Q, a series of models has been calcualted using the same terminal velocity v_∞, but different β-exponents for the wind regime plus a consistent stratification in the quasi-hydrosatic regime. The results are illustrated in Fig. 4.1, where the depth-dependent radiative acceleration of all models is plotted against the depth index, denoting the radial grid index which increases inwards. It can be clearly seen that the wind region, which dominates the integrated radiative acceleration, is affected if β is changed, but the overall change of Q remains

small. Between two models with $\Delta\beta = 0.2$ the change is on a percent level, which means that they are small enough to be neglected for one hydro iteration. In other words, Q will not change dramatically if only the form of the velocity law is adjusted while v_∞ and $\dot{M}$ remain approximately the same.

After considering all major contributions to Q, it becomes clear that models with $Q \approx 1$ are the best start approximation for calculating hydrodynamially-consistent models. Especially if they have already been calculated with a consistent quasi-hydrostatic stratification, they are promising candidates that could converge to a hydrodynamically-consistent solution on in shorter computing times than in the original approach from Gräfener & Hamann (2005). The precise number of iterations for a model will of course depend on the complexity and the parameter regime. Usually WR models converge faster than OB models, simply because the radiative transfer can be calculated with a higher Doppler velocity. For both WR and OB models covergence is reached in one or at most a few days, with WR models being more on the order of one day, except for complex situations, such as WO stars or very thick winds. Nevertheless, the models need to be checked regularly as it can happen that the effect of the hydrodynamic velocity update is exactly canceled by the shift of the $\tau_{\max}$-iteration and the velocity field is therefore not really improved in a hydro step.

4.2 A model for a hot WO star

The application to a very hot WO star provides an excellent example to demonstrate the necessary steps, but also the problems which can occur on the way to a hydrodynamically consistent solution. Therefore, the application to the WO star is described in more detail than the other results discussed afterwards. The actual steps are basically the same for all stars, even though the parameters can differ significantly. The problems which will be listed do not occur for all cases, but they are a good example for the difficulties that one can be faced with, especially in the thick wind regime, when trying to obtain HD models.

4.2.1 The test candidate: WR102 - A rare WO2 star in the Milky Way

The Wolf-Rayet star WR102 (also known as [S71d] 4) is one of only four known WO stars in the Milky Way. Of those four, WR 102 and WR 142 are both classified as WO2, making them the earliest WO stars known* with WR 102 seen as the slightly earlier† and maybe more evolved one (Kingsburgh et al., 1995; Tramper et al., 2015).

WR 102 was analyzed in Sander et al. (2012) by using a small grid of WO models. Very recently, Tramper et al. (2015) studied WR 102 and almost all other known WO stars with CMFGEN and new X-SHOOTER spectra. Already the models in Sander et al. (2012) required an oxygen mass fraction of $X_\mathrm{O} = 0.3$ to reproduce the prominent WO features, much higher than the typcal value of $X_\mathrm{O} \approx 0.05$ in WC stars. The more detailed analysis by Tramper et al. (2015) confirmed the enhanced oxygen fraction, even though their value is a bit lower than in the grid analysis. The mass fractions obtained by Tramper et al. (2015) are $X_\mathrm{He} =$

*Recently, another WO2 star has been found in the LMC by Massey et al. (2014). No spectral analysis has been published yet, but a first look at the spectrum shows a stronger C IV 5808 Å emission than WR 142, suggesting that this star is slightly cooler.

†WR 102 was classified as WO1 instead of WO2 before the WC/WO classification has been revised by Crowther et al. (1998).

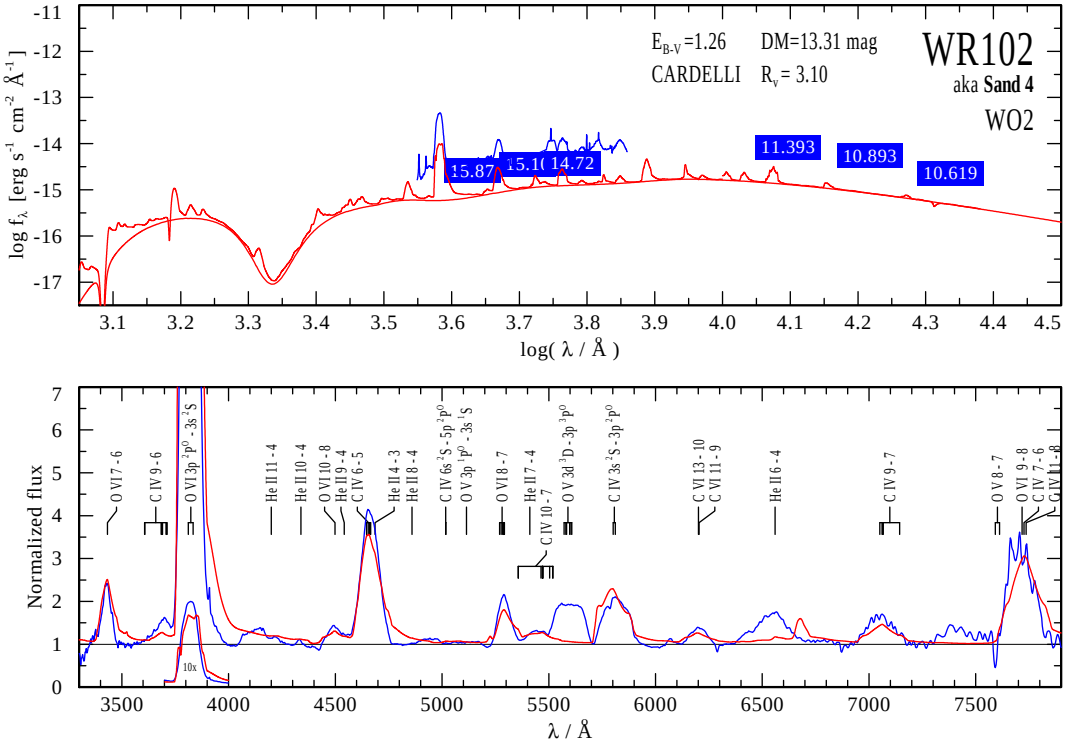

Figure 4.2 – WR 102: The spectral energy distribution (upper panel) and the normalized optical spectra (lower panel) for an unclumped PoWR model (D = 1, $\log \dot{M} = -4.92$) using the parameters obtained by Tramper et al. (2015) are compared to observations and photometry. While the most prominent line features are reproduced, the SED and the luminosity are severely underestimated.

0.14, $X_C = 0.62$, and $X_O = 0.24$, giving WR 102 the lowest helium and the highest oxygen abundance of all studied WO stars.

4.2.2 Obtaining a starting model

WO models tend to be hard to calculate. The proper treatment of their high temperatures requires to take Fe ions higher than Fe X into account, which leads to a significant increase of the total number of superlevels. This in turn requires a sophisticated treatment of the iron superlevels which works properly on ions of more than ten different ionization stages. Typical PoWR models calculated for WO stars contain Fe IV to Fe XVII, but test calculations have shown that stages up to Fe XX can get excited in the innermost parts of the atmosphere models. However, the contribution of ions above Fe XVI to the radiative acceleration and also their effect on the emergent spectra are hardly recognizable, so these ions can be neglected in the model calculations.

As a parameter study is not the scope of this work, the recent abundances from Tramper et al. (2015) are adapted to calculate a PoWR model that serves as starting approximation for the hydrodynamical calculations. It has to be mentioned that the high Fe ions (> Fe X) were not included in the CMFGEN models by Tramper et al. (2015), which could result in differences between the obtained spectra.

The PoWR model with the same parameters as Tramper et al. (2015) with $D = 1$ is shown

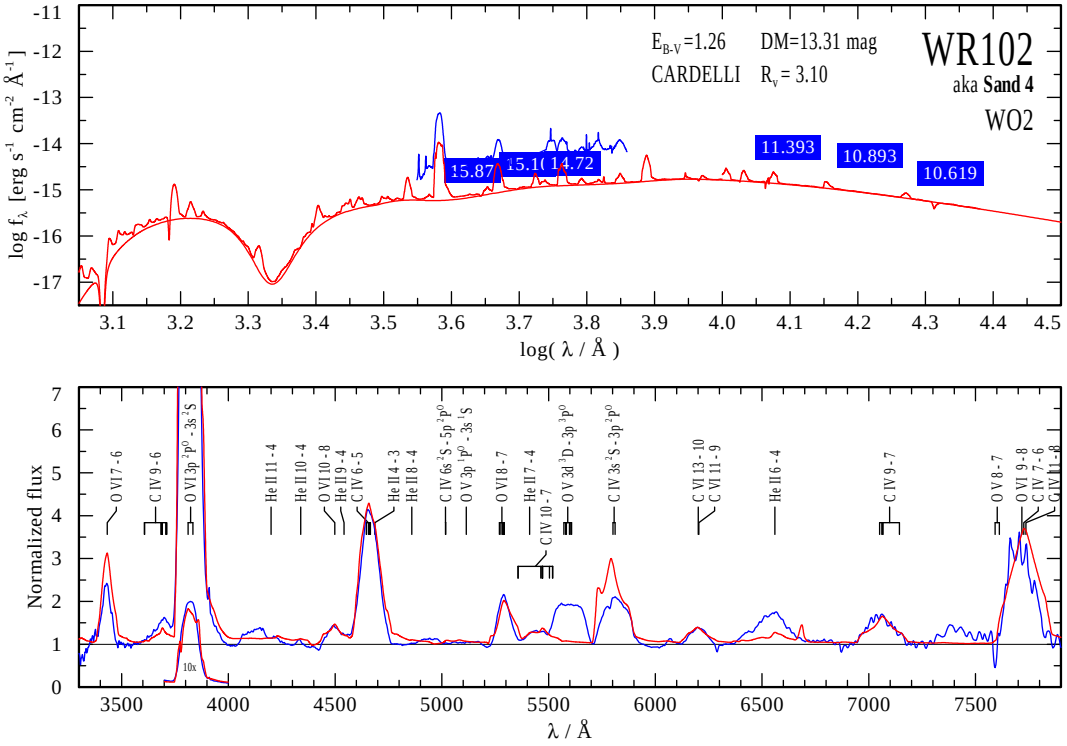

Figure 4.3 – Same as Fig. 4.2, but with a PoWR model for $\log \dot{M} = -5.3$ and $D = 10$. The luminosity is still underestimated, but the electron scattering wing of the O VI 3811 Å line is reproduced much better than in the unclumped model.

in Fig. 4.2. The main features of the normalized WO star spectrum are reproduced, but the resulting spectral energy distribution does not fit the observed photometry, even though the same distance is used ($d = 4.6\,\mathrm{kpc}$, taken from Drew et al., 2004). The same basically holds if a clumped model with $D = 10$ (and in turn a lower mass-loss rate) is used, as shown in Fig. 4.3. Clumping improves the SED fit only very mildy (by about 0.1 dex in L) as the clumped model did use a slightly higher mass-loss rate than one would obtain with simply scaling $\dot{M}$ by $D^{-1/2}$. Significant clumping seems to be necessary to avoid the strong electron scattering wings in Fig. 4.2 that are not observed. This questions the constraint of $D \leq 2.5$ which Tramper et al. (2015) deduced based on evolutionary calculations and the observed low helium mass fraction. However, if the luminosity is significantly higher, as the PoWR models demand for the assumed distance, these evolutionary calculations would have to be adjusted anyhow.

A simple scaling of the WO model suggests a luminosity around $\log L/L_\odot \approx 6$ instead of 5.45, which would be significantly higher than what has been found for the Galactic WC and WO stars so far. In order to have a sufficient model in this regime a pure shift of $\log L$ is not sufficient, as the resulting normalized spectrum will no longer be the same. In order to have approximately the same spectrum, the transformed radius R_t (cf. Eq. 2.2) needs to be fixed, which implies a scaling of $\dot{M} \propto L^{3/4}$ if all other parameters stay the same. This leads to a model with $\log \dot{M} = -4.88$, which tends to give a bit too strong emission lines. A better agreement is obtained for a model with $\log \dot{M} = -5.0$ and depth-dependent clumping, as can be seen in Fig. 4.4. The model SED points also to a slightly higher reddening than assumed

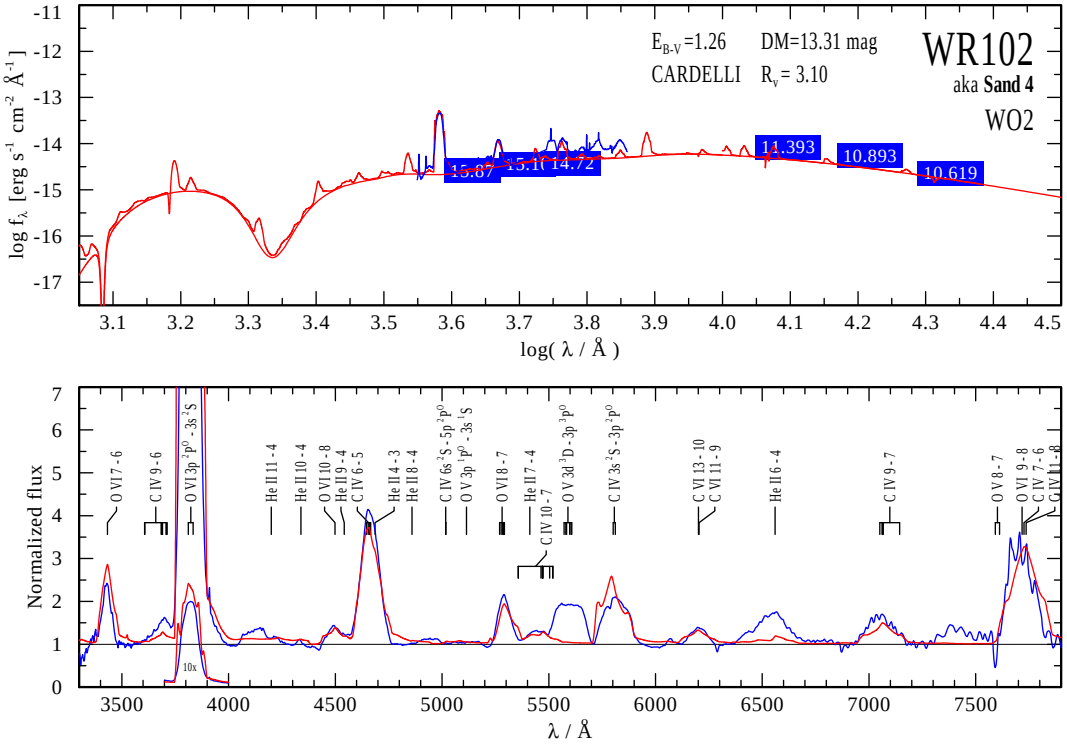

Figure 4.4 – Same as Figs. 4.2 and 4.3, but with a PoWR model using a higher luminosity of $\log L/L_\odot = 6.0$ and $\log \dot{M} = -5.0$. The clumping factor is increasing outwards with an outer maximum of $D = 10$.

by Tramper et al. (2015), as it reproduces the the observed blue optical measurements, but tends to underestimates the redder ones.

The agreement in the normalized spectrum could possibly be improved with the help of more models with finer steps in $\dot{M}$ and other parameters, but this is not the scope of the present work.

4.2.3 The hydrodynamic approach

WR 102 is an interesting test case for the hydrodynamical studies, as it provides the chance to check if such extremely fast winds ($v_\infty \approx 5000\,\mathrm{km/s}$) can be driven by radiation only. As discussed in Sect. 4.1, the work ratio is an indicator to check if a model with a prescribed velocity law has an overall sufficient radiative driving and could thus be used to start a hydrodynamically consistent model iteration.

The work ratio Q for the model with the original parameters from Tramper et al. (2015) with $D = 1$ yields only $Q = 0.38$. The introduction of clumping lowers the mass-loss rate and thus raises the value to $Q = 0.65$ for the model shown in Fig. 4.4. For the model with the higher luminosity of $\log L/L_\odot = 6.0$ and $\log \dot{M} = -5.0$, the work ratio increases to $Q = 0.98$. The work ratio increases even more, if depth-dependent clumping is introduced ($Q = 1.09$) and the additional elements sodium and magnesium are added ($Q = 1.19$). In the standard models, only helium, carbon, oxygen, neon, and the generic element for the iron group were used. The effect of sodium and magnesium on the optical spectrum is negligible, but they contribute to the radiative acceleration in the wind raising Q by about 10%. This is in line

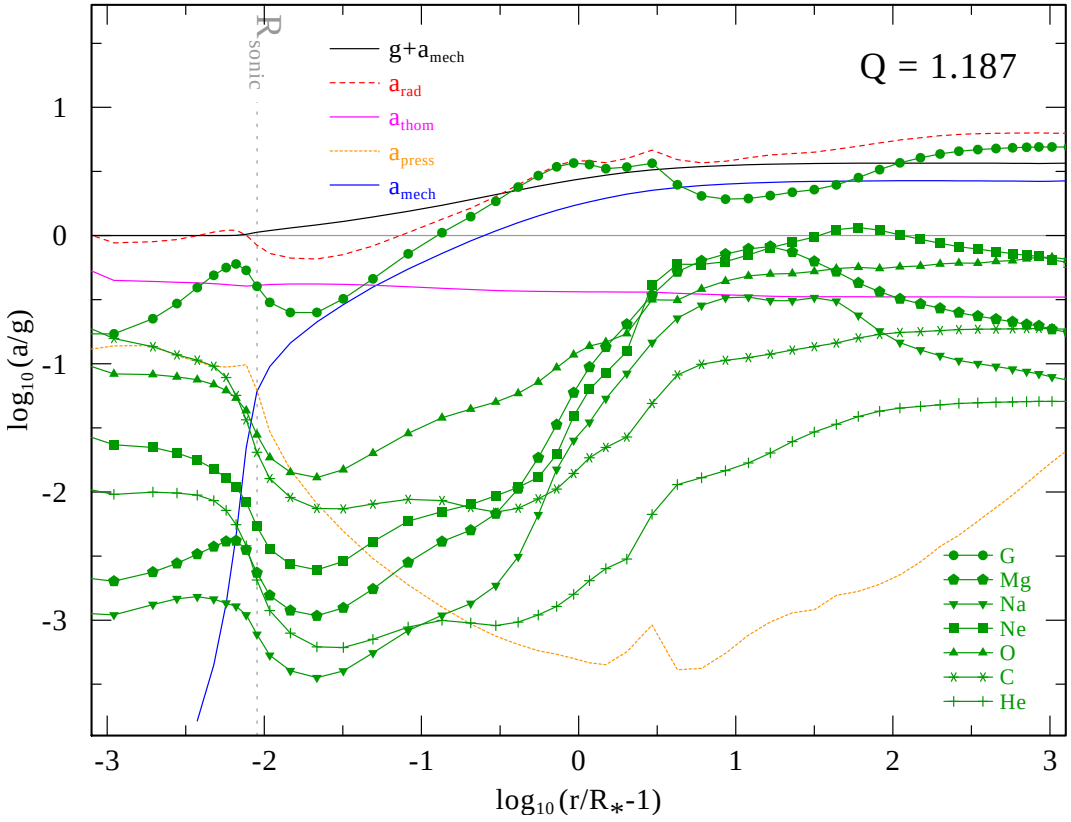

Figure 4.5 – Detailed contributions to the radiative acceleration in the best-fitting non-HD PoWR model for WR 102. The green curves denote the radiative acceleration due to the different elements considered in the model. The red dashed curve marks the total radiative acceleration. For comparison, the gas pressure term (yellow dashed line) and the contribution due to scattering of free electrons (purple line) are also shown. The combined repulsing forces of gravity and inertia are indicated by the black line. The inertia contribution to the black line is shown in blue. All accelerations are normalized to gravity. G denotes the generic iron group element.

with ealier, non-HD, CMFGEN-based studies from Herald et al. (2001), who noticed that the inclusion of iron and other metals such as neon or magnesium significantly improved the work ratio of their models.

The contributions to the radiative acceleration for the model including sodium and magnesium are shown in Fig. 4.5. This model already includes the proper treatment of the quasi-hydrostatic regime, therefore the total radiative acceleration basically matches gravity inwards of the sonic point. The gas pressure is about one order of magnitude lower than the radiative pressure, even in the subsonic layers. (No turbulence pressure is included in this model.) In the wind regime, the gas pressure term drops even further and is quickly less important than all other acceleration contributions. Outward of the sonic point, first only the accelerations from the iron group elements and the free electrons provide a significant contribution, but this changes at $\approx 4\,R_*$, where the iron acceleration drops a bit while all other elemental contributions increase. It is noteworthy that even though carbon contributes more than 60% to the mass, it never provides a contribution to the radiative acceleration that would at least be comparable to the Thomson term. The only elements apart from iron which contribute more than the Thomson scattering are neon ($X_{\mathrm{Ne}} = 1.7 \cdot 10^{-3}$), magnesium ($X_{\mathrm{Ne}} = 6.9 \cdot 10^{-4}$)

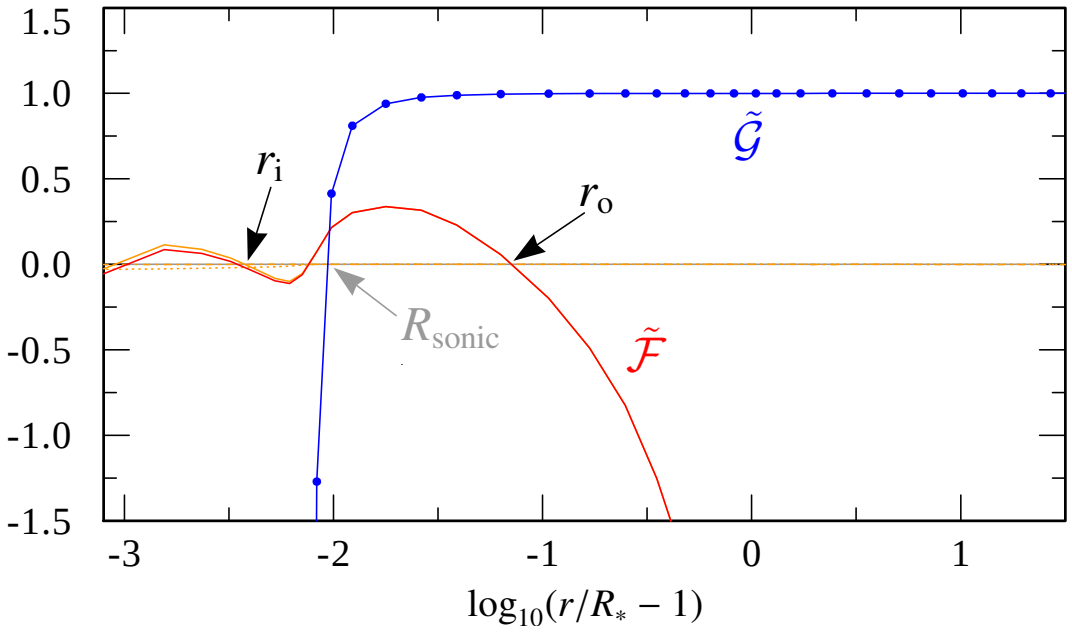

Figure 4.6 – $\mathcal{F}$-$\mathcal{G}$-analysis plot for the WO starting model with an already consistent quasi-hydrostatic part. The two positions of $\mathcal{F} = 0$ and $\frac{\mathrm{d}\mathcal{F}}{\mathrm{d}r} < 0$ are marked with r_i (inner) and r_o (outer) and denote the two possible candidates for the critical point in the current situation. The current sonic point, which should be identical to the critical point in a converged model, is also indicated.

and oxygen ($X_\mathrm{O} = 0.24$). In a region between $7\,R_*$ and $40\,R_*$, the contribution of sodium ($X_\mathrm{Na} = 2.7 \cdot 10^{-5}$) is comparable to the Thomson term. These results underline that the abundance of an element as such does not provide any hint on its wind driving contribution.

In order to save calculation time, the majority of hydrodynamic calculations have been performed using models without sodium and magnesium, as these two elements provide about 30% of the total number of considered atomic levels (571 without Na and Mg vs. 803 including both). As the work ratio of the starting model is already very close to unity, one would expect that the terminal velocity will not change significantly in a hydrodynamically-consistent model. However, a look at the $\mathcal{F}$-$\mathcal{G}$-analysis plot for this model (Fig. 4.6) reveals that an integration of the equation of motion would yield a non-monotonic velocity field. Furthermore, there are multiple radii with $\mathcal{F} = 0$, raising the questions which of them marks the correct critial point. For a monotonic $v(r)$, the gradient of $\mathcal{F}$ must be negative at $\mathcal{F} = 0$, which excludes the point closest to the current sonic point. The two other points, marked with r_i (inner) and r_o (outer) in Fig. 4.6, would give very different mass-loss rates. Given that r_o will likely lead to a much lower mass-loss rate, below what is usually known for Wolf-Rayet stars, r_i is the proper candidate here.

The candidate radius r_cand for a critical point is now given, yielding already the velocity $v(r_\mathrm{cand}) = a(r_\mathrm{cand})$. Nevertheless, the trend of $\tilde{\mathcal{F}}$ in Fig. 4.6 still would lead to a non-monotonic velocity law with a deceleration region between the current sonic point and r_o. To avoid this, the value of Γ_rad used in the hydrodynamic integration is manipulated such that $\mathcal{F} > 0$ is avoided outward of r_cand and $\mathcal{F} < 0$ is avoided inwards of r_cand. The resulting $\tilde{\mathcal{F}}$ is shown in Fig. 4.7, illustrating the situation still before the hydrodynamic integration. After the integration, the situation will stay the same for $\tilde{\mathcal{F}}$ (at least before performing the next

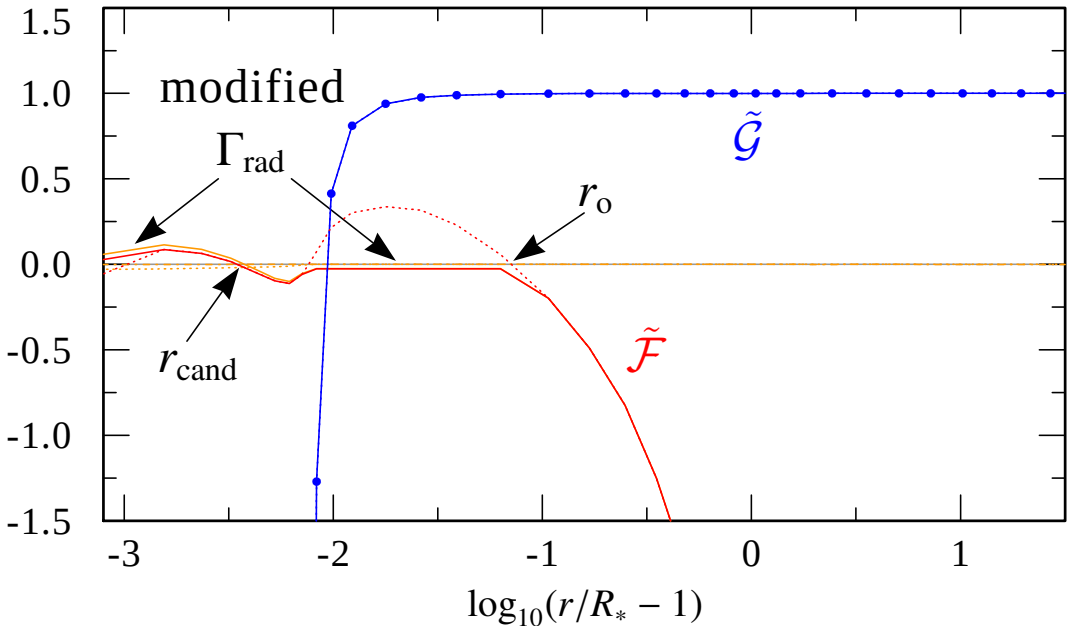

Figure 4.7 – Same as Fig. 4.6, but now with an automatic adjustment of $\Gamma_{\rm rad}$ ensuring that $\mathcal{F} = 0$ is reached only once. The method choses the innermost candidate and thus automatically removes any additional critical point candidates.

radiative transfer calculation), but $\tilde{\mathcal{G}}$-term using the new velocity field will then smoothly pass zero at $r_{\rm cand}$.

Unfortunately, the modification of $\mathcal{F}$ has a very subtle effect on the velocity field, that can also be illustrated via Fig. 4.7. While the gradient outside of what has been denoted with $r_{\rm o}$ in Figs. 4.6 and 4.7 is correct, the actual wind velocity v is not. Due to the modification in the deceleration region, the wind velocity is artificially kept at a higher value than it would have been in the non-monotonic case. In the end, this leads to an offset in the terminal velocity. To account for this situation that has been forced by the numerics while keeping the gradient, the obtained velocity field is scaled with a correction factor afterwards. This correction again stems from the work ratio Q, which automatically changes when $\Gamma_{\rm rad}$ is modified. The correction factor is then obtained by comparing the Q-values between the unmodified and the modified velocity field in a similar way than explained in Sect. 3.11.2.

The presence of a deceleration region is a disturbing phenomenon. On the one hand there is no physical reason that a velocity gradient cannot be negative in a particular region of a stellar atmosphere. On the other hand, the trend of $\Gamma_{\rm rad}$ is heavily influenced by the density stratification and thus by the velocity field used in the starting approach. In some cases the deceleration eventually vanishes throughout the model iterations, e.g. in the OB models discussed below, while in other cases, such as for the WO model discussed here, it does not. This might indicate a "real" deceleration region, but it cannot be ruled out that it is a numerical artifact. A radiative transfer code that can handle non-monotonic velocity fields would be required to shed more light on this question.

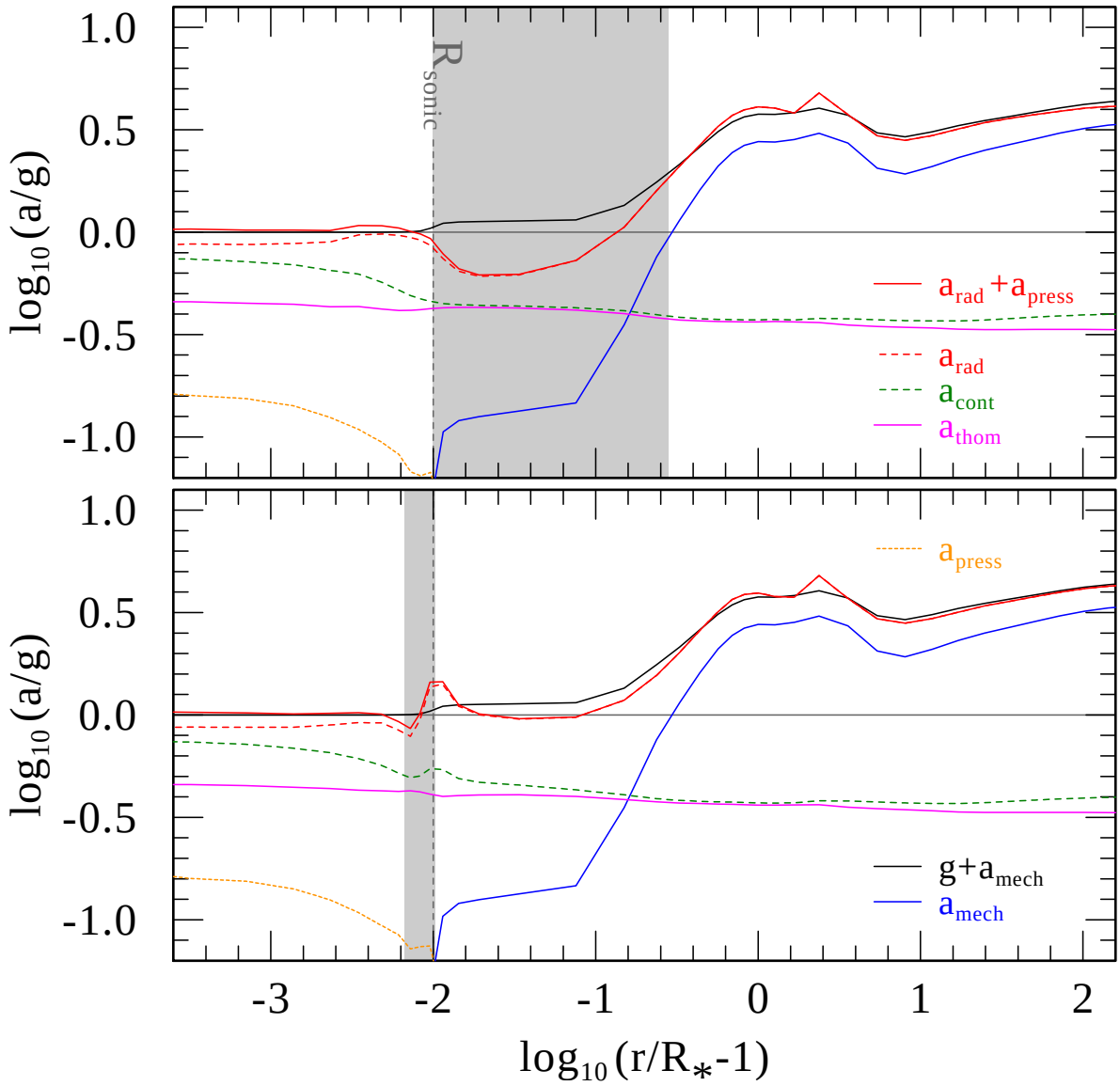

Figure 4.8 – Depth-dependent accelerations for WO models with the "near-HD" velocity field using a clumping onset above the sonic point (upper panel) and below (lower panel). The grey-shaded areas are indicating the regions where D increases from 1 (smooth wind) to 10.

4.2.4 The onset of clumping

As indicated above, the "converged" model for WR 102 shows a deceleration region. In this region, a hydrodynamically consistent solution cannot be found, as indicated in the upper panel of Fig. 4.8, where the red solid curve denoting the sum of the outward pushing accelerations cannot balance the black solid curve denoting the sum of gravity and inertia. A closer inspection of the model reveals that the deceleration region coincides more or less exactly with the region where the clumping factor increases (grey-shaded area). In the starting model, the clumping onset has been set to the sonic point with an increase to $D = 10$ at $v = 1000\,\mathrm{km/s}$. After each update of the velocity field, the clumping stratification is adjusted according this prescription, therefore the clumping factor increases exactly above the sonic point also in the hydrodynamic model, even if the position of the sonic point might have changed with respect to the starting model.

This coincidence raises the question if the deceleration region is caused by the increase of the clumping factor. To test the influence, a test model has been calculated where the velocity field is fixed to the results of the hydrodynamic calculations, but the clumping factor now increases in a region below the sonic point. The resulting radiative acceleration indeed changes, as can be seen in the lower panel of Fig. 4.8. There is an increase of a_{rad} in the region below the sonic point where D increases, but there is also still a decrease above the sonic point. In the last years it has been suggested that clumping could already exist in layers below the sonic point (see, e.g. Cantiello et al., 2009; Muijres et al., 2011), contrary to ealier studies. At least from the technical standpoint, a subsonic clumping onset seems to improve the situation.

4.2.5 The resulting velocity field and spectrum

Despite some shortcomings in the inner part, the remaining wind region, where important parts of a WO spectrum are formed, is hydrodynamically consistent ($\log r/R_* - 1 \gtrsim -0.6$). The model thus provides an interesting insight in the wind velocity field of a WO2 star like WR 102.

In Fig. 4.9, the resulting velocity field (red) is compared to a few β-laws (green, black, and blue). In the outermost part, the slope of the velocity field for the hydrodynamic model roughly resembles a law with $\beta = 0.6$, but the increase in the inner part is steeper than predicted by any β-law. The hydrodynamic inconsistency in the region above the sonic point prevents to draw more general conclusions here, but a steep increase of the radiative acceleration is seen in several of the WO models calculated during this work. For a consinstent model, this would have to be reflected in the velocity field, assuming it is not an artifact of the starting model. As WO models are generally hard to calculate (which is not restricted to PoWR, see also Tramper et al., 2014, 2015), further code improvements would be necessary before it is possible to perform an in-depth study with various different starting models that could confirm or deny that a steep increase in the velocity field is typical for WO stars. These improvements are not concerning the hydrodynamics and are therefore beyond the scope of the present work. C

An interesting detail in the obtained WO velocity field, is the absence of a clear velocity plateau in the wind, even though the inertia term in Fig. 4.8 is clearly non-monotonic. Such a plateau was seen in the hydrodynamic solution obtained for the WC star WR 111 by Gräfener & Hamann (2005) (see inlet of Fig. 4.9) and it also does in occur for the WNE model which will

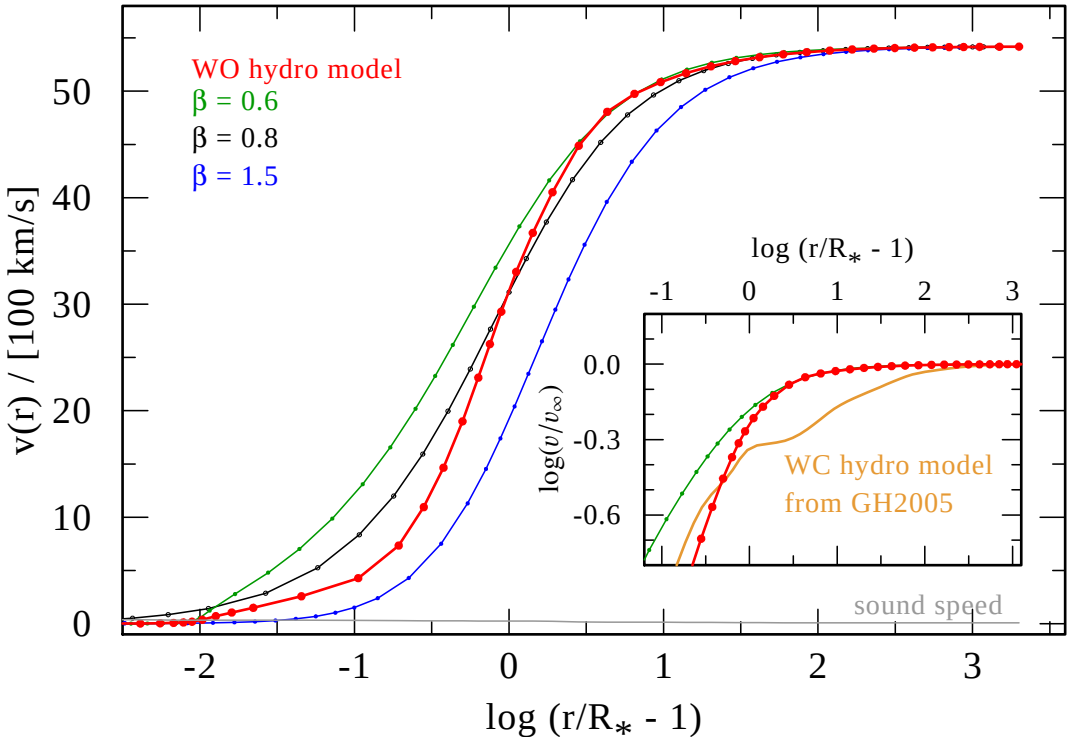

Figure 4.9 – The velocity field of the hydrodyamic WO model (red curve) is compared to different beta-laws (green, black, and blue curves) with an emphasis on the wind region. The inlet shows the outer wind part in comparison to the WC velocity field obtained by Gräfener & Hamann (2005). For a better comparison, the velocity fields are normalized to their terminal velocity in the inlet.

be presented in the following Sect. 4.3. However, the "dip" in the inertia term is not as deep and it occurs in WO model at a radius where the velocity is already close to v_∞. Both facts prevent the appearance of a noticeable plateau. The actual origin of the hydrodynamically consistent velocity gradient is of course the form of $a_{\rm rad}(r)$, which has a "dip" in all of the WR models due to the iron group elements. While no other element is able to fully compensate this feature, Fig. 4.5 shows that in the case of the WO model, the contribution of elments like neon and magnesium are increasing exactly in the wind region where the contribution of the iron group elements goes down. Hence, these elements, which are neither considered by Gräfener & Hamann (2005), nor in the WNE model in this work, might be important for damping the drop of the total radiative acceleration.

Due to the different terminal velocity of the hydrodynamic model, the resulting emergent spectrum shows a bit weaker, but slightly broader lines, as illustrated in Fig. 4.10. When compared to the observation, the model does not provide a fit as good as Tramper et al. (2015), but this is not due to the hydrodynamic calculations, but attributed to the fact that in the process of approaching $Q \approx 1$ some stellar parameters were adjusted and this mildly affected the spectrum. Still, the resulting models resonably well reproduces the appearance of an early WO star.

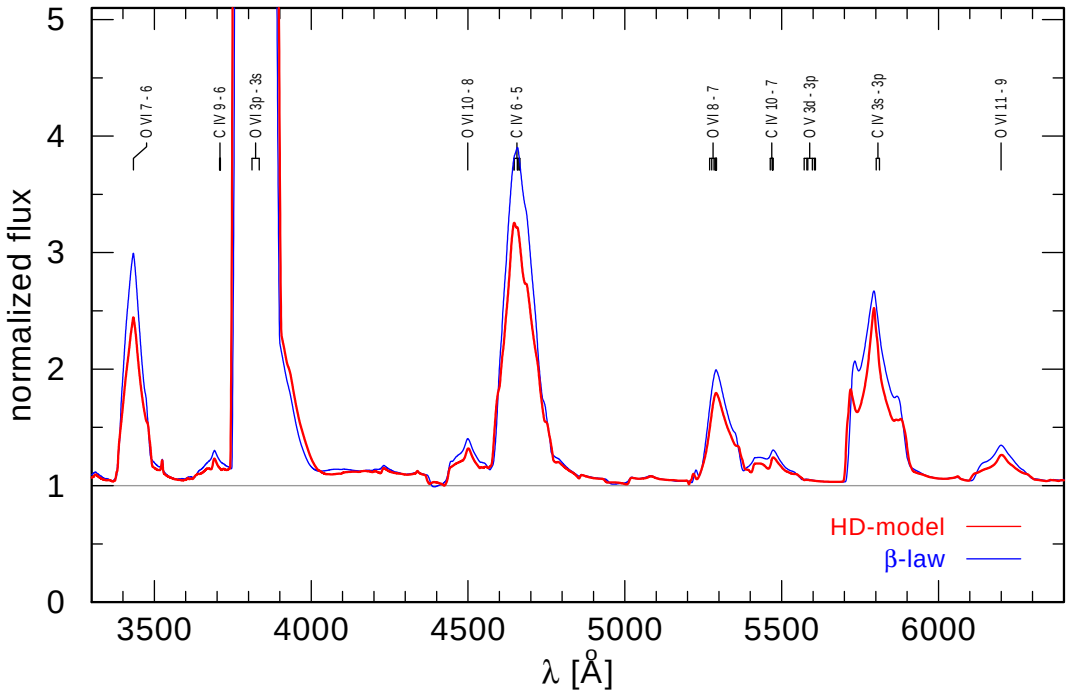

Figure 4.10 – The optical spectrum of the hydrodyamic WO model (red curve) is compared to the starting model using a prescribed wind velocity law with $\beta = 1$. Most differences are due to the higher terminal velocity of the HD model.

4.2.6 Revised role of WR 102?

The much higher luminosity than obtained by Tramper et al. (2015) for WR 102 drastically changes the position of the star in the Hertzsprung-Russell diagram (HRD). This can be seen in Fig. 4.11, where the new position of WR 102 is compared to the results from Tramper et al. (2015) and Sander et al. (2012). For comparsion, the positions of the other Galactic WR stars analyzed in Hamann et al. (2006), Martins et al. (2008), Liermann et al. (2010), Sander et al. (2012), and Oskinova et al. (2013) as well as the other Galactic WOs analyzed by Tramper et al. (2015) have been added. The new position of WR 102 would significantly seperate this WO2 star from the known early WN and WC stars. While the position obtained by Tramper et al. (2015) suggests that this star is quite typcial descendant from a WC, the evolutionary status for a WO star with million solar luminosities and a current mass of 30 $M_\odot$ would raise new questions. However, this value of course relies on the distance taken from Drew et al. (2004) who basically came to this value by performing an M_V-calibration between WR 102 and WR 142. WR 142 is another Galactic WO2 which seems to be associated with the Be 87 cluster (Massey et al., 2001; Knödlseder et al., 2002). This means that the distances of the only two analyzed WO2 stars are directly connected. A future cross-check could come from the recently discovered LMC195-1 found by Massey et al. (2014), which is now the third known WO2 star and the first outside the Milky Way.

The situation thus remains unclear so far, both from the distance and the modelling side. Future updates of the PoWR code (see chapter 6) could improve the stability of WO models and thus provide better constrains on the model parameters, possibly even allowing a fully hydrodynamically-consistent model. An analysis of the LMC WO2 could also give a better hint

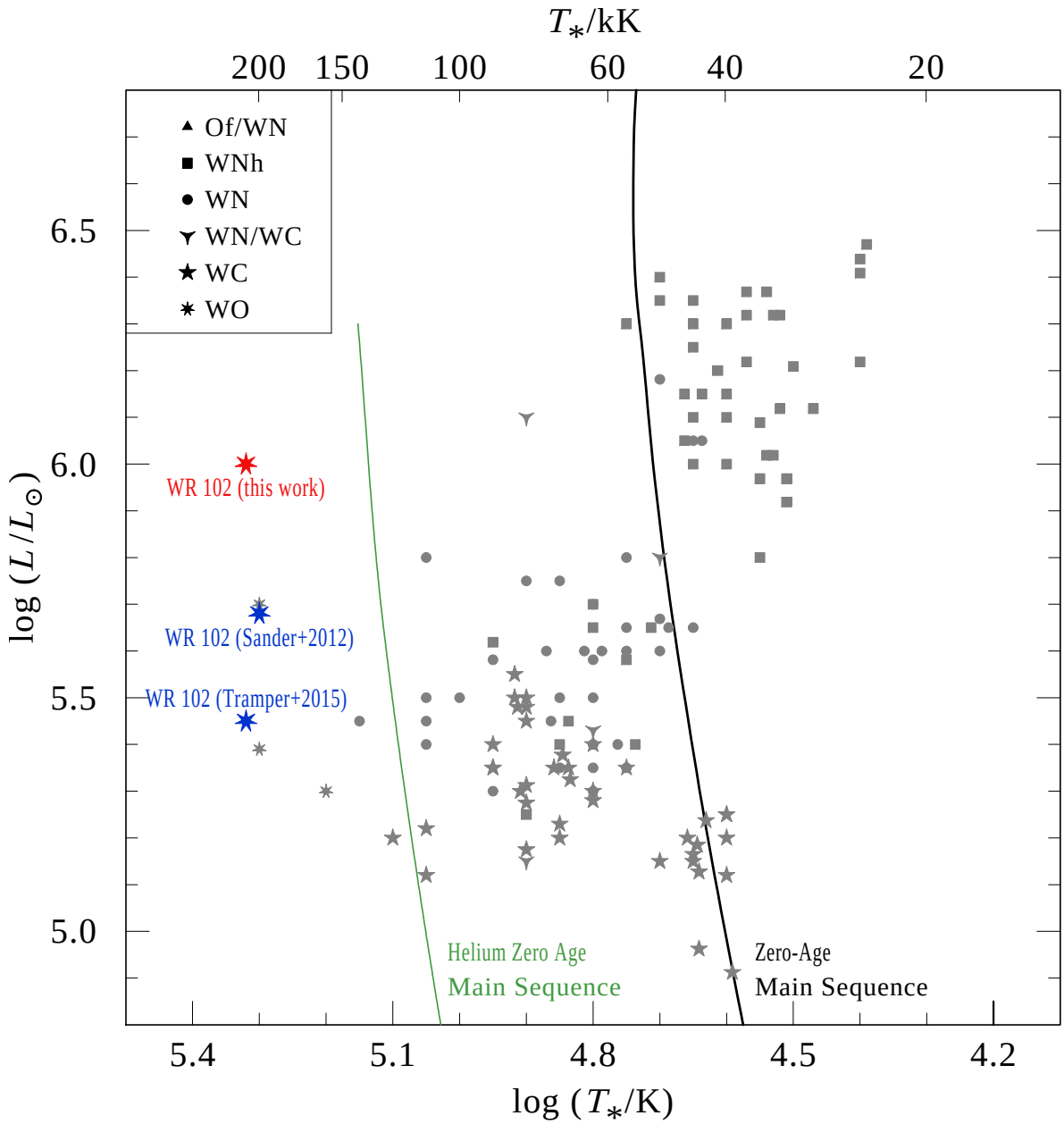

Figure 4.11 – The Hertzsprung-Russell diagram (HRD) of the Galactic Wolf-Rayet stars (grey symbols) which have been analyzed by Hamann et al. (2006), Martins et al. (2008), Liermann et al. (2010), Sander et al. (2012), Oskinova et al. (2013), and Tramper et al. (2015). The different symbols refer to the different spectral types as indicated in the upper left corner. The positions obtained for WR 102 in Sander et al. (2012), Tramper et al. (2015), and this work are highlighted by blue and red symbols. For comparison, also the zero age main sequence (ZAMS) for hydrogen and helium stars is shown.

on the absolute visual magnitude, eventually leading to a better constraint for the luminosity and even the mass.

4.3 A model for a hydrogen-free WN star

Other hydrogen-free Wolf-Rayet stars are not quite as hot as the WO-type stars, but usually still have much stronger winds than OB stars. In most of the early WC and WN stars, at least at Galactic metallicity, the spectrum is formed in the wind and not affected by the quasi-hydrostatic layers. Since Gräfener & Hamann (2005) already provided a model for a WC star, a model for an early WN star is the most urgent task in order to cover the main Wolf-Rayet types on a broad scale. Although a few early-type WN (WNE) stars are found to contain hydrogen (see, e.g. Hainich et al., 2014, 2015), almost all Galactic WNE are hydrogen-free (Hamann et al., 2006). In order to understand these stars and their thick winds it is therefore sufficient to use a model without hydrogen.

The model for the hydrogen-free WN star served as a kind of prototype to study the implementations with and without the use of a force multiplier parameter (see Sects. 3.8 to 3.11). With a temperature of $T_* \approx 140\,\mathrm{kK}$ the test model is set in the range of early subtypes (WN2-5). A more precise assignment to a particular subtype would depend on the spectral appearance, which cannot be simply correlated with a certain temperature T_*. For thick wind models, T_* is furthermore not really a good reference value as models with the same value of $R_\mathrm{t} \cdot T_*^2$ yield approximately the same emergent spectrum (see, e.g., discussions in Hamann et al., 2006; Sander et al., 2012).

The Wolf-Rayet model grids, which provide the basis for the analysis of larger samples, are calculated with a luminosity of $\log L/L_\odot = 5.3$ (Hamann & Gräfener, 2004; Todt et al., 2015). Models from such a grid usually do not reach $Q \approx 1$ in the parameter regime where the emergent spectra match observations. These models were calculated to obtain stellar parameters from fitting observed spectra and thus include only the important elements visible in the spectrum. They also do not include the iron group elements for ionization stages above G X. As explained above for the WO example, both simplifications lead to an underestimation of the opacity and thus the radiative acceleration. For the hydrodynamic calculations, higher ions up to G XVII need to be included. Due to the test character of the model, no additional elements are considered, but only helium, carbon, nitrogen, and the iron group elements. To compensate for that, the maximum clumping factor was moderately enhanced from $D = 4$ to $D = 20$. The more recent results from the Potsdam group (e.g. Sander et al., 2012; Hainich et al., 2014) favor a typcial value of $D = 10$, leaving a factor of two to be covered by additional elements. Future calculations will include more elements that are important for the wind driving, and will – based on the experience from the WO models – likely allow a reduction of the clumping factor back to $D = 10$. Finally, the luminosity of the WNE model was moderately increased to $\log L/L_\odot = 5.45$, a typcial value obtained for a WNE star like WR 2 (Hamann et al., 2006). WR 2 is one of the Galactic WN stars where the distance can de deduced from a probable membership of the CAS OB1 association (van der Hucht, 2001).

Thick wind models tend to have a complitated stratification around the sound point, as illustrated for the WO star in the $\mathcal{F}$-$\mathcal{G}$-diagram. If Γ_rad is very close to unity in the subsonic part, $\tilde{\mathcal{F}}$ will be very close to zero and small pertubations can lead to large changes in the resulting $v(r)$ by introducing additional critical point canditates. Whether this situation is realized in nature is debated. For $\Gamma_\mathrm{rad} \gtrsim 1$ in a subsonic part, phenomena like inflation (see,

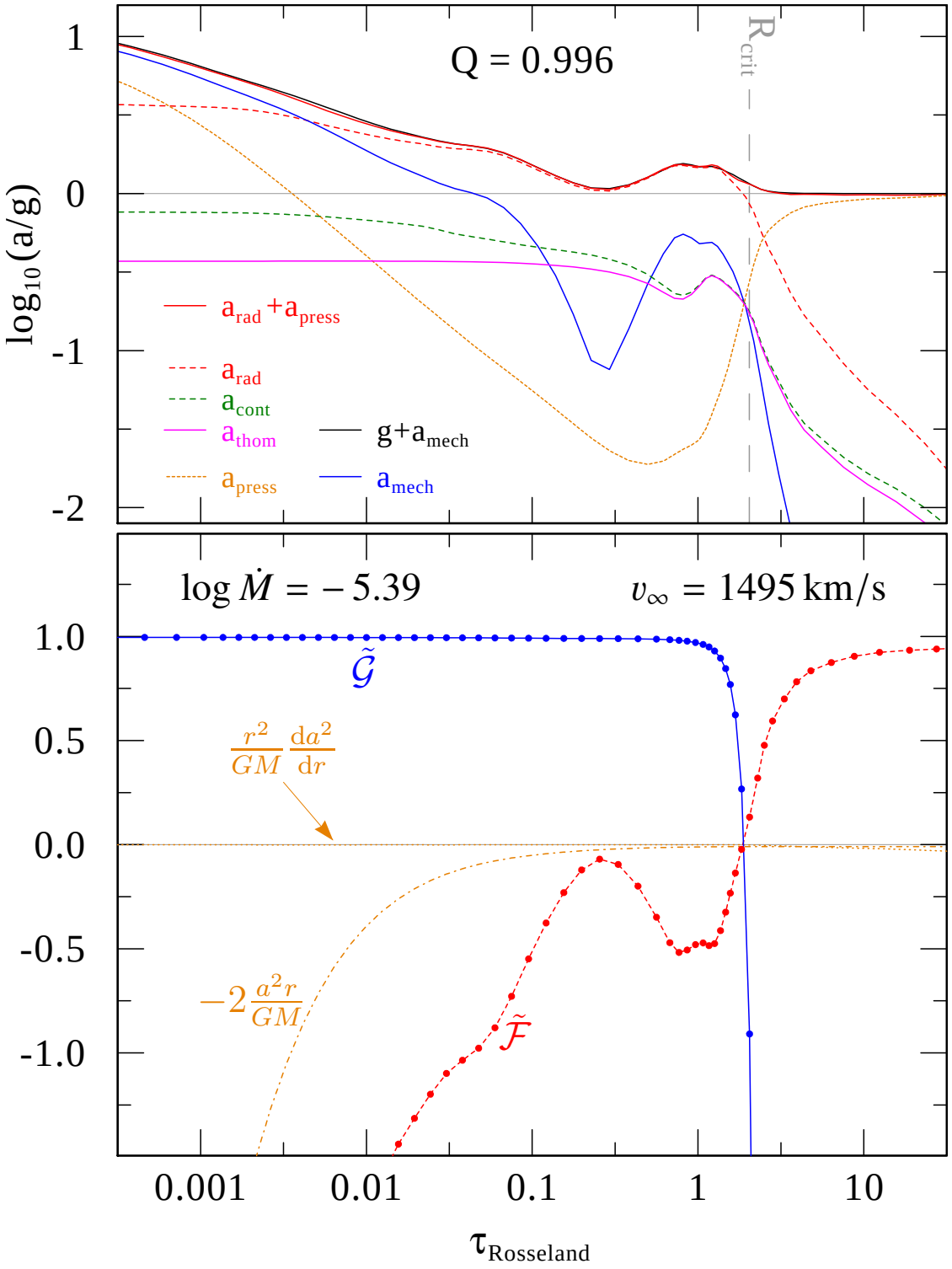

Figure 4.12 – Upper panel: Acceleration plot for the hydrodynamically consistent WNE model. Lower panel: $\mathcal{F}$-$\mathcal{G}$-analysis plot for same model. Due to the $\kappa_{\rm eff}$-formalism in the innermost part, $\mathcal{F}$ reaches higher values than normal. The "bump" after the sonic point in the supersonic region is typcial for Wolf-Rayet stars with dense winds and can be attributed to an opacity bump in the iron group elements.

e.g., Gräfener et al., 2012; Sanyal et al., 2015) or the breaking into optically thick clumps (see, e.g. Oskinova et al., 2007; Sundqvist et al., 2014) are discussed. Especially in the latter case not the full opacity would have to be considered, but instead only an effective opacity $\kappa_{\rm eff}$ would contribute to the radiative acceleration. With this motivation a formalism has been introduced which will be explained in Sect. 5.4. Due to its restriction to the innermost regime, the κ-reducing hardly affects the work ratio Q. While this arbitrary modification prevents to draw any physical conclusions from the subsonic part, it can significantly simplify the $\mathcal{F}$-$\mathcal{G}$-stratification.

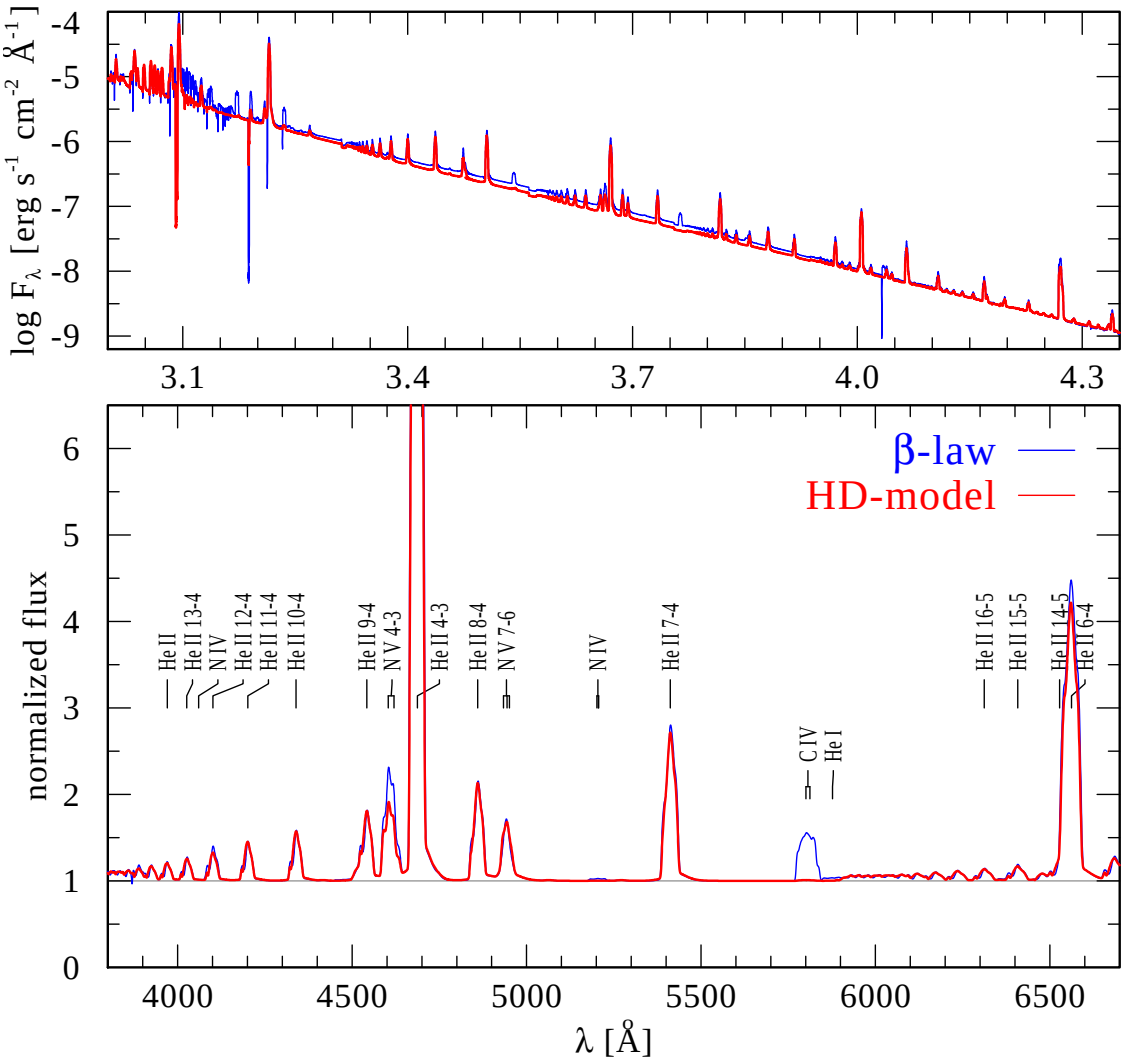

Figure 4.13 – The emergent spectrum of the hydrodynamic WNE model is compared to the spectrum of a model with a β-law using the same T_*, v_∞, and $\dot{M}$. The upper panel shows the flux-calibrated spectrum as seen from a distance of 10 pc while the lower one compares the normalized optical part.

The acceleration stratification and the $\mathcal{F}$-$\mathcal{G}$-trend for the hydrodynamically consistent WNE model are shown in Fig. 4.12. The obtained values of $v_\infty = 1495\,\mathrm{km/s}$ and $\log \dot{M} = -5.39$ are in the expected region for early WN stars. Both values would be somewhat higher if opacities for more elements would be considered. In the analysis of the Galactic WN stars

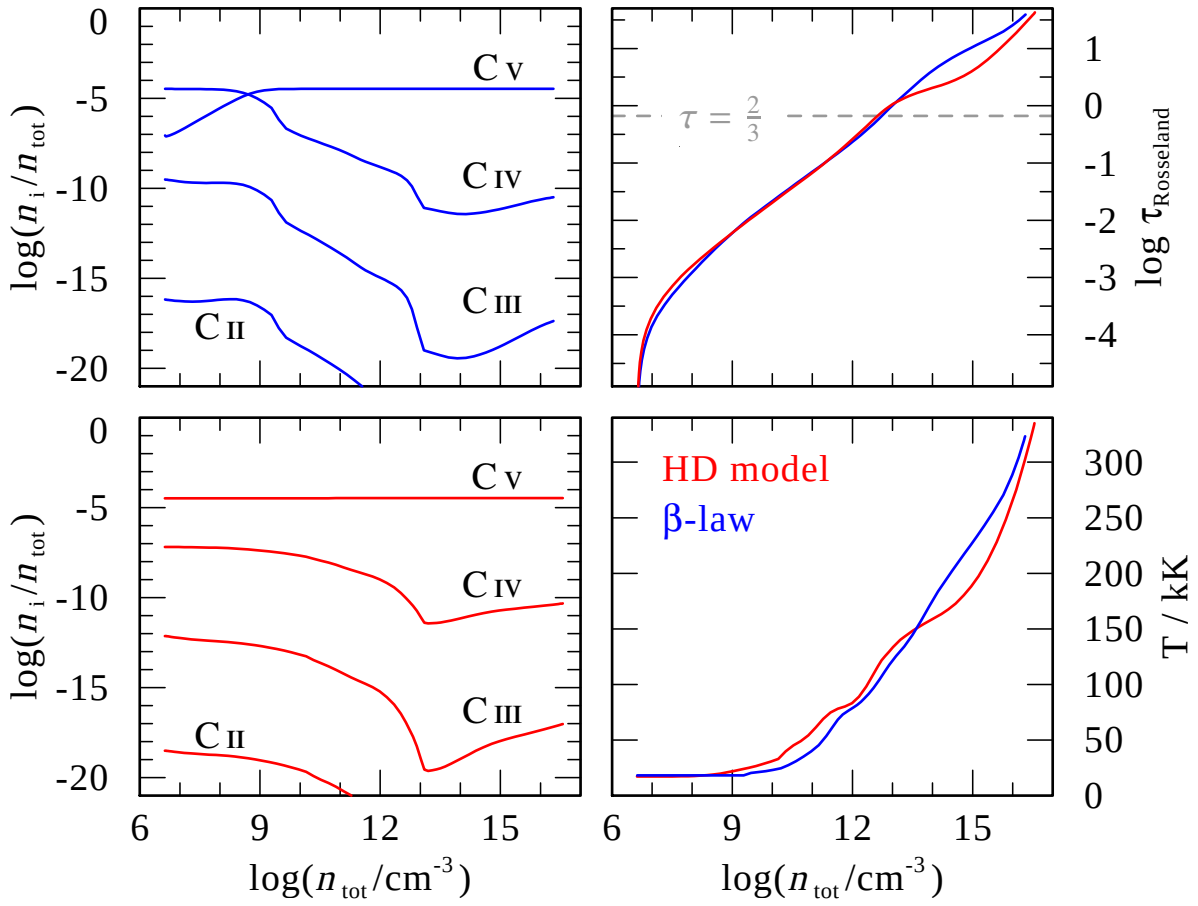

Figure 4.14 – Comparison of the carbon ionization (left panels), the electron temperature (lower right panel), and the optical depth stratification (upper right panel). The red curves refer to the hydrodynamic model in all panels while the blue curves show the same quantities for the model with a prespecified wind velocity law using the same T_*, v_∞, and $\dot{M}$. In the hydrodynamic model the temperature in the outer region is slightly higher, so that C V does not recombine. This leads to the absence of the C IV-line in the emergent spectrum (see Fig. 4.13). For clarity, only the ground level of each ion is shown in the ionization stratification panels.

by Hamann et al. (2006), values up to 2700 km/s were deduced, while most WNE stars had terminal velocities between 1600 and 2300 km/s.

The emergent spectrum of the hydrodynamically consistent model is shown in Fig. 4.13. For comparison, a model with the same stellar parameters (T_*, v_∞, $\dot{M}$, R_t) has been calculated. In the comparison model, the inner part of the velocity structure is obtained by integrating the hydrostatic equation as described in Sect. 3.4 while the outer part is described by a β-law with $\beta = 1.5$. Both velocity laws are connected such that the velocity and its gradient are continious. By comparing this model with the hydrodynamic model it is possible to identify the differences that arise when using a hydrodynamically consistent solution. The comparison of the normalized spectra (lower panel in Fig. 4.13) reveals that the helium lines are hardly affected while C IV 5808 Å completely vanishes in the hydrodynamic model. Also N V 4603/19 Å gets slightly weaker, but this line complex is very sensitive to any changes in a model. It should be noted that the chemical composition is exactly the same in both

models and the absense of the C IV-line is purely a result of the stratification changes. This is illustrated in Fig. 4.14, where the carbon ionization and the temperature structure of both models are compared. The hydrodynamic model has a higher electron temperature in the wind except for the outermost part. In this situation C V remains the leading ion while it otherwise recombines to C IV. This demonstrates also how dangerous it would be to deduce any carbon abundance from this line doublet.

The most striking differences in the spectral appearance are revealed when looking at the spectral energy distribution (SED, upper panel of Fig. 4.13). The iron forest redwards of He II 1215 Å is much stronger in the non-HD model. Furthermore, in the optical range the total flux is lower in the hydrodynamic model. A closer look on the model details reveals that while both models have the same T_*, i.e. the same effective temperature at $\tau_{\max}$, the effective temperature at $\tau_{\mathrm{Ross}} = \frac{2}{3}$ differs by 10 kK (115 kK for the non-HD model vs. 105 kK for the HD model). The τ-stratification (upper right panel of Fig. 4.14) shows significant differences only in the innermost part, where the optical depth of the hydrodynamic model is lower for the same (particle) density. The same trend can be seen in the temperature stratification (lower right panel of Fig. 4.14) and coincides with differences in the ionization of the iron group superlevels. This could explain the differences in the iron forest eventually seen in the SED.

From the fact that the hydrodynamic model reaches a higher density at the inner boundary one can already deduce that the velocity here must be smaller compared to the model with the prescribed wind velocity law. This might seem surprising at first since $\dot{M}$ is the same for both models and the hydrodyamic equation transitions into the hydrostatic equation, i.e. the inertia term is of no importance at the inner boundary. However, both equations basically provide a velocity gradient. The absolute value then follows from a given value at a certain point, either the critical point (hydrodynamic solution) or a boundary value (hydrostatic solution). Therefore, the inner boundary value of v and thus also the density can differ between the two approaches. The velocity fields for both models are shown in Fig. 4.15, where the velocity is plotted on a logrithmic (lower panel) and a non-logarithmic scale (upper panel). The logarithmic plot in the lower panel gives better insights into the low-velocity part of both laws. The sonic point ($v = a$) differs considerably between the two models and the hydrodynamic solution increases much steeper than the beta-law, which is connected to the hydrostatic integration at the radius R_{con}.

For the wind part, the non-logarithmic velocity scale fully reveals the deviance of the hydrodynamic solution from the β-law and shows that there is a plateau in the velocity field at about $2\,R_*$ with $v \approx \frac{2}{3} v_\infty$[‡]. This step of course corresponds to the "dip" in the inertia term seen in the upper panel of Fig. 4.12, which itself is caused by the decreasing radiative acceleration in this region. This can be attributed to the opacities of the iron group elements since the other considered elements not only have significantly weaker contributions, but also show an increasing outward trend. Due to the plateau the hydrodynamic solution cannot be approximated by a single β-law. Using a double-β-law with the right weighting factors (see purple and yellow curve in the upper panel of Fig. 4.15) gives a better approximation for the slope, but cannot provide the increase so far inwards as observed in the hydrodynamic solution. However, this is likely due to the connection with the hydrostatic solution and forcing a continous gradient between two regimes. While the latter is very helpful, if not even

[‡] Interestingly, the plateau occurs at about the same fraction of the terminal velocity as proposed by Hamann (1980) for ζ Pup using line opacity calculations to obtain a so-called "tailored" velocity law.

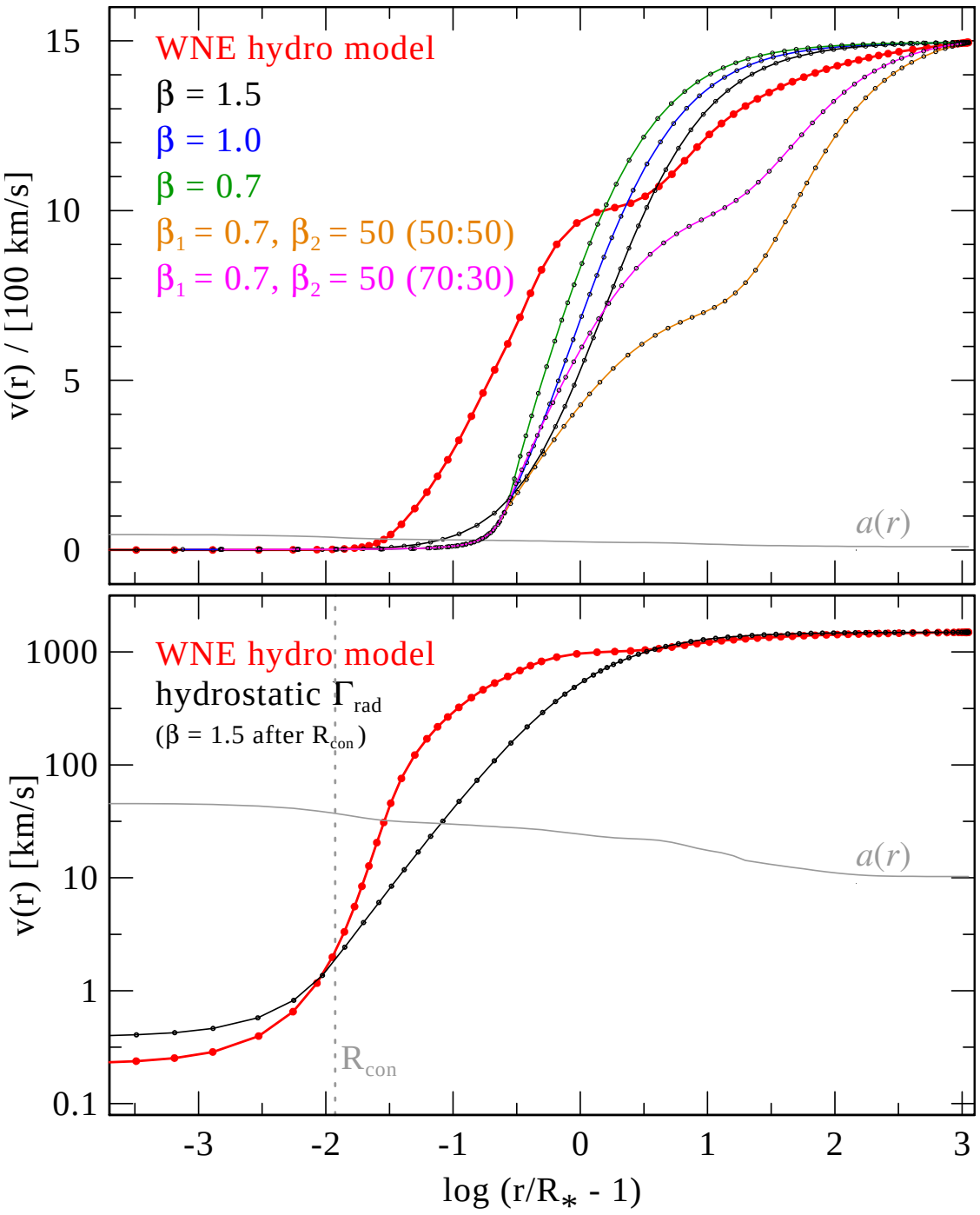

Figure 4.15 – The velocity field of the hydrodynamic WNE model (red curve) is compared the velocity field of the model with a prefixed wind velocity law (with $\beta = 1.5$) in the outer part and a correct hydrostatic integration in the inner part (black curve). Both models have the same T_*, v_∞, and $\dot{M}$. Additional prescribed wind velocity laws have been added for comparison. While the upper panel focusses on the wind domain, the lower panel shows the velocity on a logarithmic scale and thus focusses on the quasi-hydrostatic part. The vertical dashed line denotes the connection point for the fixed velocity law (black curve).

needed, to avoid "connection artifacts" in the radiative acceleration, an even more sophisticated treatment of the connection regime might be helpful as neither the hydrostatic nor the (double-)β-law, representing the outer wind region, is a really sufficient approximation around the sonic point. For a pure description of the the wind regime, a shifted double-beta law might be a valid treatment.

4.4 Hydrodynamical consistent OB star models

With the new implementation introduced in Sect. 3.11, hydrodynamical solutions can not only be calculated for WR, but also for OB stars. Unfortunately, OB star models need much longer calculation times as they require lower Doppler velocities v_{dop}, which decreases the frequency steps in the CMF calculations, and also need more elements (which increases the calculation time for the solution of the statistical equations). Nevertheless, the calculation of hydrodynamically consistent models for O and B stars allows a direct comparision with CAK-like approximations, making it worth to invest this additional effort.

The hydrodynamic calculations were performed for a model representing an evolved B-star with $T_* = 26\,\mathrm{kK}$, $\log L/L_\odot = 5.5$, $\log g = 2.8$, and solar abundances apart from a slightly reduced hydrogen content.[§] As a compromise between calculation time and a realistic value, $v_{\mathrm{dop}} = 40\,\mathrm{km/s}$ was chosen. As this is rather high for a B-star, a turbulence velocity of $v_{\mathrm{turb}} = 30\,\mathrm{km/s}$ was adopted, leaving the remaining thermal contribution to v_{dop} in a more realistic range.

The starting model used a consistent hydrostatic part connected to a prescribed wind velocity law with $\beta = 0.8$ and $v_\infty = 700\,\mathrm{km/s}$, assuming a mass-loss rate of $\log \dot{M} = -6.33$ ($Q = 0.93$). The converged model had a slightly higher terminal velocity of $v_\infty = 765\,\mathrm{km/s}$ and also a higher mass-loss rate of $\log \dot{M} = -6.07$. The $\mathcal{F}$-$\mathcal{G}$-plots for both the starting and the converged model were already shown in Fig. 3.2 in Sect. 3.10.1 as the slope of $\tilde{\mathcal{F}}$ is kind of prototypical and does not show the complex behaviour seen in Wolf-Rayet stars. The acceleration stratification of the converged hydrodynamical model can be seen in Fig. 4.16. The upper panel reveals that in the subsonic part the total continuum acceleration significantly exceeds the Thomson term, which means that the true continuum cannot be neglected here. In the wind part, the contribution of the true continuum is less important, which is typical for OB stars, illustrating that the assumption of $a_{\mathrm{true\ cont}} = 0$ which is inherent to all CAK-like theories is justified at least in the outer wind. Note, however, that this is different for Wolf-Rayet stars. While for the previously discussed WO model the true continuum is only important in the inner part, the terms is more promiment in very thick winds, as can be seen in the WNE model (Fig. 4.12) example.

In the lower panel of Fig. 4.16, the contributions to the radiative acceleration from all considered elements are shown. The generic element representing the iron group is leading throughout the stellar atmosphere here, but the contribution from the other elements is strongly depth-dependent. In the wind regime, silicon, carbon, nitrogen, and sulfur – in this order – are the next important drivers. All of them have contributions exceeding Γ_{e}, which is on the same order as the contribution due to hydrogen. In the inner part, all of the contributions are less important and only the generic element and hydrogen have a contribution above a few percent, but still below Γ_{e} and the acceleration due to gas pressure.

[§]To save calculation time, one of the candidate models for high-mass X-Ray binary donors (see Martínez-Núñez et al., 2015) was re-used as a starting model for this work.

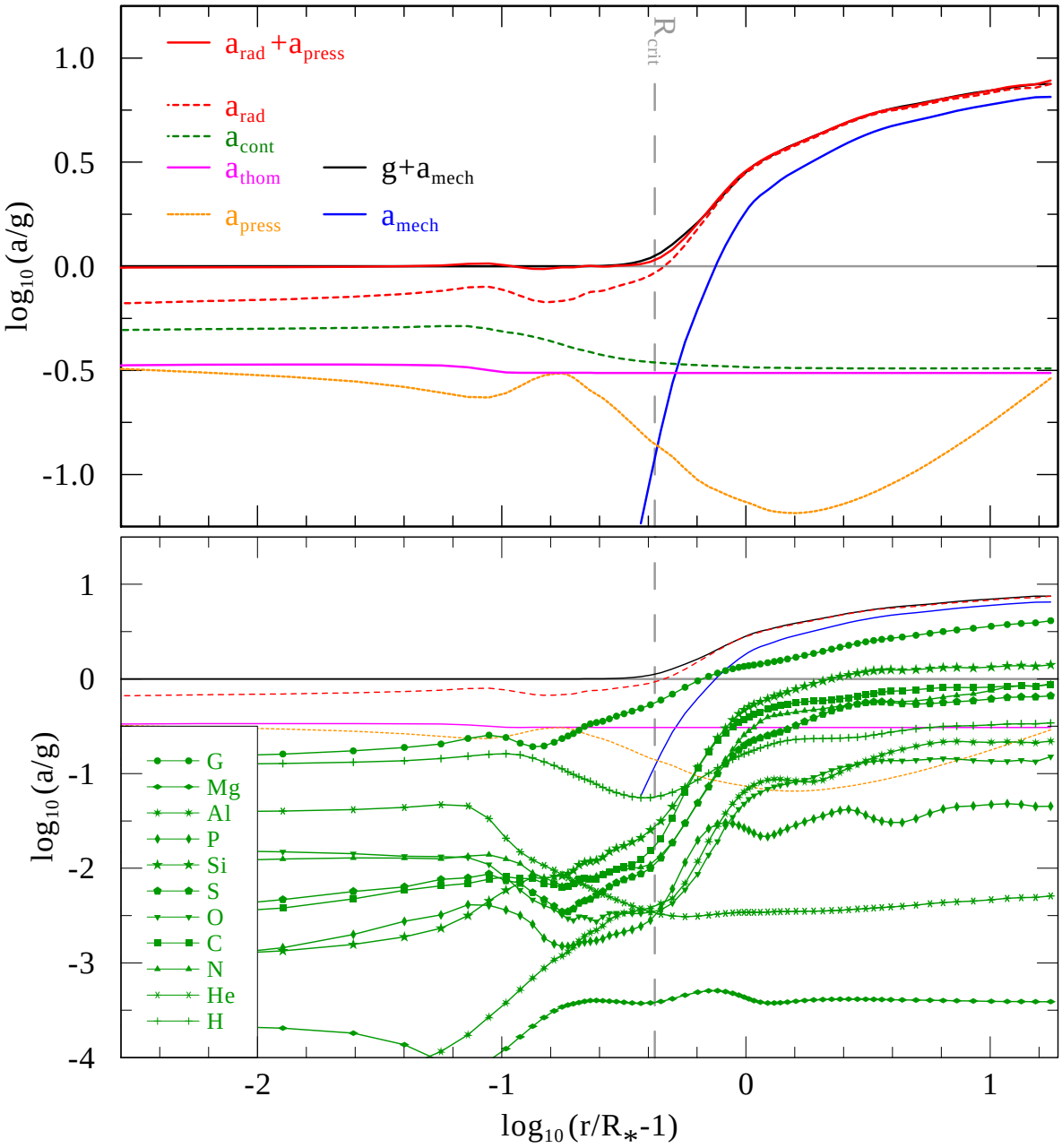

Figure 4.16 – Acceleration plot for a hydrodynamic B-star model: The upper panel shows the total radiative acceleration (dashed red line) as well as its total continuum (green dashed line), and Thomson (purple line) fractions. The total outward acceleration due to radiation and gas pressure (yellow dashed line) is shown by a red solid line. In a hydrodynamically consistent model, this sum is balanced by the sum of inertia (blue line) and gravity, which is indicated by a black line.
The lower panel shows the same model, but now the different green lines indicate the acceleration contributions (line and true continuum) due to the various elements accounted for. The other lines have the same meaning as in the upper panel.

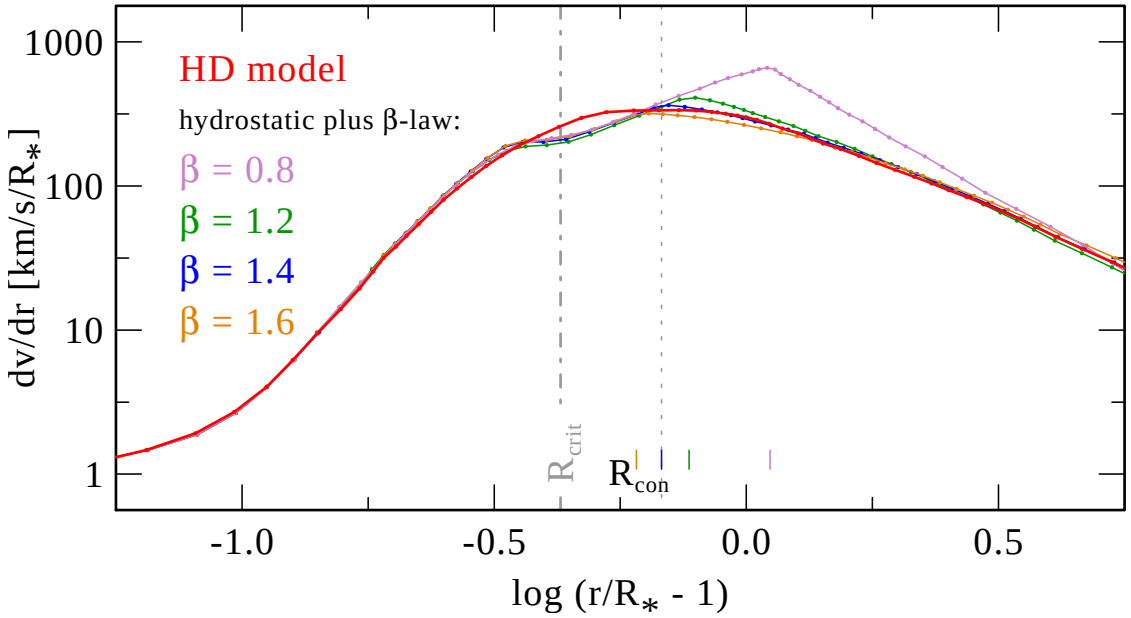

Figure 4.17 – The velocity gradient of the hydrodynamic B-star model (red curve) is compared to models with a prescribed β-law connected to a consistent hydrostatic solution. The thick grey dashed-dotted line denotes the location of the critical point (i.e. $v = a$) of the hydrodynamic model. The connection points for the models with a prescribed wind velocity law are indicated by correspondingly colored dashes. The grey dotted line additionally indicates the connection point for the model with $\beta = 1.4$.

The resulting velocity field of the hydrodynamic (HD) model can be seen in Fig. 4.18. The hydrodynamic solution for $v(r)$ is almost identical to a β-law with $\beta = 1.4$ connected to an inner velocity field obtained from the hydrostatic equation. It is surprising that the form of the HD velocity field is so well reproduced by the model with the prescribed wind velocity law, especially in the region between the sonic point and the connection point. In this region the inertia term cannot be neglected and thus one would expect that the hydrostatic solution, which also cannot handle $\Gamma_{\rm rad} \geq 1$, would differ significantly from the HD solution. A close inspection of the velocity gradients shown in Fig. 4.17, however, reveals that none of the β-law approximations is able to exactly reproduce the smooth velocity gradient produced by the hydrodynamic model.

In order to understand why the approximation between the sonic point and the connection region works reasonably well, it helps to take a look at the acceleration plot for both models. In Fig. 4.19, the approximative model is shown in the upper panel, while the HD-model is shown in the lower one. In contrast to the other acceleration plots, this plot is shown in a non-logarithmic y-scale, making it easier to compare areas. In the upper panel one can see that the area between $R_{\rm crit}$ and $R_{\rm con}$ below the inertia term (blue curve) does not differ much from the area below the $a_{\rm rad}$-term in the same boundary, at least when subtracting what is covered in the hydrostatic quations, which is the rectangle up to the red, dashed-dotted line. This means that both effects considered in the hydrostatic equation, namely the neglect of the inertia term on the one hand and the limitation of $\Gamma_{\rm rad}$ to 0.9 on the other hand, almost cancel each other. As one enters the nominator and the other one the denominator of the work radio Q, the energy balance is also affected only on a sub-percentage level as the contribution

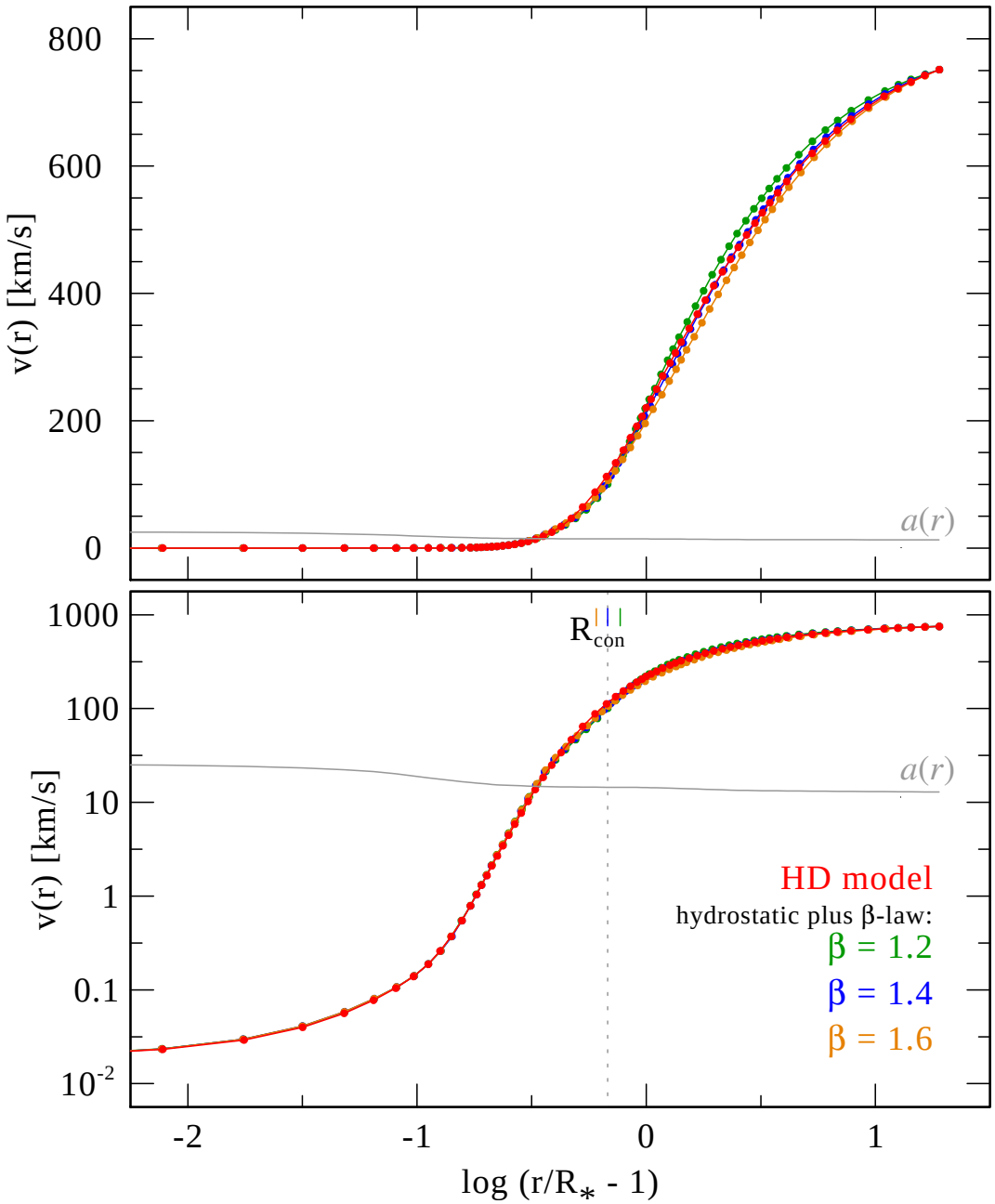

Figure 4.18 – The velocity field of the hydrodynamic B-star model (red curve) is compared to models with a prescribed β-law connected to a consistent hydrostatic solution. The upper panel shows the velocity in a non-logarithmic scale while the lower panel has a logarithmic velocity scale and therefore highlights the inner part. The hydrodynamic solution is extremely close to the model using a prescribed wind velocity law with $\beta = 1.4$. The connection points for the models with a prescribed wind velocity law are indicated by correspondingly colored dashes at the top of the lower panel. The combined speed of turbulence and sound a is indicated by a grey curve.

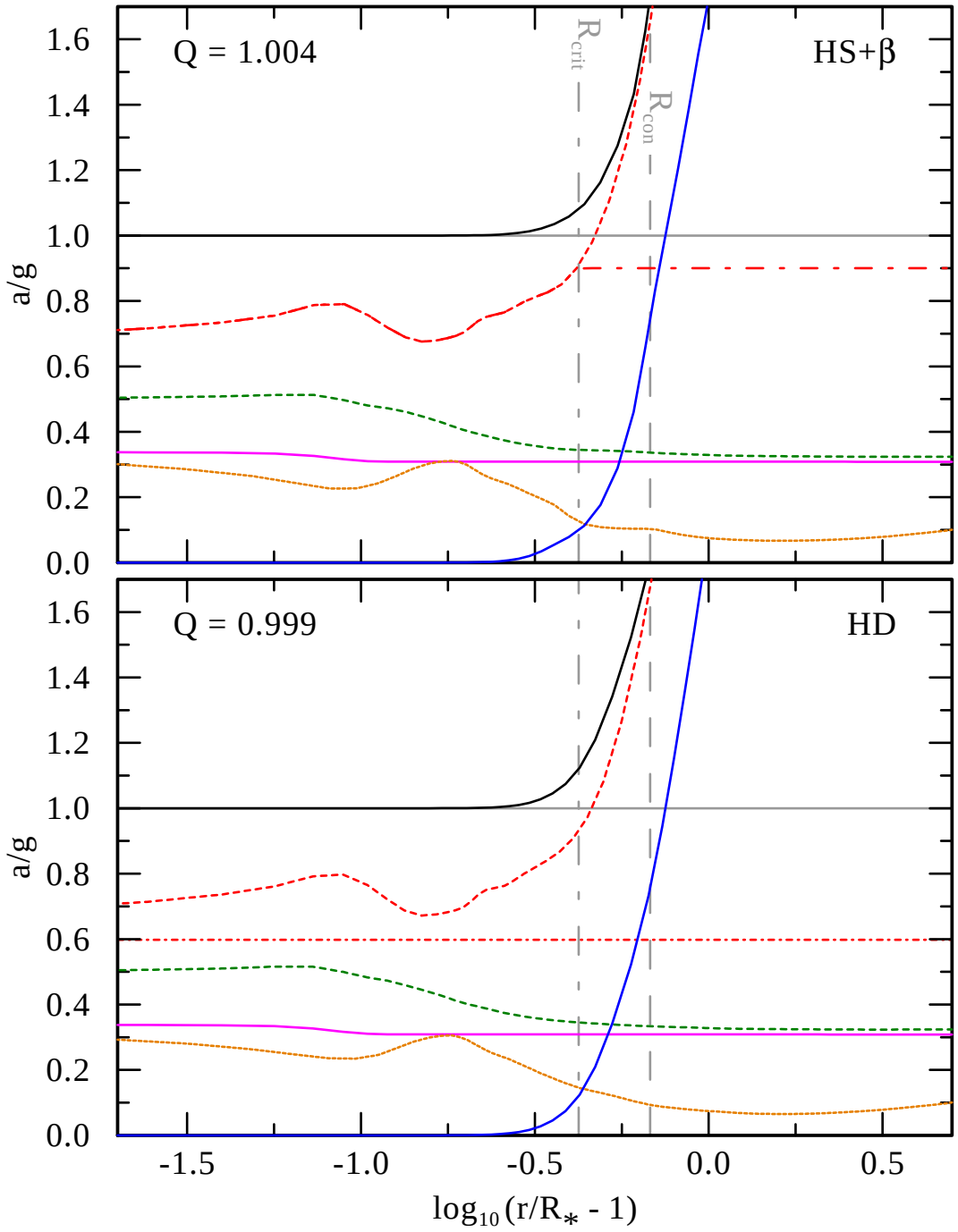

Figure 4.19 – The contributions to the acceleration around the onset of the wind are shown for the hydrodynamic model (lower panel) and for the best approximation using a consistent hydrostatic integration connected to a β-law (upper panel). The critical point of the HD model is denoted by a vertical dash-dotted line. The connection point of the β-law-model is denoted by a vertical dashed line. The dashed-dotted red line in the upper panel marks the value of $a_{\rm rad}$ which enters the hydrostatic equation and is capped at $\Gamma_{\rm rad} = 0.9$.

Table 4.1 – Parameters of the hydrodynamical models: For the WO model, the abundances in brackets are only considered in the test models mentioned in Sect. 4.2, not in the final model.

Model type	WO	WNE	B
T_* [kK]	210	141	24
$T_{\tau=\frac{2}{3}}$ [kK]	174	115	22
$\log g_{\mathrm{grav}}$ [cm s^{-2}]	6.16	5.62	2.80
Γ_{e}	0.39	0.36	0.31
R_* [$R_\odot$]	0.76	0.89	32.6
$\log \dot{M}$ [$M_\odot$ yr^{-1}]	−4.995	−5.385	−6.069
$\log L$ [$L_\odot$]	6.0	5.45	5.5
M_* [$M_\odot$]	30.2	12.0	24.5
v_∞ [km/s]	5418	1495	765
v_{turb} [km/s]	0	100	30
v_{dop} [km/s]	150	150	40
R_{crit} [R_*]	1.010	1.045	1.428
v_{crit} [km/s]	38.3	100.3	33.6
X_{H}	–	–	0.70
X_{He}	0.137	0.983	0.288
X_{C}	0.62	1.0×10^{-4}	5.0×10^{-4}
X_{N}	–	0.015	2.2×10^{-3}
X_{O}	0.24	–	6.0×10^{-3}
X_{Ne}	1.7×10^{-3}	–	–
X_{Na}	(2.7×10^{-5})	–	–
X_{Mg}	(6.9×10^{-4})	–	7.1×10^{-4}
X_{Al}	–	–	7.0×10^{-5}
X_{Si}	–	–	5.5×10^{-4}
X_{P}	–	–	5.8×10^{-6}
X_{S}	–	–	3.1×10^{-4}
X_{G}	1.6×10^{-3}	1.4×10^{-3}	1.3×10^{-3}

of a_{press} is small, so that the slightly different slope of the pressure terms has only a marginal effect.

Given this close approximation, the emergent spectra of both models are basically indistinguishable, as illustrated in Fig. 4.20. Unlike the WNE model discussed above the stratification is almost identical, which is reflected in the values of $T_{\mathrm{eff}}\left(\tau_{\mathrm{Ross}} = \frac{2}{3}\right)$ or $T_{\mathrm{eff}}\left(\tau_{\mathrm{Ross}} = 1\right)$, which differ only on the one-Kelvin level between the two models. However, this close resemblence is only obtained if β is chosen according to the hydrodynamic velocity law. The starting model with $\beta = 0.8$ instead shows significant differences and a much less consistent behaviour in the connection region. This is best seen in Fig. 4.17 where the velocity gradient is compared to models with a prescribed wind velocity law and will be further illustrated in the next chapter when discussing the importance of the starting model (Sect. 5.5.2).

The parameters of all three hydrodynamically consistent models are listed in Table 4.1. While three models are not much more than a first glimpse, the large differences between the models nicely already demonstrates that the calculation method for hydrodynamical models presented in this work is sufficient over a wide range of different stars and spectral types.

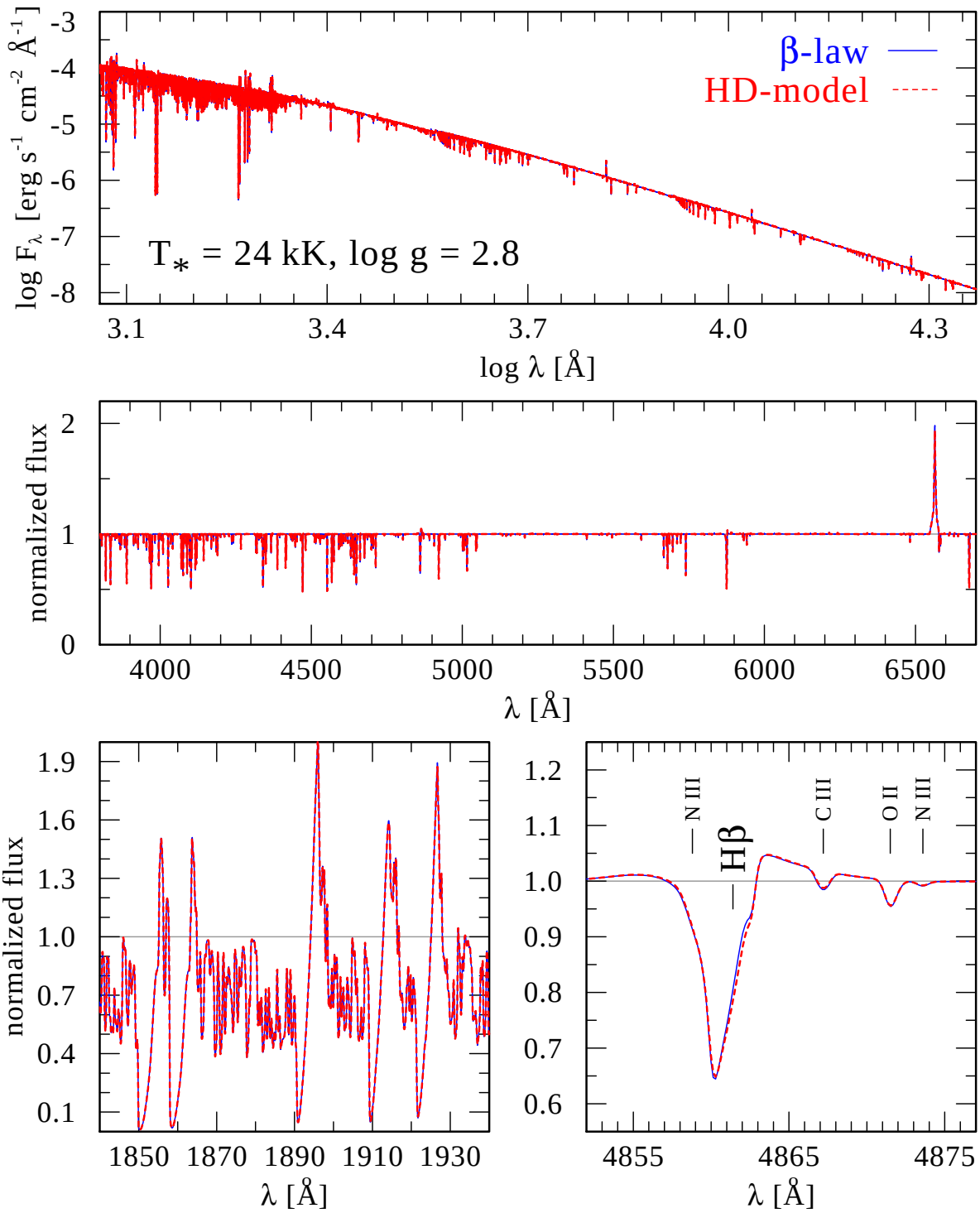

Figure 4.20 – Emergent spectrum of the hydrodynamically consistent model (red curve) and a model using prescribed wind velocity with $\beta = 1.4$ connected to a consistent hydrostatic solution (blue curve). The uppermost panel shows the spectral energy distribution over a broad wavelength range. The second upper panel shows the normalized optical spectrum. The lower two panels show small parts in the UV (left panel) and around Hβ (right panel). The spectra from both models are almost indistinguishable.

Chapter 5

Discussion

5.1 What sets the mass-loss rate?

Since the discovery of Lucy & Solomon (1970) that a continuous outflow could be driven by momentum transfer from radiation to spectral lines, the theoretical prediction of the mass-loss rate $\dot{M}$ has become one the most important aspects of stellar wind theory. The fundamental question is how $\dot{M}$ is physically determined and which stellar parameters and properties are relevant.

In the CAK-like descriptions (including Gräfener & Hamann, 2005) the condition that is required to obtain a solution passing smoothly through the critical point fixes the mass-loss rate, leading to a formula that allows the calculation of $\dot{M}$ from other known quantities at the critical point. One of the easiest cases is the CAK model with the zero sound speed approximation. Using Eq. (3.80) in the corresponding equation of motion leads immediately to an expression for the constant C:

$$C = \frac{GM_*\,(1-\Gamma_\mathrm{e}) + \frac{\alpha}{1-\alpha} GM_*\,(1-\Gamma_\mathrm{e})}{\left[\frac{\alpha}{1-\alpha} GM_*\,(1-\Gamma_\mathrm{e})\right]^{\alpha}} \tag{5.1}$$

$$= (1-\alpha)^{(\alpha-1)}\,\alpha^{-\alpha}\,(GM_*)^{(1-\alpha)}\,(1-\Gamma_\mathrm{e})^{(1-\alpha)} \tag{5.2}$$

Combining this result with the definition of C (see Sect. 3.6.1), the mass-loss rate $\dot{M}$ can be directly obtained,

$$\dot{M}_\mathrm{CAK} = \frac{4\pi GM_*}{\sigma_\mathrm{e} v_\mathrm{th}} \alpha \left(\frac{1-\alpha}{1-\Gamma_\mathrm{e}}\right)^{\frac{1-\alpha}{\alpha}} (k\Gamma_\mathrm{e})^{\frac{1}{\alpha}}\,. \tag{5.3}$$

As Castor et al. (1975) already pointed out, this expression holds approximately also for a non-vanishing sound speed, if $a^2 \ll GM_* r_\mathrm{c}^{-1}\,(1-\Gamma_\mathrm{e})$ at the CAK critical point r_c and the temperature stratification follows a power-law $T \propto r^{-n}$. Hence, in the original CAK-theory the mass-loss rate $\dot{M}$ is implicitly fixed by the value needed for the constant C in the solution. The definition of C slightly changes for a non-zero sound speed, i.e.

$$C = \frac{k\Gamma_\mathrm{e} GM_*}{a^2 R_*} \left(\frac{\dot{M}\varkappa_\mathrm{e} v_\mathrm{th}}{4\pi a^2 R_*}\right)^{-\alpha} \tag{5.4}$$

(Friend & Abbott, 1986), and the finite disk (FD) correction (Friend & Abbott, 1986; Pauldrach et al., 1986) can be accounted for by $C \to C \cdot D_f$ in the equation of motion with D_f

being the FD-correction factor. The modifications from Pauldrach et al. (1986) add additional complexity and thus require an iteration. Using a few justified simplifications, one still obtains a formula of the same kind, namely

$$\dot{M}_{\mathrm{mCAK}} = \left[c_1 \left(\frac{2\pi}{D_{\mathrm{He}}} \right)^{\delta} \left(\frac{\sigma_{\mathrm{e}} v_{\mathrm{th}}}{4\pi} \right)^{\alpha} \frac{1}{k\Gamma_{\mathrm{e}} M_* 2^{-\frac{\delta}{2}}} \right]^{\frac{1}{\delta-\alpha}} \tag{5.5}$$

with D_{He} accounting for different helium abundances and a rather complex factor $c_1 = c_1(R_*,M_*,\Gamma_{\mathrm{e}},\alpha)$ whose detailed expression is of no importance for this discussion. An analytic approximation made by Kudritzki et al. (1989) again shows a similar relation between the mass-loss rate and C which acts as an eigenvalue of a non-linear differential equation, leading to what they called a "cooking recipe for $\dot{M}$". Newer extensions, such as Kudritzki (2002), do not change this fundamental aspect, but only add further "correction factors" to $\dot{M}_{\mathrm{CAK}}$.

The Eq. (3.155) from Gräfener & Hamann (2005), using the generalized CAK approach, is similar in the sense that it provides $\dot{M}$ for given values at the critical point. What makes it different from the recipes above, is the explicit dependence on the wind velocity at the critical point v_{c}, which cannot be expressed by other quantities in this approach. Therefore, the velocity field needs to be known here and the formula can only be used in an iterative way, while the other ones above do not include the resulting wind velocity law. Although the calculation of $\alpha(r)$ in the approach from Gräfener & Hamann (2005) is based on a CAK-like description of a_{rad}, the hydrodynamic equation that is eventually used for obtaining $v(r)$ and $\dot{M}$ is linearized.

Nevertheless, all the concepts mentioned above have in common that $\dot{M}$ is fixed by a constraint affecting the overall solution. This stems from the description of the radiative acceleration $a_{\mathrm{rad}}(r) = g(r) \cdot \Gamma_{\mathrm{rad}}(r)$ in the hydrodynamic equation. In the "standard form" the hydrodynamic equation

$$\frac{\mathrm{d}v}{\mathrm{d}r} = -\frac{g}{v}\frac{\tilde{\mathcal{F}}}{\tilde{\mathcal{G}}} \tag{5.6}$$

$$= \frac{g\left(\Gamma_{\mathrm{rad}} - 1\right) + \frac{2a^2}{r} - \frac{\mathrm{d}a^2}{\mathrm{d}r}}{v\left(1 - \frac{a^2}{v^2}\right)} \tag{5.7}$$

is linear in the velocity gradient and the critical point of the equation is identical to the sonic point. However, when inserting the ansatz

$$\Gamma_{\mathrm{rad}} \propto \left(r^2 v \frac{\mathrm{d}v}{\mathrm{d}r} \right)^{\alpha}, \tag{5.8}$$

the equation contains a second term involving the velocity gradient and thus becomes non-linear. Furthermore, due this additional term, the critical point is no longer identical to the sonic point. This is the case in all CAK-like theories and in Gräfener & Hamann (2005).

When this description is dropped, however, and e.g. a constant value for Γ_{rad}, i.e. $a_{\mathrm{rad}} \propto r^{-2}$, is used, the critical point of the equation is again identical to the sonic point with an easy calculation of the corresponding radius via

$$r_{\mathrm{c,Parker}} = \frac{GM_*\left(1 - \Gamma_{\mathrm{rad}}\right)}{2a^2} \tag{5.9}$$

in the case of an isothermal wind ($a = \text{const}$). In fact, Eq. (5.9) is an only slight generalization of Parker's solar wind description (cf. Lamers & Cassinelli, 1999) and thus the radius is labelled as $r_{\text{c,Parker}}$. In this description, i.e with constant Γ_{rad} (including $\Gamma_{\text{rad}} = 0$) and constant temperature, the mass-loss rate $\dot{M}$ does not enter the hydrodynamic equation* which means that any amount of mass could be driven.

In the iterative approach without force multiplier parameters presented in this work, Γ_{rad} enters the hydrodynamic equation as a precalculated quantity that has only a radial dependence, i.e. $\Gamma_{\text{rad}} = \Gamma_{\text{rad}}(r)$. The same is done in the Monte Carlo (MC) calculations e.g. by Lucy & Abbott (1993), Vink et al. (1999, 2000, 2001); Vink & de Koter (2005) or, more recently, Muijres et al. (2012). While this leads to a more complex trend in $\tilde{\mathcal{F}}$, the basic situation is comparable to the Parker case as the hydrodynamic Eq. (5.7) stays linear in the velocity gradient and thus the critical point in the equation is identical to the sonic point.

Does this mean that this approach also implies that any amount of mass could be driven and $\dot{M}$ is not fixed by the hydrodynamics? If one considers $\Gamma_{\text{rad}}(r)$ and $T(r)$ as given quantities, this is true. A velocity field could always be obtained via integrating Eq. (5.7) with these given values, regardless of $\dot{M}$, although this solution might not be monotonic.

Even if one assumes for a moment that the solution could be used in a model atmosphere calculation, its application would not necessarily give a hydrodynamically consistent stratification, as $\Gamma_{\text{rad}}(r)$ and $T(r)$ will usually change if $v(r)$ is changed. This has been demonstrated in the calculations of the response factor (Sect. 3.11.1) and the α-parameter (Sect. 3.9), which reflect the sensitivity of a_{rad} to changes of $\dot{M}$ and the velocity gradient, respectively. These changes require that the whole process needs to be iterated if Γ_{rad} is given as a function of the radius only.

Moreover, the mass-loss rate cannot be calculated analytically from an eigenvalue of the hydrodynamic equation. Instead it has to be calculated numerically and requires an iteration†. Lucy & Solomon (1970) calculated $\dot{M}$ from requiring $g_{\text{eff}} = 0$, i.e. $\Gamma_{\text{rad}} = 1$ at the sonic point. This condition is not exact for a spherical, non-isothermal atmosphere, but a close inspection of the acceleration plots for the HD models in chapter 4 reveals that the radius of $\Gamma_{\text{rad}} = 1$, which is for a consistent model equal to the point where $a_{\text{press}} = a_{\text{mech}}$, is actually very close to the sonic point. The reason for this is the small contribution of the $2a^2r$-term and the $\frac{\mathrm{d}a^2}{\mathrm{d}r}$-term to $\tilde{\mathcal{F}}$, which can be seen in all of the $\mathcal{F}$-$\mathcal{G}$-analysis plots (see, e.g., Fig. 3.2). With $\tilde{\mathcal{F}} \approx 1 - \Gamma_{\text{rad}}$, the hydrodynamic equation reduces to

$$\left(1 - \frac{a^2}{v^2}\right) v \frac{\mathrm{d}v}{\mathrm{d}r} = -g \cdot \tilde{\mathcal{F}} \tag{5.10}$$

$$\approx g\,(\Gamma_{\text{rad}} - 1) \tag{5.11}$$

which immediately shows that Γ_{rad} must be unity if the right-hand side should vanish at $v = a$.

In the original concept of Lucy & Solomon (1970), $\dot{M}$ is iteratively adjusted until this condition is fulfilled with sufficient accuracy. The $\mathcal{F}$-adjustment described in Sect. 3.11.1 can be seen as an extension of this method as $\dot{M}$ is adjusted such that the non-approximated $\mathcal{F}$,

*It should be noted that this is only true in the isothermal model. For a more accurate description of the solar coronal wind, Parker (1960) published a non-isothermal approach where the density and thus also $\dot{M}$ remains in the equation. The value of $\dot{M}$ then follows from the lower boundary values.

†It has to mentioned that iterative treatments are also required in modern CAK-like approaches, e.g. Kudritzki et al. (1989) and thereafter. Nevertheless, in these approaches the mass-loss rates are still obtained from conditions at a critical point which is not identical to the sonic point.

i.e. with the additional two terms, vanishes at $v = a$. As $\dot{M}$ still needs to have a certain value in order for the solution to pass smoothly through the critical point, the mass-loss rate can still be interpreted as an eigenvalue of the system, but now actually fixed at the sonic point, without having used an analytical approach for the calculation.

When looking at the Q-method or the τ-method (cf. Sect. 3.11.4) for fixing $\dot{M}$, one might argue that the mass-loss rate is not fixed by a condition at the sonic point in these cases. However, as in those cases the integration always starts from the radius $r_c = r(\mathcal{F} = 0)$ with a velocity $v_c = a(r_c)$, the same condition is fulfilled as above, i.e $\mathcal{F}$ vanishes at the sonic point. Thus, this point – potentially adjusted to also account for a turbulent velocity – remains the important point that sets the physics, even though $\dot{M}$ is then calculated by other conditions closing the system of equations. In this sense it can be understood that both, Pauldrach et al. (1986), who use a τ-method for their CMF-based calculations, and Vink et al. (1999), who are basically using the Q-method for their MC-based calculations, name the sonic point as the physically important point.

In contrast to the sonic point, which has a clear physical meaning, the physical role of a CAK-like critical point is debated (see, e.g., Owocki & Rybicki, 1986; Feldmeier, 1998; Owocki & Puls, 1999, 2002). Due to the different form of the hydrodynamic equation, it is clear that a CAK-like critical point sets the mass-loss rate, but there is no deeper physical meaning of the corresponding radius in a stationary situation. The situation, however, becomes more complex when stationarity is dropped. Using a density pertubation analysis, Abbott (1980) found radiative-acoustic waves, later also termed "Abbott waves", which propagate inwards and outwards (with very different speed) from the CAK critical point. For a Sobolev line force, the inward mode propagates at the CAK critical point with a velocity equal to the wind speed at this point. A detailed study about Abbott waves was later performed by Feldmeier & Shlosman (2002) who analyzed how these waves are shaping an eventually stationary solution for the wind velocity law. However, the CAK approximations are inherent to these studies which often also make use of the Sobolev approximation, thereby fueling the debate whether these waves might stem actually from the approximations themself (Feldmeier, 1998). Nevertheless, one can conclude that if it would be able to express the full radiative force correctly via an analytic expression that contains the velocity gradient, the inevitale result would be a critical point that is not identical to $v = a$, but further out. This point would then set a constraint to the mass-loss rate $\dot{M}$, thereby raising the question how this is possible from an information standpoint if the point is located in the supersonic regime. Insterestingly, if accounting for the fact that the quantity $a(r)$ can include a (micro-)turbulent velocity, even a critical point at $v = a$ is actually further out than the "raw" sonic point where $v = \sqrt{\mathcal{R}T/\mu}$, but here one could argue that the microturbulence should correspond to a turbulent motion while in the other case a completely new type of radiative-acoustic waves is needed for a physical information transport. Since this is debated and such critical point can only be approximately obtained, the only point than can be directly calculated is the one which is used in this work, namely the sonic point, potentially adjusted for turbulence.

Apart from this point, there is another physically meaningful point that comes to mind, namely the radius where radiation pressure balances gravity, i.e. $r(\Gamma_{\rm rad} = 1)$. Due to the hydrodynamic equation, also gas pressure must balance inertia at the same point. This point is located slightly further out than the sonic point. While this point is interesting and can be used to check hydrodynamical consistency, it is not a critical point if the hydrodynamic equation is written in the conventional form of Eq. 5.7. This means that although one could

in principle use $\Gamma_{\rm rad} \stackrel{!}{=} 1$ at $r(a_{\rm press} = a_{\rm mech})$ as an adjustment criterion for $\dot{M}$, it would not provide the value of $v(r_{\rm c})$ which is needed to smoothly pass through the sonic point.

Instead of adjusting $\dot{M}$ at all, one can of course instead modify only the velocity law and integrate the hydrodynamic equation inwards and outwards from $v = a$ for a given $\dot{M}$. However, as the terminal velocity can be deduced directly from observations, it is often more interesting to adjust $\dot{M}$ and mainly the form of the velocity field, so that v_∞ stays in a certain region that matches with the observations. Nevertheless, a pure velocity adjustment with a fixed $\dot{M}$ is just as doable with the implemented code, and opens the gate for future calculations revealing how a stellar atmosphere "should" look like for a given mass-loss rate $\dot{M}$.

5.2 The importance of the inner layers, especially for Wolf-Rayet stars

If the mass-loss rate is determined at the sonic point, the next question that pops up almost immediately is naturally: "What determines the location of the sonic point?" In a hydrodynamically consistent situation, the sonic point is located at $\tilde{\mathcal{F}} = 0$, i.e. the form of $\tilde{\mathcal{F}}(r)$ is a key ingredient here, in particular in the region inwards of the sonic point. Apart from the regime very close to the sonic point, the hydrodynamic equation can be approximated very well by the hydrostatic equation (cf. Sect. 3.4), which means that the inertia term is not important. Writing the remaining equation in the more general form

$$a_{\rm press} + a_{\rm rad} = g \tag{5.12}$$

$$-\frac{1}{\rho}\frac{{\rm d}P}{{\rm d}r} + a_{\rm rad} = g \tag{5.13}$$

already reveals which quantities are important in the subsonic regime: The density $\rho(r)$, the radiative acceleration $a_{\rm rad}(r)$, and the pressure due to thermal and turbulence motion $P(r)$. Using $P(r) = \rho(r) \cdot a^2(r)$ (ideal gas) as the equation of state and remembering that

$$a^2(r) = \frac{\mathcal{R}T(r)}{\mu(r)} + v_{\rm turb}^2 \tag{5.14}$$

yields that the pressure $P(r)$ can be expressed by more basic terms, leading to these four important quantities: $a_{\rm rad}(r)$, $\rho(r)$, $T(r)$, and $v_{\rm turb}$. The depth dependence of $\mu(r)$ will be omitted in the further discussion as the effect is small, though not completely negligible, especially for certain WR atmospheres where $\mu(r)$ can change on the order of up to 10% between R_* and $R_{\rm sonic}$.

The velocity itself it not important in the subsonic regime. It can be obtained via the hydrostatic equation and the equation of continuity (2.1), but since the hydrostatic equation provides a solution for the density stratification $\rho \propto \dot{M}/v$, only the ratio of $\dot{M}$ and v matters. As the hydrostatic equation does not contain a critical point, any combination of v and $\dot{M}$ yielding the same density would fulfill the hydrostatic equation. Only if $\dot{M}$ is given from another constraint, such as $Q = 1$ or from a boundary value as e.g. in the case of a wind driven by pure gas pressure, a unique solution for $v(r)$ and $\dot{M}$ is forced.

The acceleration due to radiation $a_{\rm rad}(r)$ can be split into three parts as explained in Sect. 3.6. The response calculations revealed that $a_{\rm lines}$ reacts to changes of the mass-loss

rate $\dot{M}$ and thus to changes of the density $\rho \propto \dot{M}$, while the α-calculations demonstrated that the velocity gradient has virtually no influence in the subsonic regime. Nevertheless, all models shown in the last chapter have demonstrated that none of the three parts of $a_{\rm rad}$ – neither line, nor Thomson, nor the true continuum contribution – are negligible here. While the line acceleration could be overpredicted due to the use of a depth-independent Doppler broadening velocity $v_{\rm dop}$ in the CMF calculations, it would not vanish completely if a more sophisticated treatment would be used, since significant contributions from certain elements are already expected as soon as the outflow velocity $v(r)$ exceeds the corresponding thermal velocity $v_{\rm th}$. This causes the iron group elements to become important already in the deeper layers, since they have the highest atomic mass of all considered elements. Furthermore, a significant turbulent velocity, i.e. $v_{\rm turb} \gtrsim v_{\rm th}$, would lead to a significant line contribution in the whole subsonic regime in any case[‡].

Any modification of the four quantities listed above will affect the location of the sonic point. Any turbulent velocity $v_{\rm turb} > 0$, for example, will shift the location of $v = a$ further outwards, leading eventually to a lower mass-loss rate (see also Lucy, 2007). For OB star atmospheres, there is at least some handle on the turbulent velocity $v_{\rm turb}$ by comparing observations with model spectra and deducing a required microturbulence from photospheric lines. For Wolf-Rayet atmospheres, the situation is worse. Most "classical" WR stars do not show any lines from the quasistatic region, i.e. there is no way of deducing a turbulent velocity using static models[§]. Furthermore, empirically deduced stellar parameters for WR stars clearly indicate that – at least for some subtypes – there is inflation and possibly even subphotospheric clumping (see, e.g., Cantiello et al., 2009; Gräfener et al., 2012; Gräfener & Vink, 2013; Sanyal et al., 2015). Typically, non-HD atmosphere models for Wolf-Rayet stars also show a strong radiative force in the innermost part with $\Gamma_{\rm rad} > 1$, something that could be avoided when introducing an effective opacity formalism (see Sect. 5.4 below) which could be motivated by optically thick clumps ("macroclumping", "porosity") already existing in these deep layers. One has to be aware that modifications of $\Gamma_{\rm rad}$ due to clumping or inflation can have significant effects on the location of the critical point and thus on the mass-loss rate. However, such modifications are in some cases propably the only way to combine the hydrodynamics with the expanding atmosphere models. In fact, the hydrodynamics could help to constrain the new free parameters of these modifications, such as the $\kappa_{\rm eff}$-mechanism which will be described in Sect. 5.4, thereby providing a certain insight into the otherwise hidden deeper layers of Wolf-Rayet stars.

5.3 The incompleteness of the line opacities

Although the PoWR code has been updated during this work to account for more atomic levels than ever before, the total number of atomic levels considered in an atmosphere models is still an important issue as the calculation time is crucially affected. As demonstrated in the previous chapter, it is essential to include all elements and ionization stages important for the driving of the wind. As a compromise between calculation time and considering all elements,

[‡]It should be kept in mind that a significant turbulent velocity will furthermore increase the total outward acceleration in the outermost wind part as the $2a^2/r$-term contributing to $a_{\rm press}$ becomes important at very large radii since it drops off much slower than gravity.

[§]A handle on the microturbulent velocities could potentially be obtained from short-time variabilities observed in WR spectra and their correlations with the stellar parameters (see, e.g., Michaux et al., 2014). This of course only works if the underlying phenomena indeed stem from the subsonic layers.

one can think of a scaling factor for the line opacity which could account for the elements not included in a model.

As the important contributions of the additional elements only affect the acceleration due to line absorption, a quick and easy ad-hoc modification would be to scale this contribution with a factor s_{lines}, i.e.

$$a_{\mathrm{rad,eff}}(r) = s_{\mathrm{lines}} \cdot [a_{\mathrm{rad}}(r) - a_{\mathrm{cont}}(r)] + a_{\mathrm{cont}}(r). \tag{5.15}$$

The "effective" $a_{\mathrm{rad,eff}}$ denotes the values taken into account for by the hydrodynamic equation, while a_{rad} and a_{cont} refer to the actual output from the radiative transfer calculation. The benefit of this simple approach is that it could be limited to the hydrodynamic calculations and thus is easy to implement and to handle.

However, a problem with this simple scaling of the line acceleration is that the quantity $a_{\mathrm{line}} = a_{\mathrm{rad}}(r) - a_{\mathrm{cont}}$ is often dominated by one element, mostly the generic one summarizing the iron group elements. If one thinks of this factor as something that should account for additional elements not covered in the calculation, then this scaling might actually be far away from the real situation. The detailed contribution plots (see, e.g., Fig. 4.5) reveal that each element contributes differently to a_{rad}, not only in strength, but often also in its depth-dependence. Still there are usually certain depth-dependent trends seen in several elements, so some kind of scaling rule is not completely unphysical. Unfortunately, the contribution of the generic element usually differs significantly from this rule, which means that a more sophisticated approach in the future could be to scale the line contributions of all elements without the generic one or going even more into detail by defining groups of elements with similar behavior which could then be scaled separately.

Another step could be to drop the idea that the scaling should be limited to the hydrodynamic calculations and instead implement the scaling directly to the opacities entering the radiative transfer calculation and the radiative rates. This would require a much more sophisticated implementation, but with the benefit that the whole model actually reflects what happens due to these additional opacities.

5.4 Macroclumping (Porosity)

A monotonic velocity field and a stable stratification in the subsonic regime can only be obtained for $\Gamma_{\mathrm{rad}} < 1$. However, non-HD stellar atmosphere models for certain stars, most notably Wolf-Rayet stars with thick winds, can yield a strong radiative acceleration which is so large that the Eddington limit could be violated even in the quasi-static regime, i.e. $\Gamma_{\mathrm{rad}} > 1$. The spectra resulting from such models do reflect particular observations, but the subsonic layers are not directly affecting the emergent spectrum, so it is basically unknown what happens there. As such stars tend to be stable, the "true" or "effective" Γ in these regions cannot exceed unity and instead something happens which is not covered by the basic assumptions of the model atmospheres (cf. Sect. 2.2).

One explanation is that $\Gamma_{\mathrm{rad}} > 1$ would imply a whole layer is lifted and there is either a mass eruption, which is not observed for these stars, or that there are things like an inflated envelope and/or convection (Gräfener et al., 2012; Sanyal et al., 2015, see, e.g.,). Handling inflation in the PoWR code is a problem as it comes with a density inversion which would imply a non-monotonic velocity field. Alternatively, one could argue that small-scale instabilities could arise and only fractions of the material are significantly lifted (Shaviv, 2001a,b). This could

potentially mark the onset of clumping as such. As these clumps are optically thick in this scenario, the microclumping approximation would not be sufficient here. Instead one has to account for the optical depth of the clumps, using a so-called "macroclumping" approach.

With a one-dimensional, spherically symmetric stellar atmosphere model it is impossible to describe the multidimensional clumping phenomenon in detail. However, one can try to account for the macroclumping effects, which is effectively the reduction of the opacity (see, e.g., Owocki et al., 2004). Following the concept of Oskinova et al. (2007), one can define an *effective* opacity

$$\kappa_{\mathrm{eff}} = \kappa_{\mathrm{f}} \, \frac{1 - e^{-\tau_{\mathrm{Cl}}}}{\tau_{\mathrm{Cl}}} \equiv \kappa_{\mathrm{f}} \, C_{\mathrm{macro}} \tag{5.16}$$

with κ_{f} being the opacity from the microclumping approximation. The optical depth of the clump τ_{Cl} is calculated via

$$\tau_{\mathrm{Cl}} = \kappa_{\mathrm{f}} D L_0 \sqrt[3]{\frac{3}{4\pi D} \frac{r^2}{R_*^2} \frac{v(r)}{v_\infty}} \tag{5.17}$$

assuming spherical clumps as, e.g., in Šurlan et al. (2012). The parameter L_0 is an additional free parameter describing a typical clump separation in units of the stellar radius. For $L_0 \to 0$, the clumps become optically thin and the microclumping approximation is recovered ($C_{\mathrm{macro}} \equiv 1$).

The formalism is of course ad-hoc only and the current implementation is such that not the opacity, but simply the resulting accelerations in the radiative transfer are reduced afterwards. In particular, all radiative acceleration terms are multiplied with the macroclumping factor, hence

$$a_{\mathrm{rad,eff}}(r) = C_{\mathrm{macro}}(r) \cdot a_{\mathrm{rad}}(r), \tag{5.18}$$

$$a_{\mathrm{cont,eff}}(r) = C_{\mathrm{macro}}(r) \cdot a_{\mathrm{cont}}(r), \tag{5.19}$$

$$\text{and} \qquad a_{\mathrm{thom,eff}}(r) = C_{\mathrm{macro}}(r) \cdot a_{\mathrm{thom}}(r), \tag{5.20}$$

where the "effective" values again denote the quantities entering the hydrodynamic calculations. This approach as been used for the inner layers of the WNE model shown in Sect. 4.3 but not for the other models in chapter 4.

Constraints could potentially come from stellar structure calculations or 3D Monte Carlo simulations with optically thick clumps, such as Šurlan et al. (2012) or Sundqvist et al. (2013), but these calculations have so far not been performed for Wolf-Rayet stars. Similar to what has been mentioned above for the "incomplete line opacities", the implementation could also be improved by considering the effective opacity directly in the radiative transfer calculation, even though this would be much more complex due to κ_{eff} not being simply scaled with a fixed factor. Instead, κ_{f} enters the scaling factor C_{macro} itself, which complicates a consistent implementation significantly.

5.5 Influences of the numerics

When discussing the results of the hydrodynamic calculations, one has to keep in mind that the stellar atmosphere models are subjected to numerical inaccuracies. The underlying numerical influence can be subtle sometimes, but needs to be considered in order to not confuse numerical effects with physical ones. For example, if the hydrodynamic equation would be integrated on

a too coarse grid, the errors – especially when integrating around the critical point – would be so large, that the resulting velocity field would be extremely inaccurate. Therefore, a 4th order Runge-Kutta method with an adaptive step size is applied in this work.

A way to check the accuracy of the Runge-Kutta integration is to ensure that the solution actually fulfills the hydrodynamic integration reasonably well. A visualized example for a Wolf-Rayet atmosphere is shown in Fig. 5.1, where the uppermost panel shows the

$$\text{HD-ratio} := \frac{a_{\text{rad}} + a_{\text{press}}}{a_{\text{mech}} + g}. \tag{5.21}$$

In general, the hydrodynamic equation is precisely recovered with very few outliers on the order of a percent in the wind part. In the quasi-hydrostatic part the ratio drops to ≈ 0.99, i.e. is off by 1%, most likely due to the exponential drop of the velocity which harms the precise calculation of the gas pressure term. With an error of one percent, the result is acceptable, but underlines why the exponential term needs to be seperated in the hydrostatic approach (see Sect. 3.4), where the integration is performed on the coarse grid without an adaptive fine spacing.

Apart from the direct numerics of the hydrodynamics, two more concerns come to mind, which will be discussed below:

5.5.1 Doppler velocity

As mentioned in Sect. 2.8, the radiative transfer in the comoving frame uses a constant Doppler velocity v_{dop}, which describes the "typical" line broadening. In the formal integral of the emergent spectrum, the line broadening is calculated fully depth-dependend for each line using the element's thermal speed and the microturbulence. However, for establishing the non-LTE population numbers, treating v_{dop} as a depth-independent quantity has proven to be sufficient and is therefore widely used in stellar atmosphere codes, such as PHOENIX (Hauschildt, 1992), FASTWIND (Santolaya-Rey et al., 1997), CMFGEN (Hillier & Miller, 1998), and PoWR. Nevertheless, the actual value of v_{dop} has to be carefully chosen in order to reflect the conditions in the type of star which is modeled, i.e. $v_{\text{dop}} \approx \sqrt{\bar{v}_{\text{th}}^2 + 2v_{\text{turb}}^2}$. For OB models, the choice of v_{dop} for the calculation of the population numbers can even have an influence on the emergent spectrum, as e.g. illustrated in Sander et al. (2015) or Shenar et al. (2015). In the context of hydrodynamical models, it is furthermore interesting to study the effect of v_{dop} on the radiative acceleration a_{rad}. Indeed, v_{dop} may have a crucial impact on the hydrodynamical solution and thus on $\dot{M}$ and v_∞.

In order to estimate the v_{dop}-influence, the hydrodynamically consistent B-star model which used $v_{\text{dop}} = 40\,\text{km/s}$ (due to the large value of the assumed turbulence) was recalculated with $v_{\text{dop}} = 100\,\text{km/s}$. Such a high velocity is of course not an appropriate representation of the physics in a B star, but it provides an excellent demonstration of the importance of v_{dop}. Calculating the radiative transfer with a higher v_{dop}-value based on a starting model using the converged population numbers from the solution with the lower v_{dop} mainly preserves the continuum optical depth scale and the model immediately has a consistent inner part. In the outer part, the calculated acceleration due to radiation and gas pressure now exceeds the sum of inertia and gravity and raises the work ratio up to $Q \approx 1.05$, i.e. by about 5%. If the hydrodynamic calculations are now performed, the mass-loss rate will be raised to compensate for the higher work ratio. The converged acceleration plots for both values of v_{dop} are shown in Fig. 5.2. The resulting mass-loss rate is $\log \dot{M} = -5.8$ for the model with $v_{\text{dop}} = 100\,\text{km/s}$,

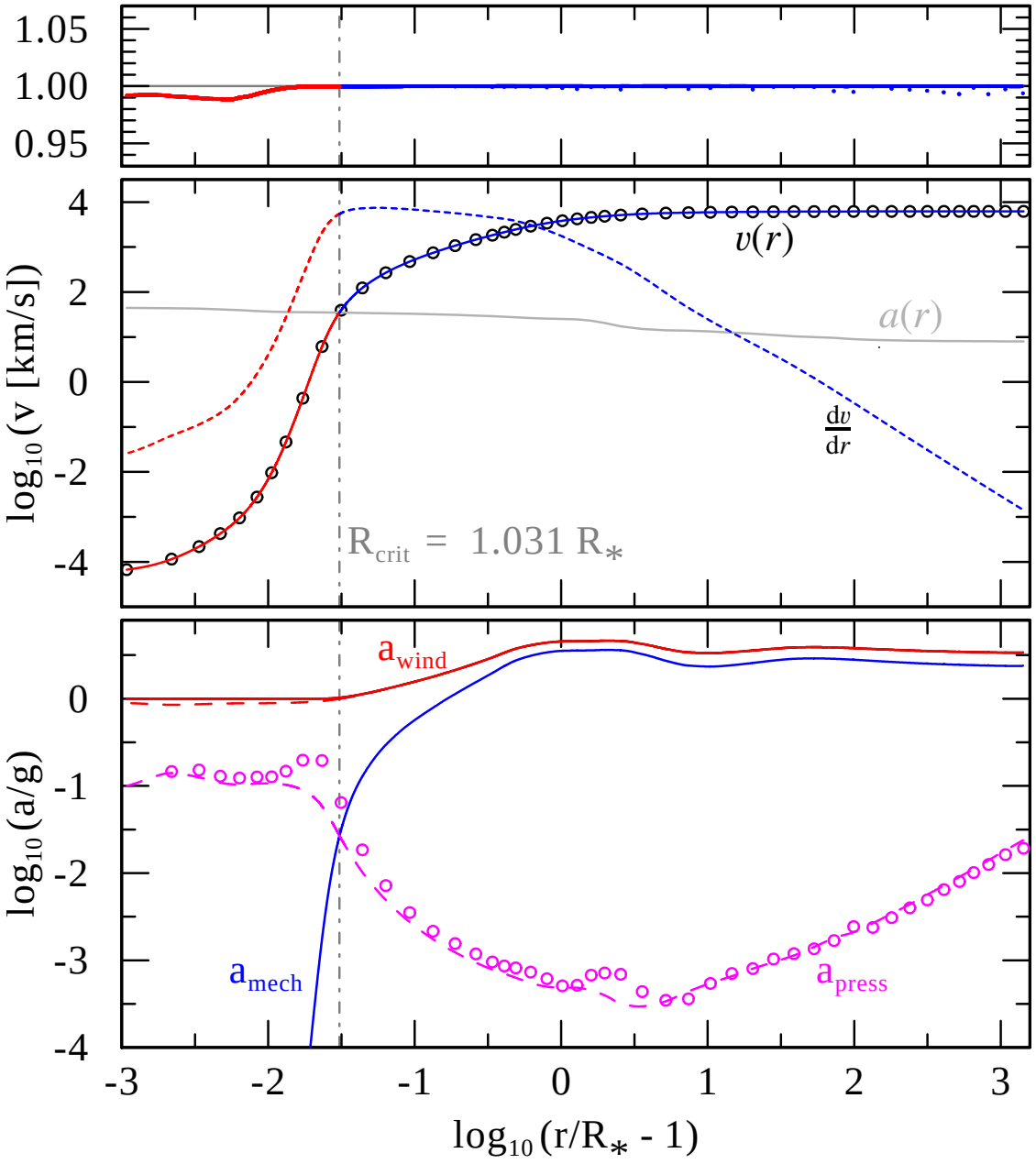

Figure 5.1 – Visualized detailed results of the Runge-Kutta (RK) integration of the hydrodynamic equation: The uppermost panel indicates how good the hydrodynamic equation is fulfilled while the second panel shows the results for the velocity field (solid line with circles) and the gradient (dashed line). In both panels, the red color highlights the results obtained by inward integration from the sonic point while the blue color highlights those from the outward integration. In the lowest panel, the accelerations are drawn using the fine grid points calculated by the adaptive step-size RK integration. To illustrate the importance of the fine grid ($\sim$ 5000 points in total), the results for $a_{\rm press}$ are also calculated using only the coarse grid steps (purple circles, 50 points in total). The dashed red curve in the inner part is the pure acceleration due to radiation only, while the the solid red curve refers to the sum of radiation and gas pressure.

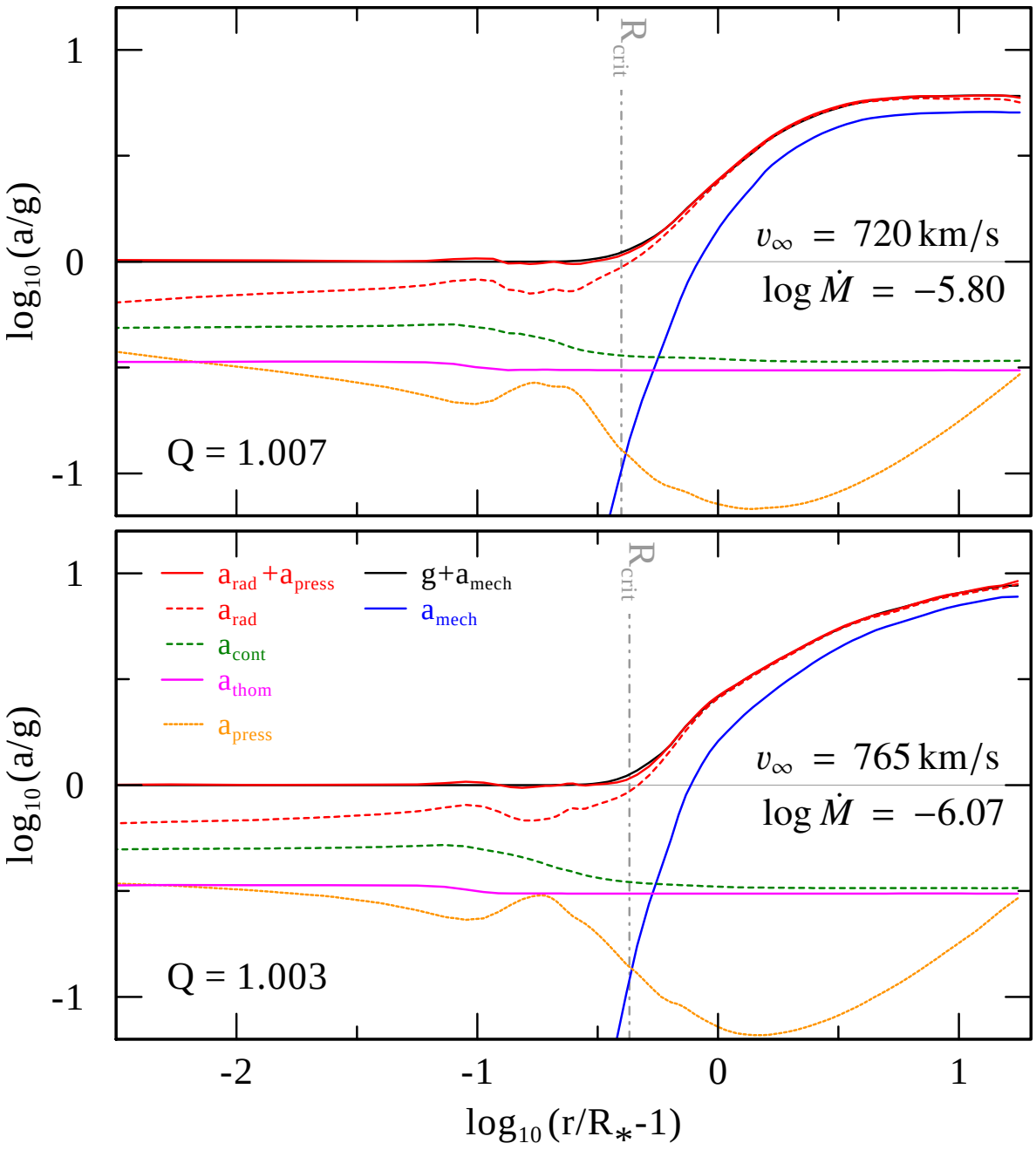

Figure 5.2 – Acceleration plot for the two hydrodynamic solutions using different values of $v_{\rm dop}$ in the radiative transfer. The upper panel shows the converged model obtained by using $v_{\rm dop} = 100\,{\rm km/s}$ while the lower one refers to the model calculated with $v_{\rm dop} = 40\,{\rm km/s}$. The critical point for both models is indicated by a dashed-dotted vertical line.

i.e. almost a factor of two higher than in the original model. In contrast, the terminal velocity is only slightly lower than in the original model with $v_\infty = 765\,\mathrm{km/s}$ and still on the order of $\approx 1.6\,v_\mathrm{esc}$ with $v_\mathrm{esc} = 443\,\mathrm{km/s}$. Given that with $T_{2/3} \approx 22\,\mathrm{kK}$ this model is close to the bistability jump where the expected ratio v_∞/v_esc raises from ~ 1.3 to ~ 2.6 (Lamers et al., 1995), this intermediate result is not surprising. However, since these models originate from a model that was made to represent an evolved HMXB donor, these ratios should not be overinterpreted.

The test calculation nevertheless underlines that it is essential to use an appropriate value of v_dop. Potentially, the PoWR code could be updated to use a depth-dependent value of v_dop which could be calculated directly from the assumed microcturbulence and the thermal speed. However, this requires significant updates of the comoving frame calculations and would introduce another direct interaction with the temperature stratification, which has always the risk of adding new sources of numerical instabilities. Regardless, such vital modifications are beyond the scope of the present work and will be performed in a follow-up DFG project.

5.5.2 The importance of a proper starting model

While the influence of v_dop is obvious, there is another, somewhat more subtle but important influence due to the starting model used for the hydrodynamic calculations. The fact that a successful convergence of a stellar atmosphere model essentially depends on having a proper starting model is inherent to modern stellar atmosphere codes. Due to the complex mechanisms used in them, some codes like CMFGEN do not even allow it to start a calculation without having an old, converged model as a starting approach (Hillier, 2003). In PoWR it is usually more convenient to start from a old, converged model, but it is also possible to start from "scratch", i.e. either from LTE or a slightly "tuned" version that can be more helpful for calculating objects with higher T_*. For non-HD models, the choice of the start approximation mostly affects how much iterations are needed to obtain a converged model, while only in some cases the start approximation is so bad, that convergence cannot be obtained at all. However, for the successful convergence of a consistent hydrodynamic model, the standard start approximations alone are not sufficient and additional constraints have to be taken into account in a starting model.

Before the first calculation of the velocity field via the hydrodynamic equation, there needs to be some start approximation for $v(r)$. While in the inner regime the consistent hydrostatic solution can be used early on as it can be applied for any value of $\dot{M}$, the wind velocity law must be prescribed, usually by a β-law. The choice of the β-value turns out to be quite important due the slope of its gradient in the inner part.

The gradient of a β-type velocity law has the form

$$\frac{\mathrm{d}v}{\mathrm{d}r} = v_\infty \cdot \beta \frac{R_*}{r^2} \left(1 - \frac{R_*}{r}\right)^{\beta-1} \tag{5.22}$$

which is monotonically increasing inwards for $\beta \leq 1$, but has a turning point for $\beta > 1$. The gradient of the hydrostatic solution, to which the β-law is connected, increases outwards, apart from possible small-scale deviations due to situations like a non-monotonic situation in the temperature stratification. As PoWR usually demands that not only the velocity $v(r)$, but also the gradient must be continuous, it can happen that the gradient reaches much larger values in the case of $\beta \leq 1$ than it would if $\beta > 1$ is used. This is illustrated in the left panel of Fig. 5.3, where the velocity gradient for two WO models are compared. The model that

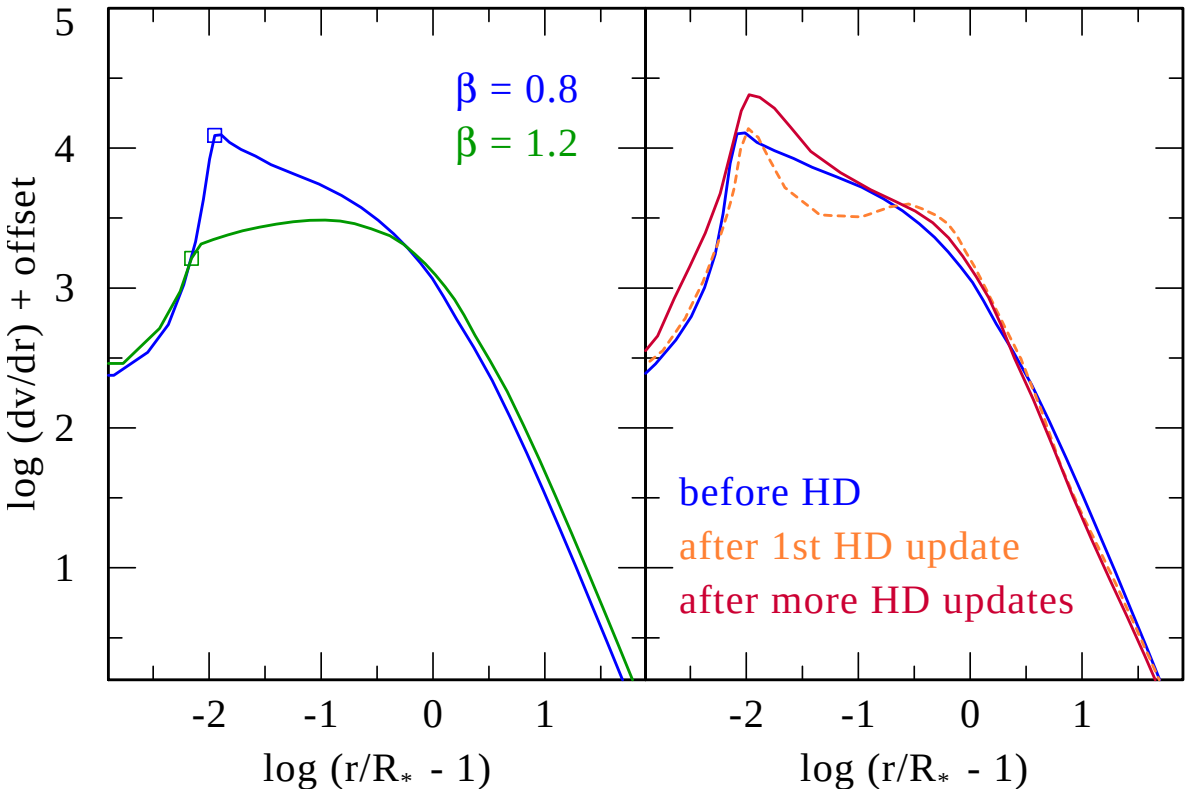

Figure 5.3 – Left panel: The velocity gradient is compared for two WO star models using different β-laws in the wind. The connection point to the hydrostatic solution is indicated by a square. Right panel: The velocity gradient of a starting model with $\beta = 0.8$ in the wind is compared to the gradient after the first and several more hydrodynamic velocity updates.

uses $\beta = 1.2$ has a much smoother transition to the inner region and the absolute value of the gradient outside of the connection point is about a factor of five lower than for the model using $\beta = 0.8$.

The effects of the velocity field on the radiative acceleration are so significant, that a "bad" choice of the starting model can prevent the success of the hydrodynamic calculations, i.e. the model never converges to a consistent solution. This is illustrated in the right panel of Fig. 5.3 where a WO model with $\beta = 0.8$ has been used as the starting model and then the inclusion of the hydrodynamics has been switched on. The velocity gradient of the starting model has a peak which cannot be smoothed out even after several hydrodynamic velocity field updates. An inspection of the acceleration balance would reveal that in this region the hydrodynamic consistency has not been achieved.

The outcome of this test calculations underlines that a proper starting model is vital for the success of the HD calculations and the demands for such a starting model are higher than for non-HD stellar atmosphere models. While in priciple the choice of β in the starting model would not lead to different hydrodynamic solutions, a "bad" choice can lead to the effect that this solution cannot be found. Thus, for HD starting models the choice of β should be made based on the connection condition, as the form of the velocity field in the wind will quickly be adjusted to radiative acceleration after very few, sometimes even just one or two HD updates if the calculations do not require a significant damping.

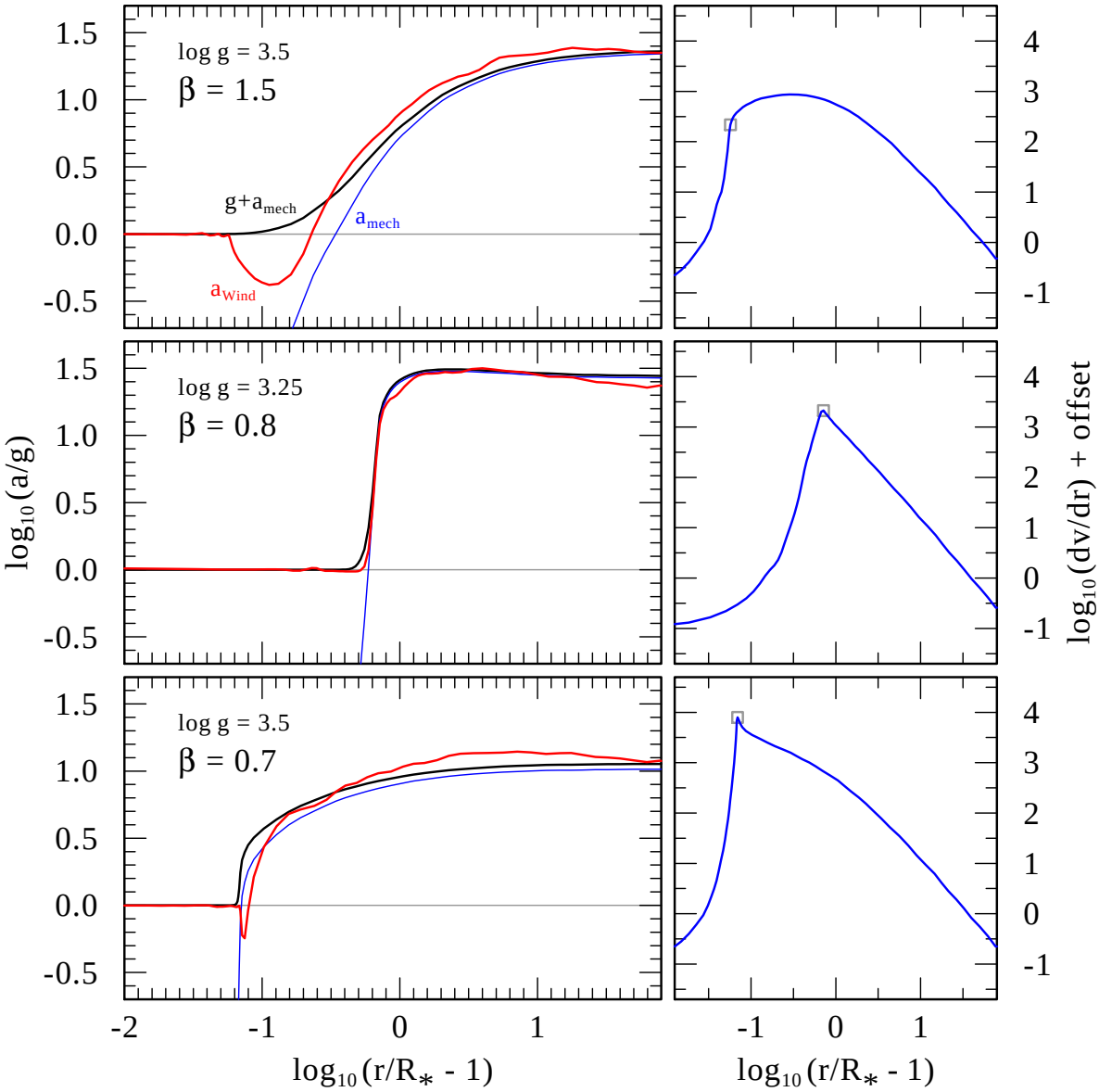

Figure 5.4 – Acceleration balance (left panels) and velocity gradients (right panels) for three O-star models with $T_* = 32.5\,\mathrm{kK}$ using different prescribed wind velocity laws connected to a quasi-hydrostatic part. In the acceleration plots, only the sum of radiation and gas pressure (a_{Wind}), the inertia (a_{mech}), and the sum of inertia and gravity are shown. In the right panels, the gradient for the resulting velocity fields are displayed with a gray square indicating the connection point between the β-law and the quasi-hydrostatic solution.

It should be mentioned that while $\beta > 1$ usually provides a better connection, there is no obvious "golden value" for starting models. The connection of the two velocity domains is rather complex and sometimes even models with $\beta < 1$ can have a decent connection situation, if the connection point happens to be further out. A few examples for non-HD O star models with different β-laws are illustrated in Fig. 5.4, where acceleration plots and corresponding velocity gradients are shown. The uppermost panels show a model with a smooth gradient, while the lowest ones illustrate the previously discussed typical problem for $\beta < 1$. The panels in the center show the rare situation where the supersonic connection point leads to a moderate gradient maximum, even though the transition in gradient is not really smooth between the two regimes.

5.6 Line driving and metallicity

All models presented in Chapter 4 were calculated for Galactic metallicity. In all these models the iron group elements turned out to be the main drivers. However, when transitioning to lower metallicity environments, the abundance of the iron group decreases for all kinds of stars as theses elements cannot be produced by the stars themselves unless shortly before or during the core collapse. Although the models also demonstrate that a high abundance of an element does not correlate with a major role in the wind driving, the contribution from a particular element to the radiative driving should still go down if the abundance is reduced.

A detailed study for different metallicities Z is beyond the scope of this work. Gräfener & Hamann (2008) calculated a series of models for WN stars and obtained that in order to have the same mass-loss rates as observed at $Z_\odot$, the stars need to reside closer to the Eddington limit $\Gamma_e = 1$, i.e. their luminosity will be higher if one compares stars with the same mass M_*. Gräfener & Hamann (2008) further calculated a few models without iron group elements and thereby simulated the winds of the first WNh stars where CNO had been produced by their own nuclear burning. Although the detailed contribution of the elements to the radiative acceleration could not be studied at this time, the iron-free models already indirectly proved that with lowering the abundance of the iron group elements, other elements like CNO are sufficiently able to take over the wind driving. This is also indicated by the Monte Carlo results from Vink & de Koter (2005), who found that WR mass-loss rates does significantly depend on Z around solar metallicity, but this dependency weakens for lower Z. For WC stars, it in fact almost vanishes for metallicities lower than $\log Z/Z_\odot \simeq -3$ because the wind is then driven by carbon which the stars have produced themselves.

With the additions made in this work, it is now possible to get an even more detailed look on the models and one can study the depth-dependent contribution of each element. An example for an O-star at SMC metallicity with $Q \approx 1$, which will serve as a starting candidate for future HD calculations, is shown in Fig. 5.5. It clearly reveals that, for this star, the iron group elements do not contribute significantly to the acceleration as their contribution is below the Thomson term throughout the atmosphere. Instead, oxygen, carbon, and nitrogen – in this order – are the main driving elements in the wind. This illustrates that not only for WN stars with their enriched nitrogen, but also for OB stars with a standard CNO-distribution, the CNO elements can provide a sufficient wind driving, even though their abundances are also lower in the SMC.

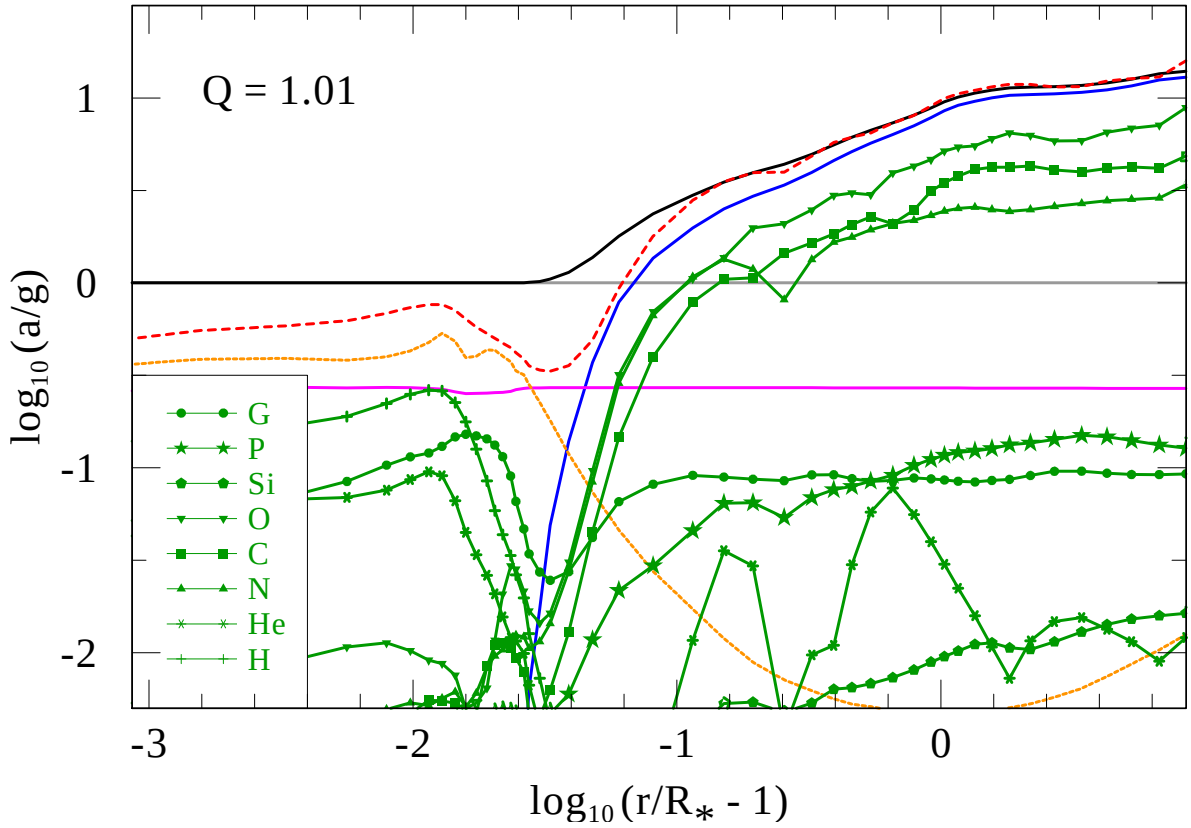

Figure 5.5 – Acceleration contributions from different elements (green curves with symbols) for a non-HD, but energy-consistent O-star model with $T_* = 34\,\mathrm{kK}$, $\log L/L_\odot = 5.8$, and SMC metallicity. In contrast to the Galactic models, now CNO is driving the wind instead of the iron group elements (denoted by G).

5.7 Influence of rotation

In the stellar atmosphere models used in this work, the stars are not rotating. Nevertheless, it is worth to discuss the potential effects of rotation on the hydrodynamics and the resulting wind parameters. If rotation is present, the wind is in principle not spherical. However, noticeable deviations from spherical symmetry should only occur if a star rotates at significant fraction of the critical velocity

$$v_{\mathrm{crit,rot}}(r) = \sqrt{\frac{GM_*}{r}\,(1-\Gamma_\mathrm{e})}, \tag{5.23}$$

i.e. the rotational velocity where the centrifugal acceleration would equalize gravity reduced by the Thomson acceleration. Note that this critical velocity refers to the rotational velocity and should not be confused with the wind velocity $v(r_\mathrm{c})$ referring to the wind speed at critical point of the hydrodynamic equation, i.e. where $\mathcal{F} = \mathcal{G} = 0$.

For a first study, it is helpful to restrict the analysis to the equatorial plane, where the effects of rotation are largest anyhow. Assuming no co-rotation beyond R_*, the hydrodynamic equation can be augmented by replacing $\tilde{\mathcal{F}}$ with

$$\tilde{\mathcal{F}}_\mathrm{rot} = \tilde{\mathcal{F}} - \frac{v_\mathrm{rot}^2(R_*)\cdot R_*}{r^3}. \tag{5.24}$$

In the case of co-rotation up to a certain radius $R_{\rm cor} > R_*$, the additional term in $\tilde{\mathcal{F}}$ needs to be split up into two parts:

$$r \leq R_{\rm cor}: \quad \tilde{\mathcal{F}}_{\rm rot} = \tilde{\mathcal{F}} - \frac{v_{\rm rot}^2(R_{\rm cor}) \cdot r}{R_{\rm cor}^2} \tag{5.25}$$

$$r > R_{\rm cor}: \quad \tilde{\mathcal{F}}_{\rm rot} = \tilde{\mathcal{F}} - \frac{v_{\rm rot}^2(R_{\rm cor}) \cdot R_{\rm cor}^2}{r^3} \tag{5.26}$$

For a non-spherical wind, the global mass-loss rate $\dot{M}$ has to be obtained by integrating over the mass flux for all latitudes. Instead of using $\dot{M}$ in the equations, it is therefore more convenient to use the mass flux $F_{\rm m}$ in the equatorial plane. To account for this difference, the replacement

$$\frac{\dot{M}}{4\pi} \rightarrow R_*^2 \cdot F_{\rm m} \tag{5.27}$$

is sufficient in all equations where $\dot{M}$ usually occurs.

Assuming that rotation is only considered in the hydrodynamics as described above and potentially in the formal integral (see Shenar et al., 2014, for details on how the latter is treated in the PoWR code) to check the visual effects in the emergent spectrum, the additional term in $\mathcal{F}$ leads to a decreasing of $\mathcal{F}$, most notably around the co-rotation radius $R_{\rm cor}$, since its influence is monotonically decreasing inwards and outwards from there. From this one can conclude, that – unless $R_{\rm cor}$ is located far out in the wind – the mass flux $F_{\rm m}$ should be higher than in the non-rotating case as the radius where $\mathcal{F}$ vanishes will be shifted inwards compared to the non-rotating case. As a consequence, the terminal velocity will likely be lower. This result has indeed been found by Friend & Abbott (1986) using the CAK approach with the finite disk correction plus a rotation term[¶] similar to the one above (without considering co-rotation beyond the photosphere). More recent calculations by Curé et al. (2012) using an mCAK approach with a limb-darkened finite-disk correction factor studied three different cases and obtained an $\dot{M}$-increase of about 10% together with a reduction of v_∞ of the same order for the fast-rotating case. For slow rotation, the effects turned out to be negligible. In a potential follow-up to this work, the rotational term described above could be added to the PoWR code routines. Calculating the hydrodynamic solution would not only allow a cross-check of the findings from Friend & Abbott (1986) and Curé et al. (2012), which were performed for O stars, but also allow an extension to Wolf-Rayet stars. A more sophisticated treatment for fast rotating stars, which would account for latitude-dependent stellar parameters, such as $T_{\rm eff}(\theta) \propto \sqrt[4]{g_{\rm eff}(\theta)}$ (von Zeipel, 1924), and should lead to a latitude-dependent terminal velocity v_∞, would require a multi-dimensional approach and is beyond of what could be reached with CMF calculations on the current generation of computers.

[¶]Friend & Abbott (1986) also studied the pure effect of rotation on a CAK model without the finite disk (FD) correction. The isolated effect has a similar trend, i.e. the terminal velocity is reduced. However, the FD-correction is large and thus even the combined effect will usually lead to higher terminal velocities when comparing the combined (FD + rotation) results with uncorrected CAK.

Chapter 6

Summary and conclusions

The goal of this work was to develop an expanding stellar atmosphere code that is able to calculate hydrodynamically consistent models, especially for dense stellar winds. This has been achieved by extending the Potsdam Wolf-Rayet (PoWR) code such that the velocity field and the mass-loss rate can be obtained from the detailed solution of the hydrodynamical equation. In order to provide realistic models and results, the PoWR code has been significantly upgraded beyond the pure implementation of the hydrodynamics. These updates include a more sophisticated handling of the inner boundary, the assurance of the prescribed total continuum optical depth, the inclusion of the thermal balance method for obtaining the temperature stratification, and a more efficient treatment for the solution of the statistical equations that enabled the code to handle more atomic levels.

An ancillary outcome of this work was the development of a relatively fast and reliable consistent treatment of the quasi-hydrostatic layers, even in standard models which are not hydrodynamically consistent, but use a prescribed wind velocity law. This new method, which has become a standard in the PoWR models, is described in detail in Sander et al. (2015) and allows to calculate accurate O and B star models with PoWR.

Beside CAK-like and Monte Carlo (MC) methods, hydrodynamically consistent stellar atmosphere models using a comoving frame (CMF) radiative transfer provide a third approach to obtain theoretical mass-loss rates. Their detailed treatment of the radiative transfer allows a depth-dependent solution of the momentum equation, enabling them to provide a locally and globally consistent treatment, which is superior to both of the other methods. This consistency, however, comes with high computational costs, so that the total number of atomic levels has to be restricted. Even though this limit has been lifted in this work and the new generation of PoWR models are able to treat more atomic levels than ever, the total number of considered lines is still significantly below what can be done in the MC approach. In contrast to the CAK-like methods, the CMF calculations take much longer and calculations in more than one dimension or time-dependent calculations are impractical. The advantage of the CMF calculations is, however, that they do not assume any line strength distribution and do not become deficient when applied to denser winds. Lamers & Leitherer (1993) demonstrated that the mass-loss rates predicted by the modified CAK (mCAK) recipe from Kudritzki et al. (1989) increasingly deviate from what is deduced from observations as the winds become denser. Furthermore, as the CMF calculations basically perform a brute force integration to obtain $a_{\rm rad}$, they automatically take various effects like multiple scattering or line overlapping into account. Furthermore, they do not rely on the Sobolev approximation that is used in most CAK-like and MC methods. This is not only crucial when analyzing

Wolf-Rayet atmospheres, but also for studying the detailed stratification around the sonic point, where the Sobolev approximation is not well justified.

To obtain the velocity field and the mass-loss rate in a consistent way, the hydrodynamic equation is solved using the radiative acceleration calculated in the CMF radiative transfer. As the latter already requires a velocity stratification, an iterative approach is needed. Since the radiative acceleration is provided as a function of the radius by the CMF radiative transfer, the critical point of the hydrodynamic equation is the sonic point. To obtain the velocity field, the equation is integrated inwards and outwards from this point.

Three examples for hydrodynamically consistent stellar atmosphere models have been presented in this work: a WO model, a hydrogen-free WN model, and a B-star model. The broad range of applications stems from a new approach that considerably differs from earlier studies performed by Gräfener & Hamann (2005, 2008) and does no longer rely on force multiplier parameters. For the first time, a hydrodynamically consistent PoWR model could therefore be calculated for an OB-type star.

While more quantitative results will require much more models, one can already draw the following conclusions:

- The winds of Wolf-Rayet stars can be sufficiently explained by radiative driving, if multiple scattering is taken into account. In order to produce realistic atmosphere models for both, WR and OB stars, the inclusion of all elements and ionization stages that contribute to the total opacity is inevitable. If such elements are not taken into account, the deduced mass-loss rates will artificially be lower than the ones obtained via MC calculations or CAK-like predictions, simply due to the incompleteness of opacities. As a consequence, various elements, such as neon, magnesium, or sulfur need to be considered, even though they might not imprint on the emergent spectra, especially in the case of Wolf-Rayet stars.

- One of the biggest unknowns in Wolf-Rayet atmospheres is the magnitude of turbulent motion. The turbulent velocity has an important influence on the location of the critical point and thus has a hand in setting the mass-loss rate $\dot{M}$. However, unlike in O and B stars, where spectral fitting of photospheric lines does provide a certain handle on the microturbulence, the emergent spectrum for Wolf-Rayet stars is completely formed in the expanding layers in most cases, thereby giving no information about the turbulence around the sonic point. Constraints could only stem from such WR objects where at least a part of the spectrum is formed in the quasi-hydrostatic layers (see, e.g., Hainich et al., 2015; Massey et al., 2015) or potentially also from wind variabilities (e.g. Michaux et al., 2014), assuming that they are originating from these deeper layers.

- An inspection of the detailed contributions to the radiative acceleration of the B-star model (see lower panel of Fig. 4.16) yields that the elements important for line driving show the same trend as the inertia term, thereby demonstrating that for this star the line force is correlated with the inertia as predicted by the (m)CAK theory. Nevertheless there are deficiencies in the mCAK models, since they fail for WR winds. As line driving is sufficient to explain WR winds, these deficiencies have to stem from the underlying approximations made in the mCAK models.

- For Wolf-Rayet stars with thick winds, the velocity fields show deviations from a simple β-law and can have a plateau in the wind. As long as the precise behavior around and

below the sonic point is not important, hydrodynamic solutions can be approximated with prescribed velocity laws, such as a double-β-law, but its parameters seem to depend significantly on the spectral subtype.

- At Galactic metallicity, the iron group elements are most important for the wind driving in both, WR and OB stars. In lower metallicity regimes, where their abundances are lower, carbon, nitrogen, and oxygen are instead the main driving elements even though their abundances are also smaller.

Given that wind driving in hot stars is still poorly understood, the new hydrodynamic models developed in this work provide an excellent tool for follow-up studies that might help to revise the theory of radiation-driven stellar winds. While this will require additional efforts, the goal is to have a set of hydrodynamically consistent stellar atmosphere models over a wide range of mass-loss rates. If sufficiently designed, these models will eventually gain a predictive power, allowing to obtain mass-loss recipes and other relations that could be used in a larger astrophysical context, including

- a study of the $\dot{M}(\Gamma_\mathrm{e})$-relation in the region of $\eta \approx 1$, where different trends have been predicted (see, e.g. Kudritzki, 2002; Gräfener & Hamann, 2008; Vink et al., 2011) based on different approaches;
- the influence due to feedback (mass-loss, ionizing photons, kinetic energy, ...) from WR and OB stars on their surroundings, especially in clusters;
- a better constraint for the evolution of massive stars, including an independent prediction of the stellar mass from the atmosphere analyses;
- a precise quantification of the discrepancies with CAK-like predictions to provide hints for a potential "calibrated" CAK ansatz, which would provide a useful input to time-dependent and/or multidimensional calculations;
- a detailed insight in the metallicity dependence and the corresponding stellar yields across cosmic times.

Due the complete inclusion of the continuum contributions, it will even be possible to calculate hydrodynamically consistent models for the very first generation of stars and check whether they could have had continuum-driven winds. In summary, one can say that the models and techniques developed in this work will provide the basis for a variety of projects that can lead to a better understanding of massive stars, stellar winds, and their role in our universe from the first stars up the present day and beyond.

Appendix A

PoWR implementation details

In this appendix, the concepts and implementation schemes of certain routines are described in detail. The various sections are meant as an addition to the theoretical descriptions and discussions in the corresponding sections of the main text. They are not intended as a manual or even a full description of the PoWR code. A true manual for PoWR has been started by the members of the Potsdam group and is consistantly expanded. The current version of the manual is available online*.

A.1 Overall PoWR program scheme

What is referred to as "the PoWR code" technically consists of a set of programs which are executed in a certain order. The execution of these programs is performed by shell scripts, called "jobs". These jobs are what is actually started by the user. For a smoothly running model, only the first job ("wrstart") needs to be submitted, while all other ones are automatically started if the preceding one ended successfully. All executable programs are written in Fortran, the shell scripts are written using the Bourne-again shell (bash).

In capitals are the particular programs of the PoWR code, job names are written in italics:

1. Model Start (*wrstart*)
   a) WRSTART: Setup of radius and frequency grid, first velocity stratification, start approximation for n_i and J_ν
   b) STEAL: First solution of statistical equations (without iron)
   c) ADAPTER: (optional) Transfer of population numbers from on an old model to the new one
2. Main iteration (*wruniq*)
   a) WRCONT: Radiative transfer for continuum only
   b) COMO: Solution of the moment equations for continuum only
   c) COLI: Radiative transfer for continuum and lines in the co-moving frame

*`http://www.astro.physik.uni-potsdam.de/~htodt/manpowr.pdf`
Please note that the PoWR manual is currently neither a fully complete documentation, nor does it necessarily include all of the latest additions. Furthermore it documents the standard branch of the code and therefore does not include several additions presented in this work unless they were already merged into the standard branch.

d) STEAL: Temperature corrections, solution of the statistical equations, (optional) velocity stratification update

e) MODIFY: Interpolation of n_i and/or T for non-converged depth points in the solution of the statistical equations

3. Formal integration (*formal*)

a) WRCONT: Radiative transfer for continuum only

b) COMO: Solution of the moment equations for continuum only

c) FORMAL: Calculation of the emergent spectrum in the observer's frame

The major tasks of the main iteration, namely the solution of the statistical equation, the temperature corrections, the solution of the radiative transfer in the co-moving frame and the (optional) update of the velocity stratification are performed in the STEAL and COLI programs.

The input for a model atmosphere calculation is provided via the following files:

- CARDS: main input file containing all main settings for the calculation of a PoWR model
- DATOM: main atomic data input file, containing all considered elements, levels and transitions except for the iron group elements
- FORMAL_CARDS: additional input file for the calculation of the emergent spectrum in the `FORMAL` program containing the wavelength ranges and full list of lines which should be taken into account
- FEDAT: precalculated data file for the superlevel handling of the iron group elements, containing for example the detailed superlevel cross sections
- FEDAT_FORMAL: special version of FEDAT for the formal integral

If starting from an old, converged model, the old model file is of course also required.

A.2 Connection with a prescribed wind velocity law

Unless the velocity field is obtained via the hydrodynamic equation as presented in the main part of this work, PoWR models use a prescribed velocity law for the wind domain connected to another approximation for the inner part. The latter is either a simple barometric law or obtained by integrating the hydrostatic equation using the results from the comoving frame radiative transfer calculation as outlined in the Sects. 3.4 and A.5). In any case, the connection to the wind domain is made such, that the velocity gradient and the velocity itself are continous at the connection radius R_{con}.

In the PoWR code, the wind velocity law can be either a β- or a double-β-law. The β-law is parameterized as

$$v(r) = p_1 \left(1 - \frac{R_*}{r + p_2}\right)^{\beta}. \tag{A.1}$$

The parameters are adjusted such that v_∞ is reached at $R_{\max}$, maximum value of the model's radius grid, and a specified velocity v_{con} is reached at R_{con}. With given values for R_{con} and v_{con} from the approximation for the inner part, the beta-law parameters are

$$p_1 := v_{\mathrm{con}} \left(1 - \frac{R_*}{p_2 + R_{\mathrm{con}}}\right)^{-\beta} \tag{A.2}$$

$$p_2 := \sqrt{\frac{1}{4}\left(R_{\max} - R_* + R_{\mathrm{con}}\right)^2 + \frac{R_{\max} - \left(\frac{v_{\mathrm{con}}}{v_\infty}\right)^{1/\beta} R_{\mathrm{con}}}{1 - \left(\frac{v_{\mathrm{con}}}{v_\infty}\right)^{1/\beta}}} - \frac{1}{2}\left(R_{\max} - R_* + R_{\mathrm{con}}\right). \tag{A.3}$$

For a two-beta law, p_1 and p_2 are taken for the summand with the smaller β-value with v_∞ being replaced by $(1-q)v_\infty$. For the other one with the larger β (with weight q), it is assumed that the gradient does not contribute around the connection point and the parameters, which are defined in a similar way as in Eq. (A.1) have the simple form

$$p_1^{(2)} := q v_\infty \left(1 - \frac{R_*}{p_2^{(2)} + R_{\max}}\right)^{-\beta_2} \qquad \text{and} \tag{A.4}$$

$$p_2^{(2)} := R_* - R_{\mathrm{con}}. \tag{A.5}$$

A.3 Conservation of optical depth (for non-HD models)

As soon as the current Rosseland continuum optical depth $\tau_{\mathrm{Ross,cont}}(R_*)$ differs from the $\tau_{\max}$-value specified in the CARDS file by more than ε_τ (also given in CARDS), the inner part of the velocity field is adjusted to re-ensure that $\tau_{\mathrm{Ross,cont}}(R_*)$ matches $\tau_{\max}$. In models with a prescribed velocity law for the wind regime, a new velocity field can be calculated relatively easy, even if the innermost part is consistently solved using the hydrostatic equation.

There are two reasons why this mechanism uses only the Rosseland continuum optical depth $\tau_{\mathrm{Ross,cont}}$ instead of the total Rosseland optical depth τ_{Ross} which would include all line opacities. The first one is that line opacities can change significantly between two jobs, even when the overall changes to the model are only of minor order. The continuum usually does not react such a way and is therefore a better choice in order to avoid constant back and forth changes of the velocity stratification. The second reason is the complex calculation of the total Rosseland optical depth. While the continuum part requires only the continuum opacities and thus can be calculated with the help of a few subroutines, the total value requires the line opacities and thus can only be calculated during comoving-frame radiative transfer. Due to this major obstacle it would be impossible to immediately check if a certain change in the velocity field is sufficient in order to conserve the optical depth. In fact, this would mean that only rough trend changes could be made instead of precise adjustments. With the Rosseland continuum optical depth instead, direct checks and therefore precise adjustments of $v(r)$ are no problem.

The conservation of $\tau_{\mathrm{Ross,cont}}$ is done by the routine `ENSURETAUMAX` which is called after the corrections to the temperature and the population numbers in the `STEAL` program. In detail it performs the following steps:

1. Calculation of the current $\tau_{\mathrm{Ross,cont}}$-scale

2. Check if $\tau_{\max}$-iteration needs to be done. Criteria are:
   - $|\tau_{\mathrm{Ross,cont}}(R_*) - \tau_{\max}| > \varepsilon_\tau$
   - optional: hydrostatic equation is violated by more than 5%
3. Check if $\tau_{\max}$-iteration should be skipped due to one the following criteria (if switched on):
   - The full radiative acceleration has either not been computed or is unphysical (i.e. $a_{\mathrm{rad}}(r) \leq 0$)
   - optional: population number corrections are higher than an specified `CORLIMIT`
   - optional: Non-converged depth points during the Scharmer iteration (population number corrections)
   - optional: The flux consistency is violated by more than a specified limit

If none of the skipping criteria are fulfilled and the $\tau_{\max}$-iteration is executed, the routine continues as follows:

4. Calculation of g_{grav} or g_{eff}, depending on the model specifications. For fixed g_{eff}, also M_* is updated.
5. Calculation of depth-dependent $\Gamma_{\mathrm{rad}}(r)$
6. Main iteration loop:
   a) Calculation of a reference scale height and β-law parameters
   b) First grid construction (r, v, ρ) based on the wind law (outer part) and a barometric law (inner part)
   c) Interpolation of electron temperature T, sound speed a, population numbers n_i, and g_{eff}(r) on the new grid
   d) Precise integration of the hydrostatic equation to obtain the correct $v(r)$
   e) Redefined grid (r, ρ) based on the improved $v(r)$
   f) Interpolation of electron temperature T, sound speed a, population numbers n_i, and g_{eff}(r) on the improved grid
   g) Calculation of the current $\tau_{\mathrm{Ross,cont}}$-scale
   h) Optional "Overshooting check" during the first iteration only:
   If the current value of $\tau_{\mathrm{Ross,cont}}$ is larger than $\tau_{\max}$, but the initial guess before the iteration was below or vice versa, the new solution might not improve the situation as it could go too far into the opposite direction. This can be suppressed by mixing the current $\Gamma_{\mathrm{rad}}(r)$ with those values from the last `STEAL` job with a $\tau_{\max}$-iteration. If overshooting suppression is enabled, the mixing factor will be increased (i.e. the older $\Gamma_{\mathrm{rad}}(r)$ will be used to a larger fraction) until overshooting does no longer occur or the influence of the current $\Gamma_{\mathrm{rad}}(r)$ reaches a minimum of 0.1%.
   i) Comparison of new $\tau_{\mathrm{Ross,cont}}(R_*)$ with specified $\tau_{\max}$. If the difference is still larger than ε_τ, $v_{\min}$ is adjusted
      - via $v_{\min} = v_{\min,\mathrm{last}} \left(\frac{\tau_{\mathrm{Ross,cont}}(R_*)}{\tau_{\max}}\right)^{0.5 \cdot f_{\mathrm{damp}}}$ if $\tau_{\mathrm{Ross,cont}}(R_*) < \tau_{\max}$,

- via averaging between the last two values of $v_{\min}$ if $\tau_{\mathrm{Ross,cont}}(R_*) > \tau_{\max}$,
- via spline interpolation $v_{\min} = v(\tau_{\max})$ if $\tau_{\mathrm{Ross,cont}}(R_*) > \tau_{\max}$ and averaging was not successful.

The damping factor f_{damp} starts with a value of one and is divided by two each time the solutions start to oscillate.

Not more than 100 iterations are performed. If the difference between the intended $\tau_{\max}$ and the actual value is still larger than ε_τ, the velocity field from the iteration with the smallest difference is used.

7. Optional Damping: The new $v_{\min}$-value can be mixed with the old one in order to damp the corrections to the velocity field. An additional calculation of the iteration steps above is performed in this case.

8. Calculation of the velocity gradient and $R(\tau_{\mathrm{Ross,cont}} = 2/3)$

9. Interpolation of the temperatures and populations numbers of the last three `STEAL` jobs on the new radius grid.

After a successful run of the `ENSURETAUMAX` routine, the updated stratification is stored in the model file and the overall iteration continues with the calculation of the radiative transfer. The call of `ENSURETAUMAX` is caused by adding the FIX-parameter to the TAUMAX-line in the CARDS file. As this routine updates the velocity field with a prescribed law in the wind regime, this parameter should never be set when calculating hydrodynamically-consistent models. In such models, the conservation of the total optical depth can be ensured directly in the `HYDROSOLVE` routine and its subroutines.

A.4 The concept of the radiative transfer calculation

In the PoWR code, the radiative transfer in the comoving frame (CMF) is performed in the `COLI` program. This complex program calls a variety of routines whose listing would be beyond the scope of this work. However, the basic concepts described in Sect. 2.8 will be outlined here and can mostly be mapped to certain subroutines performing most of the task described in each item.

The ray-by-ray solution and thus the update of the Eddington factors is typically done only every 5th or 6th iteration. These jobs are referred to as `COLI+`[†], while those skipping them are simply called `COLI`.

In short, the radiative transfer scheme in the PoWR code can be summarized as follows:

1. Radiative transfer for continuum only (performed in the `WRCONT` and `COMO` programs before the start of `COLI`)

2. Main frequency loop:

   a) Calculation of opacities and emissivities for the current frequency range

[†]If the temporary file for the Eddington factors does not exist at all or belongs to a wrong model, the job is internally called `COLI++`. Apart from the creation of a new EDDI (fort.17) file, the `COLI++` also differs from `COLI+` in its redistribution handling.

b) `COLI+` only: Calculation of the Eddington parameters (f, g) from ray-by-ray solution using short characteristics (`SHORTRAY` routine)
Normal `COLI`: Load saved Eddington parameters from last `COLI+`

c) Calculation of J_ν and H_ν via solution of the moment equations using a differencing scheme (`COLIMO` routine)

d) Running frequency integration for J, H, κ_{Ross}, etc. (`FREQUINT` routine)

e) `COLI+` only: Storage of Eddington factors

3. Normalization of opacities and calculation of τ_{Ross} (`FREQUNORM` routine)

4. Optional: Calculation of response to velocity and/or density modification (requires double run of `COLI`)

A.5 Solving of the hydrostatic equation numerically

Note: This routine is only called if the full hydrodynamic treatment is ***not*** *switched on.*
The numerical implementation of the hydrostatic solution is done in the `velthin` routine which is called during the start of a model and at each time the velocity field is updated in `ensuretaumax` as described in Sect. 2.7. On top of the check whether the supposed value of $\tau_{\max}$ is reached at R_*, this routine will be executed additionally if the hydrostatic equation is violated by more than 5% (in the quasi-hydrostatic regime). To avoid a major disturbance of the model, additional options can be switched on that will suppress the calling of this routine in case of current large corrections to the population numbers or the temperature stratification.

The `velthin` routine is responsible for the actual integration of the hydrostatic equation and the proper connection to the prescribed wind velocity law. By default, the connection point is chosen such that $v(r)$ and $\frac{\mathrm{d}v}{\mathrm{d}r}$ are continuous. Alternatively, there is the option to force the connection point at a prespecified fraction of a, i.e. the combined speed of sound and turbulence. Here is a brief outline of the tasks performed in the `velthin`:

- outward integration of $b(r)$ to obtain $v(r)$ via the hydrostatic equation
- comparison with $a(r)$ to determine the outer boundary of the subsonic regime
- if necessary: monotonic enforcement of the calculated $v(r)$
- iterative search for the connection point with the predefined wind velocity law
  (can be reduced to one iteration if the sonic point or a fraction of the sound speed is specified as the connection criterion)
  1. The β-law parameters for the current connection point candidate $R_{\mathrm{con,cand}}$ are calculated
     $\rightarrow v(R_{\mathrm{con,cand}})$ stems from hydrostatic solution, ensuring a continuous $v(r)$
  2. The velocity gradients $\frac{\mathrm{d}v}{\mathrm{d}r}$ for the inner and outer velocity field in the region around $R_{\mathrm{con,cand}}$ are calculated
     $\rightarrow$ The point where both gradients match is the new $R_{\mathrm{con,cand}}$ for the next iteration
- Failsafe handling in the case of an oscillating solution for R_{con}

Table A.1 – Quantities in the hydro equation and their calculation in the PoWR code

Quantity	Symbol	calculated in program	calculated in subroutine
mean particle mass	μ	`STEAL`	`LINPOP`
electron temperature	T	`STEAL`	`TEMPCORR`
radiative acceleration	$a_{\rm rad}$	`COLI`	`FREQUINT`
optional:			
response factor	$\mathfrak{r}(\dot{M})$	`COLI`	`COLI`
force multiplier parameter	$\alpha(H_{\rm tot}, a_{\rm rad}, a_{\rm cont})$	`COLI`	`COLI`
force multiplier parameter	$k(\alpha, a_{\rm rad}, a_{\rm cont})$	`STEAL`	`HDSOLUTION`

- Storing of the results and warnings in case of a purely subsonic or supersonic regime

For a successful iteration, the location of $v(R_{\rm con,cand})$ is identical to the location where the difference of the velocity gradients vanishes. Due to the fact that the hydrostatic equation does not have a critical point and the separation of the exponential term from the equation (see Sect 3.4), there is no need for a finer grid as it is required for the hydrodynamic solution. Instead, a simple rectangular integration on the normal depth point grid (with 50 to 70 depth points) has proven to give sufficient results.

In the consistent approach using the full radiative acceleration $a_{\rm rad}$ from the CMF radiative transfer, the corrections, especially in the early iterations after starting a model, are usually very large and therefore might cause an unstable situation in the inner part of the model. The most efficient way to avoid large perturbations of the model and obtain generally decreasing corrections is to damp the values of $\Gamma_{\rm rad}$ with those from the last call of `ensuretaumax`.

A.6 Obtaining the hydrodynamically consistent velocity field

A.6.1 Calculation of the required quantities

The calculation of the velocity gradient via the hydrodynamic equation requires the following quantities:

1. the stellar mass M_* and radius grid (from R_* to $R_{\rm max}$),
2. the microturbulence in the form of $v_{\rm turb}$,
3. the temperature stratification $T(r)$ and the mean particle mass $\mu(r)$,
4. the radiative acceleration $a_{\rm rad}(r)$, and
5. the velocity at one given point, either the critical point or at one of the boundaries

From these values, only the first two are exactly given at the start of the model. While there are start approximations available for the temperature and $\mu(r)$, the radiative acceleration requires a comoving frame calculation. Thus, the first calculation of a velocity field via the hydrodynamic equation has to be after the first run of the full comoving frame radiative transfer done in a so-called `COLI++` job. From now on, all values are in principle given, even

though the level of corrections from the radiation field to population numbers is so high, that it is usually more helpful to wait until these corrections fall below a certain level.

The given quantities, which are updated in the routines listed in Table A.1, are passed to the `HYDROSOLVE` routine and further reduced in the hydrodynamic equation by introducing

$$a(r) = \sqrt{\frac{\mathcal{R}T(r)}{\mu(r)} + v_{\mathrm{turb}}^2}. \tag{A.6}$$

The `HYDROSOLVE`-routine acts as a container for everything that is related to the coupling of the hydrodynamics to the PoWR code. It reads out the corresponding options from the input file, calls the actual solution routine `HDSOLUTION` and handles the conservation of the optical depth and the update of the radius grid after a successful integration.

A.6.2 Integrating the hydrodynamic equation

While a depth point grid with 50 to 70 points is sufficient for all other tasks in the PoWR code, the integration of the hydrodynamic equations requires a much finer spacing, especially around the critical point $v = a$. Similar to the concept described in Gräfener & Hamann (2005), this is done using a fourth-order Runge-Kutta method with an adaptive step-size control. However, the integration is done over the radius in this work instead of the column depth s (see Eq. 3.92). Furthermore, the integration starts at the critical point and not at the outer boundary. While this does not fundamentally change the concept, it completely removes the number of iterations that Gräfener & Hamann (2005) needed to find the critical point. Instead the critical point is searched before the start of the integration using the current fine interpolations on the course grid. This is sufficient as the new implementation is now inside the `STEAL` program while it was a separate program in Gräfener & Hamann (2005), requiring a fully converged model. The advantage of the new approach is that it is possible to continue the main iteration between the radiative transfer and the solution of the statistical equations after a hydrodynamic velocity field update without going back to the approximations made at the start of a model. In turn, usually more hydrodynamic updates have to be performed, but as they do not require a converged model, this is generally computationally still much faster than the method from Gräfener & Hamann (2005).

The code routines for the fourth-order Runge-Kutta method with adaptive step-size control are based on Chapter 16.2 in "Numerical Recipes" (Press et al., 1992), providing basic routines for the solution of a ordinary differential equation system. The derivatives for the particular functions, here $v(r)$, of course have to be inserted by the user. The corresponding routine with the equations is named `cpderivs` and contains the expressions for $\frac{\mathrm{d}v}{\mathrm{d}r}$ in the normal form

$$\frac{\mathrm{d}v}{\mathrm{d}r} = -\frac{GM\left[1-\Gamma_{\mathrm{rad}}\right] - 2a^2 r + r^2 \frac{\mathrm{d}a^2}{\mathrm{d}r}}{\left(1-\frac{a^2}{v^2}\right) r^2 v} \tag{A.7}$$

and for the region close to the critical point, where l'Hospital's rule needs to be used, in the

form

$$\frac{\mathrm{d}v}{\mathrm{d}r} = -\frac{1}{2A}\left(B \pm \sqrt{B^2 - 4AC}\right) \tag{A.8}$$

with

$$A = -\frac{1}{v}\left(1 + \frac{a^2}{v^2}\right), \tag{A.9}$$

$$B = -\frac{2}{r}\left(1 - \frac{a^2}{v^2} - r\frac{a}{v^2}\frac{\mathrm{d}a}{\mathrm{d}r}\right), \tag{A.10}$$

$$\text{and} \quad C = \frac{GM_*}{r^2v^2}\frac{\mathrm{d}\Gamma}{\mathrm{d}r} + 2\frac{a^2}{r^2v} - \frac{1}{v}\frac{\mathrm{d}^2}{\mathrm{d}r^2}\left(a^2\right). \tag{A.11}$$

These expressions refer to the method without force multiplier parameters (cf. Sect. 3.11) and can be derived similar to the expressions given in Sect. 3.10 referring to the approach from Gräfener & Hamann (2005). The l'Hospital-version is used as soon as $|1 - a/v| < 10^{-2}$.

While a detailed discussion of the Runge-Kutta integration would be beyond the scope of this work and can e.g. be found in Chapter 16 of Press et al. (1992), the basic routines of the method and their interaction with the main hydro routines shall be outlined here:

- The Runge-Kutta routines are called `CPODEINT`, `CPDERIVS`, `CORKQS`, and `CPRKCK` and are based on their counterparts without the "CP"-prefix in Chapter 16.2 of Press et al. (1992). The base routine is `CPODEINT` which calls the other subroutines and is called itself for the integration of the velocity v in a given radius interval.

- As all quantities listed in Sect. A.6.1 as only available on the standard (coarse) depth point grid, their values on the fine grid have to be obtained via monotonic spline interpolation. This is also done in the `CPDERIVS` routine.

- After the critical point candidate has been determined via $r_\mathrm{c} = r(\mathcal{F} = 0)$ in the `HDSOLUTION`-routine, the routine `CPINT` is called, which manages the whole integration. Starting with $v(r_\mathrm{c}) = a(r_\mathrm{c})$, the inward integration is done first. For this `CPODEINT` is called with r_c as the starting point and the radius of the next inner coarse grid depth point as end point. Afterwards the routine is called again with the integration intervals matching the radius intervals of the coarse grid. This allows an easy storage of the resulting velocity field on the coarse grid. The same is then done for the outward integration.

- A slightly adjusted treatment had to be added in `CPINT` for the case that the critical point candidate radius r_c is numerically indistinguishable from a coarse grid point.

- In order to be able to check the integration results, all fine grid points that are calculated by the adaptive step size method in `CPODEINT` are stored, together with their integration results. A visualization example of these fine grid results can be seen in Fig. 5.1.

Afterwards, the mass-loss rate is adjusted according to one of the methods described in Sect. 3.11, depending on which options have been specified for the model. In some cases, it can also be necessary to exclude the inner and/or outer boundary points from the Runge-Kutta integration. If this is the case, the velocity field is extrapolated afterwards to the corresponding radii, using a grid that is ten times finer than the coarse grid.

A.7 Adjustments before the hydrodynamic solution

Unless performed on an already consistent or at almost consistent atmosphere model, the integration of the hydrodynamic equation usually cannot be performed without adjusting the input. In fact, if the integration would be performed right away using all input values as they are, most models would either crash during the integration or cause large perturbations in a model that might completely prevent the calculations from converging. It is therefore crucial to perform a few adjustments to the input values, in particular to $\Gamma_{\rm rad}$. The adjustments can basically be sorted into two groups, which occur in the code in the same order as they are listed here.

A.7.1 Damping adjustments

It is generally helpful, if not necessary to damp the input provided to the hydrodynamic integration routines. The velocity field is coupled to the density structure and changes there require an interpolation of the population numbers from the old to the new structure. The larger the changes in the density structure, the larger are usually be the following corrections, even if the interpolation is done properly as the number of total depth points is limited and the points are spaced in order to reflect several criteria, including a proper coverage of the velocity field. Large corrections from the statistical equation can in turn lead to significant changes in the radiative acceleration, which in the end determines the slope of the velocity field as it enters the hydrodynamic equation as a major factor. It is therefore important to produce situations that – at least in general – do not lead to large corrections, but instead cause relatively small adjustments which do not lead to a major perturbation of a current model situation.

To reach this goal, damping adjustments of $\Gamma_{\rm rad}(r)$ turned out to be very successful. From all terms entering $\mathcal{F}$, the $\Gamma_{\rm rad}$-term is by far the most important as it is usually much larger than the other two, i.e. it mainly determines the slope of the resulting velocity field $v(r)$. It is also the only term that depends directly on the results of the radiative transfer, even though there is of course also an indirect connection via the temperature on the gas-pressure terms. However, the temperature-dependent terms are small except the one entering $\mathcal{G}$ which determines the velocity at the sonic point. Therefore, $\Gamma_{\rm rad}$ is the "natural" candidate when thinking about damping input to the hydrodynamic equation.

In all cases, only the values $\Gamma_{\rm rad}(r)$ that enter the hydrodynamic equations and its preceding calculations are modified while the general calculation of $a_{\rm rad}$ in the CMF radiative transfer or the stellar mass M_* of a model are left untouched. Two major concepts are used to adjust $\Gamma_{\rm rad}(r)$ before the integration of the hydrodynamic equation. These are performed in the `hydro_prepcak`-subroutine and will be described in the following:

Reducing $\Gamma_{\rm rad}$-changes

An easy, but very effective approach to damp the effects of a hydrodynamic step to the velocity field (and thus to all other quantities as well) is to reduce the change between the $\Gamma_{\rm rad}$-values of the last hydro step and the current one. This is achieved by weighting the current values $\Gamma_{\rm rad,cur}$ with a damping factor $0 < f_{\rm reduce} < 1$ and adding the values from the last step $\Gamma_{\rm rad,last}$ with the remaining weight, i.e.

$$\Gamma_{\rm rad,use}(r) = f_{\rm reduce} \cdot \Gamma_{\rm rad,cur}(r) + (1 - f_{\rm reduce}) \cdot \Gamma_{\rm rad,last}(r) \tag{A.12}$$

with $\Gamma_{\rm rad,use}$ denoting the values which will actually be used in the hydrodynamic equation. This technique is similar to what happens in the `ensuretaumax`-routine if the correct hydrostatic integration is performed using also the full radiative acceleration.

Technically this damping requires the values of $\Gamma_{\rm rad,last}$ to be saved in the MODEL file. The vector containing the values is called GRDYN, in analogy to GRSTATIC which is used for the static case.[‡] Note that GRDYN contains the values of $\Gamma_{\rm rad,use}$, i.e. those values including all adjustments that have been made in the preceding hydro step as these are the values that have determined the (current) velocity field.

Mixing with an implied $\Gamma_{\rm rad}$

Another approach to reduce the effect on the velocity field is to mix the current value of $\Gamma_{\rm rad}$ with a quantity that will be referred to as $\Gamma_{\rm imp}$. It can be calculated by resorting the hydrodynamic equation, so that Γ is obtained instead of the velocity gradient. Using the present velocity field as an input then, one obtains an "implied Γ", i.e.

$$\Gamma_{\rm imp}(r) = \frac{{\rm d}v}{{\rm d}r}\left(1-\frac{a^2}{v^2}\right)\frac{r^2 v}{GM} - 2\frac{a^2 r}{GM} + 2\frac{r^2 a}{GM}\frac{{\rm d}a}{{\rm d}r} + 1. \tag{A.13}$$

Entering the hydrodynamic routines with this $\Gamma_{\rm imp}$ instead of $\Gamma_{\rm rad}$ would return the current velocity field without any changes. This means that such a situation also would always result in a solvable situation. However, one would not get closer to hydrodynamical consistency by using just $\Gamma_{\rm imp}$, so instead this value is mixed with the actual $\Gamma_{\rm rad}$ in a similar way as described for mixing current with previous values in Eq. (A.12).

As the current situation will in generally not be hydrodynamically consistent, the $\Gamma_{\rm imp}$ can be normalized, so that at least the overall work ratio Q (see Sect. 3.2) using the implied radiative acceleration is unity, i.e.

$$\Gamma_{\rm imp,norm}(r) = \Gamma_{\rm imp}(r)\cdot\frac{\int\limits_{R_*}^{R_{\rm max}}\Gamma_{\rm imp}(r)\frac{GM}{r^2}{\rm d}r}{\frac{1}{2}\left[v^2(R_{\rm max})-v^2(R_*)\right]+\frac{GM}{R_*}-\frac{GM}{R_{\rm max}}+\int\limits_{R_*}^{R_{\rm max}}\frac{1}{\rho}\frac{{\rm d}P}{{\rm d}r}{\rm d}r}. \tag{A.14}$$

Mixing the current $\Gamma_{\rm rad}$ with $\Gamma_{\rm imp}$ usually leads to small corrections, which is helpful, but it tends to preserve the present velocity field if this is done before each hydro step, if the mixing factor is around 0.5 or larger. Thus this method is not successful for a permanent use throughout the iterations, but it provides a great start for the first hydro step where no previous $\Gamma_{\rm rad}$ values are available for the damping method described previously. Therefore $\Gamma_{\rm imp}$ is used to initialize the GRDYN-vector, while afterwards the normal $\Gamma_{\rm rad}$-reducing is performed. This creates a smooth transition throughout the hydro iterations from the implied $\Gamma_{\rm rad}$-values representing a prescribed velocity field towards a consistent solution for a converged model.

A.7.2 Solvability adjustments

Even more fundamental than obtaining small corrections from a solution is to ensure that there is a solution at all. For some start models this is not a problem and no adjustments

[‡]The same vector cannot be used for both methods as the values for the quasi-hydrostatic method have an internal upper cut at $\Gamma_{\rm rad} = 0.9$

are required, but other models, especially the ones for WR stars, if they are taken from the model grids, show a complex behavior in a_{rad}, leading to a situation where $\mathcal{F}$ becomes zero at more than one depth point or even $\mathcal{F} < 0$ at the inner boundary. In such cases, monotonic solutions for $v(r)$ are not guaranteed and it might even be clear which $r(\mathcal{F} = 0)$ is the proper candidate for the sonic point. The $\mathcal{F}$-$\mathcal{G}$-plot introduced in Sect 3.10.1 provides a very good diagnostic tool here, helping to get an easy overview of a complex situation and understanding the troubles of a given model.

There are situations where the hydrodynamic integration just cannot be performed because $\mathcal{F} = 0$ or $\mathcal{G} = 0$ never occurs. In such cases local adjustments are not justified and the basic model parameters of the current model might simply not be appropriate for obtaining a model with $Q \approx 1$, i.e. which is at least roughly balanced energetically. The four situations where either $\mathcal{F}$ or $\mathcal{G}$ never becomes zero can be attributed to physical reasons, namely:

$\mathcal{F} < 0$ This usually implies $\Gamma_{\mathrm{rad}} > 1$ at all depths, i.e. the radiative pressure is larger than gravity everywhere in the stellar atmosphere. Unless all elements are completely ionized, which indicates that the main iteration between the CMF radiative transfer and the solution of the statistical equations ran into trouble, this means that either the assumed luminosity of the star is too high or its mass is too low.

$\mathcal{F} > 0$ The opposing situation implies $\Gamma_{\mathrm{rad}} < 1$ at all depths, which in turn means that the assumed luminosity is too low or the stellar mass is too high. On the numerical side, it should also be checked if the used model atom is correctly reflecting the current situation, in particular in the outer part where Γ_{rad} should be above unity. Especially if leading iron ions are only considered in the form of a control level, a significant fraction of the driving opacity might be missing. In those cases, adding additional iron levels and recalculating the model should help.

$\mathcal{G} < 0$ The wind speed is always subsonic. This basically never happens when starting from a model with a prescribed velocity field, but it could happen if v_∞ was not much above the sound speed and major temperature adjustments have been performed after the last hydro step. This either points to problems occurring in the temperature correction or an unphysical combination of stellar parameters.

$\mathcal{G} > 0$ The wind speed is already supersonic at the inner boundary. If all important elements and ions are already considered, the inner boundary is not deep enough in the atmosphere to reach a subsonic regime. Increasing the desired value of τ_{max} significantly and restarting the model atmosphere calculation should help here.

Unless one of these situations occur, adjustments can usually help to start hydrodynamic calculations, even if there is more than one point with $\mathcal{F} = 0$. It should be noted that the Γ_{rad}-damping including the start from Γ_{imp} already helps to reduce these cases significantly, but there will still be situations left, especially after a few hydro iterations when the "true" Γ_{rad} is more and more considered in the integration. Therefore if $\mathcal{F} = 0$ occurs more than once, the following adjustment scheme is executed:

- The radius with $\mathcal{F} = 0$ and $\frac{\mathrm{d}\mathcal{F}}{\mathrm{d}r} < 0$ that is nearest to $\mathcal{G} = 0$ is taken as the candidate radius r_{c} for the sonic point.
- For $r > r_{\mathrm{c}}$ all values of $\mathcal{F} > 0$ are prevented by adjusting the used value of Γ_{rad}

- For $r < r_c$ all values of $\mathcal{F} < 0$ are prevented by adjusting the used value of Γ_{rad}

The selection of the candidate radius r_c is of course crucial here and further adjustments or additional options might have to be added here in the future, but for the test cases so far this criterion is working fine. The adjustments in the inner and outer part are only performed at depth points where $\mathcal{F}$ would have the "wrong" sign, i.e. due to Eq. (3.150) no monotonic velocity field would be obtained. For this case the value

$$\Gamma_1(r) := 1 - 2\frac{a(r)\,r}{GM}\left(a(r) - r\frac{\mathrm{d}a}{\mathrm{d}r}\right) \tag{A.15}$$

is calculated and used via $c_f\Gamma_1(r)$ as a maximum value in the inner or via $c_f^{-1}\Gamma_1(r)$ as a minimum value for $\Gamma_{rad}(r)$ in the outer parts. The parameter c_f is a value close to unity. In the test calculations so far $c_f = 0.975$ has been used. To avoid artifacts in the calculated $v(r)$ and ensure a smooth transition through the sonic point, no adjustments to Γ_{rad} are made in the regime of $\frac{\mathrm{d}\mathcal{F}}{\mathrm{d}r} < 0$ around r_c.

A.8 Adjustments after the hydrodynamic solution

The velocity field calculated from the hydrodynamic equation is only used if it has been obtained by a successful, i.e. converged, iteration. If the hydro iteration was terminated by any other case, such as reaching the maximum number of iterations, no results from the hydro calculation are used and the model is left as if the hydro routine had never been called.

After a successful calculation of the hydrodynamic velocity field, several steps have to be performed in order to continue the overall model iteration. These steps are described in the following subsections.

A.8.1 Damping of the hydrodynamic solution

The first adjustment after the calculation of a hydro velocity field is the damping of the result, which is performed in the subroutine `hydro_dampresult`. In general, input damping (see Sect. A.7) turned out to be the most efficient way to ensure a smooth insertion of the hydro steps into the overall conversion regime, so in the best case nothing needs to be done here. Nevertheless methods for damping the resulting velocity field have been implemented, as they have been used in the first approach by Gräfener & Hamann (2005) and are unavoidable in some cases where the resulting velocity field differs too much from the previous one. In particular, the `hydro_dampresult`-routine performs the following tasks:

1. If the innermost value of the Rosseland continuum opacity is significantly larger than the suggested τ_{max}, the velocity field is shifted to ensure that the actual damping is performed in a regime with similar τ-value. This is ensured by an iterative process between shifting and recalculating the $\tau_{Ross,cont}$-scale after each shift. The radius grid is adjusted to cover the shifted velocity field properly.

2. If the radius grid has been changed, the old velocity field is now interpolated on the new grid points. In some cases this might require an extrapolation of the old velocity field. This is done using an exponential function that preserves both v and $\frac{\mathrm{d}v}{\mathrm{d}r}$ at the connection point:

$$v_{extrap}(r) = v_{ND} \cdot e^{\frac{\frac{\mathrm{d}v}{\mathrm{d}r}\big|_{ND}}{v_{ND}}\cdot(r - R_{ND})} \tag{A.16}$$

3. For every depth point, the old ($v_{\rm old}$) and new ($v_{\rm hydro}$) velocity fields are now mixed:

$$v_{\rm new}(r) = (1 - f_{\rm damp}) \cdot v_{\rm old}(r) + f_{\rm damp} \cdot v_{\rm hydro}(r) \tag{A.17}$$

The damping factor $f_{\rm damp}$ has to be specified in the model input (CARDS) file and has to be between zero and unity. For $f_{\rm damp} = 1$, the velocity field is completely changed to the new hydro solution. If no input damping is used, output damping factors around 0.1 or 0.2 are a good choice to avoid major disruption of a model. However, in cases with sufficient input damping or where the model is well situated and the overall energy balance is already fulfilled, $f_{\rm damp} = 1$ can actually be used and helps a lot to speed up the overall model calculation.

A.8.2 Conservation of optical depth (for HD-models)

Unless the new velocity field has been calculated via the method in Sect. 3.11.3, i.e. the conservation of $\tau_{\rm max}$ was already included in the hydro iteration, the solution does not conserve the total optical depth by default. In such cases the resulting velocity field has to be adjusted afterwards or the total (Rosseland continuum) optical depth will differ from the specified $\tau_{\rm max}$. In fact it can happen that during each hydro step the total optical depth decreases and the final model might end up with a maximum value of only ≈ 5 or even $\lesssim 2$ in some cases, i.e. the quasistatic layers have essentially been lost in the model and a significant part where the emergent spectrum is formed might be missing. This has to be avoided as the resulting spectra and stellar parameters cannot be compared to any real star.

The general iteration mechanism to conserve the optical depth is not that different from its counterpart in the `ensuretaumax`-routine described in Sect. 2.7, but the fact that the velocity field is given from the numerical solution of the hydrodynamic equation and thus only available in a tabulated form has to be considered. Thus, the mechanism here consists of the following steps:

1. Calculation of the current $\tau_{\rm Ross,cont}$-scale
2. Main iteration loop:
   a) Comparison of current $v(R_*)$ with $v_{\rm min}$ suggested from $\tau_{\rm Ross,cont}$-scale.
   b) Inner boundary extrapolation or interpolation to obtain $R(v_{\rm min})$. The various details of the different methods used here are described in detail in Sect. A.8.3.
   c) The radius grid is shifted by $\Delta R = R_* - R(v_{\rm min})$
   d) Redefined radius and density grid (r, ρ) based on the new $v(r)$
   e) Interpolation of electron temperature T and population numbers n_i one the new grid
   f) Calculation of the current $\tau_{\rm Ross,cont}$-scale
   g) Comparison of new $\tau_{\rm Ross,cont}(R_*)$ with specified $\tau_{\rm max}$. If the difference is still larger than ε_τ, $v_{\rm min}$ is adjusted
      - via $v_{\rm min} = v_{\rm min,last} \left(\frac{\tau_{\rm Ross,cont}(R_*)}{\tau_{\rm max}} \right)^{0.5 \cdot f_{\rm vdamp}}$ if $\tau_{\rm Ross,cont}(R_*) < \tau_{\rm max}$,
      - via averaging between the last two values of $v_{\rm min}$ if $\tau_{\rm Ross,cont}(R_*) > \tau_{\rm max}$,

- via spline interpolation $v_{\min} = v(\tau_{\max})$ if $\tau_{\mathrm{Ross,cont}}(R_*) > \tau_{\max}$ and averaging was not successful.

The damping factor f_{vdamp} starts with a value of one and is divided by two each time the solutions start to oscillate.

Not more than 100 iterations are performed. If the difference between the intended $\tau_{\max}$ and the actual value is still larger than ε_τ, the velocity field from the iteration with the smallest difference is used.

3. Optional Damping: The new $v_{\min}$-value can be mixed with the old one in order to damp the corrections to the velocity field. An additional calculation of the iteration steps above is performed in this case.

4. Calculation of the velocity gradient and $R(\tau_{\mathrm{Ross,cont}} = 2/3)$

5. Interpolation of the coarse grid radiation field XJC as well as the temperatures and populations numbers of the last three `STEAL` jobs on the new radius grid.

A.8.3 Inner boundary adjustments due to conservation of optical depth

The most striking difference in the conservation of the total Rosseland (continuum) optical depth after the hydrodynamic integration compared to the "standard" method in Sect. 2.7, is the adjustment of the velocity field during the $\tau_{\max}-$iteration, as the hydrodynamic solution is not described by a certain function and therefore one cannot easily adjust the velocity field like it would be able with a given velocity law. Especially if the innermost point does not reach $\tau_{\max}$, the velocity field needs to be extrapolated, which requires approximations and thus is the most crucial part.

In order to reach the required $\tau_{\max}$ and thus a suitable $v_{\min}$, different methods can be used. All methods, which have been implemented into the PoWR code, are described in following. The methods are referenced with numbers which are similar to those which can be specified in the CARDS file to enforce the use of a particular method.

Method 1: Velocity field approximation plus HD-cutoff

One of the simplest approaches is to use a general law in the innermost part and avoid any case selection between $\tau_{\mathrm{Ross,cont}}(R_*) > \tau_{\max}$ and $\tau_{\mathrm{Ross,cont}}(R_*) < \tau_{\max}$. For such an implementation one simply cuts off the hydro solution at a radius R_{hy}, such that $R_{\mathrm{crit}} > R_{\mathrm{hy}} > R_*$. To obtain the velocity field between R_* and R_{hy}, a velocity field of the following form is applied:

$$v(r) = a \cdot \left(\frac{r}{R_{\mathrm{hy}}}\right)^c \cdot e^{b\cdot\left(r - R_{\mathrm{hy}}\right)} \tag{A.18}$$

This function has an exponential decay known from the classical hydrostatic approach and the parameters a, b, and c can be adjusted to fit all three boundary conditions, namely:

$$v(R_*) = v_{\min} \tag{A.19}$$

$$v(R_{\mathrm{hy}}) = v_{\mathrm{hy}} \tag{A.20}$$

$$\left.\frac{\mathrm{d}v}{\mathrm{d}r}\right|_{r=R_{\mathrm{hy}}} = \left.\frac{\mathrm{d}v}{\mathrm{d}r}\right|_{\mathrm{hydro}} =: X \tag{A.21}$$

Solving this system of equations yields the following velocity field $v(r)$:

$$v(r) = v_{\mathrm{hy}} \cdot \left(\frac{r}{R_{\mathrm{hy}}}\right)^{\left[\frac{X}{v_{\mathrm{hy}}} - \frac{\ln\frac{v_{\mathrm{hy}}}{v_{\mathrm{min}}} + \frac{X}{v_{\mathrm{hy}}}\ln\frac{R_*}{R_{\mathrm{hy}}}}{R_{\mathrm{hy}} - R_* + \ln\frac{R_*}{R_{\mathrm{hy}}}}\right]} \cdot e^{\frac{\ln\frac{v_{\mathrm{hy}}}{v_{\mathrm{min}}} + \frac{X}{v_{\mathrm{hy}}}\ln\frac{R_*}{R_{\mathrm{hy}}}}{R_{\mathrm{hy}} - R_* + \ln\frac{R_*}{R_{\mathrm{hy}}}} \cdot \left(r - R_{\mathrm{hy}}\right)} \tag{A.22}$$

The implementation of this method is straight forward, but its biggest disadvantage is that this prespecified law usually does not fulfill the hydrodynamic equation. To achieve this goal, more complex methods need to be considered.

Method 2: Exponential extension plus regula falsi

Instead of cutting away a fraction of the hydrodynamic solution in any case, it makes sense to check first if the innermost point might already outrange the required value of τ_{max}. If this is case, its velocity v_{hy} will be larger than the required velocity v_{min} and it is sufficient to use the hydrodynamic solution up to a radius that can be obtained simply by interpolation. Following the efforts of Gräfener & Hamann (2005) one can improve this concept and replace a simple spline interpolation over $r(v)$ by an iterative approach using a regula falsi method with a spline interpolation over $v(r)$.

In the case of $v_{\mathrm{hy}} > v_{\mathrm{min}}$ however, the need for an extrapolation is still there. Similar to the previously described method this is done with an exponential function, but with a slightly different approach in the details. Here the exponential function is defined such that the exponent becomes zero at v_{hy}, which avoids the polynomial factor from the previous approach. The new approach therefore reads:

$$v(r) = v_{\mathrm{hy}} \cdot e^{-\alpha\cdot(R_{\mathrm{S}} - r)} \tag{A.23}$$

One can see immediately that for $R_{\mathrm{S}} = R_{\mathrm{hy}}$ the condition $v(R_{\mathrm{hy}}) = v_{\mathrm{hy}}$ is fulfilled. In order to furthermore achieve $v(R_*) = v_{\mathrm{min}}$ plus a velocity gradient fixed by the hydro solution at R_{hy}, the distance between R_{S} and R_* must not be arbitrary. Instead one obtains the condition

$$R_{\mathrm{S}} = R_* + \ln\left(\frac{v_{\mathrm{hy}}}{v_{\mathrm{min}}}\right) \cdot \frac{1}{\alpha}. \tag{A.24}$$

The second summand ensures that $v(R_*) = v_{\mathrm{min}}$ will be obtained. For the remaining parameter α we obtain a condition by requiring a continuous transition between the extrapolation and the hydrodynamic solution also for the gradient:

$$\left.\frac{\mathrm{d}v}{\mathrm{d}r}\right|_{r=R_{\mathrm{S}}} = \alpha \cdot v_{\mathrm{hy}} \tag{A.25}$$

This method comes at the cost of a small radius shift that affects usually the innermost grid points. Unless R_{S} has exactly the value of R_{hy}, the outer velocity field (i.e. the hydro solution) is shifted such that it fits with R_{S}.

Method 3: Quasi-hydrodynamic continuation plus regula falsi

Instead of performing an extrapolation using a predefined function, one can also try a direct extrapolation by using the hydrodynamic equation itself. This approach requires a few assumptions and might therefore not lead to a fully selfconsistent solution in any case, but

it has the least constrains compared to the other methods. This method is therefore called "quasi-hydrodynamic continuation" as it uses the same equations, but makes a few input assumptions. In fact this continuation is only performed if extrapolation is required at all. In case of $v_{\rm hy} < v_{\rm min}$, the regula falsi is used, similar to the previous method 2.

In order to perform the extrapolation, the radius grid is continued inwards using small steps, starting with a fraction of 0.7 of the innermost step size. The velocity v is then calculated by using $\frac{{\rm d}v}{{\rm d}r} = -\rho\mathcal{F}\mathcal{G}^{-1}$ from the hydrodynamic equation, assuming that $\Gamma(r)$ will approach 1. The the sound speed a is extrapolated by using the gradient that is obtained in between the grid points. This procedure is continued inwards until $v(r) \leq v_{\rm min}$.

Method 4: Velocity field shifting

In contrast to the previous two methods which usually require a radius shift, one could also think of shifting the velocities directly while keeping the radius grid fixed. Indeed it is the easiest way to add simple positive or negative shift Δv to the hydro solution $v_{\rm HDsol}$, i.e.

$$v(r) = v_{\rm HDsol}(r) + \Delta v. \tag{A.26}$$

This method keeps the slope of the overall hydro solution. As Δv is adjusted to keep the required $\tau_{\rm max}$, it is usually on the order of $v_{\rm min}$ and thus $\Delta v \ll v_\infty$. Therefore the velocity field in the outer part does not really differ from the hydrodynamic solution and the hydrodynamic equation is still fulfilled after shifting. In the innermost part however, the shifting is a significant change to the velocity field and the hydrodynamic equation is usually no longer fulfilled. Especially during early hydro iterations which can cause significant changes to the overall velocity slope, this method might even lead to a model situation where the hydrodynamic equation can no longer be solved. The regula-falsi plus extension methods (2 and 3) are therefore recommended at the start of a hydro calculation.

A.9 Overall implementation scheme of the hydrodynamic solution

The hydrodynamic calculations are implemented in the `steal` program and encapsulated in the `hydrosolve`-routine, which is called after all corrections to the temperature and population numbers have been performed. After describing the concepts and several details in the past sections, the overall scheme of the routine is outlined here:

1. Decoding of all parameters on the HYDRO and ALPHA input card
2. Determination of the number of jobs since the last hydrodynamic iteration
3. Check if all criteria for a new hydrodynamic calculation are fulfilled:
   - The hydrodynamic equation is not fulfilled with an accuracy better than 5% for all depth points
   - Enough jobs have passed since the last iteration (interval number is a user-defined input, default is 10)
   - Flux consistency is obtained for all depth points (better than a used-defined accuracy, default is 5%, criterion can be switched off)

- Optional: current corrections are below a specified limit

4. The main calculation routine `hdsolution` is called, containing:
   a) Adjustments performed before the hydro solution, see Sect. A.7
   b) Creation of analysis plot ($\mathcal{F}$-$\mathcal{G}$-plot) and corresponding parameter table
   c) Fine calculation of the candidate radius r_{crit} for the critical point
   d) Main hydro iteration:
      i. Integration of the hydrodynamic equation using a fourth-order Runge-Kutta scheme, starting inwards and outwards from r_{crit} (default)
      ii. Conversion criterion is checked
      iii. If not converged: Adjustment of $\dot{M}$ and/or v_{crit}, depending on the selection of the method
   e) Creation of the fine integration result plots
5. Adjustments performed after the hydro solution, see Sect. A.8

After a successful velocity update all stratifications have been changed. Thus a renewal of the Eddington factors (via `WRCONT` and `COLI+`) is enforced in the following radiative transfer calculation.

Appendix B

References

Abbott, D. C. 1980, ApJ, 242, 1183

Abbott, D. C. 1982, ApJ, 259, 282

Abbott, D. C., Bieging, J. H., & Churchwell, E. 1981, ApJ, 250, 645

Abbott, D. C. & Lucy, L. B. 1985, ApJ, 288, 679

Abbott, D. C., Telesco, C. M., & Wolff, S. C. 1984, ApJ, 279, 225

Auer, L. H. & Mihalas, D. 1968, ApJ, 151, 311

Auer, L. H. & Mihalas, D. 1969, ApJ, 156, 157

Auer, L. H. & Mihalas, D. 1972, ApJS, 24, 193

Barlow, M. J. & Cohen, M. 1977, ApJ, 213, 737

Baron, E., Hauschildt, P. H., Allard, F., et al. 2003, in IAU Symposium, Vol. 210, Modelling of Stellar Atmospheres, ed. N. Piskunov, W. W. Weiss, & D. F. Gray, 19

Beals, C. S. 1929, MNRAS, 90, 202

Böhm, K.-H. 1954, ZAp, 34, 182

Bouret, J.-C., Lanz, T., Hillier, D. J., et al. 2003, ApJ, 595, 1182

Cantiello, M., Langer, N., Brott, I., et al. 2009, A&A, 499, 279

Cassinelli, J. P. & Olson, G. L. 1979, ApJ, 229, 304

Castor, J. I. 1970, MNRAS, 149, 111

Castor, J. I., Abbott, D. C., & Klein, R. I. 1975, ApJ, 195, 157

Castor, J. L. 1974, MNRAS, 169, 279

Crowther, P. A., De Marco, O., & Barlow, M. J. 1998, MNRAS, 296, 367

Cunto, W. & Mendoza, C. 1992, Rev. Mexicana Astron. Astrofis., 23, 107

Curé, M., Cidale, L., & Rial, D. F. 2012, ApJ, 757, 142

de Koter, A., Heap, S. R., & Hubeny, I. 1997, ApJ, 477, 792

de Koter, A., Schmutz, W., & Lamers, H. J. G. L. M. 1993, A&A, 277, 561

Dessart, L. & Owocki, S. P. 2003, A&A, 406, L1

Dessart, L. & Owocki, S. P. 2005, A&A, 437, 657

Drew, J. E., Barlow, M. J., Unruh, Y. C., et al. 2004, MNRAS, 351, 206

Eversberg, T., Lépine, S., & Moffat, A. F. J. 1998, ApJ, 494, 799

Feldmeier, A. 1995, A&A, 299, 523

Feldmeier, A. 1998, A&A, 332, 245
Feldmeier, A. & Shlosman, I. 2002, ApJ, 564, 385
Friend, D. B. & Abbott, D. C. 1986, ApJ, 311, 701
Friend, D. B. & Castor, J. I. 1983, ApJ, 272, 259
Gabler, R., Gabler, A., Kudritzki, R. P., Puls, J., & Pauldrach, A. 1989, A&A, 226, 162
Gayley, K. G. 1995, ApJ, 454, 410
Gräfener, G. & Hamann, W.-R. 2005, A&A, 432, 633
Gräfener, G. & Hamann, W.-R. 2008, A&A, 482, 945
Gräfener, G., Koesterke, L., & Hamann, W.-R. 2002, A&A, 387, 244
Gräfener, G., Owocki, S. P., & Vink, J. S. 2012, A&A, 538, A40
Gräfener, G. & Vink, J. S. 2013, A&A, 560, A6
Gräfener, G., Vink, J. S., de Koter, A., & Langer, N. 2011, A&A, 535, A56
Hainich, R., Pasemann, D., Todt, H., et al. 2015, ArXiv e-prints
Hainich, R., Rühling, U., Todt, H., et al. 2014, A&A, 565, A27
Hamann, W.-R. 1980, A&A, 84, 342
Hamann, W.-R. 1981, A&A, 93, 353
Hamann, W.-R. 1985, A&A, 148, 364
Hamann, W.-R. 1986, A&A, 160, 347
Hamann, W.-R., Feldmeier, A., & Oskinova, L. M., eds. 2008, Clumping in hot-star winds
Hamann, W.-R. & Gräfener, G. 2003, A&A, 410, 993
Hamann, W.-R. & Gräfener, G. 2004, A&A, 427, 697
Hamann, W.-R., Gräfener, G., & Liermann, A. 2006, A&A, 457, 1015
Hamann, W.-R. & Koesterke, L. 1998, A&A, 335, 1003
Hamann, W.-R. & Schmutz, W. 1987, A&A, 174, 173
Harnden, Jr., F. R., Branduardi, G., Gorenstein, P., et al. 1979, ApJ, 234, L51
Hauschildt, P. H. 1992, J. Quant. Spec. Radiat. Transf., 47, 433
Herald, J. E., Hillier, D. J., & Schulte-Ladbeck, R. E. 2001, ApJ, 548, 932
Hillier, D. J. 1987, ApJS, 63, 947
Hillier, D. J. 1990, A&A, 231, 116
Hillier, D. J. 1991, A&A, 247, 455
Hillier, D. J. 2003, in Astronomical Society of the Pacific Conference Series, Vol. 288, Stellar Atmosphere Modeling, ed. I. Hubeny, D. Mihalas, & K. Werner, 199
Hillier, D. J. & Miller, D. L. 1998, ApJ, 496, 407
Hubeny, I., Heap, S. R., & Altner, B. 1991, ApJ, 377, L33
Hummer, D. G. 1963, MNRAS, 125, 461
Hummer, D. G. & Seaton, M. J. 1963, MNRAS, 125, 437
Jefferies, J. T. 1968, Spectral line formation (Waltham, Mass.: Blaisdell Pub. Co., 1968)
Johnson, M. C. 1925, MNRAS, 85, 813
Kingsburgh, R. L., Barlow, M. J., & Storey, P. J. 1995, A&A, 295, 75
Knödlseder, J., Cerviño, M., Le Duigou, J.-M., et al. 2002, A&A, 390, 945

Koesterke, L., Hamann, W.-R., & Gräfener, G. 2002, A&A, 384, 562
Kosirev, N. A. 1934, MNRAS, 94, 430
Kramer, R. H., Cohen, D. H., & Owocki, S. P. 2003, ApJ, 592, 532
Kubát, J. 2001, A&A, 366, 210
Kubát, J., Puls, J., & Pauldrach, A. W. A. 1999, A&A, 341, 587
Kudritzki, R. P. 2002, ApJ, 577, 389
Kudritzki, R. P., Pauldrach, A., Puls, J., & Abbott, D. C. 1989, A&A, 219, 205
Kurucz, R. L. 1979, ApJS, 40, 1
Lamers, H. J. G. L. M. & Cassinelli, J. P. 1999, Introduction to Stellar Winds (Cambridge, UK: Cambridge University Press, June 1999)
Lamers, H. J. G. L. M., Gathier, R., & Snow, Jr., T. P. 1982, ApJ, 258, 186
Lamers, H. J. G. L. M. & Leitherer, C. 1993, ApJ, 412, 771
Lamers, H. J. G. L. M., Snow, T. P., & Lindholm, D. M. 1995, ApJ, 455, 269
Langer, N. 1989, A&A, 210, 93
Liermann, A., Hamann, W.-R., Oskinova, L. M., Todt, H., & Butler, K. 2010, A&A, 524, A82
Lucy, L. B. 1964, SAO Special Report, 167, 93
Lucy, L. B. 1982, ApJ, 255, 278
Lucy, L. B. 1984, ApJ, 284, 351
Lucy, L. B. 2007, A&A, 468, 649
Lucy, L. B. & Abbott, D. C. 1993, ApJ, 405, 738
Lucy, L. B. & Solomon, P. M. 1970, ApJ, 159, 879
Lucy, L. B. & White, R. L. 1980, ApJ, 241, 300
MacGregor, K. B., Hartmann, L., & Raymond, J. C. 1979, ApJ, 231, 514
Martens, P. C. H. 1979, A&A, 75, L7
Martínez-Núñez, S., Sander, A., Gímenez-García, A., et al. 2015, A&A, 578, A107
Martins, F., Hillier, D. J., Paumard, T., et al. 2008, A&A, 478, 219
Massey, P., DeGioia-Eastwood, K., & Waterhouse, E. 2001, AJ, 121, 1050
Massey, P., Neugent, K. F., Hillier, D. J., & Puls, J. 2013, ApJ, 768, 6
Massey, P., Neugent, K. F., & Morrell, N. 2015, ApJ, 807, 81
Massey, P., Neugent, K. F., Morrell, N., & Hillier, D. J. 2014, ApJ, 788, 83
Michaux, Y. J. L., Moffat, A. F. J., Chené, A.-N., & St-Louis, N. 2014, MNRAS, 440, 2
Mihalas, D. 1978, Stellar atmospheres /2nd edition/ (San Francisco, W. H. Freeman and Co., 1978. 650 p.)
Mihalas, D., Kunasz, P. B., & Hummer, D. G. 1975, ApJ, 202, 465
Mihalas, D., Kunasz, P. B., & Hummer, D. G. 1976, ApJ, 206, 515
Milne, E. A. 1924a, MNRAS, 84, 354
Milne, E. A. 1924b, MNRAS, 85, 111
Milne, E. A. 1925, MNRAS, 86, 8
Milne, E. A. 1926, MNRAS, 86, 459
Morton, D. C. 1967a, ApJ, 150, 535

Morton, D. C. 1967b, ApJ, 147, 1017

Muijres, L. E., de Koter, A., Vink, J. S., et al. 2011, A&A, 526, A32

Muijres, L. E., Vink, J. S., de Koter, A., Müller, P. E., & Langer, N. 2012, A&A, 537, A37

Nelson, G. D. & Hearn, A. G. 1978, A&A, 65, 223

Oskinova, L. M., Hamann, W.-R., & Feldmeier, A. 2007, A&A, 476, 1331

Oskinova, L. M., Steinke, M., Hamann, W.-R., et al. 2013, MNRAS, 436, 3357

Owocki, S. 2004, in EAS Publications Series, Vol. 13, EAS Publications Series, ed. M. Heydari-Malayeri, P. Stee, & J.-P. Zahn, 163–250

Owocki, S. P. 1992, in Lecture Notes in Physics, Berlin Springer Verlag, Vol. 401, The Atmospheres of Early-Type Stars, ed. U. Heber & C. S. Jeffery, 393

Owocki, S. P., Castor, J. I., & Rybicki, G. B. 1988, ApJ, 335, 914

Owocki, S. P., Gayley, K. G., & Shaviv, N. J. 2004, ApJ, 616, 525

Owocki, S. P. & Puls, J. 1996, ApJ, 462, 894

Owocki, S. P. & Puls, J. 1999, ApJ, 510, 355

Owocki, S. P. & Puls, J. 2002, ApJ, 568, 965

Owocki, S. P. & Rybicki, G. B. 1984, ApJ, 284, 337

Owocki, S. P. & Rybicki, G. B. 1986, ApJ, 309, 127

Parker, E. N. 1960, ApJ, 132, 821

Parker, E. N. 1965, Space Science Reviews, 4, 666

Pauldrach, A. 1987, A&A, 183, 295

Pauldrach, A. & Herrero, A. 1988, A&A, 199, 262

Pauldrach, A., Puls, J., & Kudritzki, R. P. 1986, A&A, 164, 86

Pauldrach, A. W. A., Hoffmann, T. L., & Lennon, M. 2001, A&A, 375, 161

Pauldrach, A. W. A., Kudritzki, R. P., Puls, J., Butler, K., & Hunsinger, J. 1994, A&A, 283, 525

Press, W. H., Teukolsky, S. A., Vetterling, W. T., & Flannery, B. P. 1992, Numerical recipes in FORTRAN. The art of scientific computing (Cambridge: University Press, |c1992, 2nd ed.)

Puls, J. 1987, A&A, 184, 227

Puls, J. 2008, in IAU Symposium, Vol. 250, IAU Symposium, ed. F. Bresolin, P. A. Crowther, & J. Puls, 25–38

Puls, J., Kudritzki, R.-P., Herrero, A., et al. 1996, A&A, 305, 171

Puls, J., Springmann, U., & Lennon, M. 2000, A&AS, 141, 23

Puls, J., Urbaneja, M. A., Venero, R., et al. 2005, A&A, 435, 669

Puls, J., Vink, J. S., & Najarro, F. 2008, A&A Rev., 16, 209

Saha, M. N. 1919, ApJ, 50, 220

Sander, A., Hamann, W.-R., & Todt, H. 2012, A&A, 540, A144

Sander, A., Shenar, T., Hainich, R., et al. 2015, A&A, 577, A13

Santolaya-Rey, A. E., Puls, J., & Herrero, A. 1997, A&A, 323, 488

Sanyal, D., Grassitelli, L., Langer, N., & Bestenlehner, J. M. 2015, A&A, 580, A20

Schmutz, W., Hamann, W.-R., & Wessolowski, U. 1989, A&A, 210, 236

Seward, F. D., Forman, W. R., Giacconi, R., et al. 1979, ApJ, 234, L55
Shaviv, N. J. 2001a, ApJ, 549, 1093
Shaviv, N. J. 2001b, MNRAS, 326, 126
Shenar, T., Hamann, W.-R., & Todt, H. 2014, A&A, 562, A118
Shenar, T., Oskinova, L., Hamann, W.-R., et al. 2015, ArXiv e-prints
Snow, Jr., T. P. & Morton, D. C. 1976, ApJS, 32, 429
Sobolev, V. V. 1957, Soviet Astronomy, 1, 678
Struve, O. & Elvey, C. T. 1934, ApJ, 79, 409
Sundqvist, J. O., Petit, V., Owocki, S. P., et al. 2013, MNRAS, 433, 2497
Sundqvist, J. O., Puls, J., & Owocki, S. P. 2014, A&A, 568, A59
Todt, H., Sander, A., Hainich, R., et al. 2015, A&A, 579, A75
Tramper, F., Sana, H., de Koter, A., Kaper, L., & Ramírez-Agudelo, O. H. 2014, A&A, 572, A36
Tramper, F., Straal, S. M., Sanyal, D., et al. 2015, A&A forthcoming, ArXiv e-print 1507.00839
Unsöld, A. 1951, Naturwissenschaften, 38, 525
Unsöld, A. 1955, Physik der Sternatmosphären, mit besonderer Berücksichtigung der Sonne (Berlin, Springer, 1955. 2. Aufl.)
Šurlan, B., Hamann, W.-R., Kubát, J., Oskinova, L. M., & Feldmeier, A. 2012, A&A, 541, A37
van der Hucht, K. A. 2001, New A Rev., 45, 135
Vink, J. S. & de Koter, A. 2005, A&A, 442, 587
Vink, J. S., de Koter, A., & Lamers, H. J. G. L. M. 1999, A&A, 350, 181
Vink, J. S., de Koter, A., & Lamers, H. J. G. L. M. 2000, A&A, 362, 295
Vink, J. S., de Koter, A., & Lamers, H. J. G. L. M. 2001, A&A, 369, 574
Vink, J. S., Muijres, L. E., Anthonisse, B., et al. 2011, A&A, 531, A132
von Zeipel, H. 1924, MNRAS, 84, 665
Wolf, C. J. & Rayet, G. 1867, Comptes rendus de l'Académie des sciences, 65, 292
Wright, A. E. & Barlow, M. J. 1975, MNRAS, 170, 41

List of Abbreviations

For convenience, the following journal abbreviations are used in the list of references:

A&A	Astronomy & Astrophysics
A&AS	Astronomy & Astrophysics, Supplement Series
AJ	Astronomical Journal
ApJ	The Astrophysical Journal
ApJS	The Astrophysical Journal, Supplement Series
MNRAS	Monthly Notices of the Royal Astronomical Society
ZAp	Zeitschrift für Astrophysik

Appendix C

List of Figures

Danksagung

An dieser Stelle möchte ich mich ganz herzlich bei allen bedanken, die mich direkt oder indirekt bei der Anfertigung dieser Arbeit unterstützt haben. Die entspannte, aber zugleich stets konstruktive Atmosphäre in der Arbeitsgruppe ist ein ganz wesentlicher Faktor, um auch über Jahre hinweg die Motivation zu erhalten, die für das Gelingen eines solchen Projekts nötig ist. Die permanente Hilfs- und Diskussionsbereitschaft aller Kollegen mag manchem selbstverständlich erscheinen, ist aber Ausdruck einer positiven, unterstützenden Haltung, die alles andere als selbstverständlich ist.

Besonders erwähnen möchte ich hier Wolf-Rainer Hamann, der nicht nur mit seinem Projektantrag diese Arbeit erst möglich gemacht hat, sondern auch immer ein offenes Ohr für Fragen und Probleme hatte. Ein besonderes Dankeschön geht an dieser Stelle auch an Rainer Hainich, der sich nicht gescheut hat immer wieder meine zuweilen noch nicht bugbefreiten Testversionen des PoWR-Codes auszuprobieren sowie an Helge Todt, der mit seiner Bereitstellung der im notwendigen Format aufbereiteten Atomdaten einen wichtigen Baustein zum Gelingen dieser Arbeit geliefert hat. Herzlich bedanken möchte ich mich auch bei meinem langjährigen Bürokollegen Martin Steinke, der neben hilfreichen Werkzeugen zuweilen schon Lösungen für Probleme lieferte, noch bevor man ihn auch nur darauf angesprochen hatte. Nicht zu vergessen sind natürlich auch Tomer Shenar, Lida Oskinova und David Gruner, die mir – mal direkter, mal indirekter – durch diverse Gespräche zusätzliche Ideen und Inspirationen geliefert haben. Dank geht auch an Götz Gräfener, der in seiner Zeit in Potsdam mit seiner Pionierarbeit zum Thema hydrodynamisch-konsistente WR-Atmosphären wichtige technische Grundlagen für diese Arbeit geschaffen hat.

Ein ganz besonderer Dank geht auch an Andrea Brockhaus, die nicht nur eine wertvolle Stütze auf dem Weg durch den Formaliendschungel und die Untiefen der Bürokratie ist, sondern auch immer die Bedürfnisse der Mitarbeiter der Arbeitsgruppe im Blick hat und mit ihrem Engagement einen entscheidenden Beitrag für das gute Arbeitsklima leistet.

Mein ganz besonderer Dank geht auch an meine Eltern, Ursula und Manfred Sander, die mich in all den Jahren in meinen Zielen und Wünschen bestärkt haben. Euer Verständnis und euer Vertrauen hat stets mir einen wertvollen Rückhalt verschafft. Dank geht auch an alle meine Freunde außerhalb der Astrophysik, die mir dabei geholfen haben gerade auch in stressigen Zeiten mal den Kopf frei zu bekommen.

Nicht zuletzt möchte ich mich bei allen bedanken, die diese Arbeit im Vorfeld gegengelesen und so zur Beseitigung von Gedankensprüngen, Tippfehlern und irreführenden Wortneuschöpfungen beitragen haben.

Während der Erstellung dieser Dissertation wurde ich von der Deutschen Forschungsgemeinschaft finanziell unterstützt, die das Projekt unter dem Kennzeichen HA 1455/22 förderte.